



HAL
open science

Développement d'imagerie métabolique rapide et robuste chez l'homme à haut champ magnétique

Thaddée Delebarre

► **To cite this version:**

Thaddée Delebarre. Développement d'imagerie métabolique rapide et robuste chez l'homme à haut champ magnétique. Physique Médicale [physics.med-ph]. Université Paris-Saclay, 2024. Français. NNT : 2024UPAST001 . tel-04559246

HAL Id: tel-04559246

<https://theses.hal.science/tel-04559246>

Submitted on 25 Apr 2024

HAL is a multi-disciplinary open access archive for the deposit and dissemination of scientific research documents, whether they are published or not. The documents may come from teaching and research institutions in France or abroad, or from public or private research centers.

L'archive ouverte pluridisciplinaire **HAL**, est destinée au dépôt et à la diffusion de documents scientifiques de niveau recherche, publiés ou non, émanant des établissements d'enseignement et de recherche français ou étrangers, des laboratoires publics ou privés.

Development of fast and robust metabolic imaging in humans at high magnetic field

*Développement d'imagerie métabolique rapide et
robuste chez l'homme à haut champ magnétique*

Thèse de doctorat de l'université Paris-Saclay

École doctorale n°575, electrical, optical, bio : physics and engineering (EOBE)
Spécialité de doctorat: Physique et Imagerie Médicale
Graduate School : Sciences de l'ingénierie et des systèmes
Réfèrent : Faculté des sciences d'Orsay

Thèse préparée dans l'unité de recherche **BAOBAB** (Université Paris-Saclay, CEA, CNRS), sous la
direction de **Luisa CIOBANU**, directrice de recherche et le co-encadrement de **Nicolas
BOULANT**, directeur de recherche

Thèse soutenue à Paris-Saclay, le 19 janvier 2024, par

Thaddée DELEBARRE

Composition du jury

Membres du jury avec voix délibérative

Marc DHENAIN
Directeur de recherche, Université Paris-Saclay
Guillaume DUHAMEL
Directeur de recherche, Aix-Marseille Université
Shaihan MALIK
Reader (eq. MCF HDR), King's College London
Julien FLAMENT
Chargé de recherche, Université Paris-Saclay

Président du jury
Rapporteur & Examineur
Rapporteur & Examineur
Examineur

Titre: Développement d'imagerie métabolique rapide et robuste chez l'homme à haut champ magnétique

Mots clés: CEST, IRM, haut-champ magnétique, transmission parallèle, métabolisme cérébral

Résumé: L'imagerie par résonance magnétique du transfert de saturation par échange chimique (IRM CEST) représente un outil puissant pour l'étude du métabolisme, offrant une résolution temporelle et spatiale supérieure ainsi qu'une sensibilité accrue par rapport à la spectroscopie par résonance magnétique. L'IRM CEST permet la détection indirecte de certains métabolites grâce à l'interaction entre leurs protons et ceux de l'eau. Le CEST peut cartographier le glucose, le glutamate et la créatine, qui sont des métabolites importants impliqués dans les cancers et les maladies neurodégénératives et musculosquelettiques, ce qui en fait un outil de bio-imagerie prometteur. Le développement rapide de l'IRM à haut champ magnétique (≥ 7 T) au cours des dernières décennies a grandement bénéficié au CEST, ouvrant la voie à de nouvelles applications et suscitant ainsi un intérêt croissant. L'objectif de cette thèse est de développer l'IRM CEST dans un contexte clinique, en tirant pleinement parti des champs magnétiques élevés pour augmenter la robustesse et la vitesse des acquisitions CEST. Pour ce faire, nous nous concentrons sur deux objectifs principaux. Le premier est de développer la méthode d'imagerie CEST dans un environnement clinique, en surmontant les limitations pratiques associées aux scanners IRM cliniques à haut champ, notamment les contraintes strictes du débit d'absorption spécifique (DAS) et des hétérogénéités de champ (B1) des RadioFréquences (RF).

Pour atteindre ce premier objectif, une séquence CEST en transmission parallèle a été mise au point. La transmission parallèle utilise une antenne d'émission RF multicanal, qui peut être contrôlée indépendamment pour réduire l'hétérogénéité B1. En utilisant la transmission parallèle, nous avons mis en œuvre une stratégie d'acquisition qui nous a permis de produire des images CEST avec trois fois moins d'hétérogénéité B1, et deux fois plus rapidement que l'état de l'art de la littérature. Le deuxième objectif est d'évaluer la performance du CEST, pondérée en glucose et glutamate, dans la détection et la caractérisation du vieillissement normal et pathologique. Une étude clinique a été réalisée, impliquant des volontaires sains jeunes et âgés ainsi que des patients atteints de la maladie d'Alzheimer. Les résultats ont montré que le CEST peut détecter les variations globales de glutamate et de glucose dans le cerveau associées au vieillissement. L'acquisition et l'exploitation de données provenant de patients atteints de la maladie d'Alzheimer sont, eux, toujours en cours. En conclusion, cette thèse a permis de développer des méthodes CEST à haut champ et d'évaluer leurs performances dans l'étude du vieillissement. Ces résultats ouvrent des perspectives encourageantes pour l'utilisation du CEST comme biomarqueur de la maladie d'Alzheimer et d'autres maladies neurodégénératives.

Title: Development of fast and robust metabolic imaging in humans at high magnetic field

Keywords: CEST, MRI, high magnetic field, parallel transmission, cerebral metabolism

Abstract: Chemical Exchange Saturation Transfer Magnetic Resonance Imaging (CEST MRI) represents a powerful tool for the study of metabolism, offering superior temporal and spatial resolution as well as increased sensitivity compared to Magnetic Resonance Spectroscopy (MRS). CEST MRI enables the indirect detection of certain metabolites through the interaction between their labile protons and those of bulk water. CEST can map glucose, glutamate, creatine, which are important metabolites involved in cancers, and neurodegenerative and musculoskeletal diseases, representing therefore a promising bioimaging tool. The rapid development of high magnetic field MRI (≥ 7 T) in recent decades greatly benefits CEST, opening up new applications and generating growing interest. The aim of this thesis is to develop CEST MRI in a clinical context, taking full advantage of high magnetic fields to increase the robustness and speed of CEST acquisitions. To this end, we focus on two main objectives. The first is to develop the CEST imaging method in a clinical environment, overcoming the practical limitations associated with high-field clinical MRI scanners, notably the strict constraints of Specific Absorption Rate (SAR) and RadioFrequency (RF) field heterogeneities (B1). To achieve this first objective, a parallel transmission CEST sequence was de-

veloped. Parallel transmission uses a multi-channel RF transmit antenna, which can be controlled independently to reduce B1 heterogeneity. Moreover, parallel transmission also allows optimized energy management using virtual observation points (a strategy developed in the laboratory) By making use of parallel transmission we have implemented an acquisition strategy which allowed us to produce CEST images with three times less B1 heterogeneity, and two times faster than compared to the state of the art literature reports. The second objective is to evaluate the performance of CEST, glucose, and glutamate weighted, in detecting and characterizing normal and pathological aging. A clinical study was carried out, involving young and elderly healthy volunteers as well as Alzheimer's disease (AD) patients. The results showed that CEST can detect global variations in glutamate and glucose in the brain associated with aging. The acquisition and exploitation of data from AD patients is still in progress. In conclusion, this thesis has enabled the development of high-field CEST methods and the evaluation of their performance in the study of aging. These results open up encouraging prospects for the use of CEST as a biomarker of AD and other neurodegenerative diseases.

Remerciements

J'entame ces lignes avec une profonde gratitude envers tous ceux qui m'ont accompagné tout au long de ces trois années et sans qui ce travail n'aurait probablement pas abouti.

Un sincère merci à toi, Luisa, pour avoir été mon guide tout au long de ce projet. Ton énergie inébranlable et ta persévérance ont été des sources d'inspiration constantes.

Nicolas, je te suis reconnaissant pour ta rigueur et ton esprit critique aiguisé, qui ont grandement contribué à la qualité et à la pertinence de ce travail.

Merci à l'ensemble des membres de mon jury de thèse pour le temps et l'intérêt que vous avez accordés à la lecture de mon manuscrit et pour les échanges enrichissant lors de la soutenance.

Merci aux permanents des équipes METRIC et CIEL pour les discussions techniques qui ont élargi ma perspective sur le projet. Un merci particulier à Frank, Vincent et Alexandre qui ont généreusement partagé leur expertise et consacré du temps aux premières manipulations. Davide, merci pour tes conseils et ton aide, je me souviendrai de ton motto. Merci Michel pour ton implication dans le projet.

Un chaleureux remerciement aux manips radio, Chantal, Valérie, Yann, et Lucile, pour le temps passé en salle des consoles, et à l'ensemble des membres d'UNIACT qui rendent possible les expériences sur volontaires.

Aux membres de l'équipe CIEL, Sébastien, Fawzi, Benoit, Françoise, merci pour les moments conviviaux autour des repas, les discussions enrichissantes sur des sujets divers et variés. Une pensée particulière pour Erwan, dont la capacité à élever les débats a été une source d'inspiration constante.

Un grand merci aux doctorants, post-doctorants, alternants et stagiaires qui ont partagé ce chemin avec moi. Solène, Marianne, Paul, Corentin, Clémentine, Gaëlle, Koven, Aurélien, Camille, Flavie, Roxane, Pauline, les membres de l'équipe Ginko, merci pour ces échanges mémorables. Romain et Camélia, qui reprenez le flambeau du CEST, amusez vous bien.

À mes amis qui m'ont entouré jusqu'à la soutenance, merci pour votre soutien.

Un immense merci à mes parents qui ont été des modèles pour moi, à mes soeurs, mon frère.

Merci à toi, Sophie, pour ta présence à mes côtés, ton soutien est inestimable.

Table of contents

Remerciements	iii
Table of contents	v
Synthèse en français	vii
List of symbols and abreviations	xxi
Context and objectives	1
Context	1
Thesis outline	2
1 Introduction	3
1.1 Introduction to CEST MRI	4
1.1.1 Metabolic imaging	4
1.1.2 Origin of CEST	5
1.1.3 CEST contrast estimation	12
1.1.4 Applications	14
1.2 High field MRI for CEST	18
1.2.1 Benefits and challenges of high-fields MRI	18
1.2.2 Parallel Transmission	19
1.2.3 Specific absorption rate consideration	21
1.3 Conclusion	21
2 Background	23
2.1 Imaging System	24
2.1.1 Magnets	24
2.1.2 Coils	25
2.1.3 Adjustments	25
2.2 Phantoms	26
2.3 In vivo experiments	28
3 Development of CEST at 7 T	31
3.1 CEST-EPI Sequence	32
3.1.1 CEST-EPI pTx	32
3.1.2 CEST-EPI fast	34
3.2 GlucoCEST and GluCEST optimal saturation	37
3.2.1 GlucoCEST	38
3.2.2 Pulse shape	39
3.2.3 Saturation parameters	42
3.2.4 Similar developpement for GluCEST	44
3.2.5 Discussion and conclusion	44
3.3 Experimental validation	45

3.3.1	CEST-EPI	46
3.3.2	CEST-EPI fast	50
3.3.3	MetaPulses	52
3.4	Static field inhomogeneities artifacts correction	55
3.4.1	Consequences of inhomogeneities of static field on CEST	55
3.4.2	Post-processing mitigation	55
3.4.3	Discussion and conclusion	58
4	Efficient CEST saturation using pTx and VOPs	59
4.1	Introduction	60
4.2	Theory	60
4.3	Methods	61
4.3.1	CEST acquisitions	62
4.3.2	Data analysis	63
4.4	Results	63
4.4.1	Pulse scheme efficiency	63
4.4.2	In vitro CEST results	66
4.4.3	An attempt of Dynamic Glucose-Enhanced CEST MRI	67
4.4.4	In vivo pTx CEST results	70
4.5	Discussion and perspectives	73
4.6	Conclusion	76
5	Application in young, elderly and Alzheimer’s disease patients	77
5.1	Introduction	78
5.2	Methods	78
5.2.1	MRI protocol	79
5.2.2	PET protocol	80
5.2.3	CEST processing pipeline	81
5.3	Results	82
5.3.1	Posterior brain volume	82
5.3.2	Hippocampi volume	85
5.4	Discussion and perspectives	85
5.4.1	An unbiased CEST metric	86
5.5	Conclusion	93
6	Conclusion and perspectives	95
6.1	General conclusion	96
6.2	Perspectives	97
6.2.1	CEST acquisition	97
6.2.2	CEST quantification	97
6.2.3	Futures applications	97
6.3	Conclusion	98
7	List of publications	99
A	Glutamate CEST experiments	101
B	Motion correction	105

Synthèse en français

L'IRM par transfert de saturation par échange chimique (CEST en anglais) est une méthode récente qui permet la détection de molécules autre que l'eau, par IRM. Sa plus grande sensibilité par rapport à la spectroscopie par résonance magnétique permet d'imager en un temps plus court, avec une meilleure résolution spatiale et une meilleure couverture de la zone imagée. Les développements récents des IRM à haut champ magnétique (≥ 7 T) bénéficient énormément à l'imagerie CEST en augmentant ses capacités de détection ainsi qu'en permettant de détecter d'autres métabolites que ceux observables à plus bas champ.

Les patients atteints par la maladie d'Alzheimer présentent un métabolisme du glucose altéré dans le cerveau. Cette altération peut être détectée par tomographie par émission de positrons mais cette méthode requiert la prise d'un radiotracer radioactif qui est lourd et cher à synthétiser. L'utilisation de l'IRM CEST pour l'étude de cette maladie pourrait ouvrir de nouvelles portes quant à son diagnostic, sa caractérisation et sa compréhension.

L'objectif de cette thèse est de développer l'IRM CEST à haut champ magnétique chez l'Homme, ce qui porte son lot de défis, et d'ensuite évaluer les performances de cette technique comme moyen d'obtenir des biomarqueurs de la maladie d'Alzheimer.

Introduction à l'imagerie CEST

Depuis l'invention des rayons X, l'imagerie médicale permet de réaliser des images du corps humain. Aujourd'hui, plusieurs techniques co-existent pour des applications différentes. La tomodensitométrie (CT-scan en anglais) est issue du développement de la radiographie et permet de réaliser des images 3D des tissus solides ou des os. Les ultrasons, tout comme l'IRM, permettent de distinguer les tissus mous. Enfin, les méthodes d'imagerie nucléaire, comme la tomographie par émission de positon (TEP), consiste à l'injection d'un produit radioactif dont la détection de sa désintégration permet la production d'une image. Les applications de ces techniques peuvent fournir différentes informations sur le corps, celles-ci étant d'ordre structurelles, fonctionnelles, vasculaires voire moléculaires.

L'IRM est une technique d'imagerie qui repose sur la résonance des noyaux d'hydrogène lorsqu'ils sont placés dans un champ magnétique. En appliquant une onde radio à la fréquence de ces noyaux, ils deviennent excités. Ils retournent à leur état d'équilibre en ré-émettant une onde radio qui est détectée par une antenne. Un pilotage judicieux de la machine permet d'en reconstruire une image 2D ou 3D. Un des atouts de l'IRM est que cette technique d'imagerie est non-ionisante; contrairement aux méthodes basées sur les rayons X ou de scintigraphie. L'IRM est particulièrement intéressante pour sa versatilité, en pilotant le système d'une manière spécifique, il est possible d'observer différents types de tissus, de détecter la réponse hémodynamique lors de l'activation neuronale, de visualiser les faisceaux d'axones dans la substance blanche ou encore de mesurer les concentrations de certains métabolites.

Une technique d'IRM récente, le transfert de saturation par échange chimique (CEST en anglais), permet notamment de détecter les métabolites pour en réaliser la cartographie. Cette technique repose sur l'échange de protons qui a lieu entre des molécules différentes. L'eau étant la principale source de protons dans notre corps, on peut considérer que les échanges chimiques n'ont lieu qu'entre l'eau libre et un soluté (le métabolite). Lorsque l'on applique une onde RadioFréquence (RF)

sélective assez longtemps, le signal de résonance magnétique émis par le soluté disparaît (Figure 1B). Les échanges chimiques ayant cours entre l'eau et le soluté, des protons saturés du soluté vont passer dans le groupe de l'eau et des protons non saturés vont rejoindre le soluté. Cela offre de nouveaux protons que l'onde RF peut saturer et qui vont pouvoir s'échanger, et ainsi de suite. Les protons saturés se trouvent donc de plus en plus nombreux dans le groupe de l'eau, jusqu'à faire diminuer de manière significative le signal de résonance magnétique de l'eau (Figure 1C). Au bout de quelques secondes, un état d'équilibre est trouvé entre la saturation CEST, qui ajoute des protons saturés, et la relaxation T_1 qui permet à la magnétisation de retourner à l'équilibre. La différence de la quantité de magnétisation de l'eau avant et après saturation permet de mesurer de manière indirecte la quantité du soluté.

Le rapport entre le nombre de protons du soluté et le nombre de protons saturés qui sont stockés dans le groupe de l'eau peut être de plusieurs centaines voire davantage lorsque le soluté est une molécule exogène, conçue pour le CEST. Ce rapport important permet d'améliorer d'autant le rapport signal sur bruit (SNR en anglais) par rapport à la détection directe du métabolite par spectroscopie par résonance magnétique.

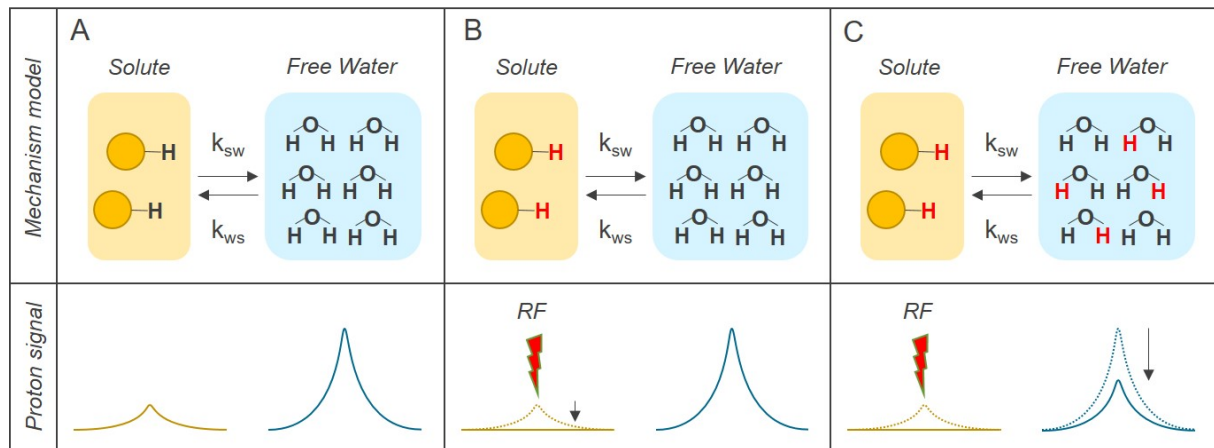


Figure 1: Schéma du mécanisme à l'œuvre en CEST, entre deux groupes, celui de l'eau libre et celui d'un soluté. (A) Situation initiale à l'équilibre, les protons du soluté produisent un faible signal RMN, proportionnel à leur concentration. (B) Sous une saturation sélective, le signal du soluté est effacé. (C) Avec l'échange chimique, la saturation du soluté est transférée au groupe de l'eau, qui devient alors saturé, et le signal RMN de l'eau diminue.

Avec l'avènement des IRM à haut champ magnétique, les possibilités de détection en CEST se trouvent améliorées. Des avancées significatives dans la détection de métabolites comme le glutamate, le glucose ou la créatine ont vu le jour, ainsi que des applications nombreuses. Toutefois, l'IRM à haut champ magnétique chez l'homme n'est pas sans difficultés et deux éléments principaux limitent le CEST à ces valeurs champs.

Avec les champs magnétiques plus intenses, la longueur d'onde des impulsions RF utilisées pour exciter les spins se trouve raccourcie au point d'être plus petite que la dimension du cerveau (12 cm à 7 T). Par un phénomène d'interférences constructives et destructives, des inhomogénéités de contraste apparaissent dans le cerveau (Figure 2). Corriger ces inhomogénéités est essentiel pour produire des images CEST robustes car elles entraînent des erreurs de quantification importantes. Un autre élément à prendre en compte lorsque l'on réalise du CEST à haut champ magnétique est le dépôt d'énergie. Le Débit d'Absorption Spécifique (DAS ou SAR en anglais) renseigne sur l'énergie déposée par les ondes RF dans un élément de tissu. Le DAS augmente presque de manière quadratique avec le champ magnétique et fait l'objet d'une norme précise afin de protéger les sujets passant dans l'IRM. Or, l'imagerie CEST nécessite de longues saturations RF pour maximiser le contraste, ce qui est intensif en terme de DAS. L'enjeu est donc de concevoir des saturations CEST permettant l'obtention d'un contraste optimal tout en respectant les normes de DAS.

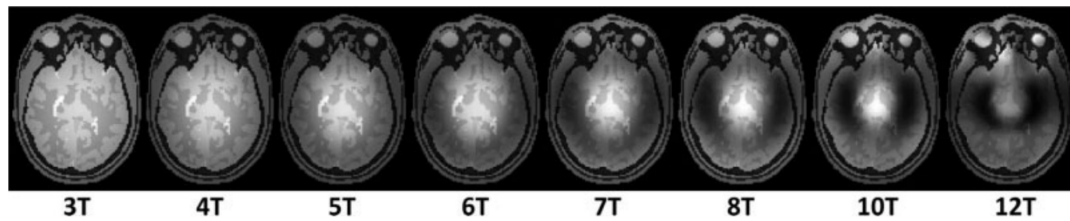


Figure 2: Simulation des effets des inhomogénéités de B_1^+ en fonction du champ magnétique. Figure adaptée de [Webb and Collins \(2010\)](#).

Cette thèse porte dans un premier temps sur l'élaboration d'une séquence CEST à 7 T et son optimisation pour réaliser l'imagerie du glucose. Par la suite, l'optimisation du module de saturation en transmission parallèle est étudié en utilisant les VOPs (Point d'Observation Virtuels), afin de permettre une imagerie CEST rapide et robuste. Enfin, les outils développés sont utilisés pour caractériser l'efficacité du CEST pour l'étude du vieillissement et de la maladie d'Alzheimer.

Développement du CEST à 7 T

Séquences CEST

Le premier élément à développer pour obtenir des images CEST était la séquence d'IRM CEST. Afin de résoudre les inhomogénéités de B_1^+ , une méthode élégante est l'utilisation de la transmission parallèle (pTx). Cette technique consiste à piloter plusieurs canaux de l'antenne RF de manière judicieuse afin que le motif d'interférences obtenu soit le plus homogène possible. Ainsi, avoir une saturation CEST en transmission parallèle est un des éléments importants du cahier des charges de la séquence CEST qui a été développée.

Comme nous l'avons abordé plus haut, une longue saturation RF est appliquée lors d'une expérience CEST. Cette saturation peut se faire de manière continue, pendant plusieurs secondes sur les IRM précliniques, mais n'est généralement pas réalisable sur les systèmes cliniques, qui limitent la durée des impulsions RF à une centaine de millisecondes.

La séquence CEST qui a été développée est basée sur une séquence EPI Siemens qui a été modifiée. Nous y avons adjoint un module de saturation pulsée en pTx. Le schéma de saturation retenu comporte deux modes pTx qui sont entrelacés et répétés un certain nombre de fois pour rendre la saturation suffisamment longue. Le diagramme de cette séquence est schématisé en Figure 3.

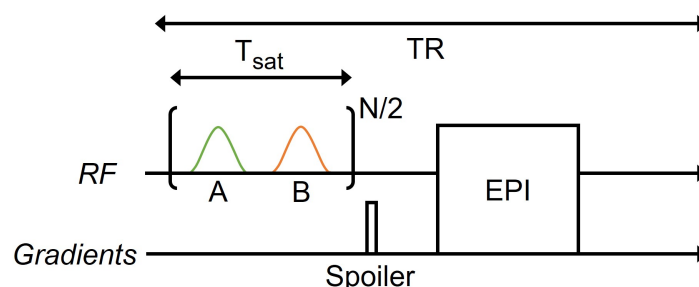


Figure 3: Diagramme temporel de la séquence CEST-EPI. Ici, une saturation à deux modes est représentée avec les impulsions colorées A et B.

Une autre séquence, basée sur la séquence précédente a été développée par la suite. Cette dernière permet de réaliser l'acquisition de plusieurs slices dans le même laps de temps que la séquence CEST-EPI, grâce à l'utilisation du CEST en régime permanent. Cette séquence utilise aussi les MetaPulses,

qui permettent d'utiliser le pTx également lors de l'excitation. Cela permet une amélioration notable du SNR de la séquence.

Paramètres optimaux pour le GlucoCEST

Pour les deux séquences, la saturation se fait de manière pulsée. L'enjeu pour obtenir un contraste maximal est de définir les paramètres de la saturation : durée des impulsions, intensité et durée de la saturation, ainsi que durée d'interpulses.

Le glucose possède plusieurs groupes hydroxyles échangeants avec l'eau. Situées entre 0,8 ppm et 2,5 ppm, ils s'échangent rapidement avec l'eau (conditions d'échange rapide) ce qui complique l'obtention d'un effet CEST sélectif avec ce métabolite.

Plusieurs méthodes permettent de modéliser le système physique régissant le CEST. À l'aide des solutions analytiques et sous des hypothèses simplificatrices, il a été possible d'estimer une valeur d'intensité de saturation (B_1) optimal pour le CEST du glucose. Ce modèle ne prend pas en compte la complexité qui peut avoir lieu pour des saturations pulsées et pour des métabolites échangeant rapidement, sous des intensités de saturation élevées. Des simulations ont donc été entreprises pour définir les paramètres de saturation optimaux pour le glucose (Figure 4). Elles ont permis de définir le protocole qui sera suivi par la suite pour réaliser des cartes de CEST maximisant le contraste par glucose. Les cartes obtenues sont toutefois appelées ici 'cartes pondérées en hydroxyle' car de nombreux autres métabolites contribuent aussi à la mesure.

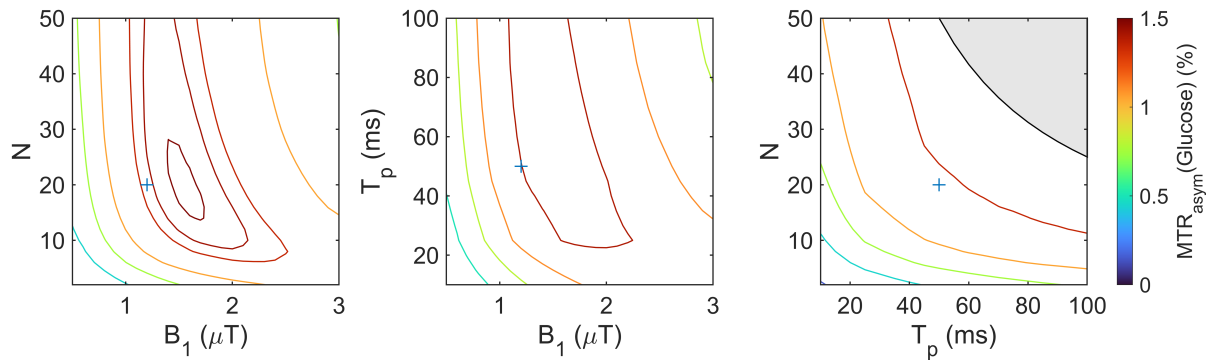


Figure 4: Paramètres de saturation optimaux pour le CEST du glucose. Les isolignes de MTR_{asym} sont tracées respectivement à T_p , N et $B_{1,\text{mean}}$ constants. Le réglage retenu est indiqué par une croix bleue. La zone grise n'est pas réalisable ($T_{\text{sat}} > TR$).

Le même travail a été fait pour le glutamate et la validation expérimentale de ces simulations sur des phantoms a été réalisée. (Un phantom est un objet imitant le cerveau humain et qui permet des mesures IRM dans des conditions maîtrisées et sans avoir besoin d'avoir recours à des volontaires.)

Inhomogénéités de champ statique

Comme cela est mis en évidence en Figure 5, les inhomogénéités de champ statique (B_0) peuvent avoir une influence importante sur la mesure du CEST.

Il a été important de mettre au point une méthode robuste de correction de ces effets. Une approche standard est la méthode WASSR (WATER Saturation Shift Referencing). Elle consiste à utiliser la même séquence que celle des données CEST à corriger, mais avec une saturation extrêmement faible, afin de ne pas provoquer d'échange de saturation mais de mesurer la position du pic de l'eau. Des comparaisons ont été faites entre plusieurs méthodes de correction et nous avons retenu la meilleure solution : faire correspondre une courbe lorentzienne à nos données WASSR pour estimer la position du pic. Cette méthode s'est avérée la plus précise et robuste.

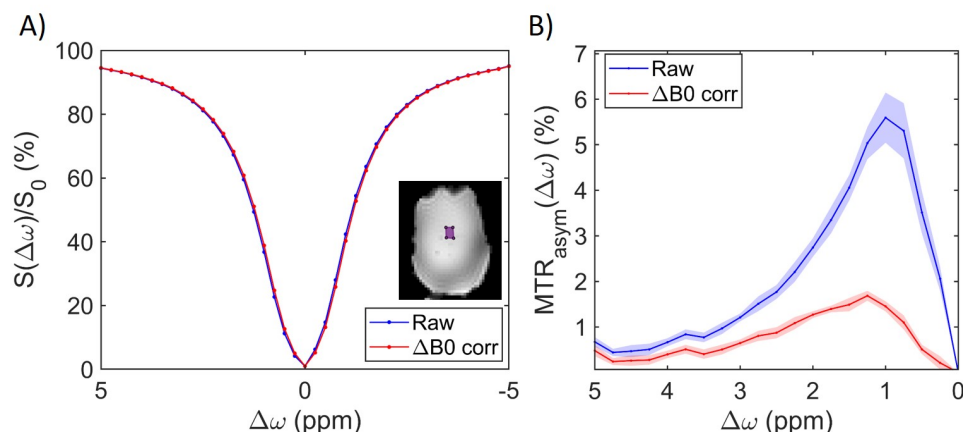


Figure 5: Spectres Z expérimentaux (A) et MTR_{asym} (B) sur phantom avant et après la correction B_0 . Spectres moyens dans une Région d'Interêt (ROI). L'écart-type du MTR_{asym} est représenté par la zone colorée. La moyenne de ΔB_0 dans la ROI est de 0,05 ppm.

Après la mise au point de ces différentes méthodes, qui permettent l'obtention de spectre Z de bonne qualité (outil couramment utilisé pour représenter les données obtenues lors d'une expérience CEST), la correction des inhomogénéités de B_1^+ a été étudiée.

Optimisation de la saturation CEST par le pTx et les VOPs

Afin d'optimiser la saturation CEST, nous avons utilisé une saturation en transmission parallèle, ainsi que des VOPs optimisés pour la gestion du DAS. La transmission parallèle consiste à piloter plusieurs canaux de l'antenne indépendamment de sorte que la somme des contributions des différents canaux produise une distribution homogène de la saturation. Les VOPs sont des matrices issues de simulations électromagnétiques de l'antenne et permettant de calculer le DAS de manière efficace. Les VOPs utilisés ici ont été développés dans notre laboratoire et permettent d'estimer le DAS plus finement que ceux utilisés nativement par les IRM Siemens. Dans ce travail, les paramètres de pilotage de l'antenne (amplitude et phase des canaux) sont optimisés sous la contrainte des VOPs. L'optimisation de ces paramètres se fait en réalisant des simulations de la saturation. Elle peut se faire en utilisant une carte de B_1^+ du sujet, pour lequel ces impulsions sont conçues. On parle alors d'impulsion sur mesure (Tailored pulses, TP en anglais). Il est aussi possible de réaliser ces impulsions en optimisant sur plusieurs sujets à la fois, en amont de l'examen, avec l'idée que les pulses fonctionnant sur un grand nombre de sujets fonctionnent aussi sur un sujet qui ne fait pas partie de la base de données. On parle alors d'impulsion universelle (Universal pulse, UP en anglais). Afin de gagner en degrés de liberté, la saturation pTx est constituée de deux modes optimisés conjointement. La combinaison de ces deux modes permet l'obtention d'une saturation homogène (Figures 6A et B).

Cette méthode optimisée a été comparée avec une gestion du DAS standard et en utilisant la technique MIMOSA (Multiple Interleaved MOde SATuration), qui est la principale technique utilisée en CEST-pTx. Des simulations ont permis de montrer que la solution de saturation CEST utilisant les UP et les VOPs permettait de réduire les inhomogénéités de B_1^+ d'un facteur 2 par rapport à une utilisation de l'IRM 7 T sans pTx. Par rapport à MIMOSA, la technique développée ici permet de réduire davantage les inhomogénéités, de l'ordre de 30%, mais surtout, par une gestion optimale du DAS, de réduire le temps d'acquisition d'un facteur 2. Des comparaisons sur phantom (Figure 6) ont été réalisées ainsi que sur 6 volontaires sains. Pour chacun de ces cas, la solution proposée permettait d'obtenir de meilleures données CEST que ce qui était permis par l'état de l'art.

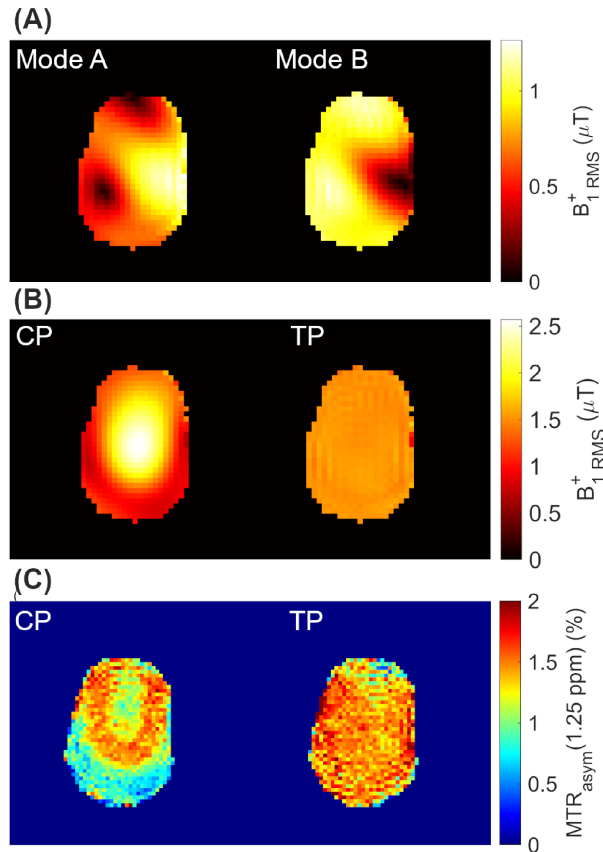


Figure 6: *Simulations et expériences sur phantom. (A) Simulation des deux modes d'une impulsion TP. (B) Simulation du $B_{1,RMS}^+$ pour une utilisation sans pTx (CP) et pour la combinaison des modes TP montrée en (A). (C) Cartes expérimentales de $MTR_{asym}(1,25 \text{ ppm})$.*

Le schéma de saturation proposé permet de résoudre les inhomogénéités de B_1 de manière plus efficace que l'état de l'art, tout en réduisant la durée d'acquisition. Ces deux points permettent donc un gain important pour rendre les acquisitions CEST plus fiables et rapides, rendant le CEST un peu plus facile d'accès pour d'une utilisation clinique.

Application sur des sujets jeunes, âgés, et patients de la maladie d'Alzheimer

Afin d'évaluer les performances du CEST comme biomarqueur de la maladie d'Alzheimer, plusieurs groupes de volontaires sains ont été recrutés. Dix volontaires jeunes ont permis de valider le bon fonctionnement de la séquence CEST multi-slice en pTx puis dix volontaires âgés ont été scannés. Enfin sur le groupe de volontaires atteints d'Alzheimer, un seul a été imagé à ce jour. Lors de l'examen, plusieurs protocoles sont réalisés afin d'acquérir des données CEST pondérées en hydroxyle, en glutamate et en effet rNOE (relayed Nuclear Overhauser Effect). Le rNOE n'est pas un effet CEST mais est observable sur les spectres Z, il apparaît avec la présence de macro-molécules mobiles, notamment dans la substance blanche. Parce que la séquence CEST ne permet que l'acquisition d'une région réduite du cerveau, deux volumes ont été imagés successivement. L'un est positionné de manière oblique dans le plan sagittal et comprend des régions postérieures comme le precuneus et le cortex visuel, l'autre garde cette orientation oblique mais est centrée sur les hippocampes. Les différentes cartes obtenues pour un volontaire sont montrées en Figure 7.

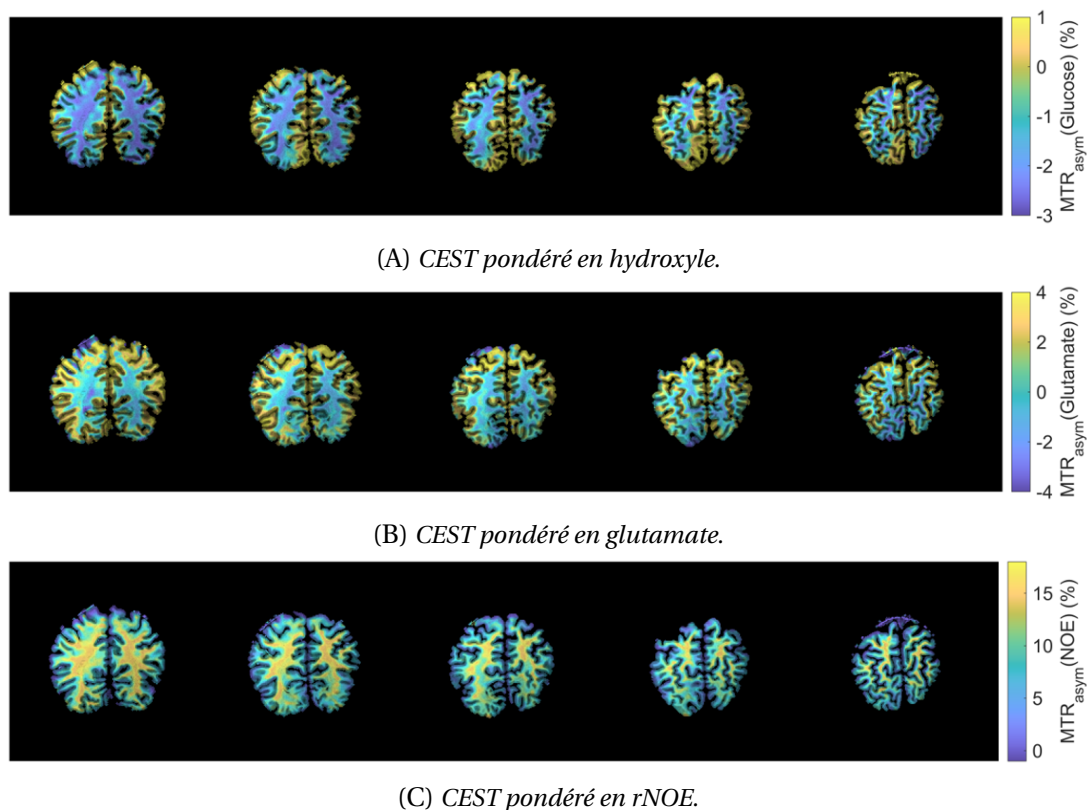


Figure 7: MTR_{asym} cartes obtenues sur le volume de cortex visuel/precuneus, sur un sujet sain. Les cartes MTR_{asym} sont superposées sur des images anatomiques pondérées en T₁.

Les données obtenues ont été parcellisées à l'aide d'un atlas du cerveau pour permettre l'extraction des données et leur concaténation entre les différents participants. Les données obtenues, présentées en Figure 8, ont permis de montrer qu'avec l'âge, le CEST pondéré en hydroxyles ou en glutamate évolue de manière significative, et cela dans toutes les régions du cerveau. Nous n'avons toutefois pas assez de données pour conclure si certaines régions présentent une évolution plus importante que d'autres. Le seul patient Alzheimer scanné présente un contraste similaire à celui que l'on observe chez les volontaires âgés. Là encore, davantage de volontaires seront nécessaires pour déterminer une tendance propre aux patients Alzheimer, ainsi que pour déterminer des biomarqueurs.

Ces premières mesures ont permis de montrer que la méthode développée pouvait détecter des variations métaboliques liées à l'âge. Ces résultats encourageants nous invitent à penser qu'il sera possible de détecter des biomarqueurs de la maladie d'Alzheimer grâce au CEST.

Une métrique non biaisée pour le CEST en régime permanent

Les données CEST obtenues jusqu'ici ont été analysées avec le MTR_{asym} qui est une métrique largement utilisée en CEST. Cette métrique permet d'estimer la proportion de contraste CEST sur un spectre Z. Cette métrique est simple mais souffre de nombreux défauts, à commencer par son manque de sélectivité. De nombreuses autres approches ont été proposées mais aucune n'émerge comme la solution idéale. Par ailleurs, l'utilisation des séquences CEST en régime permanent peut parfois biaiser les données en fonction de la trajectoire utilisée pour échantillonner le spectre. Pendant cette thèse, une métrique prenant en compte cet effet a été introduite. Nous avons montré en simulations, puis expérimentalement chez la souris et l'homme que cette métrique pouvait apporter un avantage conséquent pour l'analyse des données CEST. Elle permet d'obtenir une estimation du CEST d'un métabolite de manière plus sélective que le MTR_{asym}, tout en retirant le biais des séquences CEST en

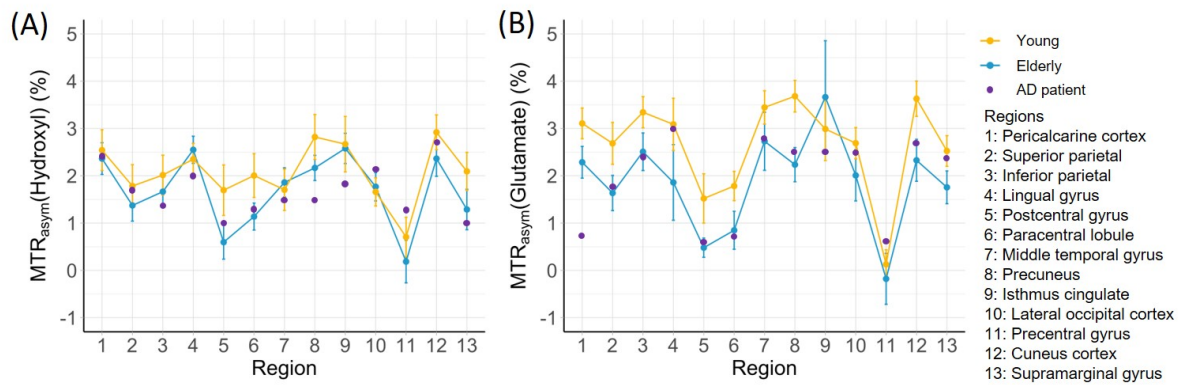


Figure 8: *Distribution de la médiane du MTR_{asyM} pour les données CEST pondérés en hydroxyle et glutamate dans chaque ROI du volume postérieure pour les volontaires jeunes et âgés ainsi que pour le patient atteint de la maladie d'Alzheimer.*

régime permanent. Cette métrique n'a toutefois pas été utilisée pour l'analyse de nos données acquises sur les volontaires jeunes/âgés et Alzheimers car son réglage est difficile et, qu'à l'état actuel, elle souffre trop du bruit dans la mesure. Des travaux supplémentaires sont nécessaires pour en faire une métrique fiable et robuste.

Conclusion

Les travaux réalisés lors de cette thèse ont permis de développer l'IRM CEST à haut champ magnétique et ensuite d'évaluer son utilisation comme biomarqueur du vieillissement et des maladies neurologiques. Le CEST s'est révélée être une technique d'imagerie efficace et prometteuse. Les améliorations apportées aux séquences CEST à haut champ permettent d'obtenir des acquisitions plus rapides et plus robustes, facilitant ainsi leur utilisation dans un contexte clinique. Les résultats obtenus lors de l'étude du métabolisme cérébral révèlent des variations significatives d'hydroxyle et de glutamate liées à l'âge. Parmi les axes d'amélioration identifiés, on peut noter que le développement de méthodes plus précises de quantification des données CEST permettrait d'exploiter pleinement le potentiel du CEST.

En conclusion, ce travail contribue au développement du CEST en tant qu'outil clinique potentiel dans l'étude des maladies neurodégénératives, il ouvre des perspectives prometteuses pour le développement de biomarqueurs et une meilleure prise en charge de ces pathologies.

List of Figures

1.1	Scheme of the CEST mechanism	6
1.2	Schematic diagram illustrating a standard CEST measurement	7
1.3	Spectra obtained for two-site exchange under various rates of exchange	10
1.4	Schematic model of the various contributions visible on a Z-spectrum	13
1.5	Conventional and APT MR images of a patient with lung cancer metastasis and a patient with stroke at 5 days postonset	15
1.6	Glutamate weighted CEST in encephalitis rats	16
1.7	DGE _{ρ} time curves and DGE _{ρ} maps of a patient suffering from a glioblastoma	17
1.8	Simulated B_1 inhomogeneities effect with field strength	19
1.9	Representation of $k - space$ trajectories for various parallel transmission strategies	20
1.10	MIMOSA modes flip angle maps in a phantom	21
2.1	The 7 T Magnetom MRI in Neurospin	24
2.2	The 17.2 T pre-clinical MRI	25
2.3	Nova 8Tx/32Rx head coil	26
2.4	Volumic coil used for the experiments on the 17.2 T	27
2.5	The realistic head shaped phantom, Skully	28
2.6	The glutamate ball phantom	29
3.1	Diagram of events of the CEST-EPI sequence	32
3.2	Interface of the CEST-EPI Sequence	33
3.3	Different Z-spectrum sampling trajectories	34
3.4	CEST _{fast} sequence diagram	36
3.5	Z-spectrum sampling trajectories of CEST-EPI and CEST-EPI-fast	36
3.6	Interface of the CEST-EPI fast sequence	37
3.7	Chemical structure of glucose	38
3.8	Finding the optimal B_1 for glucoCEST at 7 T with a continuous wave saturation	39
3.9	Diagram of two presaturation pulses	40
3.10	Shape and spectrum of a block pulse and a Gaussian pulse	41
3.11	Simulations of Z-spectra obtained on Skully with 50 ms Block or Gaussian pulse	42
3.12	Parameters space to achieve 90%, 95% and 99% of the maximal glucoCEST	44
3.13	Saturation parameters for optimal glucose weighted CEST	45
3.14	Evolution of MTR _{asym} with T_d for the parameters retained for glucoCEST aquisitions	45
3.15	Glutamate chemical structure	46
3.16	Saturation parameters for optimal glutamate weighted CEST	46
3.17	Effect of temperature on the MTR _{asym}	47
3.18	Saturation parameters for optimal glucose weighted CEST at 20 °C	47
3.19	Comparison of experimental spectra obtained with different $B_{1,RMS}$	49
3.20	Comparison of experimental spectra obtained with different T_d	49
3.21	Comparison of experimental spectra obtained with variable T_p and N	49

3.22 Comparison of experimental spectra obtained with different $B_{1,RMS}$, using the CEST-fast sequence	51
3.23 Comparison of experimental spectra obtained with different frequency offset steps, using the CEST-fast sequence	51
3.24 Comparison of experimental spectra obtained with a variable number of slices N_{slice} and number of pulses per slice N_p , using the CEST-fast sequence	52
3.25 Comparison of experimental spectra obtained with different T_d , using the CEST-fast sequence	52
3.26 Simulations of flip angle and its error maps obtained with CP and MetaPulse excitation	53
3.27 Experimental SNR maps of CEST volume acquired using a CP or a MetaPulse excitation	53
3.28 Experimental Z-spectra and MTR_{asym} on Skully before and after B_0 correction	56
3.29 Simulations of different ΔB_0 estimation methods	57
3.30 Estimation of B_0 inhomogeneities with the spline minimum, the original WASSR algorithm, and the Lorentzian function fit on human data	58
4.1 $B_{1,RMS}^+$ RMSE of UPs designed using various number of modes	64
4.2 Magnitude and phase of optimized TP and spatial distribution of effective $B_{1,RMS}^+$	65
4.3 $B_{1,RMS}^+$ distribution obtained on the evaluation data set using CP and UP	66
4.4 $B_{1,RMS}^+$ RMSE of CP, MIMOSA, TPs and UPs under different optimization and energy management strategies	67
4.5 $B_{1,RMS}^+$ simulation results and maps for CP and TP modes	68
4.6 Experimental and simulated Z-spectra in the phantom and MTR_{asym} in the ROIs	69
4.7 The 10 MTR_{asym} maps obtained after grape juice ingestion	70
4.8 Time drift of water resonance frequency	71
4.9 MTR_{asym} maps after correction shows a constant dynamic of hydroxyl-weighted CEST	72
4.10 Evolution of MTR_{asym} averaged on the slice, on gray and white matters	72
4.11 Comparison of MTR_{asym} maps obtained with CP and UPs on four volunteers with $B_{1,RMS}^+$ and flip angle maps	73
4.12 Distribution statistics of the MTR_{asym} obtained in vivo for CP or UP CEST presaturation	74
4.13 MTR_{asym} and $B_{1,RMS}^+$ maps obtained on two subjects using CP, MIMOSA and UPs	75
4.14 In vivo rNOE and glutamate-weighted CEST MTR_{asym} maps obtained with UP CEST presaturation overlaid on T_1 weighted anatomical images	76
5.1 Sagittal view of volume position over a T_1 anatomical image	80
5.2 Examples of 18-FDG map.	81
5.3 Scheme of the pipeline used for CEST data processing in this work	82
5.4 Atlas normalized in subject reference No 15 frame	83
5.5 Z-spectra obtained in a 50 voxels ROI in the white matter of subject N° 15	83
5.6 MTR_{asym} maps obtained on visual cortex/precuneus slice from subject N° 2	84
5.7 Median MTR_{asym} distribution for each volunteers groups	85
5.8 Results obtained on the hippocampi centred slices	86
5.9 Z-spectrum and MTR_{asym} obtained for different sampling trajectories	87
5.10 Experimental data obtained for $\{+, -\}$ and $\{-, +\}$ sampling trajectories	88
5.11 Simulated performances for glutamate CEST estimation using MTR_{asym} , VP and modVP	89
5.13 Map of parameter obtained for a direct and iterative estimation	90
5.12 Pipeline used for residual estimation, with iterative downsampling	90
5.14 Human experimental residuals, obtained for VP and modVP	91
5.15 Human and mouse experimental CEST contrasts with the two studied trajectories	92
A.1 Comparison of experimental spectra obtained with different B_1 and pulse number N , with the CEST-EPI sequence	102

LIST OF FIGURES

A.2	Comparison of experimental spectra obtained with different B_1 and pulse number N , with the CEST-EPI-fast sequence	102
A.3	Comparison of experimental spectra obtained with different B_1 and pulse number N , with the CEST-EPI-fast sequence	103
B.1	Example of motion correction before and after regularization	106

List of Tables

2.1	List of phantoms and description of their composition	27
3.1	Five-pool model used for glucoCEST simulation	43
3.2	Experimental parameters used for the glucoCEST optimization using the CEST-EPI sequence as well as those obtained from simulations.	48
3.3	Experimental parameters used for the glucoCEST optimization using the CEST-EPI-fast sequence as well as those used for the CEST-EPI sequence	50
4.1	Performance summary of different presaturation strategies for hydroxyl-weighted CEST and glutamate-weighted CEST acquisitions in the study	66
4.2	Average $B_{1,RMS}^+$ and $B_{1,RMS}^+$ RMSE	76
5.1	The different CEST acquisition settings used	80
A.1	Experimental parameters used for the gluCEST optimization using CEST-EPI and CEST-EPI-fast sequence as well as those obtained in simulation	101

List of symbols and abbreviations

$\delta\omega$	Saturation offset	FDG	Fluorodeoxyglucose (^{18}F)
α	Saturation efficiency	FOV	Field Of View
γ	1H nuclear gyromagnetic ratio ($\gamma = 42.576 \text{ MHz}\cdot\text{T}^{-1}$)	FWHM	Full Width at Half Maximum
B_0	Static Magnetic Field	GM	Gray Matter
B_1^+	Emitted RF magnetic field	GRE	Gradient Echo
B_1^-	Received RF magnetic field	GdCE-T₁w	Gadolinium Contrast Enhanced T ₁ weighted
MTR_{asym}	Magnetic Transfer Ratio Asymmetric	LD	Lorentzian Difference
1H	Hydrogen-1 or protium	MR	Magnetic Resonance
k_{ex}	Exchange Rate	MRI	Magnetic Resonance Imaging
AD	Alzheimer's Disease	MRS	Magnetic Resonance Spectroscopy
APT	Amide Proton Transfer	MRSI	Magnetic Resonance Spectroscopy Imaging
BTP	Bandwidth Time Product	MT	Magnetic Transfer
CEST	Chemical Exchange Saturation Transfer	MTR	Magnetic Transfer Ratio
CP	Circular Polarization	NMR	Nuclear Magnetic Resonance
CSF	Cerebrospinal Fluid	NOE	Nuclear Overhauser Effect
CT	Computed Tomography	NRMSE	Normalized Root-Mean-Square Error
CW	Continuous Wave	PET	Positron Emission Tomography
DGE	Dynamic Glucose Enhanced MRI	PTR	Proton Transfer Ratio
DS	Direct Saturation (of Water)	R1	Longitudinal Relaxation rate
EPI	Echo Planar Imaging	R2	Transverse Relaxation rate
FA	Flip Angle		

RARE Rapid Acquisition with Relaxation Enhancement	UP Universal Pulse
RF Radio Frequency	VOP Virtual Observation Point
RMSE Root-Mean-Square Error	VP Voigt profile
ROI Region of Interest	WM White Matter
Rx Reception	Z-spectrum Spectrum obtained with a CEST Sequence
SAR Specific Absorption Rate	fMRI Functional Magnetic Resonance Imaging
SNR Signal-to-Noise Ratio	gluCEST Glutamate-weighted CEST
T1 Longitudinal (Spin-Lattice) relaxation time	glucoCEST Glucose-weighted CEST
T2 Transverse (Spin-Spin) relaxation time	pTx Parallel Transmission
TE Echo Time	ppm Parts Per Million
TP Tailored Pulse	rNOE Relayed Nuclear Overhauser Effect
TR Repetition Time	
Tx Transmission	

Context and objectives

Context

Medical imaging has revolutionized the field of medicine, providing a non-invasive way to visualize the internal structures of the body. The story of medical imaging began in the late 19th century with the discovery of X-rays by Wilhelm Conrad Roentgen. This marked the beginning of a new era in medicine, allowing physicians to see inside the human body without surgery. Throughout the 20th century, medical imaging technology advanced rapidly with the development of medical ultrasound, Computed Tomography (CT), and Magnetic Resonance Imaging (MRI). Each imaging technique has its unique advantages and applications. For instance, ultrasound is advantageous for real-time soft tissue imaging, while CT scans are effective for imaging bone fractures and detecting internal bleeding or blood clots. Positron Emission Tomography (PET) scans detect diseases at the metabolic level, providing information that complements the structural details provided by CT or MRI. MRI, in particular, has become a pivotal tool in modern medicine. Unlike other imaging methods, MRI uses a powerful magnet and radio waves to create highly detailed images of the body's structures, including soft tissues, nerves, and blood vessels. It does not use ionizing radiation, making it safer for repeated use. MRI provides better soft tissue contrast than CT and can differentiate better between fat, water, muscle, and other soft tissue than CT, which is usually better at imaging bones. This makes MRI particularly useful for diagnosing a wide variety of diseases and conditions, including certain cancers, injuries to soft tissue or joints, and neurodegenerative diseases.

The different ways of controlling the MRI make it possible to produce different contrasts, each serving distinct purposes. This includes resolving small anatomical structures, detecting functional activation, tracking of axonal fiber bundles, evaluating blood vessels, or even measuring molecular concentration. MRI is a cornerstone in managing diverse diseases, offering multi-modal insights into metabolism, function, and anatomical structures.

Among the innovative MRI methods, Chemical Exchange Saturation Transfer (CEST) imaging stands out. This relatively recent molecular MR technique provides a means to image metabolites with enhanced sensitivity compared to traditional Magnetic Resonance Spectroscopy (MRS). CEST MRI allows the construction of metabolite maps in a clinically feasible time frame with reasonable resolution. Its promise extends to contributing to evaluations of cerebral ischemia, neurodegenerative disorders, lymphedema, or even musculoskeletal diseases. The potential of CEST MRI marks a significant advancement in molecular imaging within the MRI domain.

The recent advancements in high-field MRI, particularly at magnetic fields of 7 Tesla or higher, significantly benefit CEST by increasing the signal-to-noise ratio and spectral selectivity, and a exchange rate ratio ($\frac{k}{\Delta\omega}$), which allows the detection of metabolites that are challenging at lower fields. However, in addition to the inherent difficulty of separating contributions from different metabolites in CEST, some other challenges arise at high field and reduce CEST efficiency. The higher magnetic field reduces the RF pulse wavelength, generating B_1 field inhomogeneities. Correcting these inhomogeneities is crucial for making CEST a robust imaging tool. The Specific Absorption Rate (SAR) also poses a major challenge for high-field CEST, as the energy deposition increases almost quadratically with the magnetic field strength and the duration and intensity of CEST saturation pulses. This limitation sometimes requires extending the Repetition Time (TR) to stay within SAR constraints.

Mitigating this challenges is, however, of outmost importance as metabolic studies play a vital role in understanding and treating numerous diseases including neurodegenerative diseases. For instance, PET is often used to study Alzheimer's disease as it exhibits cerebral distribution defects in glucose (18-FDG) uptake. Studying glucose through MRI opens new opportunities for early detection and management of this disease. Besides glucose, CEST allows the detection of other metabolite (e.g. glutamate) providing therefore an even richer metabolic information than PET.

Thesis outline

The aim of this thesis is to develop high-field CEST MRI by solving the problems associated with B_1^+ inhomogeneities and SAR limits and to evaluate the performance of CEST as a biomarker for Alzheimer's disease.

The detailed plan of this, is as follows:

[Chapter 1, Introduction](#), presents the CEST MRI technique, its origins, and its applications. It then focuses on high-field MRI benefits and challenges, and more specifically in the context of CEST imaging.

[Chapter 2, Background](#) introduces the different technical elements used for performing the work of this thesis, including the MRI system, the phantom and the software.

[Chapter 3, Development of CEST at 7T](#), presents the first developments of this project: the CEST pulse sequences and their optimization for glucose and glutamate weighted CEST, presenting both simulations and experimental results on phantoms. One section of this chapter is dedicated to the implementation of a B_0 inhomogeneities correction solution.

[Chapter 4, Efficient CEST saturation using pTx and VOPs](#), proposes a method for B_1^+ inhomogeneities mitigation using parallel transmission and VOPs for energy management, for the CEST saturation. A comprehensive study comparing in-silico, in-vitro, and in-vivo experiments was conducted to show the benefits of this solution.

[Chapter 5, Application in young, elderly and Alzheimer's disease patients](#), focuses on the comparison study of CEST results obtained for different groups of subjects: young (32 ± 4 years old), elderly (70 ± 4 years old) and Alzheimer disease patients matched in age with the elderly group. The preliminary development of a metric for CEST in steady-state is presented in the perspectives of this chapter.

Chapter 1

Introduction

This chapter presents a brief introduction to metabolic imaging, before moving on to the subject of CEST imaging. A description of the theoretical mechanism and its model are presented, along with CEST applications. We will then focus on the particularity of high-magnetic-field MRI, since CEST offers many advantages at these field levels ($\geq 7 T$).

Contents

1.1 Introduction to CEST MRI	4
1.1.1 Metabolic imaging	4
1.1.2 Origin of CEST	5
1.1.2.1 A brief history of the CEST experiments	5
1.1.2.2 General principle	6
1.1.2.3 Bloch McConnell equations	7
1.1.2.4 Analytical solution in a simple case	8
1.1.2.5 Saturation Transfer under low power irradiation	10
1.1.3 CEST contrast estimation	12
1.1.4 Applications	14
1.1.4.1 Amide Proton Transfer (APT)	15
1.1.4.2 GluCEST	15
1.1.4.3 GlucoCEST	16
1.1.4.4 Other contrasts	17
1.2 High field MRI for CEST	18
1.2.1 Benefits and challenges of high-fields MRI	18
1.2.2 Parallel Transmission	19
1.2.3 Specific absorption rate consideration	21
1.3 Conclusion	21

1.1 Introduction to CEST MRI

Since its introduction, MRI has rapidly found its place in the world of research and clinical practice. In contrast to CT-scan or PET, MRI is non-invasive, non-ionizing and enables soft-tissue imaging. MRI uses a magnetic field in which the subject is immersed. In this magnetic field, the hydrogen nuclei of water molecules are excited by a RadioFrequency (RF) wave. As they relax, they emit a radio wave that can be measured using an antenna. The three orthogonal gradient coils are cleverly controlled to encode the position of the voxels in the transmitted signal. The signal collected provides information on the quantity of water molecules and certain properties specific to the tissue, such as spin-lattice or spin-spin relaxation time. By controlling the MRI system in a specific way, it is possible to generate different contrasts. This versatility is one of the great advantages of MRI. Despite the ability of MRI to produce high-resolution images of anatomical structures, other methods are preferred for the study of metabolic mechanisms. In fact, the low sensitivity of MRI makes water images easy to obtain, but for metabolites it is much more challenging (As it is typically 10,000 times less concentrated than water).

1.1.1 Metabolic imaging

Metabolic imaging techniques allow researchers and physicians to visualize and quantify cellular metabolism non-invasively in living subjects. By mapping metabolite levels and pathways inside the body, these methods provide biomarkers of normal and diseased states at the molecular level. This has applications in both research and clinical practice for improving disease characterization, monitoring treatment response, and developing new therapies that target metabolism. Two main methods for metabolic imaging are available: PET and MR spectroscopy.

PET imaging is currently the gold standard technique, using radioactive tracers that can be paired with sugars, fatty acids, amino acids, and other molecules, to map their utilization and movement in vivo. These tracers emit positrons that annihilate with electrons, producing pairs of photons detected by the PET scanner to determine the location of biological activity. Tracers like ^{18}F -FDG (fluorodeoxyglucose) target glucose uptake, allowing visualization of hypermetabolic tissues such as tumors and metastases or investigating brain activity (Posner et al. 1988). Despite these powerful qualities, PET requires an on-site cyclotron to produce short-lived radioisotopes and exposes subjects to ionizing radiation limiting its adoption to a larger scale. Spatial resolution is also limited with a voxel size of roughly 2 mm^3 (Moses 2011) and it is more expensive than MRI.

MRS exploits the fact that hydrogen protons in different molecules resonate at different frequencies when exposed to strong magnetic fields because the local magnetic field surrounding the protons is modified by the molecular structure. MRS can be used to detect resonant frequencies of endogenous brain metabolites like N-acetylaspartate (NAA), creatine (Cr), choline (Cho), myo-inositol, and glutamate (Biria, Cantonas, and Banca 2021) without the use of tracers. MRS provides a metabolic snapshot within large voxels but is non-invasive and offers good chemical specificity. However, low sensitivity means long acquisition times, limiting then spatial and temporal resolution. Coverage is also restricted to a single voxel or small regions of interest versus full brain imaging, as it is limited by the necessity to preserve the spectral information while encoding k-space (therefore lengthening the acquisition).

Combining the strengths of different modalities may provide a more complete picture than isolated techniques. For example, integrating high-resolution anatomical MRI with molecular PET can enable precise localization of imaged biochemistry to corresponding anatomical structures. Some groups are additionally pairing PET with MRS to synergize sensitivity and specificity. Continued technical advancement will expand clinical access to multimodal metabolic imaging approaches (Min et al. 2021; Statsenko et al. 2023).

Each technology discussed has its relative advantages and challenges for mapping metabolism in vivo. Future progress integrating anatomical, functional, and molecular capabilities within single

hybrid systems may help maximize information gained from metabolic imaging examinations. With ongoing technical and methodological developments, these techniques are becoming more powerful research and clinical tools for characterizing disease states and monitoring therapeutic interventions at the level of cellular functioning.

Alongside these techniques, Chemical Exchange Saturation Transfer (CEST) is an emerging MRI-based approach that is attracting attention as a potential molecular imaging tool. CEST can detect certain metabolites such as creatine, glutamate, and glucose with increased sensitivity compared to MRS and unrivaled resolution compared to PET, making it a promising tool for better metabolism studies.

1.1.2 Origin of CEST

1.1.2.1 A brief history of the CEST experiments

CEST is a relatively new contrast mechanism in Magnetic Resonance Imaging (MRI) that has been increasingly used to detect dilute proteins through the interaction between bulk water protons and labile solute protons. The concept of CEST MRI was first proposed in the 1990s as a potential method for generating contrast based on endogenous contrast agents. However, it took several key developments in the early 2000s for CEST to emerge as a viable molecular imaging technique.

The phenomenon of saturation transfer between molecules through proton exchange has been known since the early Nuclear Magnetic Resonance experiments (NMR) in the 1950s. In 1951, Liddel and Ramsey ([Liddel and Ramsey 1951](#)) as well as Arnold and Packard ([Arnold and Packard 1951](#)) first reported the effects of chemical exchange on NMR spectra. These initial findings laid the groundwork for further exploration of this phenomenon.

A major advancement occurred in 1958 when McConnell ([McConnell 1958](#)) formally derived the Bloch equations, which mathematically describe how magnetization evolves over time when incorporating proton exchange between different molecules. This established a theoretical framework for better understanding saturation transfer. Building on this, Forsén and Hoffman ([Forsén and Hoffman 1963](#)) demonstrated in 1963 that saturation transfer experiments could be used to enhance NMR sensitivity and determine chemical exchange rates through nuclear magnetic double resonance methods. Their work showcased how saturation transfer could provide valuable information.

In 1989, Wolff and Balaban ([Wolff and Balaban 1989](#)) were the first to apply saturation transfer techniques to in vivo MRI. They generated tissue contrast from proton exchange between free water and semi-mobile macromolecules in rabbit tissues, introducing Magnetic Transfer (MT) MRI. This seminal study established the potential for saturation transfer in medical imaging. In the late 1990s, Balaban's group ([Ward, Aletras, and Balaban 2000](#); [Wolff and Balaban 1990](#)) helped develop CEST MRI. They showed that selectively saturating the labile protons on low-concentration solutes like ammonia and urea ([Guivel-Scharen et al. 1998](#); [Dagher et al. 2000](#)) led to saturation transfer to water protons, detectable as a water signal change. This new contrast mechanism was named "Chemical Exchange Saturation Transfer" or "CEST" MRI ([Ward, Aletras, and Balaban 2000](#)).

Early work in the 2000s significantly advanced CEST MRI capabilities. Van Zijl and his colleagues found polymers with many similar exchanging sites produced heightened enhancements compared to small molecules through CEST ([Goffeney et al. 2001](#); [Snoussi et al. 2003](#)). Meanwhile, researchers broadened CEST applications through endogenous molecular detection ([J. Zhou, Payen, et al. 2003](#); [J. Zhou, Lal, et al. 2003](#)) as well as exogenous CEST agents ([S. Zhang, Winter, et al. 2001](#); [S. Zhang and Sherry 2003](#); [Aime et al. 2002](#); [Donald E Woessner et al. 2005](#)). Further details of possible CEST applications are given in Section 1.1.4.

Until recently, 3 T was the highest clinically accessible MRI field, but the development of higher fields opens up new possibilities for CEST which benefits greatly from the increase in magnetic field. In 2011, the first human CEST acquisition at 7 T was carried out ([Dula, Asche, et al. 2011](#)), and significant gains in the detection of amides, amines and other metabolites were subsequently reported in

Kogan, Mohammad Haris, et al. (2014); Harris et al. (2015); Zaiss, Windschuh, Goerke, et al. (2017). The detection of hydroxyl groups, which is extremely limited at 3 T, is greatly enhanced at 7 T (Singh et al. 2012), and applications such as Dynamic Glucose Enhanced (DGE) are emerging in humans from 2015 with X. Xu et al. (2015); Jihong Wang et al. (2016); Paech, Schuenke, et al. (2017). Finally, we recently demonstrated at Neurospin that it is possible to detect functional activity in endogenous glucoCEST (Roussel et al. 2019).

In summary, while it was theoretically proposed in the 1990s, it took step-wise developments in appropriate exogenous agents, instrumentation advances, and biological validations through the early 2000s for CEST to emerge as a tangible molecular MRI technique. Continued methodological improvements now bring CEST closer to realizing its full potential for clinical and research applications (Gao et al. 2021; P. C. M. v. Zijl and Yadav 2011).

1.1.2.2 General principle

The basic principle of CEST is straightforward. It relies on the presence of solute protons resonating at a frequency different from water and engaged in the chemical exchange process, where a proton physically moves from the solute to solvent and back again. Given a chemical species of interest, capable of exchanging its ^1H protons with those of water, a radiofrequency pulse is applied at its resonant frequency to reach a saturation state. This dephases the spins and the macroscopic magnetization of the metabolite disappears, known as saturation (Figure 1.1B). This magnetic saturation will spontaneously be transferred to water over time, via the chemical exchange of the excited metabolite protons with non-excited water proton (Figure 1.1C). Because of the difference in proton concentration, for a water/solute system, exchange rate constants are considerably unbalanced such that $k_{sw} \gg k_{ws}$. This leads to the storing of the saturated protons in the water pool during the CEST saturation duration. Exchange is continuous and brings more and more protons which increases the partial saturation of water until the convergence to an equilibrium between CEST and the T_1 relaxation of water protons.

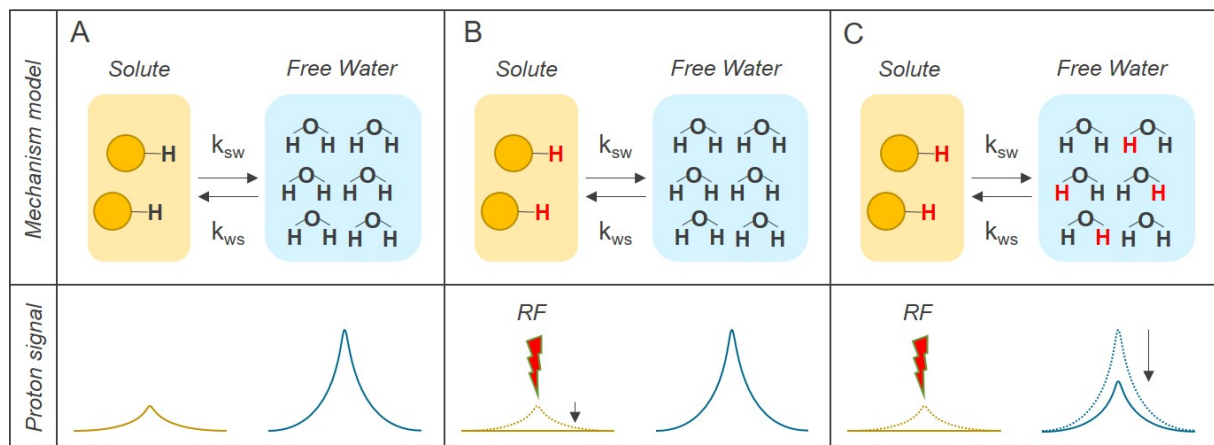


Figure 1.1: Scheme of the mechanism at work in CEST between two pools, free water and solute. (A) initial situation at equilibrium, solute protons produce a weak NMR signal, proportional to their concentration. (B) Upon RF saturation, the solute signal is erased. (C) With chemical exchange, the saturation of the solute is transferred to the water pool, which then becomes saturated, and the NMR signal of the water decreases.

The concentration of saturated protons in the water pool can be considerably larger than the concentration of solute protons, thanks to the storing of saturation protons during the saturation duration. This concentration is measured by comparing the water NMR signal with and without solute saturation and provides an indirect measure of the solute concentration with an enhancement factor of hundred to millions depending on the CEST agent (P. C. v. Zijl et al. 2018). In practice, CEST MRI

experiments usually consists of a saturation at a given frequency and followed by a water signal measurement (Figure 1.2A). This measure is repeated for various saturation frequency offsets in order to build a so-called Z-spectrum (Figure 1.2C). It is possible to use a standard imaging module for the water signal measurement, in this case, a Z-spectrum is collected for each voxels.

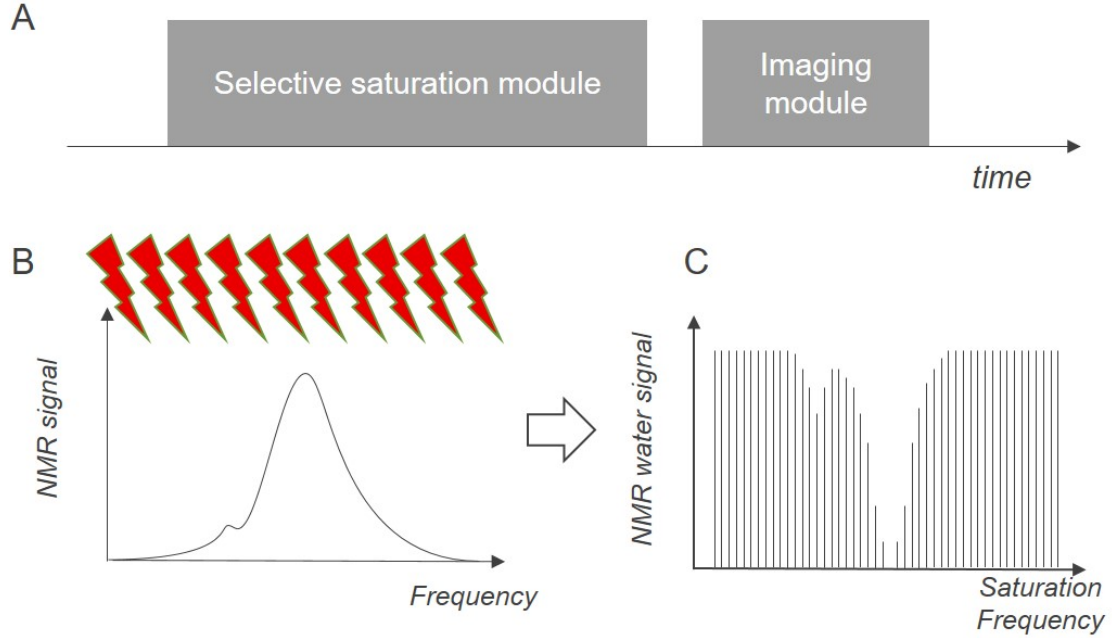


Figure 1.2: Schematic diagram illustrating a standard CEST measurement. (A) The sequence used consists of a saturation module and a readout module. (B) Saturation is performed for numerous frequency offsets. (C) Measurement of the water signal after saturation produces a spectrum called the Z-spectrum.

1.1.2.3 Bloch McConnell equations

NMR, and therefore MRI and CEST, are fundamentally quantum mechanical rather than classical phenomena. Nevertheless, the general behavior of these systems can be modeled by macroscopic equations that describe the evolution of residual magnetization. The Bloch's equations describe the evolution of the magnetization during an NMR experiment (Bloch 1946). In 1958, McConnell modified these equations to include the effect of chemical exchange (McConnell 1958; D. Woessner 1961). The Bloch-McConnell equations for the application of a RF wave flipping spins on the y -axis in the rotating reference are described in Equation (1.1).

$$\frac{d}{dt} \begin{pmatrix} M_x^A \\ M_y^A \\ M_z^A \\ M_x^B \\ M_y^B \\ M_z^B \end{pmatrix} = \begin{pmatrix} -\rho_{2A} & -\Delta_A & 0 & k_{BA} & 0 & 0 \\ \Delta_A & -\rho_{2A} & \omega_1 & 0 & k_{BA} & 0 \\ 0 & -\omega_1 & -\rho_{1A} & 0 & 0 & k_{BA} \\ k_{AB} & 0 & 0 & -\rho_{2B} & -\Delta_B & 0 \\ 0 & k_{AB} & 0 & \Delta_B & -\rho_{2B} & \omega_1 \\ 0 & 0 & k_{AB} & 0 & -\omega_1 & -\rho_{1B} \end{pmatrix} \cdot \begin{pmatrix} M_x^A \\ M_y^A \\ M_z^A \\ M_x^B \\ M_y^B \\ M_z^B \end{pmatrix} + \begin{pmatrix} 0 \\ 0 \\ R_{1A}M_0^A \\ 0 \\ 0 \\ R_{1B}M_0^B \end{pmatrix} \quad (1.1)$$

where :

- $M_{x,y,z}^A$ and $M_{x,y,z}^B$, the magnetization components in the rotating frame.
- M_0^A and M_0^B , the initial magnetization. Without RF, the equilibrium magnetization is aligned with the z -axis (collinear with \vec{B}_0).

- k_{AB} and k_{BA} are the exchange rate of protons from pool A to pool B and vice-versa.
- $\omega_1 = \gamma B_{1,sat}$ where γ is the ^1H nuclear gyromagnetic ratio and $B_{1,sat}$ is the RF pulse field strength.
- $\Delta_{A,B} = \omega_{A,B} - \omega_0$ the angular frequency shifts with respect to ω_0 , resonance frequency, with $\omega_0 = \gamma B_0$ and B_0 is the main magnetic field strength, in $\text{rad}\cdot\text{s}^{-1}$.
- $R_{1A} = \frac{1}{T_{1A}}$ and $R_{1B} = \frac{1}{T_{1B}}$, the longitudinal relaxation rates.
- $R_{2A} = \frac{1}{T_{2A}}$ and $R_{2B} = \frac{1}{T_{2B}}$, the transverse relaxation rates.
- $\rho_{1A} = R_{1A} + k_{AB}$ and $\rho_{1B} = R_{1B} + k_{BA}$, the effective longitudinal relaxation rates.
- $\rho_{2A} = R_{2A} + k_{AB}$ and $\rho_{2B} = R_{2B} + k_{BA}$, the effective transverse relaxation rates.

In a stationary state, it can be shown using Equation (1.1) that:

$$\frac{k_{BA}}{k_{AB}} = \frac{M_0^A}{M_0^B} \quad (1.2)$$

This system of equations can be numerically solved to provide an accurate simulation of the evolution of CEST under complex saturation schemes, but it is useful to study its analytical resolution in order to grasp its fundamental tendencies.

1.1.2.4 Analytical solution in a simple case

Consider that saturation consists of the application of a 90° RF wave, tilting all magnetization in the y plane. At $t = 0$, the following state is reached:

$$\begin{pmatrix} M_x^A \\ M_y^A \\ M_z^A \\ M_x^B \\ M_y^B \\ M_z^B \end{pmatrix} (t=0) = \begin{pmatrix} 0 \\ M_0^A \\ 0 \\ 0 \\ M_0^B \\ 0 \end{pmatrix} \quad (1.3)$$

The signal measured by MRI is proportional to magnetization in the transverse plane. We will therefore focus on the study of magnetization in this plane. As the x and y components are independent of z , it is possible to rewrite the system Equation (1.1) to have only the transverse plane:

$$\frac{d}{dt} \begin{pmatrix} M_x^A \\ M_y^A \\ M_x^B \\ M_y^B \end{pmatrix} = \begin{pmatrix} -\rho_{2A} & -\Delta_A & k_{BA} & 0 \\ \Delta_A & -\rho_{2A} & 0 & k_{BA} \\ k_{AB} & 0 & -\rho_{2B} & -\Delta_B \\ 0 & k_{AB} & \Delta_B & -\rho_{2B} \end{pmatrix} \cdot \begin{pmatrix} M_x^A \\ M_y^A \\ M_x^B \\ M_y^B \end{pmatrix} \quad (1.4)$$

Using complex notation $M_T^A = M_y^A - iM_x^A$, $M_T^B = M_y^B - iM_x^B$ the system can be written again as follows:

$$\frac{d}{dt} \begin{pmatrix} M_T^A \\ M_T^B \end{pmatrix} = \begin{pmatrix} i\Delta_A - \rho_{2A} & k_{BA} \\ k_{AB} & i\Delta_B - \rho_{2B} \end{pmatrix} \cdot \begin{pmatrix} M_T^A \\ M_T^B \end{pmatrix} \quad (1.5)$$

The analytical solution to this system of differential equations is obtained by linear combination of exponentials whose parameters λ_1 and λ_2 are the eigenvalues of the 2×2 matrix of the Equation (1.5). Therefore the time evolution of magnetization is obtained:

$$\begin{aligned} M_T^A(t) &= c_1^A \exp(\lambda_1 t) + c_2^A \exp(\lambda_2 t) \\ M_T^B(t) &= c_1^B \exp(\lambda_1 t) + c_2^B \exp(\lambda_2 t) \end{aligned} \quad (1.6)$$

To simplify our study, it can be assumed that the concentrations of pools A and B are identical, i.e. $M_0^A = M_0^B = M_0$, so exchange rates are equal, $k_{BA} = k_{AB} = k$ according to Equation (1.2). Neglecting also T_2 relaxation, eigenvalues can be written as :

$$\begin{aligned} \lambda_{1,2} &= i \frac{\Delta_A + \Delta_B}{2} - k \pm W \\ \text{with } W &= \sqrt{k^2 - \frac{1}{4}(\Delta_A - \Delta_B)^2}. \end{aligned} \quad (1.7)$$

The coefficients c_1^A , c_2^A , c_1^B , and c_2^B can be determined using the initial conditions.

$$\begin{aligned} c_1^A &= \frac{M_0}{2W} \left(i \left(\frac{\Delta_A - \Delta_B}{2} \right) + k + W \right) \\ c_2^A &= \frac{M_0}{2W} \left(-i \left(\frac{\Delta_A - \Delta_B}{2} \right) - k + W \right) \\ c_1^B &= \frac{M_0}{2W} \left(i \left(\frac{\Delta_A - \Delta_B}{2} \right) + k + W \right) \\ c_2^B &= \frac{M_0}{2W} \left(-i \left(\frac{\Delta_A - \Delta_B}{2} \right) - k + W \right) \end{aligned} \quad (1.8)$$

To give more meaning to these equations and to understand their implications, two distinct exchange regimes are considered: slow and fast.

Slow exchange

A slow exchange regime can be defined as $k \ll |\Delta_A - \Delta_B|$. This simplifies the formulation of eigenvalues and coefficients as follows:

$$\begin{aligned} \lambda_1 &\approx i\Delta_A - k \quad ; \quad \lambda_2 \approx i\Delta_B - k \\ c_1^A &\approx c_1^B \approx M_0 \quad ; \quad c_2^A \approx c_2^B \approx 0 \end{aligned} \quad (1.9)$$

The signal measured by MRI is therefore

$$S(t) \propto M_0 \left[\exp((i\Delta_A - k)t) + \exp((i\Delta_B - k)t) \right] \quad (1.10)$$

This signal corresponds to the superposition of two damped sinusoidal RF waves. The angular frequency of these RF waves is Δ_A and Δ_B , and the spectral sharpness is limited by damping, giving a half-value width of $2k$ (see Figure 1.3).

Fast exchange

In the same way as for the slow regime, a fast regime can be set out, such that $k \gg |\Delta_A - \Delta_B|$. In this case, the eigenvalues and coefficients are as follows:

$$\begin{aligned} \lambda_{1,2} &\approx i \frac{(\Delta_A + \Delta_B)}{2} - k \pm k \left(1 - \frac{(\Delta_A - \Delta_B)^2}{8k^2} \right) \\ c_1^A &\approx c_1^B \approx M_0 \quad ; \quad c_2^A \approx c_2^B \approx 0 \end{aligned} \quad (1.11)$$

In this case, the analytical solution of the measured signal becomes :

$$S(t) \propto M_0 \exp\left(\left(i \frac{\Delta_A + \Delta_B}{2} - \frac{(\Delta_A - \Delta_B)^2}{8k}\right) t\right) \quad (1.12)$$

This corresponds to a damped sinusoidal signal of angular frequency $\frac{\Delta_A + \Delta_B}{2}$ and spectral width $\frac{(\Delta_A - \Delta_B)^2}{4k}$ (see Figure 1.3).

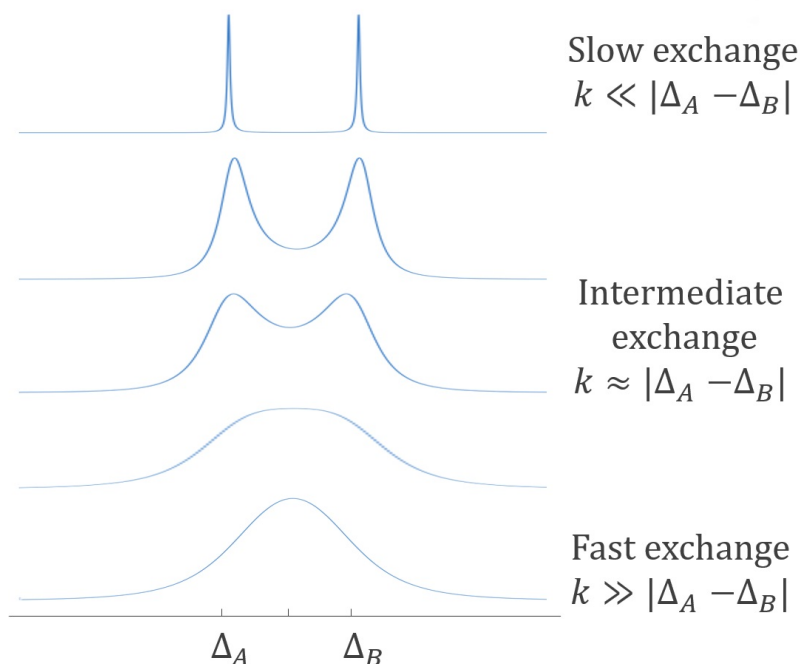


Figure 1.3: NMR spectra obtained for two-site exchange under various rates of exchange (slow, intermediate and fast).

This analytical study shows that CEST can take place in different regimes, affecting spectral width and line position to such an extent that, in the fast regime, the peaks between the two pools are non-discernible. In order to have discernible CEST peaks, it is therefore necessary to be in the slow to intermediate regime. Nevertheless, the exchange of fast protons remains detectable through the deformation and shift of the water peak.

1.1.2.5 Saturation Transfer under low power irradiation

The previous section described the conditions for obtaining peak resonance in a chemical exchange NMR experiment. Here we focus on the evolution of the magnetization of pools A and B during a CEST experiment.

To simplify the solution of the Bloch-McConnell equations, consider some simple hypotheses. Assume that saturation is reached at solute resonance (pool B, $\Delta\omega_B = 0$) and is sufficiently weak and selective to leave the water pool undisturbed (pool A, $\Delta\omega_A \rightarrow \infty$). Finally, the time evolution in the transverse plane is also neglected because the characteristic time of the rotation is small compared to the duration of the experiment. Based on these simplifying assumptions, the system of Equations (1.1) can be written as follows:

$$\frac{d}{dt} \begin{pmatrix} M_y^A \\ m_z^A \\ M_y^B \\ m_z^B \end{pmatrix} = \begin{pmatrix} -\rho_{2A} & 0 & k_{BA} & 0 \\ 0 & -\rho_{1A} & 0 & k_{BA} \\ k_{AB} & 0 & -\rho_{2B} & \omega_1 \\ 0 & k_{AB} & -\omega_1 & -\rho_{1B} \end{pmatrix} \cdot \begin{pmatrix} M_y^A \\ m_z^A \\ M_y^B \\ m_z^B \end{pmatrix} + \begin{pmatrix} 0 \\ 0 \\ \omega_1 M_0^B \\ 0 \end{pmatrix} \quad (1.13)$$

where $m_z^A = M_z^A - M_0^A$ and $m_z^B = M_z^B - M_0^B$. The solutions of this system at steady-state can be obtained by nulling the left term :

$$M_y^A(ss) = -\frac{k_{BA}}{\rho_{2A}} \frac{\omega_1 q M_0^B}{(\omega_1^2 + pq)} = -\frac{k_{AB}}{\rho_{2A}} \frac{\omega_1^2 q M_0^A}{(\omega_1^2 + pq)} \quad (1.14)$$

$$m_z^A(ss) = -\frac{k_{BA}}{\rho_{1A}} \frac{\omega_1^2 M_0^B}{(\omega_1^2 + pq)} = -\frac{k_{AB}}{\rho_{1A}} \frac{\omega_1^2 M_0^A}{(\omega_1^2 + pq)}$$

$$M_y^B(ss) = -\frac{\omega_1 q M_0^B}{\omega_1^2 + pq} \quad (1.15)$$

$$m_z^B(ss) = -\frac{\omega_1^2 M_0^B}{\omega_1^2 + pq} \quad \text{or} \quad M_z^B(ss) = \frac{pq M_0^B}{\omega_1^2 + pq}$$

with,

$$p = \rho_{2B} - \frac{k_{AB} k_{BA}}{\rho_{2A}} \quad \text{and} \quad q = \rho_{1B} - \frac{k_{AB} k_{BA}}{\rho_{1A}} \quad (1.16)$$

It is often experimentally impossible to approach the steady-state using long continuous saturation (CW). However, to estimate an analytical solution, it can be postulated that the solute is in steady-state instantaneously. This recovers the results of Equations (1.15).

With these assumptions, the longitudinal magnetization of the water pool can be described as:

$$\frac{dm_z^A}{dt} = -\rho_{1A} m_z^A + k_{BA} m_z^B(ss) \quad (1.17)$$

Assuming that saturation has taken place at equilibrium, i.e. $M_z^A(t=0) = M_0^A$, this gives the equation for the evolution of water pool saturation:

$$m_z^A(t) = \frac{k_{BA} m_z^B(ss)}{\rho_{1A}} [1 - \exp(-\rho_{1A} t)] \quad (1.18)$$

The efficiency of the saturation of the water pool can be evaluated through the Proton Transfer Ratio (PTR). Using Equation (1.15), it can be defined as:

$$PTR(T_{sat}) = -\frac{m_z^A(T_{sat})}{M_0^A} = \frac{k_{BA} M_0^B \omega_1}{M_0^A \rho_{1A} (\omega_1^2 + pq)} [1 - \exp(-\rho_{1A} T_{sat})] \quad (1.19)$$

It is possible to define a saturation efficiency of the solute pool α , such that

$$\alpha = \frac{M_0^B - M_z^B(ss)}{M_0^B} = \frac{-m_z^B}{M_0^B} = \frac{\omega_1^2}{\omega_1^2 + pq} \quad (1.20)$$

This allows the PTR to be rewritten as:

$$PTR(T_{sat}) = \frac{k_{AB} \alpha}{R_{1A} + k_{AB}} [1 - \exp(-\rho_{1A} T_{sat})] \quad (1.21)$$

The equations obtained reveal that the PTR depends on many elements, the saturation time (T_{sat}), the solute concentration (M_0^B), the chemical exchange rate of solute protons with bulk water (k_{BA}), the longitudinal relaxation time of water protons ($R_{1A} = \frac{1}{T_{1A}}$), as well as on the saturation efficiency of the solute pool (α), which itself depends on the saturation power ($\omega_1 = \gamma B_{1,sat}$).

It is worth noting that the PTR increase when T_1 increases. It is one of the main advantages provided by high-magnetic field CEST since T_1 increases with B_0 (Diakova, Korb, and Bryant 2012).

Moreover, since α increases with ω_1 and thus with the saturation power $B_{1,sat}$, the application of intense saturation also leads to an increase in the Direct Saturation (DS) of pool A (also called spill-over effect). Therefore, there exists an optimal intensity at which the trade-off between saturation transfer and direct saturation of free protons is maximized. The group of Woessner showed that the optimal value of the saturation intensity $\omega_{1,opt}$ varies linearly with k_{BA} , the exchange rate between the A and B spins (Sun, Van Zijl, and J. Zhou 2005; Donald E Woessner et al. 2005). The following equation verifies the optimal saturation intensity $B_{1,sat,opt}$ for weak saturations:

$$B_{1,sat,opt} = \frac{\omega_{1,opt}}{\gamma} = \frac{k_{BA}}{\gamma} \quad (1.22)$$

In this equation, the direct water saturation derived by Donald E Woessner et al. (2005) can be written as follows:

$$\frac{M_z^A}{M_0^A} = \frac{1}{1 + \frac{\omega_1^2 T_1^A T_2^A}{1 + (\Delta_A T_2^A)^2}} \quad (1.23)$$

So far, we have been focusing on the case of CEST under low-intensity saturation. The analytical study of the solution has brought out some key concepts, such as the fast/slow regimes or the definition of PTR, which help to grasp the important elements for obtaining CEST contrast. However, these conditions are not optimum for all metabolites.

Analytical equations can be derived under more intense saturation conditions, as was done in Sun, Van Zijl, and J. Zhou (2005). However, the conditions for obtaining CEST under high intensity are very demanding in terms of SAR (Specific Absorption Rate). This often requires saturation with pulsed scheme. In addition, analytical solution computation is feasible for block pulses, but the usual pulse shape is not necessarily a block, as it shows suboptimal selectivity performance. All of this complicates the analysis and reduces the interest that could be found in analytical solutions of the Bloch McConnell equations under these regimes. Thus, for these cases of study, numerical simulation is preferred.

1.1.3 CEST contrast estimation

As shown in Figure 1.2C, during a CEST experiment a Z-spectrum is generally collected. This spectrum carries number of information, which is schematized in Figure 1.4. In order of importance, we find the direct saturation of water, the Magnetization Transfer (MT), the relayed Nuclear Overhauser Effect (rNOE), and finally the CEST contributions of hydroxyl (-OH), amine (-NH₂), amide (-NH) groups. MT arises from dipole-dipole interactions between water protons and those of other molecules that transfer part of their saturation to water. This effect is mainly produced by macromolecules such as membranes or myelin sheets, which have a very short T_2 and strong dipolar coupling (Wolff and Balaban 1989; Henkelman, Stanisz, and Graham 2001). The rNOE is an effect transferring spin polarization from one population of spin-active nuclei to another via cross-relaxation. This effect arises in CEST experiments from through-space inter- and intramolecular dipole-dipole magnetization transfer between the water protons and aliphatic and olefinic components of mobile proteins, peptides, metabolites, and lipids (Craig K. Jones et al. 2013; Zaiss, Kunz, et al. 2013; Paech, Zaiss, et al. 2014).

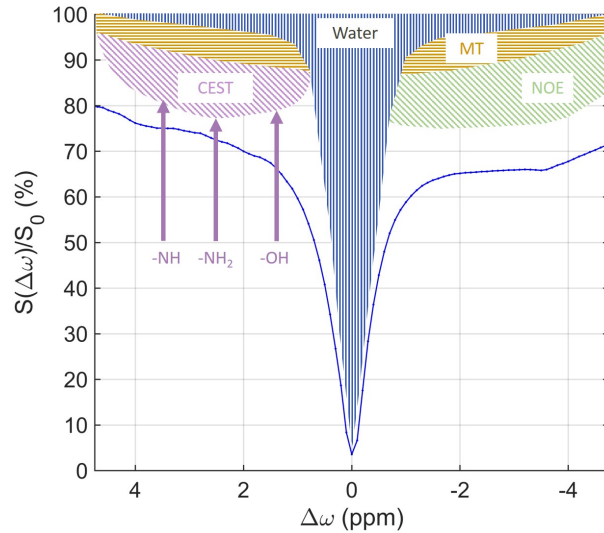


Figure 1.4: Schematic model of the various contributions visible on a Z-spectrum. The (-OH), (-NH₂) and, (-NH) groups resonate respectively roughly on [0.5 - 2] ppm, on [2 - 3] ppm, and around 3.5 ppm. The Z-spectrum plotted with the solid blue line is obtained experimentally on the brain of a healthy volunteer ($B_{1,RMS} = 0.9 \mu T$).

Several approaches exist to extract the CEST contrast produced by a metabolite of interest or in other cases for the rNOE. The most widely used approach, notably for its simplicity, is the asymmetrical Magnetization Transfer Ratio, MTR_{asym} (Hua et al. 2007; Ng et al. 2009). It is defined by :

$$MTR_{asym}(\omega) = \frac{S(-\omega) - S(\omega)}{S_0} \quad (1.24)$$

where $S(\pm \omega)$ indicates the water signals measured at the saturation offsets $\pm \omega$ (corresponding to the previous $M_z^A(\pm \omega)$) and S_0 is the reference water signal measured without any RF saturation (corresponding to the previous M_0^A). The MTR_{asym} is very easy to use, which explains its large adoption. It is a fairly reliable metric in-vitro, since subtraction from the water peak eliminates the symmetrical contribution of direct water saturation. However, this method is less reliable in-vivo. Indeed, the contributions of MT and NOE are not symmetrical with respect to 0 ppm and will give rise to an intensity of MTR_{asym} which will therefore not reflect only the CEST contributions.

Other techniques are being developed to provide precise quantification of CEST. They are generally based on the fit of Lorentzian functions to estimate the contributions of the various peaks. The simplest of these methods is what is known as Lorentzian Difference analysis (LD). This involves fitting the DS with a Lorentzian function, then subtracting it from the spectrum to obtain a residual. It is possible to find the contributions of the different proton groups to their residual (Tietze et al. 2014; X.-Y. Zhang et al. 2017). It is also sometimes modified to better match reality as in L. Zhang et al. (2019).

It is possible to fit more Lorentzians to give the approach called multi-Lorentzian fit. Typically, 5 are fitted, for water DS, MT, NOE, amides and amines (Windschuh et al. 2015; I. Y. Zhou et al. 2017). A sixth Lorentzian is sometimes added to better model the NOE by separating it into two blocks as in X.-Y. Zhang et al. (2017). There are several ways of estimating the CEST from this Lorentzian fit.

We denote Z_{ref} the acquired Z-spectrum. Consider a metabolite of interest, glutamate for the sake of example. Glutamate resonates roughly at 3 ppm and is part of the amine group, thus is taken in account in the Lorentzian curve is L_{amine} . Consider also Z_{lab} the measured Z-spectrum from which the contribution of the metabolite under study is subtracted. We have the relation $Z_{lab} = Z_{ref} - L_{amine}$.

From there, multiple way to estimate glutamate contribution exists. There is the uncorrected Lorentzian difference (Craig K. Jones et al. 2013) which is a simple metric.

$$\text{MTR}_{\text{LD}} = Z_{\text{ref}} - Z_{\text{lab}}.$$

Then MTR_{Rex} was introduced in Zaiss and Bachert (2013) to provide a more robust metric to DS and MT.

$$\text{MTR}_{\text{Rex}} = \frac{1}{Z_{\text{ref}}} - \frac{1}{Z_{\text{lab}}}.$$

This was latter improved to build the AREX contrast which correct for DS, MT and T_1 (Zaiss, J. Xu, et al. 2014; Zaiss, Windschuh, Paech, et al. 2015):

$$\text{AREX} = \frac{\text{MTR}_{\text{Rex}}}{T_1}.$$

For each of these metric, the glutamate contribution can be estimated by taking the value at 3 ppm.

There are many other methods for estimating the CEST contribution of a metabolite of interest, and only the most commonly used are presented here. In addition to these Lorentzian fit-based estimation tools, methods based on the fit of analytical solutions have also been developed. While these methods are intended to be more precise, it is mainly to obtain quantitative solutions on concentrations or pH and temperature, via exchange rate estimation that these methods have been developed (McMahon et al. 2006; Zaiss, Angelovski, et al. 2018). However, these solutions are complex and require a huge amount of data obtained with variable saturation parameters in order to obtain a solution, as this inverse problem is badly posed. Similarly, acquisitions methods relying on finger printing have been developed (S. Huang et al. 2017; Perlman et al. 2020). However, these methods are dependent on the data required to build the dictionary, which is not always easy to produce, especially for in-vivo CEST data. Solutions exploiting deep neural networks have also been recently developed, and could offer greater precision and computational simplicity (B. Kim et al. 2020).

Methods using a more exotic saturation scheme, than the one prescribed here, have been developed for exchange transfer MRI and have their own quantification tools. We can mention among others frequency-labeled exchange transfer (FLEX) (Yadav et al. 2012), combining chemical exchange saturation transfer and $T_{1,\rho}$ magnetization preparations (CESTRho) (Kogan, Singh, et al. 2012), length and offset varied saturation (LOVARS) (X. Song et al. 2012).

1.1.4 Applications

The previous section provided the theoretical basis for understanding how CEST experiments work. As discussed, CEST offers improved Signal-to-Noise Ratio (SNR) and spatial resolution, surpassing direct detection techniques such as MRS/MRSI. The promise of CEST imaging has spurred extensive development in biomedical applications, cementing its status as a rapidly growing area within MRI. Thus, CEST MRI has enabled a wide range of applications by combining the principles of magnetic resonance with the dynamics of molecular exchange.

Endogenous agents are more practical from a clinical perspective because they do not require any special authorization or infrastructure. Conversely, exogenous agents can improve CEST amplification factors by several orders of magnitude compared to endogenous agents but require a more complicated use in a practical situation (S. Zhang, Winter, et al. 2001; S. Zhang and Sherry 2003; Aime et al. 2002; Donald E Woessner et al. 2005). In this section, we will briefly examine the various endogenous CEST agent applications within the scope of this manuscript. These different agents can be grouped under the term diaCEST for diamagnetic CEST, and their exchangeable protons are found in hydroxyl, amine, and amide groups.

1.1.4.1 Amide Proton Transfer (APT)

This technique, which exploits saturation transfer by amide protons and protons of mobile proteins, is the oldest of the methods presented here (J. Zhou, Lal, et al. 2003; J. Zhou, Payen, et al. 2003). Detection of these protons is made possible by the fact that they exchange rather slowly (30 Hz) and are far from water (~ 3.5 ppm), thus allowing slow-exchange conditions to be obtained. This condition remains true even at 1.5 T, which is one of the strengths of this contrast type, and enables it to be used on a large scale. The in-vivo concentration of these protons is rather high (5-8 mM) in all tissues, enabling relatively easy detection (J. Zhou, Payen, et al. 2003; Yan et al. 2015).

APT is of interest in many pathologies because the exchange rate is highly sensitive to pH and the technique allows an indirect measurement of pH. This is particularly useful for detecting ischemic regions in stroke patients (Harston et al. 2015; Tietze et al. 2014; Sun, J. Zhou, et al. 2007). APT is also used for the detection of solid tumors, which are visible by this contrast due to the large number of mobile proteins they possess compared to surrounding tissue (Craig K Jones et al. 2006; J. Zhou, Blakeley, et al. 2008; Y. Yang et al. 2020; Togao et al. 2014; Jiang et al. 2016; Zhao, Wen, F. Huang, et al. 2011). In this context, APT also enables tumor grade to be estimated (Togao et al. 2014; Zhao, Wen, G. Zhang, et al. 2013; Wen et al. 2010). Finally, APT has been shown to exhibit hyper-contrast in the lesional regions of Alzheimer's and Parkinson's patients (R. Wang et al. 2015; C. Li et al. 2015). These results suggest that APT can be used to study the progression of these diseases in a non-invasive way. Two illustrations are given in Figure 1.5 for the study of stroke and metastases.

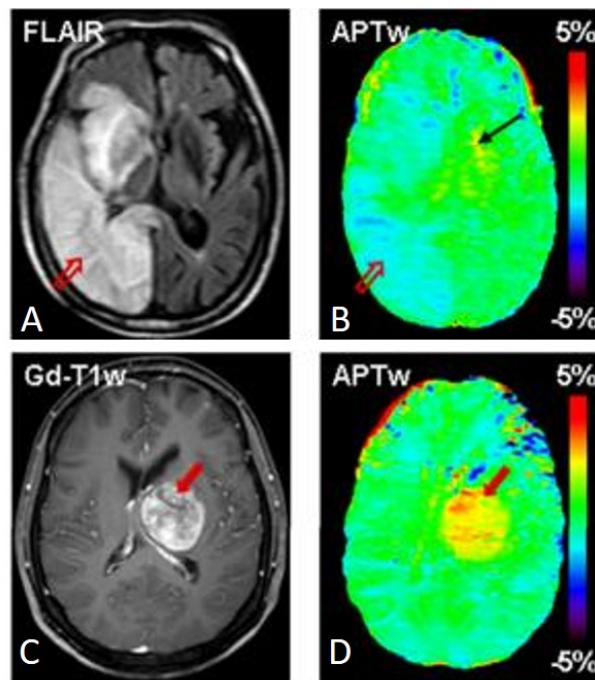


Figure 1.5: Fluid attenuated MRI (A) and APT (B) images of a patient with stroke at 5 days post-onset. GdCE- T_1w (C) and APT (D) images of a patient with lung cancer metastasis. The tumor (solid red arrow) is hyper-intense, while the stroke (open red arrow) is hypo-intense on the APT images. Figure adapted from Zhao, Wen, F. Huang, et al. (2011).

1.1.4.2 GluCEST

Glutamate (Glu) is the most common excitatory neurotransmitter in the brain and plays a crucial role in learning, memory, emotion, and cognitive function. The amine protons of glutamate resonate at around 3 ppm and are present in large quantities in the brain, making them relatively easy to detect. For example, gluCEST has been used in mouse models of neurodegenerative disease (Mohammad

Haris, Nath, et al. 2013; Crescenzi et al. 2014). In humans gluCEST has been used to study various diseases such as epilepsy, for visualization of the seizure foci (Davis et al. 2015; Hadar et al. 2021), multiple sclerosis (Dula, Pawate, et al. 2016; O’Grady et al. 2019) or in other applications such as the characterization of tumors or encephalitis (Neal et al. 2019; Jia et al. 2020). An example is given in Figure 1.6 for encephalitis in rats, in which an evolution of the gluCEST signal in the injured region can be noted.

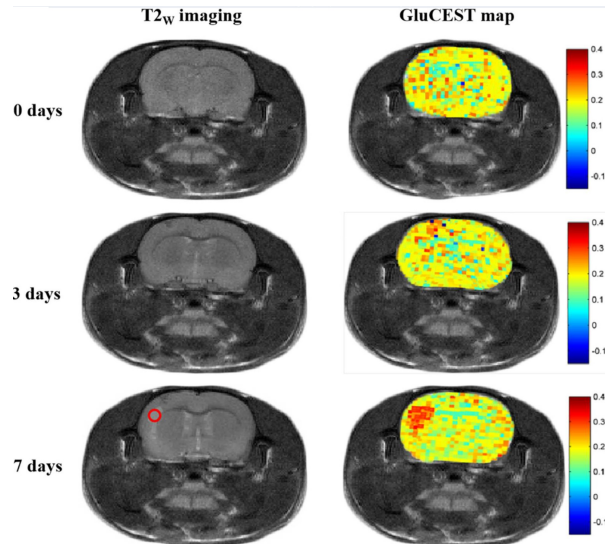


Figure 1.6: *Glutamate weighted CEST imaging in vivo in encephalitis rats. T_2w imaging and gluCEST map of encephalitis rats with *Staphylococcus aureus* infections at different time points (0, 3, and 7 days), suggest that the gluCEST signal increased with time in the injured region. Figure adapted from Jia et al. (2020).*

1.1.4.3 GlucoCEST

Glucose is the main source of energy for human body, so its measurement can reveal crucial information for the study of metabolism under normal or pathological conditions. Glucose has hydroxyl groups with chemical shifts, ranging from 0.8 to 2.2 ppm, with a maximum around 1.2 ppm under optimal saturation conditions. Glucose is naturally present in quantities just sufficient for its detection (~ 1 mM, Hwang et al. 2017), but its small chemical displacement, with respect to water. Moreover, the presence of other metabolites with hydroxyl groups, like myo-inositol or lactate, makes challenging the selective measurement of endogenous glucose (Khlebnikov et al. 2019).

The majority of GlucoCEST applications involve the infusion of D-glucose, the dynamics of which are monitored by gluCEST. This method, called Dynamic Glucose Enhanced (DGE), enables the detection of tumors, which present a hypercontrast (Chan et al. 2012; X. Xu et al. 2015; Jihong Wang et al. 2016). Non-metabolized glucose analogs are sometimes used, as their accumulation (Jin et al. 2014; Sehgal et al. 2019) enables other applications to be envisaged, such as the study of Alzheimer’s disease (Tolomeo et al. 2018). In addition, gluCEST was shown to present a reduced cerebral metabolism during anesthesia (Nasrallah et al. 2013).

Figure 1.7 illustrates the evolution of the DGE signal in different regions of interest in the brain of a patient suffering from glioblastoma. Here, gluCEST provides comprehensive information on the pathology compared with the reference method, which is the Gadolinium Contrast Enhanced T_1 weighted (GdCE- T_1w) image. In some cases, these approaches can provide a result comparable to what can be obtained with PET, without exposing the patient to ionizing radiation.

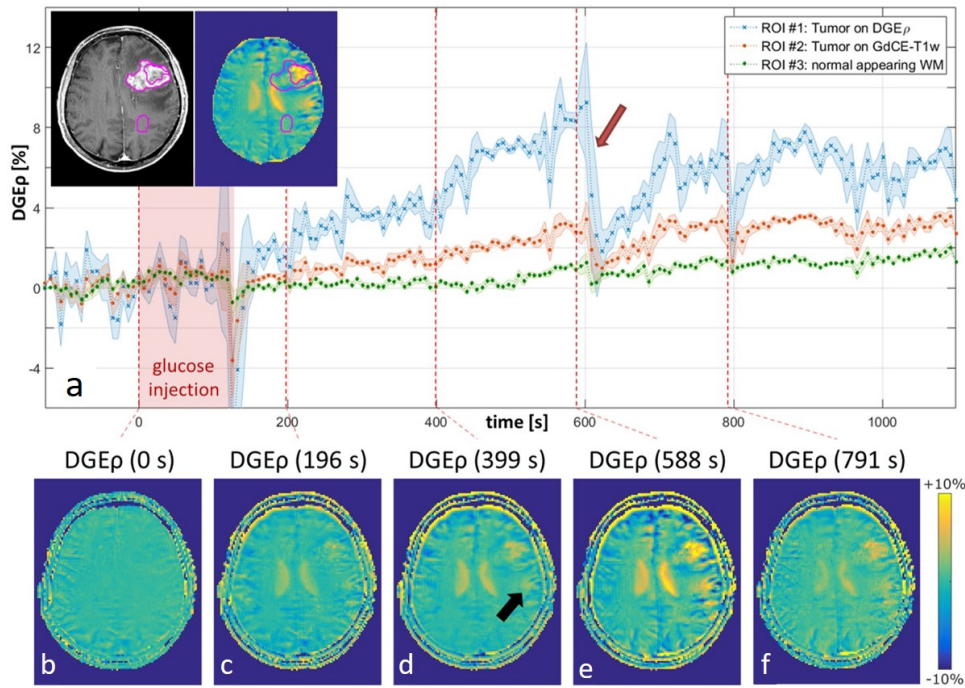


Figure 1.7: $T_{1,\rho}$ -weighted dynamic glucose enhanced MRI applied in the study of a patient with a glioblastoma. (a) DGE_{ρ} time curves in different Regions Of Interest (ROIs). Increasing DGE_{ρ} values are obtained in both tumor-ROIs after the end of the glucose injection. The red arrow marks an abrupt signal drop induced by patient motion. (b-f) DGE_{ρ} images at different time points after glucose injection. Note the hyperintense region at the bottom of the tumor area (black arrow in (d)), which is not visible in the GdCE- T_1w image. Figure adapted from Schuenke, Paech, et al. (2017).

1.1.4.4 Other contrasts

Other types of CEST contrasts are also possible. One example is creatine, which carries amine groups and is of interest for the study of tumours and epileptic foci (Cai, Singh, et al. 2015; D.-H. Lee et al. 2019). Besides glucose, other metabolites with hydroxyl groups can be detected, such as myo-inositol, a glial metabolite whose variation in concentration has been observed in Alzheimer's Disease patients (AD) in Mohammad Haris, Singh, et al. (2013). Another example is glycogen, which is not detectable in 1H MRS and whose in-vivo detection was achieved in liver in Van Zijl et al. (2007). Non-CEST effects that induce a magnetization transfer are also being studied, such as rNOE and MT. The rNOE is of particular interest for studying protein denaturation in Y. Zhou et al. (2023). Applications have been shown in the vicinity of acute tumors in Craig K. Jones et al. (2013) or in multiple sclerosis patients in J. Huang et al. (2021). Magnetization Transfer weighted contrast is used to detect early demyelination or protein alteration (Filippi and Rocca 2007; Varma et al. 2015).

The great versatility of CEST is its strength, as it can be used to characterize the development of neurodegenerative diseases, cancers or strokes. But this versatility leads to some challenges, as it is sometimes difficult to obtain a selective contrast, free from the effects of pH and temperature, as well as the CEST effect of metabolites resonating at frequencies close to those of the metabolite under study. This is why important methodological developments are being carried out in CEST to provide more reliable and robust imaging, in order to take full advantage of the sensitivity gain promised by the method.

With this in mind, the increasing field strength of available MRI scanners is proving extremely promising for CEST, enabling improvements in sensitivity, spectral selectivity, exchange conditions and other key parameters.

1.2 High field MRI for CEST

The combination of CEST and high-field MRI is proving extremely versatile, enabling the detection of more metabolites than at lower fields, particularly protons from rapidly-exchanging hydroxyl groups. This increase in field strength brings with it a whole host of benefits, but also constraints, which we will address in this section through the prism of CEST MRI. We will focus solely on clinical MRI, as the constraints of preclinical MRI, which can reach much higher magnetic fields, are less severe.

Despite technical advances, MRI is limited by the signal-to-noise ratio, which prevents imaging at finer resolutions. Noise is predominantly dominated by the sample, which means that progress in reducing machine noise will not improve much the SNR. It is therefore logical to seek to increase the signal intensity emitted by the sample. This is the approach taken by hyperpolarization techniques (Viale et al. 2009; Ross et al. 2010). Another way of increasing the polarization of the spins in the sample is to increase the magnetic field, as it can be shown that spin polarization is directly proportional to the B_0 field (Ladd et al. 2018). As a result, ultra-high-field magnetic resonance imaging (≥ 7 T) is on the increase, and since the first ultra-high-field MRI system was installed in 1997, over seventy 7 T MRI systems have been installed. Although these MRIs were initially limited to research applications, they are now becoming even more widespread, as their use in clinical settings has been authorized since 2017.

1.2.1 Benefits and challenges of high-fields MRI

As mentioned, the main advantage of switching to a high magnetic field is to benefit from a better signal-to-noise ratio. In the case of noise-dominated samples, it was initially shown that the SNR evolved linearly with the magnetic field (D. Hoult and Richards 1976; D. I. Hoult and Phil 2000). However, at high magnetic fields, the models used are no longer valid, and the SNR varies more rapidly than a simple linear law. The SNR also becomes dependent on the sample, its composition and its shape, which complicates its study. It has been shown that in the center of a spherical phantom, the SNR varies linearly with $B_0^{1.94}$ (Le Ster et al. 2022)

In addition to this gain in SNR, high magnetic fields bring other changes that benefit several MRI techniques (Ladd 2007; Moser et al. 2012; Ladd et al. 2018). Relaxation times have already been modified: increasing the magnetic field lengthens the relaxation time T_1 and shortens the relaxation times T_2 and T_2^* . Increasing the T_1 improves the results of time-of-flight (TOF) and arterial spin labeling (ASL) techniques by increasing the saturation time of the spins and therefore their concentration, ultimately improving the contrast of these methods (Petcharunpaisan, Ramalho, and Castillo 2010). Meanwhile, lower T_2^* provides contrast gains for Susceptibility Weighted Imaging (SWI) and blood-oxygen-level dependent MRI (BOLD).

Finally, the use of high magnetic fields enables better spectral selectivity of chemical species, which benefits both CEST and MR spectroscopy. In fact, the chemical displacement of species is constant in ppm values, and increases linearly with the Larmor frequency, and therefore with the static magnetic field.

In the case of CEST, increasing the chemical shift dispersion (in Hz) brings us closer to slow-exchange conditions, and thus further improves spectral selectivity. Increasing the T_1 gives a better saturation rate of the water pool (see Equation (1.21)) by delaying the return to equilibrium of saturated spins. Also, lower T_2 and T_2^* allow faster saturation of the metabolite pool, bringing a gain for rapidly exchanging protons.

Despite all these advantages, some drawbacks come with the use of a stronger magnetic field.

As the T_1 increases, a longer TR must be chosen to maintain a constant Ernst angle, lengthening the examination time accordingly. With greater susceptibility differences in tissues, distortions are exacerbated, as are intravoxel phase shift effects, which adversely affects image quality (Ladd 2007; Moser et al. 2012; Ladd et al. 2018). Two other elements appear with the transition to very high mag-

netic fields and are particularly noteworthy: the inhomogeneities of B_1 which create a loss of contrast, and the Specific Absorption Rate (SAR) which becomes limiting. These last two points are examined in more detail below.

1.2.2 Parallel Transmission

As the Larmor frequency increases, the wavelength of RF waves becomes shorter and shorter. At 7 T the wavelength is approximately 12 cm in the brain (Q. X. Yang, Jinghua Wang, et al. 2002). As the size of the brain is comparable with this wavelength, constructive and destructive interference (Van de Moortele et al. 2005) generate minima and maxima throughout the brain. Figure 1.8 shows how this effect evolves with magnetic field.

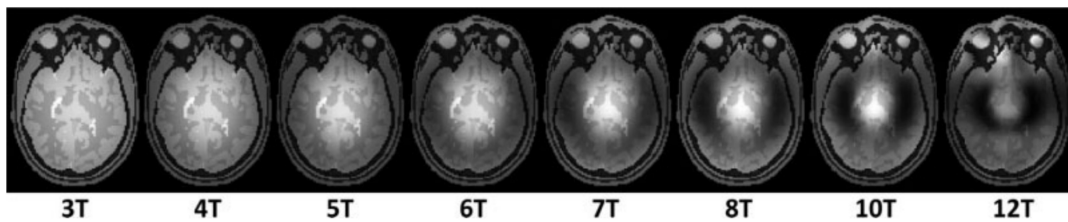


Figure 1.8: *Simulated B_1 inhomogeneities effect with field strength. Simulated gradient echo with a birdcage coil. Figure adapted from (Webb and Collins 2010).*

Several solutions exist for mitigating the B_1^+ inhomogeneities. Adiabatic pulses can be used. These pulses are insensitive to B_1^+ inhomogeneities by imposing a gradual variation in frequency around the target frequency. However, this comes with a high energy consumption, which limits its use (Tannús and Garwood 1997). It is possible to place dielectric pads that locally distort the B_1 field to reduce shadow zones (Q. X. Yang, Mao, et al. 2006), but their effectiveness is limited to the periphery of the brain. Another solution is to use a RF coil specifically designed to resolve these B_1^+ inhomogeneities; for example, a spiral-shaped coil has demonstrated better performance in terms of B_1^+ homogeneity than a conventional birdcage coil (Alsop, Connick, and Mizsei 1998).

An elegant solution is to use parallel transmission. In this case, instead of driving the RF coil via a single channel, several channels, behaving like many small antennas, are controlled independently in amplitude and phase. By controlling these channels judiciously, the inhomogeneities of B_1^+ can be greatly reduced.

The first application of parallel transmission was static RF shimming. This involves jointly optimizing the amplitude and phase of each channel. The coefficients are obtained by minimizing a cost function constrained by SAR conditions. This method offers significant gains over the parallel transmission-free mode, Circular Polarization (CP) (Adriany et al. 2005; Mao, Smith, and Collins 2006). It is possible to gain a few degrees of freedom by interleaving several RF shimming modes. This is known as Time Interleaved Acquisition of Modes (TIAMO) (Orzada et al. 2010). Combining the images acquired with the different modes produces a homogeneous image. However, this is time-consuming, since as many images have to be acquired as there are modes.

By modulating the gradients during the excitation pulse, it is possible to have more degrees of freedom, enabling excellent homogenization of the flip angle across the entire brain volume. When RF pulses are selective, they are referred to as multi-spokes; for 3D acquisition, they are called k-points (Katscher et al. 2003; Setsompop et al. 2008; Cloos et al. 2012). This is because the action of gradients corresponds to a displacement in k -space. Moving between several of these points in k -space ensures maximum coverage of 2D or 3D space, depending on the use case. These methods use a discretization of the k -space, for which a waveform is applied to each point. The SPINS and GRAPE techniques achieve even better results by using a continuous path through the k -space which

allows for more degrees of freedom (Malik et al. 2012; Van Damme et al. 2021). Figure 1.9 illustrates the trajectories of these different strategies.

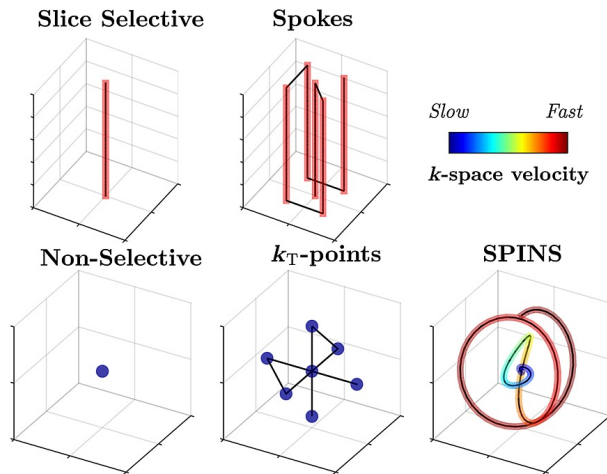


Figure 1.9: *k-space trajectories for flip angle shimming. Black lines indicate the path through k-space, and shaded regions indicate where RadioFrequency (RF) transmission occurs, with the color of the shading indicating the k-space velocity at that point. The top row shows trajectories which are spatially selective in a single direction and, consequently, much higher spatial frequencies are visited in that dimension. Figure adapted from Padormo et al. (2016).*

In general, these pulses are obtained by optimizing their constituent parameters using a gradient descent algorithm that seeks to minimize the error between a target flip angle and the simulation of pulse realization. To achieve this, a map of B_1^+ is needed, that allows to pass between pulse parameters and the flip angle map. Generating subject specific pulses during the examination with the subject's B_1^+ map is called Tailored Pulses (TP). However this means first acquiring the B_1^+ map, then optimizing the pulses, which complicates the process. It is possible to get around this by using Universal Pulses (UP) (Gras, Vignaud, et al. 2017). This class of pulses is optimized on a dataset of tens of B_1^+ maps, with the idea that it would also work for a subject not included in the dataset. This enables offline optimization to be carried out and considerably lightens the use of parallel transmission in a clinical context.

In the CEST context, B_1^+ inhomogeneities not only lead to a loss of SNR, as they also lead to quantification errors. A method inspired by TIAMO was introduced by Liebert, Zaiss, et al. (2019) to mitigate B_1^+ inhomogeneities in CEST applications. In this approach, called Multiple Interleaved Mode SATuration (MIMOSA), the CEST saturation is composed of two interleaved modes, CP mode and 90° mode, this latter corresponding to CP mode with an additional 45° phase shift between each channel. The results obtained by combining these two modes were shown to provide much more homogeneous saturation than that obtained using the CP mode alone (Figure 1.10).

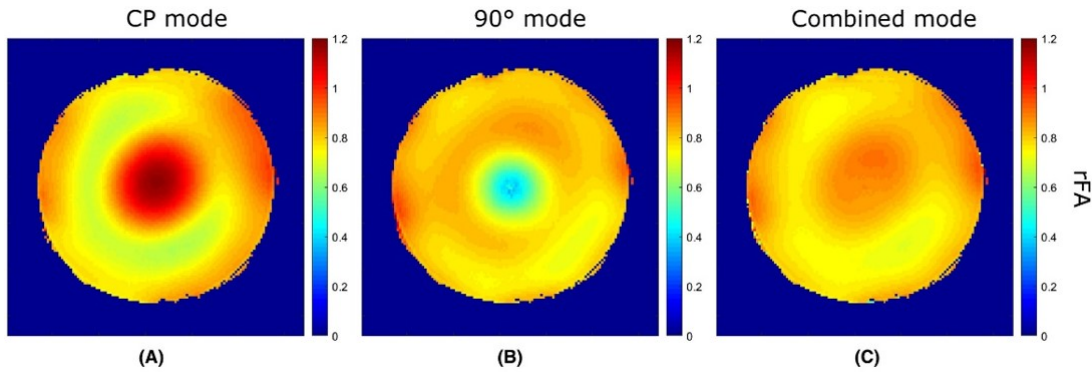


Figure 1.10: *Relative flip angle maps in a phantom for the CP mode (A), the 90° mode (B) and the combined continuous wave power equivalent of the 2 modes (C), which is used in MIMOSA. An improvement of the homogeneity of the excitation field can be observed in the combined mode. Figure adapted from Liebert, Zaiss, et al. (2019).*

1.2.3 Specific absorption rate consideration

The SAR corresponds to the energy deposited in the tissues and converted into heat. It is expressed as follows:

$$SAR(\mathbf{r}) = \frac{1}{T} \frac{\sigma(\mathbf{r})}{2\rho(\mathbf{r})} \int_0^T \|\mathbf{E}(\mathbf{r}, t)\|_2^2, dt \quad (1.25)$$

where \mathbf{E} is the electric field distribution, σ is the electrical conductivity, ρ is the sample density and T is the integration time. The SAR standard is defined by IEC 60601-2-33, which stipulates that SAR must be calculated globally and locally over a volume of 10 g of tissue, for a sliding window of 10 s and 6 min. SAR becomes a problem at very high magnetic fields because, by increasing slightly less than quadratically with B_0 (Robitaille et al. 1998; Z. Cao et al. 2015), it restricts the design possibilities of RF pulses and constrains the TR of certain sequences, CEST in particular.

Estimating precisely subject-specific SAR can be challenging as electric field distributions and anatomical details are often unknown. However, Virtual Observation Points (VOPs) provide a way to estimate in real time the maximum local SAR (Eichfelder and Gebhardt 2011; Graesslin et al. 2012). VOPs result from simulating RF waves on an electromagnetic head model to obtain SAR matrices across ten of thousands of voxels. As local SAR computation during scanning is not feasible at this scale, the information is compressed. This compression is performed ensuring that the SAR simulated across model voxels never exceeds values calculated for VOPs. VOPs leverage redundant information between neighboring voxels exposed to similar RF responses. By judiciously choosing SAR matrices, the number of SAR matrices can be reduced dramatically to only a hundred or less thus facilitating local SAR monitoring in real-time (Eichfelder and Gebhardt 2011; Boulant et al. 2018).

1.3 Conclusion

CEST MRI is a novel technique that has opened up new possibilities for preclinical and clinical molecular imaging. It has led to the development of innovative detection methods and has enabled researchers to study the exchange of molecules in tissues. Unlike other MRI contrast agents, such as gadolinium, CEST is an on/off switch contrast that can be activated at will. There are numerous CEST contrasts that can be used to explore a wide range of research areas, including cerebrovascular stroke, tumors, muscle physiology, metabolism, and neurodegenerative disorders. The topic is constantly evolving, and new applications are emerging all the time. However, there are some limitations

to the use of CEST in a clinical context, mainly due to B_1^+ inhomogeneities and SAR constraints. The selectivity of CEST is also a major challenge that still needs to be overcome.

The work presented in this manuscript aims to improve the CEST acquisitions to make it a faster and more efficient tool for studying metabolic mechanisms. This involves developing a parallel transmission sequence and optimizing its parameters to provide more reliable and rapid acquisition method, and then evaluating the tool's performance through a clinical comparison of several population groups.

Chapter 2

Background

The aim of this chapter is to present the different materials and study subjects used throughout this thesis. The magnets and radio-frequency coils will be described. Then, the various phantoms and their characteristics are presented. The settings and parameters required for the experiments are given in detail, providing everyone with the necessary details for each experiment.

Contents

2.1 Imaging System	24
2.1.1 Magnets	24
2.1.2 Coils	25
2.1.3 Adjustments	25
2.2 Phantoms	26
2.3 In vivo experiments	28

2.1 Imaging System

2.1.1 Magnets

The MRI system used for this work is the Siemens 7 T (Figure 2.1). The development of the CEST pTx sequence and the scans of the volunteer cohort were carried out on this scanner. The 17.2 T preclinical MRI system was occasionally used for methodological development, notably those presented in Section 5.4.1 for which mice were scanned.



Figure 2.1: *The 7 T Magnetom MRI in Neurospin.*

In order to mitigate RF inhomogeneities appearing at high magnetic field, the Neurospin 7 T scanner is equipped with a parallel transmission chain (pTx). This pTx system enables uniform excitation which is necessary for efficient CEST imaging as detailed later. This chain consists of eight independent modulators (manufactured by Dressler, Fort Collins, USA), individually connected to dedicated power amplifiers, each capable of delivering a maximum peak power of 1 kW. The direct power output from each RF channel can be measured in real time through the use of directional couplers. Limits are set for peak power and for average power over a moving window of 10 s and 6 min. If any of the predefined limits are exceeded, the data acquisition process is immediately interrupted. These power limits are set to ensure the safety of the patient and to protect the hardware. In addition to the simple power limits, the scanner also has a mode (called 'experimental mode') that allows the use of in-house developed VOPs. When these virtual observation points are used, the peak power limits are increased and the SAR is managed by the VOPs.

The 17.2 T is a unique preclinical MRI system (Figure 2.2). It is equipped with the world's most powerful horizontal magnet, providing a very stable and homogenous magnetic field making it an exceptional tool for CEST studies. Indeed, its high sensitivity and improved contrast facilitate the development of CEST methodology.



Figure 2.2: *The 17.2 T pre-clinical MRI.*

2.1.2 Coils

One of the essential elements in magnetic resonance imaging is the radio-frequency coil(s). To produce resonance, an oscillating magnetic field in the form of an RF wave must be emitted to excite the spins of the object being studied. The relaxation of the spins also emits an oscillating magnetic field. A coil is needed to generate and collect these RF waves. MRI coils come in all shapes and sizes, depending on the applications.

For all experiments performed on the 7 T clinical scanner, the Nova 8Tx/32Rx coil was used (Figure 2.3). This coil has transmit loops in 8 independent channels, allowing the use of parallel transmission. In addition, it has 32 independent receive loops, allowing parallel imaging (Roemer et al. 1990). The 32 channels, each acting as a surface coil, cover the entire volume of the brain with a high SNR. The METRIC team at Neurospin has developed and validated Virtual observation points for this coil (Boulant et al. 2018), allowing manageable RF pulse design algorithms in pTx.

For the experiments on the 17.2 T scanner, a volumetric quadrature antenna (Rapid Biomedical GmbH Rimpfing, Germany) was used for transmission and reception (Figure 2.4).

2.1.3 Adjustments

At the start of each MRI experiment, a number of adjustments are made. The adjustments presented below relate to the Siemens 7 T MRI with the Nova coil. The adjustments made for the few experiments on the 17.2 T are not detailed here, but broadly follow the same organisation, with a few exceptions specific to the scanner itself.

Before any experiments on human volunteers, a reference phantom is used for safety and quality testing. These tests ensure that the imaging chain works properly and that automatic shutdown procedures are in place if, for example, the SAR is exceeded.

The subject is placed comfortably on the table with the head in the coil, wedged by foam pads if necessary. The position of the coil is carefully measured and placed at the isocenter of the magnet. A first localizer scan is performed to check the position of the subject in relation to the coil and magnet. At this point the shim and working frequency are set by default. An initial shim adjustment, at first and second order, is made on the full volume of the brain and the frequency is set. A second shim and frequency adjustments are made to ensure convergence of the settings. If necessary, a third pass

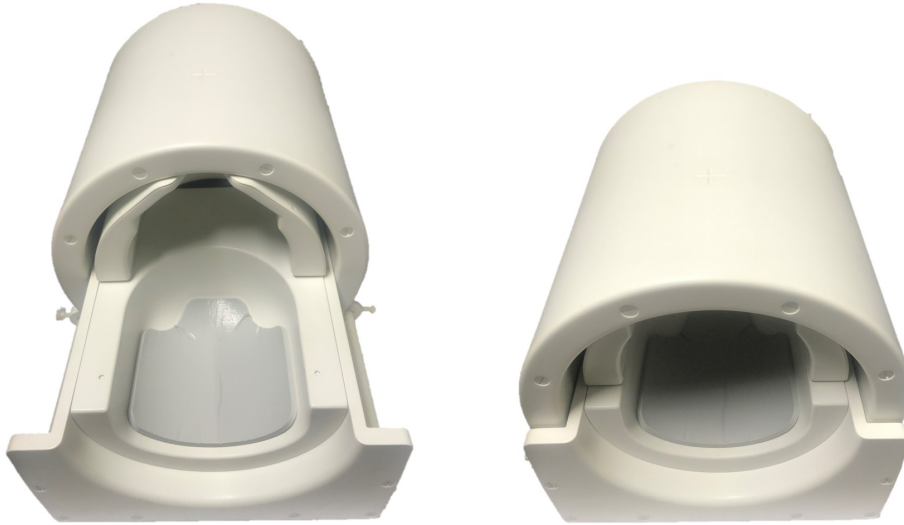


Figure 2.3: *Nova 8Tx/32Rx head coil for 7 T MRI, opened for subject positioning (left) and closed for scanning (right).*

is made. Following this, an anatomical acquisition and any B_1^+ field mapping or reference voltage adjustments are done.

Prior to the CEST acquisition, a shim and frequency adjustments are performed specifically for the region to be imaged. B_0 inhomogeneities must be minimised to ensure the best conditions for CEST. The pTx pulses are loaded and SAR management by the VOPs is activated. During a CEST acquisition session, a new B_0 map is generated every 20 minutes, often using the WATER Saturation Shift Referencing method (WASSR) (M. Kim et al. 2009). As the temperature in the MRI and of the subject can vary during the acquisition, leading to a frequency drift, it is necessary to acquire B_0 maps regularly.

2.2 Phantoms

When developing MRI sequences, it is important to test the correct functioning of the methods used on a so-called phantom. These phantoms often consist of a plastic container filled with a watery substance that mimics the characteristics of the brain. Phantoms are useful for highlighting certain phenomena, optimising protocols, testing the signal-to-noise ratio of the system in an ideal case or even obtaining real-world data for the development of data processing tools.

Several phantoms were used for the development of CEST MRI sequences. All the phantoms used to obtain the results of this manuscript are presented in the section below.

In clinical 7 T MRI for CEST applications, the inhomogeneities of B_0 and B_1 are critical. In order to effectively develop methods to correct for these inhomogeneities that are presents in vivo in humans, it is important to be able to mimic them using a realistic phantom. Our phantom, Skully was designed with this in mind and followed the design in Jona, Furman-Haran, and Schmidt (2021). With the help of Jérémy Bernard (CEA), a 90% scale model of this phantom was 3D printed (Figure 2.5). The resin used is resistant to high temperatures, so it can be filled with hot agar gel and emptied by placement in a hot oven. Skully is made up of two compartments, an internal one that imitates the brain, and an external one that imitates the muscles and skin of the head.



Figure 2.4: Volumic coil used for the experiments on the 17.2 T.

In order to develop the glutamate-weighted CEST, a phantom ball was also made (Figure 2.6).

The composition of the phantoms is given in the Table 2.1. Agarose is used as a solid matrix to create a stable structure for the phantom, additionally it creates a small MT effect making a more realistic effect. Sodium chloride reproduces the normal saline concentration of biological tissue and adjusts the conductivity of the medium. Gadolinium (DOTAREM 0.5 mmol/ml, Guerbet, Villepinte, France) was added to balance the T_1 relaxation-time. Finally, sodium azide was also added to inhibit bacterial proliferation.

The two phantom presented above were prepared as follows: the solutes were added one by one to distilled water and the solution was stirred constantly to obtain a homogeneous mixture. Agarose was added last, as it is insoluble at room temperature. The pH was then adjusted to 7.0 by adding a highly concentrated base (NaOH) or acid (HCl) and by monitoring its variation with a pH meter (Mettler-Toledo, Viroflay, France). The solution was then heated while stirring. When it reached 80 °C and the agarose had completely melted, any foam that may have formed on the surface was skimmed off and the mixture was poured into the container. The container was previously placed in an oven at 80 °C and once filled with the solution, it was placed back in the oven for a few minutes. This was done to allow the bubbles suspended in the solution to rise to the surface. Finally, the phantom was cooled to room temperature and stored at 18 °C.

When required by the experiments, the phantom was placed in a 37 °C oven for 24 hours to ensure a homogeneous temperature distribution within the phantom. Measurements were taken with an optical thermal probe to monitor the temperature inside the phantom throughout the experiments and the data were recorded using 'Evolution' software (Fiso Technologies). These measurements showed that, for Skully and in a room at 20 °C, the temperature in the center of the phantom decreased by approximately 0.3 °C per hour.

	Agarose (%)	Sodium Chloride (mM)	Gadolinium (mM)	Sodium Azide (mM)	CEST Agent (mM)
Skully, inner	2.5	68	0.06	4	10 D-Glucose
Skully, outer	2.0	68	0.06	4	15 Creatine
Ball	2.5	68	0.06	4	10 Glutamate

Table 2.1: List of phantoms and description of their composition.

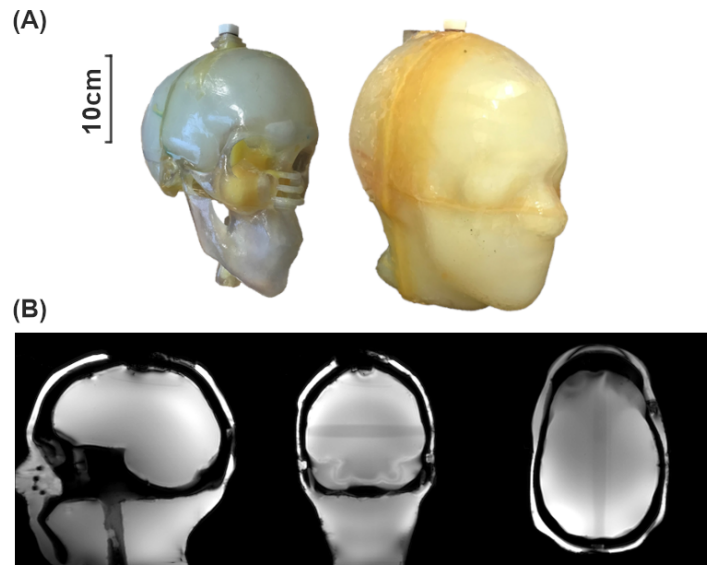


Figure 2.5: *The realistic head shaped phantom: Skully. (A) Photographs of the inner (left), and outer (right) compartments. (B) MR localizer images showing the sagittal (left), coronal (middle), and axial (right) planes.*

The phantoms thus obtained have a spin-lattice relaxation time T_1 of 1550 ± 50 ms and a transverse relaxation time T_2 of 60 ± 5 ms at 7 T. These values are close to those of water in the human brain (Wright et al. 2008; Michaeli et al. 2002) and provide realistic conditions for the experiments.

2.3 In vivo experiments

Phantoms are useful for methodological development, but their realism is always limited. It is generally necessary to perform vivo experiments in order to validate the methods tested on phantoms. As part of this work, experiments were carried out on healthy volunteers to develop the tool, and a case-control study was conducted.

All procedures involving human subjects were submitted to the relevant Comité de Protection des Personnes (CPP) and the local ethics committee. Similarly, all animal procedures were approved by the local ethic committee and by the Ministère de l'Éducation Nationale, de l'Enseignement Supérieur et de la Recherche. In addition, experiments were conducted in strict accordance with the national and European recommendations and guidelines.

Approval to conduct these experiments on human subjects was granted after a rigorous assessment of their scientific relevance, feasibility, and compliance with fundamental ethical principles, such as respect for human dignity, the physical and psychological integrity of participants and the guarantee of free and informed consent. This consent was obtained from all participants prior to their inclusion in the study. In addition, all studies involving human subjects were conducted in compliance with applicable national data protection and confidentiality regulations, including the French Data Protection Act and the European Union's General Data Protection Regulation (GDPR).

The health and well-being of the animals is central to the experiments. During each experiment, the animals were anesthetized with isoflurane, and their respiration and rectal temperature were monitored throughout. Their body temperature was maintained between 36 and 37 °C with a heated blanket.



Figure 2.6: *The glutamate ball phantom. The diameter of the ball is 14 cm.*

During the different experiments, 9 healthy young volunteers were scanned for methodological development (Chapter 4). For the study in Chapter 5, 10 young and 10 older healthy volunteers were scanned on the day of writing this manuscript. One Alzheimer's disease patient has been scanned and we expect to scan at least 10 more to continue this thesis work. For preclinical experiments, a total number of 11 wild-type mice (9M/2F between 4 and 20 month old) were scanned in order to optimize CEST protocol and produce some methodological development in Section 5.4.1.

Chapter 3

Development of CEST at 7 T

This chapter presents the optimization results for obtaining CEST contrast on clinical 7 T MRI, in simulation and in vitro. A CEST sequence was used, and several iterations of this sequence were done. These sequences are described, then the optimal pulse parameters for generating the different contrasts are defined. Finally, the effect of B_0 inhomogeneities on CEST will be discussed, as well as the solution chosen to correct it.

Contents

3.1 CEST-EPI Sequence	32
3.1.1 CEST-EPI pTx	32
3.1.1.1 Specifications	32
3.1.1.2 Sequence programming	32
3.1.2 CEST-EPI fast	34
3.1.2.1 MetaPulses	35
3.1.2.2 Steady-state CEST sequence	35
3.1.2.3 CEST-EPI fast interface	37
3.2 GlucoCEST and GluCEST optimal saturation	37
3.2.1 GlucoCEST	38
3.2.2 Pulse shape	39
3.2.2.1 Notion of pulse energy	39
3.2.2.2 Spectral selectivity	40
3.2.3 Saturation parameters	42
3.2.4 Similar developpement for GluCEST	44
3.2.5 Discussion and conclusion	44
3.3 Experimental validation	45
3.3.1 CEST-EPI	46
3.3.2 CEST-EPI fast	50
3.3.3 MetaPulses	52
3.4 Static field inhomogeneities artifacts correction	55
3.4.1 Consequences of inhomogeneties of static field on CEST	55
3.4.2 Post-processing mitigation	55
3.4.3 Discussion and conclusion	58

3.1 CEST-EPI Sequence

The first iteration of the CEST sequence was used for the experiments presented in Chapter 4. It is based on a vendor Echo Planar Imaging (EPI) sequence with a pTx pre-saturation. This sequence was later modified to enable full pTx saturation and multi-slice imaging for the acquisitions presented in Section 5.

3.1.1 CEST-EPI pTx

3.1.1.1 Specifications

The first element required for the development of clinical CEST at Neurospin was a suitable CEST imaging sequence. To mitigate the B_1^+ inhomogeneities inherent to high magnetic fields, at least the pre-saturation of the sequence must be in parallel transmission. Otherwise, correcting for B_1^+ inhomogeneities in CEST images requires additional acquisitions and therefore longer scan times for the subject. This also complexifies the data processing and may not correct the effect entirely.

Measuring a Z-spectrum means acquiring one image per spectral point (saturation frequency). Due to the time constraints of acquisition in a clinical context, it had to be done in no more than a few minutes maximum.

In summary, the sequence developed must satisfy the following points:

- Supports parallel transmission at least for saturation
- Allows the acquisition of one Z-spectrum in a few minutes

The initial approach was to base the sequence on the EPI module and adapt it to use parallel saturation transfer. This sequence was modified later to support full pTx readout and have a faster CEST acquisition.

3.1.1.2 Sequence programming

At the beginning of this PhD project, I have programmed a first CEST sequence using the Siemens IDEA development environment. Neurospin has a library that allows the development of pTx RF excitation modules. From this library, an inheritance class has been created to define a CEST saturation module. The selected saturation is composed of modes, each with a given set of the pTx parameters. The different modes are played one after the other and the set of modes can be repeated. This module is followed by a spoiler to remove any residual magnetization (see Figure 3.1).

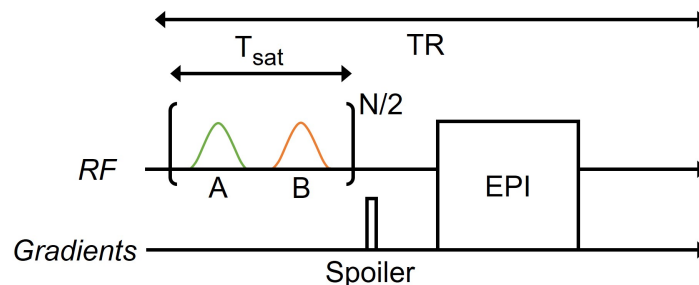


Figure 3.1: Diagram of events of the CEST-EPI sequence. Here a two modes saturation is represented, with the A and B coloured Gaussian curves.

The user can define the elements of the presaturation, by loading the pulses into the system using .ini files (each mode having its own file). An interface (Figure 3.2), accessible from the sequence protocol, is available with the following parameters :

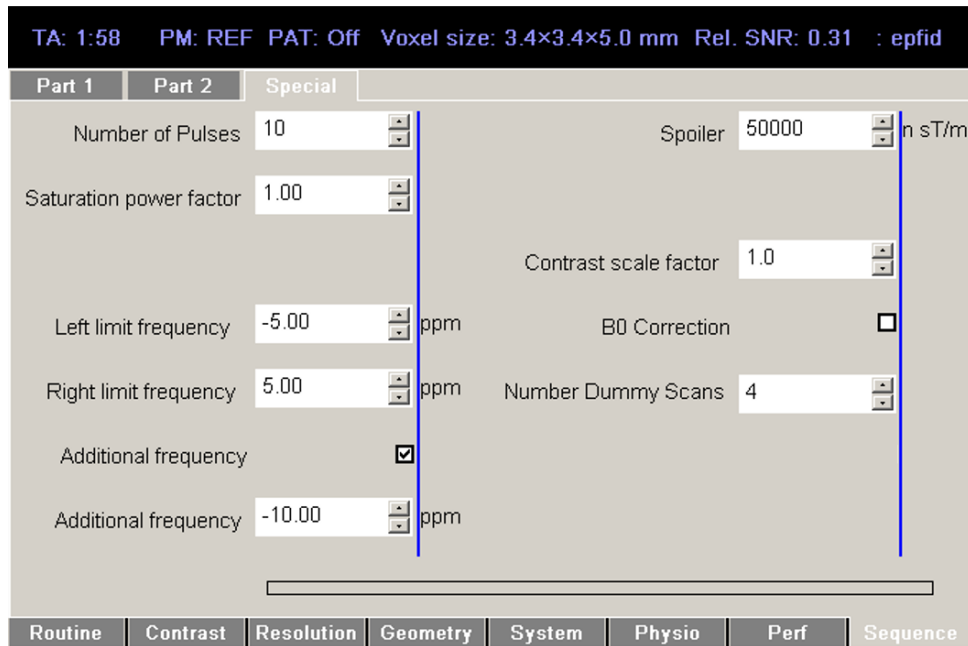


Figure 3.2: Interface of the CEST-EPI Sequence.

- Number of pulses: number of pulses that make up the saturation. If this number cannot be divided by the number of modes, the first ones will be played more. For example, for 3 saturation modes, A, B, and C, with a number of pulses = 8, the saturation scheme will be {A, B, C, A, B, C, A, B}.
- Saturation power factor: scaling factor for the pulses to adapt to a desired B_1 of the saturation.
- Left limit frequency: left sampling frequency
- Right limit frequency: right sampling frequency
- Additional frequency: additional frequency to sample, acquired in first (optional)
- Spoiler: spoiler momentum, to erase any remaining magnetization
- Contrast scale factor: scaling factor for acquired images before saving. Since the images are sampled at 2^{12} bits, the binning noise can be reduced by adjusting the image constriction to fill the 4096 bins at best. Optimal value exists depending on the CEST experiment but for a typical gluCEST experiments, it is bright enough to keep the parameter to 1.
- B_0 Correction: vendor algorithm (EPI auto B_0 correction), originally intended to assess the drift of B_0 during repetitions and compensating for this drift by applying a linear phase to the data in the phase encoding direction. The cause of the drift is mainly due to the heating of gradients, which are used intensively in fMRI, for example. Without the correction, the effect of the B_0 drift on the image is a shift in my phase encoding direction during repetitions but this correction somehow leads to a virtual motion when a CEST saturation is applied and was therefore made adjustable. For all experiments presented in this manuscript, it was deactivated.
- Number of dummy scans: number of dummy scans to have a magnetization in a steady-state.

The sequence parameterized in this way will automatically define its frequency sweep path according to the left, right limits and the additional frequency. There are several ways to perform the

frequency sweep between the right and left frequencies. For example, to sample the frequencies between -5 and 5 ppm every 1 ppm, the direct approach would be to move linearly through the spectrum, i.e. sample the frequencies in this order $\{-5, -4, -3, -2, -1, 0, 1, 2, 3, 4, 5\}$. This implies that two opposite frequencies are separated in time. However, many CEST metrics compare the positive and negative parts of the spectrum, and since subject movement can occur at any time, there is an increased probability that the spatial position of voxels acquired at a positive frequency will not match those acquired at a negative frequency.

One solution is to acquire Z-spectrum points alternately to the left and right of 0 ppm. In our example, this results in $\{-5, 5, -4, 4, -3, 3, -2, 2, -1, 1, 0\}$, which can be called a $\{-, +\}$ trajectory. The $\{+, -\}$ trajectory follows the same principle starting with a positive frequency. This way, two opposite frequencies are captured successively, minimizing the risk of motion artifacts. However, this is only a partial solution, since another problem arises: the interdependence of the measurements. By following a $\{-, +\}$ path, one side of the spectrum, in this case the negative, is systematically sampled before the other. Because the magnetization is not completely relaxed after a TR, bias in the measurement is introduced.

To reduce it as much as possible, the strategy adopted in the CEST-EPI sequence is to invert the sign of the acquired frequencies 2 times out of 4. In our example, we obtain $\{-5, 5, 4, -4, -3, 3, 2, -2, -1, 1, 0\}$, and called a $\{-, +, +, -\}$ scheme. There is still an introduced bias with this scheme, but it can be shown that the Z-spectrum average over two adjacent frequencies is unbiased. An illustration of these different frequency trajectory strategies is given in Figure 3.3.

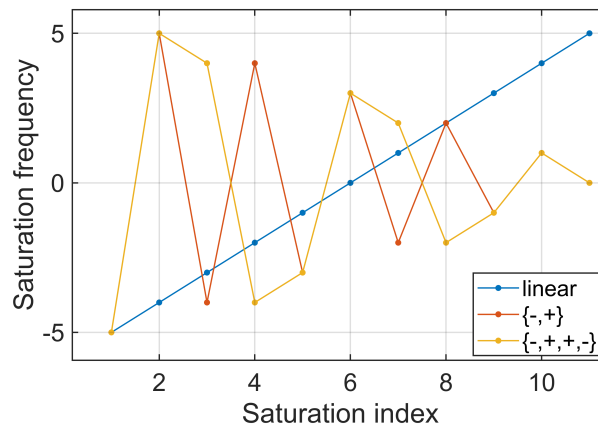


Figure 3.3: *Different Z-spectrum sampling trajectories.*

In summary, a CEST-EPI sequence has been developed which allows CEST acquisitions to be performed in a few minutes and saturation to be obtained in parallel transmission. This sequence has a number of adjustable parameters and the aim of Chapter 3 is to define and optimize these parameters in order to obtain optimal glucoCEST contrast. This sequence has been used for the pTx development described in Chapter 4. However, it can be further improved and several iterations have been made. The result of these iterations is the CEST-EPI fast sequence described below.

3.1.2 CEST-EPI fast

A first work on pTx pulses (Chapter 4) was done using the sequence described above, but it has some drawbacks. Firstly, this sequence has only parallel transmission for CEST saturation. This is detrimental to the signal-to-noise ratio because the Flip Angle (FA) is not spatially homogeneous on the slice. Secondly, the sequence allows only single-slice acquisition. In fact, the long saturation time used makes multi-slice acquisition unthinkable, as the acquisition time would easily be several tens of minutes. The CEST-EPI sequence has been improved to overcome these two limitations by the use

of MetaPulses (Mauconduit et al. 2022) for FA homogeneity on one hand and CEST_{fast} for multi-slice CEST on the other hand.

3.1.2.1 MetaPulses

As it has been presented in Chapter 1.2.2, mutli-spoke pulses provide state-of-the-art performance for slice-selective saturation. However, the use of these pulses may not be obvious in our case. The universal multi-spokes as defined by Gras, Vignaud, et al. (2017) requires to choose the geometry of the slices before knowing the subject's position. This is not a problem if the whole brain is scanned, but here it is not usable as it is. Indeed, the limited volume of coverage imposed by the CEST-fast sequence, requiring field-of-view adjustments based on the subject's brain and position. To overcome this challenge, a new pulse concept, MetaPulse-2D, has been developed in Neurospin (Mauconduit et al. 2022). In this approach, the spoke coefficients and gradient blips are smooth functions of slice position and orientation. Specifically, the pTx pulse parameters: complex spokes coefficients and gradients, are defined as images of functions of the geometry of the slice to be excited. The expression of this function can be made in spherical harmonics basis, the pulse design work will consist in finding the coefficients of n first harmonics allowing to describe the spoke parameters with sufficient precision on a span of orientations and positions. The optimization of the pulse coefficients for a set of slice positions and orientations is therefore performed jointly, and the resulting pulse promotes continuity of the solution for intermediate geometries. Together, the obtained coefficients form what we call a MetaPulse.

This design performs better than the CP mode and is equivalent to other designs. In addition, it allows tilting or repositioning of slices without the need for further optimization. Also, this solution promotes signal smoothness across the slices and can be pre-computed using the universal pulse concept. Therefore, this pulse concept was implemented on the CEST-EPI sequence. Although the MetaPulses were only tested on Gradient Echo (GRE) sequences, they were easy to implement thanks to object-oriented development and the integration of these pulses into Neurospin's sequence development library. The Matlab code for pulse generation was provided by Vincent Gras (CEA). It requires to provide subject B_1^+ , maps, and parameters such as slice position, pulse duration and bandwidth, as well as the desired flip angle.

Implementation of the MetaPulse excitation was therefore fairly straightforward, but tests were carried out on a phantom to ensure that the designed pulses worked properly, as we will see in Section 3.3.3.

3.1.2.2 Steady-state CEST sequence

Another important issue for CEST is the acquisition time. Indeed, in the "standard" CEST approach, as schematized in Figure 3.1, the duration of the saturation module is on the order of a second to ensure complete saturation of the water. This long saturation may even require a longer TR in order not to exceed the temporal energy limits. In addition, if this TR is multiplied by the number of saturation frequencies and the number of slices acquired, the duration becomes too long to be feasible in clinical experiments.

Therefore, many approaches have been studied to obtain CEST data in a short time (Y. Zhang et al. 2022). Without reviewing the literature here, there are several ways to speed up a CEST sequence. First solution is to reduce the saturation time by using a different saturation scheme (G. Liu et al. 2009; Dixon et al. 2010). Other possibility is to accelerate the readout, for instance by using compress-sensing (Lustig, Donoho, and J. M. Pauly 2007; Heo et al. 2017). Another solution that has been explored is to perform sparse sampling of the Z-spectrum (H. Lee et al. 2020). In our case, with an EPI readout, there is relatively little time to be gained by switching to a non-Cartesian readout. Also, exploiting the sparsity of the Z-spectrum requires a sufficiently high SNR so that noise and the smaller amount of data are not a limiting problem. However, the reason to use a full-pTx excitation is precisely because the SNR is not high enough. As it is, multiple repetitions are needed for signal averaging and thus

reducing the noise. As a result, approaches that tend to reduce the amount of data acquired are not the wisest choice here. What remains is to reduce the saturation time. This is made possible by using a steady-state to reduce the saturation time (Villano et al. 2021; Schüre et al. 2021). Instead of waiting for the water to relax completely and then doing a long saturation, the saturation is repeated quickly so that the magnetization does not have time to recover and remains in a steady-state. The saturation time required to maintain this steady-state is much less than the time it would have taken to fully saturate. Thus, by reducing both the saturation time and the TR, the same duty cycle is maintained as a conventional sequence and avoid further increasing the SAR, which is often close to the limits in CEST.

We therefore implement the approach in Schüre et al. (2021) on our MRI system using the CEST-EPI sequence. Figure 3.4 shows a diagram of the sequence developed using MetaPulses and steady-state saturation.

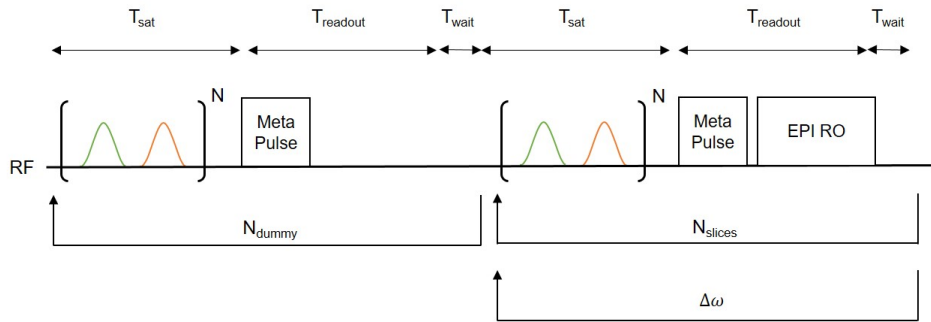


Figure 3.4: $\text{CEST}_{\text{fast}}$ sequence diagram. The pTx pulses are colored.

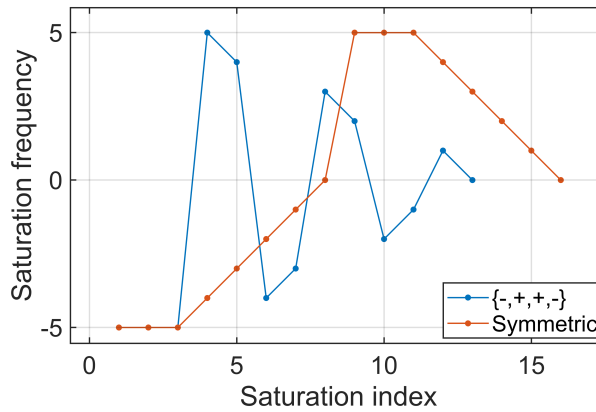


Figure 3.5: Z -spectrum sampling trajectories of CEST-EPI and CEST-EPI-fast.

However, certain precautions must be taken with this sequence, particularly with regard to steady-state quality, so that each measurement of a Z -spectrum point is made under the same conditions. This requires long dummy scans to prepare for magnetization and to start the steady-state spectrum acquisition. The $\text{CEST}_{\text{fast}}$ requires also a low Z -spectrum frequency sampling step. This implies to use another frequency trajectory than the one used for the CEST-EPI sequence. Also, we can not use a linear trajectory like the one shown in Figure 3.3 because the direction of travel with respect to 0 ppm has an important effect. Thus, to ensure that the positive and negative parts of the spectrum are acquired under similar conditions, the acquisition is divided into two parts, one from the negative limit to zero, and one from the positive limit to zero (Figure 3.5). In the context of our previous example, this gives $\{-5, -4, -3, -2, -1, 0, 5, 4, 3, 2, 1, 0\}$. If two dummy scans are required to reach a steady-state, the saturation scheme would be $\{-5, -5, -5, -4, -3, -2, -1, 0, 5, 5, 5, 4, 3, 2, 1, 0\}$. Such a frequency path increases the number of saturation offsets performed and ultimately lengthens the acquisition time by

$(N_{dummy} + 1) \times TR$, but avoids the resulting bias, and the use of the CEST_{fast} sequence is still extremely profitable in terms of acquired volume/time spent.

3.1.2.3 CEST-EPI fast interface

In the same way as for the CEST-EPI sequence, certain parameters specific to the sequence are adjustable (Figure 3.6).

The screenshot shows a software interface for configuring the CEST-EPI fast sequence. It is divided into three tabs: 'Part 1', 'Part 2', and 'Special'. The 'Special' tab is currently selected. The interface contains several adjustable parameters, each with a numerical input field and a unit or dropdown menu:

- Number of Pulses: 10
- Factor - Sat Power: 100 %
- Frequency - First: -5.00 ppm
- Frequency - Last: 5.00 ppm
- RF Excitation: MetaPulse (dropdown menu)
- Duration: 2560 us
- BTP: 2.2
- Number Dummy Scans: 4
- Spoiler: 50000 nsT/m
- Factor - Contrast: 100 %
- Duration Interpulse: 4 ms
- Duration Pre/Post: 4 ms
- B0 Correction:

Figure 3.6: Interface of the CEST-EPI fast sequence.

Some parameters are identical to the CEST-EPI sequence, but others have been added. These are listed below.

- RF Excitation: drop-down menu for choosing between "CP excitation", "MetaPulse" and "custom pTx file". The latter choice corresponds to the standard way of implementing multi-spoke excitation by providing a specific .ini file for each slice position and orientation.
- Duration: duration of the spokes, typically a few milliseconds.
- BTP: Bandwidth Time Product, to control the temporal shape of pulses. A larger BTP will produce pulses with more lobes.
- Duration Interpulse: delay between each saturation pulse, it can have an effect on CEST depending on the proton exchange rate.
- Duration Pre/Post: delay before the first and after the last saturation pulse.

In summary, the CEST-EPI-fast sequence has been developed based on the CEST-EPI sequence previously developed. It allows multi-slices CEST acquisitions to be made in a few minutes and saturation to be achieved in full parallel transmission. These sequences has a number of adjustable parameters and in the next section will show how to optimize these parameters in order to obtain optimal glucoCEST contrast.

3.2 GlucoCEST and GluCEST optimal saturation

As described above, various parameters can be set: the amplitude of the saturation, the repetition time, the interpulse duration, and the duration and shape of the pulse. We are interested here in

maximizing the contrast obtained by glucoCEST. There are many parameters and they are all inter-dependent. The difficulty is to find the right setting without falling into a local minimum. In the following section, the choice of pulse shape, duration, number, and intensity of these pulses, as well as the TR will be described. As the choice of these parameters is the subject of global optimization, it is difficult to present them one by one. The figures illustrating the arguments presented are therefore sometimes given with other fixed parameters.

3.2.1 GlucoCEST

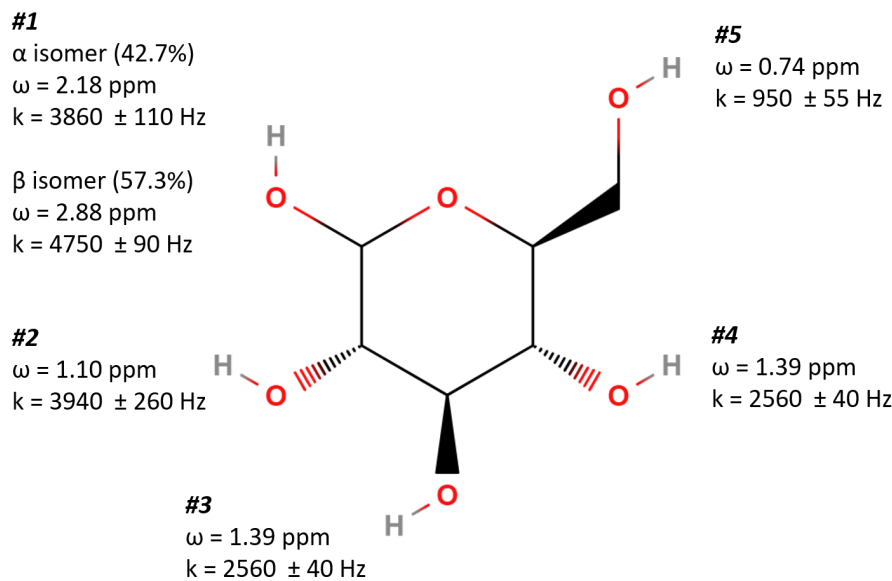
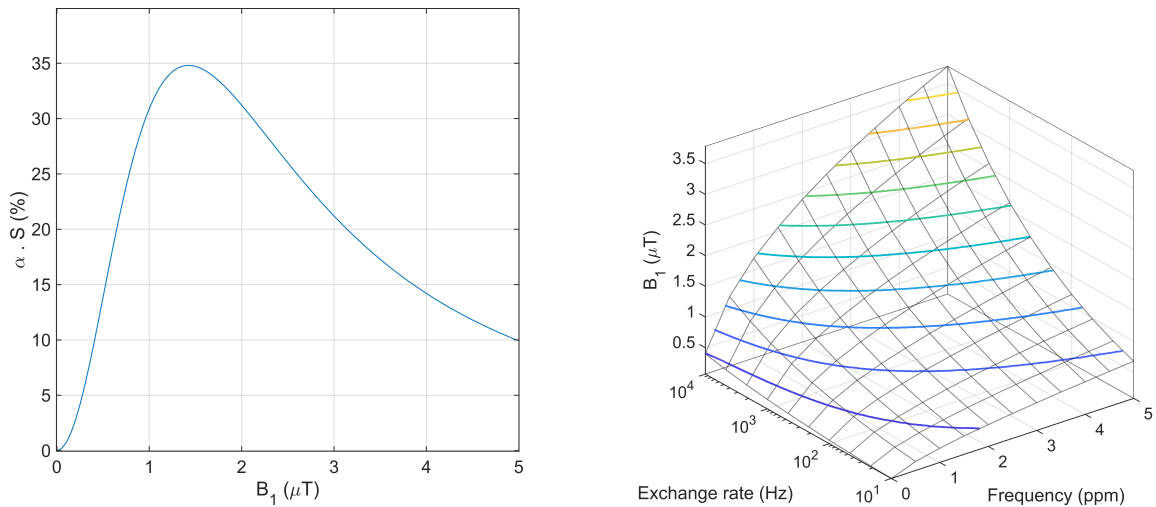


Figure 3.7: Chemical structure of glucose. Exchanging protons have different properties depending on their environment and position in space.

Glucose has rapidly exchanged protons (Khlebnikov et al. 2019) which resonate between 0.74 ppm and 2.88 ppm with the peak maximum reached around 1.2 ppm. We know from Equation (1.22) that the optimal saturation intensity under weak saturation fulfill $\gamma B_1 \approx k_{sw}$. To meet this criterion for half of the protons of glucose, we would need to achieve a RF amplitude of $B_1 \approx 60 \mu T$. This value is certainly not a weak saturation and therefore this criterion does not applies in our case. Moreover, such a saturation is not technically feasible on the Siemens 7 T system because the RF chain cannot reach more than $10 \mu T$ for a human brain and the deposited SAR would be very limiting. In reality, it is not desirable to reach this criterion for fast proton exchange, because RF saturation intensities are too high and lead to an increase in direct water saturation (or spill-over effect, Equation (1.23)). Water DS reduces the fraction of non-saturated water which impacts linearly the efficiency of the CEST. A compromise must therefore be found between saturation efficiency and water direct saturation. Also, an element to be taken into account in this compromise is the energy deposit and the limitations of the machine.

First, considering the case of continuous saturation, with a duration well beyond T_1 , we can estimate the value of the optimal B_1 for this type of saturation by maximizing the product $\alpha \cdot \frac{M_z^A}{M_0^A}$. Using the Equations (1.20) and (1.23), the graph of Figure 3.8A can be displayed for the brain glucose parameters. The maximum effect is obtained for a value of $1.46 \mu T$. This value is indicative of the value of B_1 to be maintained in order to achieve our CEST saturation, but it may differ from that obtained

experimentally. However, we will see that this simple estimation is very close to the optimal value for long saturation.



(A) Saturation efficiency when taking in account the spill-over with B_1 , for glucose protons #3 or #4.

(B) Optimal B_1 for CEST given the proton exchange rate and resonance frequency.

Figure 3.8: Finding the optimal B_1 for glucoCEST at 7 T with a continuous wave saturation.

This value of B_1 is indicative, because in reality, it is not possible to obtain a continuous saturation, since the RF chain of the system limits the duration of the pulses to 100 ms. This is also the reason why the saturation chosen consists of a repetition of pulses (Figure 3.1). It is also indicative because any other effect than the direct saturation of the water and the CEST of the proton studied has been neglected. To take the whole system into account, we would have to add the effect of Magnetization Transfer (MT), the fact that glucose has different protons, each resonating at a different frequency.

3.2.2 Pulse shape

With using a pulsed saturation, additional parameters can be optimized. In addition to the parameters for continuous saturation: T_{sat} and B_1 , the number of pulses N and the duration of the pulses T_p have to be defined. It should also be possible to consider the interpulse T_d as a parameter but it is linked to the other parameters by the formula:

$$T_{sat} = N \cdot T_p + (N - 1) \cdot T_d \quad (3.1)$$

3.2.2.1 Notion of pulse energy

Before attempting to optimise the shape of the pulses used, we need to clarify some key terms, particularly those relating to pulse energy.

Consider $w(t)$ to be the normalised waveform, so that the magnetic field produced by a single pulse is $B_1(t) = w(t) \cdot B_{1,peak}$. The mean magnetic field for a pulse can be written as $B_{1,mean}$ and is defined as follows:

$$B_{1,mean} = \frac{B_{1,peak}}{T_p} \int_0^{T_p} w(t) dt$$

Similarly, the mean magnetic field $B_1(t)$ used for presaturation over a whole TR, called $B_{1,meanTR}$ can be calculated :

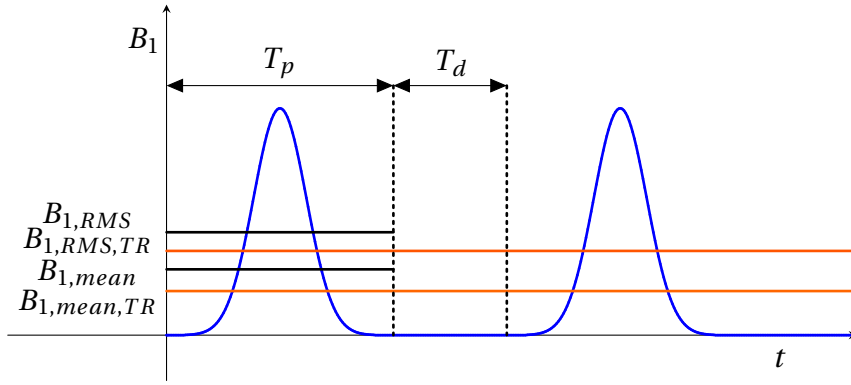


Figure 3.9: Diagram of two presaturation pulses.

$$\begin{aligned} B_{1,mean,TR} &= \frac{1}{TR} \int_0^{TR} B_1(t) dt \\ &= \frac{N \cdot T_p}{TR} B_{1,mean} \end{aligned}$$

These two values are key for CEST as the flip angle generated by a pulse depends on $B_1(t)$. Another element to consider is the energy carried by the RF wave. This energy can be quantified using the root mean square or RMS. Thus we also define the $B_{1,RMS}$ calculated for a pulse:

$$B_{1,RMS} = \sqrt{\frac{B_{1,peak}^2}{T_p} \int_0^{T_p} [w(t)]^2 dt}$$

and $B_{1,RMS,TR}$ is calculated over one TR:

$$\begin{aligned} B_{1,RMS,TR} &= \sqrt{\frac{1}{TR} \int_0^{TR} [B(t)]^2 dt} \\ &= \sqrt{\frac{T_p \cdot N}{TR}} B_{1,RMS} \end{aligned}$$

The average energy sent in one TR is proportional to $B_{1,RMS,TR}$. This means that if a saturation pattern is playable on the system, any other saturation pattern can be played as long as it has the same or lower $B_{1,RMS,TR}$ (and provided that this pattern also has the same electric field distribution, which is not necessarily the case if the pulses are pTx).

There is another aspect of the energy constraints to consider. The energy constraints implemented on the 7 T system are averaged on a sliding window of 10 s. Therefore, if the TR is not the result of dividing 10 by an integer, the average power delivery over 10 s will show fluctuations and therefore force the average power delivery to be limited. Choosing the TR as the result of dividing 10 by an integer makes it possible to create a saturation scheme that is as close as possible to the power limits imposed. We have therefore chosen a TR of 2500 ms for gluCEST acquisitions and 5000 ms for gluCEST acquisitions. These TRs allow to acquire a large amount of data quickly and still obtain a $B_{1,RMS,TR}$ that respects the energy constraints.

3.2.2.2 Spectral selectivity

An important aspect of pulse saturation is the spectral selectivity of the pulses. As the measured Z-spectrum shows structures linked to the pulse spectrum (Schmitt et al. 2011; Sun, E. Wang, et al.

2011), it is critical to choose pulses with a sufficiently clean spectrum so as not to create artifacts on the Z-spectrum at the frequencies being studied.

The simplest pulse is the square pulse. It has the advantage of having a ratio $\frac{B_{1,mean}}{B_{1,RMS}}$ equal to 1. This means that it is the pulse that saturates the most (proportional to the mean B_1) for a given energy deposit (proportional to the $B_{1,RMS}$). This pulse has the disadvantage of carrying a lot of high frequencies. This is problematic because these secondary lobes can give rise to parasitic saturation of the water. The effect of saturation begins to be visible at low flip angles and at 100° it already reaches almost its maximum (Zu et al. 2011; J. Kim et al. 2015). However, in the case of saturation with a block pulse, the secondary lobes, for example at 1 ppm, only have a difference of 40 dB compared to the main frequency (see Figure 3.10B). Thus, in the case of glucoCEST saturation with a saturation time of one second and a $B_1 = 1.5 \mu T$, -40 dB gives rise to a parasitic flip angle of 220°. This is reflected in the Z-spectrum (Figure 3.11) and results in spurious peaks, which can easily be mistaken for the contribution of a metabolite if the Z-spectrum is poorly sampled.

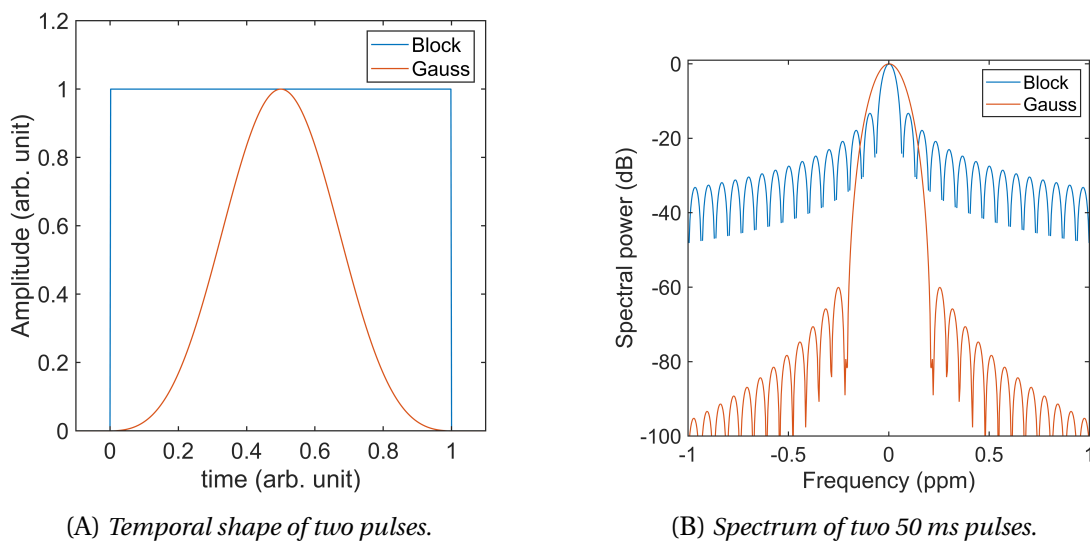


Figure 3.10: Shape and spectrum of a block pulse and a Gaussian pulse.

It is therefore important to choose a pulse other than the square, in order to maximize the frequency selectivity of the pulse and avoid spurious peaks on the Z-spectrum. The pulse shape that gives the best spectral selectivity in a given time is the Gaussian. We have therefore chosen this shape for our pulses. To avoid a truncation effect on the edges of the Gaussian we multiplied it with a Hanning window. Taken together, this results in a time-finite pulse with good selectivity. The normalized formula describing the shape of this pulse is therefore as follows:

$$w(t) = \sin(\pi t)^2 \exp\left(-\frac{(t-0.5)^2}{2\sigma^2}\right) \quad \text{where } t \in [0, 1] \quad (3.2)$$

In order to minimize the importance of the spectrum's secondary lobes, the standard deviation of the Gaussian, σ , was set at 0.25. This pulse is slightly less favorable than the square pulse from the point of view of energy efficiency, with a ratio $\frac{B_{1,mean}}{B_{1,RMS}} = 0.74$. The standard deviation is not modified throughout this work, but under conditions where energy deposition is limiting, it might be advantageous to modify the pulse shape. This would reduce spectral selectivity but would allow greater saturation at the same energy cost. For this pulse, the effects of the side lobes on any parasitic flip angle are minor. For 0.25 ppm, the parasitic flip angle is 22°, i.e. low enough not to have any saturation effect. Above 0.5 ppm, the parasitic flip angle is less than one degree, making any effect on the secondary lobes negligible. Therefore, the use of a Gaussian pulse avoids any parasitic saturation of the water peak by the secondary lobes of the pulse spectrum. Water saturation will only come from the spill-over effect and saturation transfer effects.

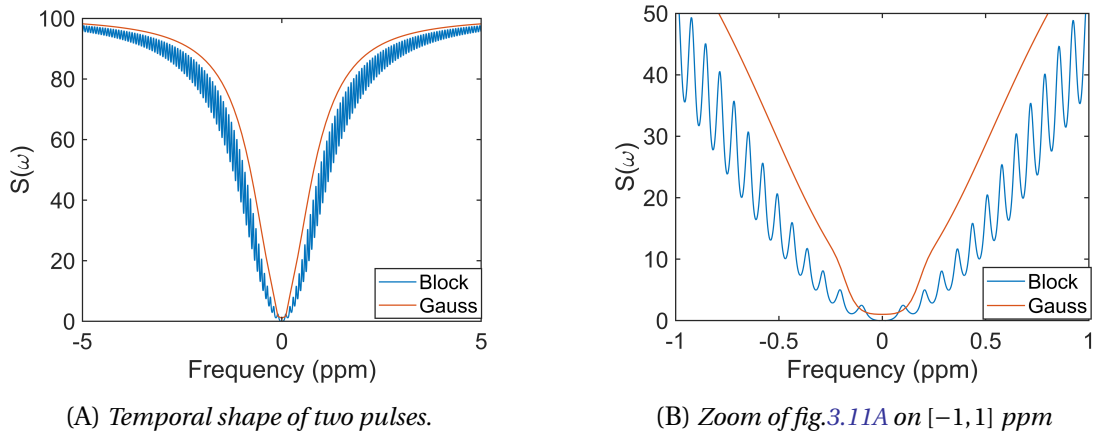


Figure 3.11: Simulations of Z-spectra obtained on Skully with 50 ms Block or Gaussian pulse. For $B_1 = 1.5 \mu T$ and $T_{sat} = 1 s$.

The discussion above considered 50 ms Gaussian pulses. Increasing the pulse duration will improve the spectral resolution, but even with a maximum duration of 100 ms a square pulse will result in a Z-spectrum affected by spurious peaks in the frequency ranges of the CEST metabolites. For the Gaussian pulse, and according to the previous reasoning, the deleterious effects of the secondary lobes between 1 and 5 ppm will be avoided if the pulse is longer than 10 ms. This is in line with the conclusions of [Schmitt et al. \(2011\)](#).

3.2.3 Saturation parameters

We have therefore chosen to use Gaussian pulses. Now that the shape is fixed, we can turn to the initial question, what values of T_{sat} and B_1 , N , T_p should we choose? This is a multi-parametric problem and analytical reasoning gives us a direction to follow, but in order to find the ideal parameters, it is necessary to carry out simulations. The simulator available at www.cest-sources.org has been used for this purpose. The simulator is described extensively by [Zaiss, Angelovski, et al. 2018](#). Here the solutions to the Bloch McConnell equations have been calculated numerically. The simulation takes into account the different glucose protons and the magnetization transfers. Because the simulator cannot handle a six-pool simulation, the protons index 2, 3, and 4 (from Figure 3.7) of glucose were taken as equal, with same exchange parameters and frequency offset. The Table 3.1 summarizes all the parameters used.

The simulations were performed for values of $B_{1,mean}$ between $0.5 \mu T$ and $3 \mu T$, for pulse duration between 10 ms and 100 ms, and for a number of pulses between 2 and 50. With the TR set at 2500 ms, some combinations of these parameters are not achievable. Also, for reasons of energy deposition and SAR, certain combinations of B_1 , T_p , and N are not feasible, but this will be explained in Chapter 4 (see Figure 4.4). The inter-pulse time T_d is fixed at 1 ms.

The results of these simulations are shown in Figure 3.12. The figure shows that it is possible to achieve a contrast of 90% of the maximum achievable with very different pulse settings. By sacrificing 10% contrast, it is possible to choose a pulse duration between 20 and 100 ms, with a $B_{1,mean}$ between 1 and $2 \mu T$ or with a number of pulses ranging from 10 to 50. However, it is interesting to choose the parameters that allow the shortest possible TR. This will maximize the volume of data acquired in a given time. The TR is limited on the one hand by the saturation time and by the readout time, and on the other hand by the energy deposition. Indeed, for CEST acquisitions, it is sometimes necessary to leave a dead time between each saturation in order to reduce the average power deposited. As the average power of the RF wave on one TR is proportional to $B_{1,RMS,TR}$, we are able to choose the setting that will minimize the deposited power.

We chose the parameters $B_{1,RMS} = 1.5 \mu T$, $N = 20$, $T_p = 50 ms$ with a TR of 2500 ms. A repre-

Pools	$\Delta\omega$	k_{ex} (Hz)	R1 (Hz)	R2 (Hz)	fraction (%)
Water	0	-	0.55	15	-
Glucose #2-3-4	1.25	2500	0.62	5	0.03
Glucose #1	2.58	4000	0.62	5	0.01
Glucose #5	0.74	950	0.62	5	0.01
MT	0 (a)	60 (b)	0.8 (c)	10 (b)	6 (b)

Table 3.1: Five-pool model used for glucoCEST simulation. The references for the parameters used are the following:

(a) (D. Liu et al. 2013)

(b) (Y. Msayib et al. 2019)

(c) (D. Liu et al. 2013; Y. K. Tee et al. 2014; Yunus Msayib et al. 2022)

sentation of the parameter space is given in Figure 3.13 with the position of the chosen setting. This setting enables a good CEST contrast to be achieved, of the order of 93% of the maximum possible, while keeping the saturation time and RF wave energy to a minimum. It is interesting to note that the conclusions drawn from Figure 3.8B, corresponding to the continuous wave ideal, are extremely close to the optimum value found in simulation when N or T_p is large. It is worth noting that for the protons studied, the characteristic time in the glucose pool is much shorter than the T_2 , so the CEST contrast here is due more to the rotation of the magnetization than to the saturation of Mz .

A final parameter to set is the interpulse time, T_d . Should it be as short as possible? Bigger than T_p ? However, we can expect it to be as short as possible, since glucose protons exchange rapidly. The average lifetime of a proton in the glucose pool is $\frac{1}{k_{ex}}$ or 0.3 ms. Thus, a few milliseconds after the end of a pulse, no glucose proton will be saturated and ready for exchange. Therefore, any further delay after the end of a pulse will not increase the number of saturated protons in the water pool and this will even decrease with T_1 regrowth. It is, therefore, necessary to reduce as much as possible the duration between two pulses in order to increase the number of saturated protons in the water as much as possible.

Simulations were used to validate this reasoning. Figure 3.14 shows the evolution of the MTR_{asym} obtained by glucoCEST as a function of interpulse time. The result is clear, the shorter the better. This simulation was carried out with $B_{1,RMS} = 1.5 \mu T$, $N = 20$, $T_p = 50 ms$ but similar result would be found with other saturation settings, as long as $T_p \gg \frac{1}{k_{ex}}$.

To summarize, the following parameters for our glucoCEST prototype sequence have been chosen: a saturation composed of Gaussian-Hanning pulses, a TR of 2500 ms, $B_{1,RMS} = 1.5 \mu T$, $N = 20$, $T_p = 50 ms$, $T_d = 5 ms$. These parameters make it possible to achieve more than 90% of the maximum CEST effect for glucose in a reduced time. These optimal values are found in accordance with Chan et al. (2012). Other parameters could have been chosen, to the detriment of the MTR_{asym} or, on the contrary, the TR. For example, Figure 3.13 may tempt us to choose $B_{1,mean} = 1.5 \mu T$ in order to gain 7% of additional CEST signal. But such a choice would have meant increasing the TR to 4000 ms in order to keep the $B_{1,RMS,TR}$ constant. The time saving obtained with a TR of 2500 ms allows us to acquire more spectra in the same time, and therefore a gain in SNR of 26%. In this case, the SNR gain/MTR gain ratio is in favor of a setting that initially seems less optimal.

It would be possible to integrate the gain in SNR into the simulations presented and to start looking for an even more global optimum than the one presented above. But some things cannot always be quantified, and the flexibility offered by a short sequence and the need for a fast sequence with

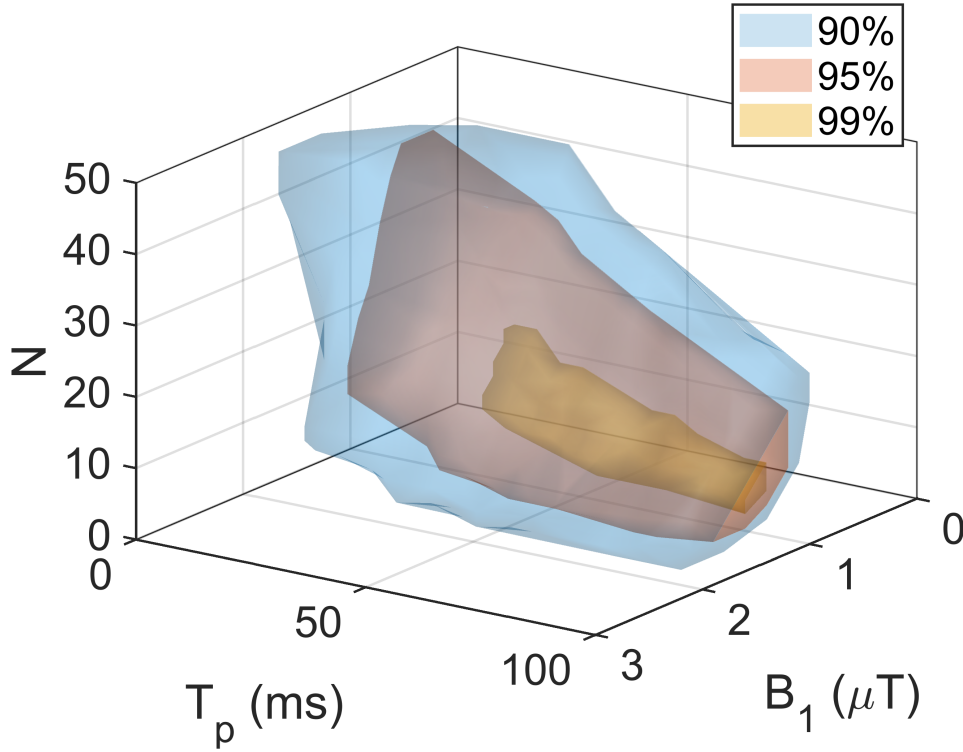


Figure 3.12: A view of the space of parameters to achieve 90%, 95% and 99% of the maximal glucoCEST.

a view to achieving functional glucoCEST cannot be measured in percentages. Thus, the settings proposed here are the result of an arbitrary compromise, illustrated by the simulations carried out.

3.2.4 Similar developpement for GluCEST

Not all metabolites are optimal for the glucose protocol defined above. This is particularly the case for glutamate, for which we are establishing a protocol here.

Glutamate has 3 exchangeable protons, sharing the same characteristics. These protons resonate at 3.2 ppm and exchange with a $k_{ex} = 7480 \text{ Hz}$ (Khlebnikov et al. 2019). According to Figure 3.8B, the optimum $B_{1,mean}$ should be in the region of $2.5 \mu T$.

In the same way as for glucose, the parameters have been chosen to find the right compromise between the energy deposited by the RF wave and the CEST contrast produced. Glutamate needs intense saturation, which requires a long TR in order to obtain a high $B_{1,mean}$ with an acceptable $B_{1,RMS,TR}$. However, it is not wise to have a TR greater than 5 s, as the acquisition time becomes too long for the applications envisaged. For a TR of 5 s, the setting for which glutamate contrast is maximum can not be reached: $B_{1,mean} = 3.5 \mu T$, $N = 25$, $T_p = 60 \text{ ms}$. Instead, the following parameters were chosen: $B_{1,mean} = 2.3 \mu T$, $N = 16$, $T_p = 50 \text{ ms}$ with a TR of 5000 ms. With glutamate, the T_d must be minimal to maximize the CEST and was set at $T_d = 5 \text{ ms}$. Similarly, these optimal values are found in accordance with Cai, Mohammad Haris, et al. (2012).

3.2.5 Discussion and conclusion

A number of more complex approaches would make it possible to extract more CEST contrast by playing on the shape of the pulses. Some have studied the possibility of playing with freeform pulses, which in simulation show promising results (Stilianu et al. 2022). Other possible approaches would be to co-design the pulses and the CEST data processing algorithm. Examples are pulses whose spectrum has characteristics that make it easy to deconvolve the Z-spectrum and therefore improve spec-

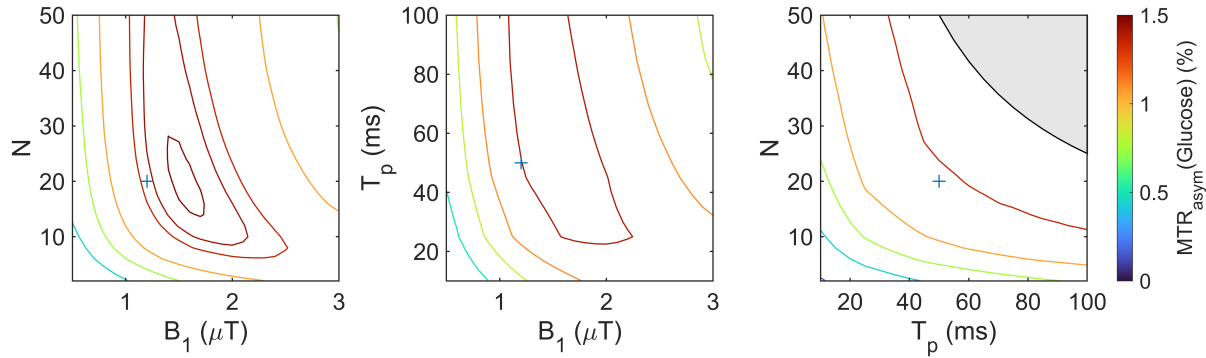


Figure 3.13: Saturation parameters for optimal glucose weighted CEST. Isolines of MTR_{asym} are plotted respectively at constant T_p , N and $B_{1,\text{mean}}$. The retained setting is marked by a blue cross. Area where $T_{\text{sat}} > TR$ is filled in gray.

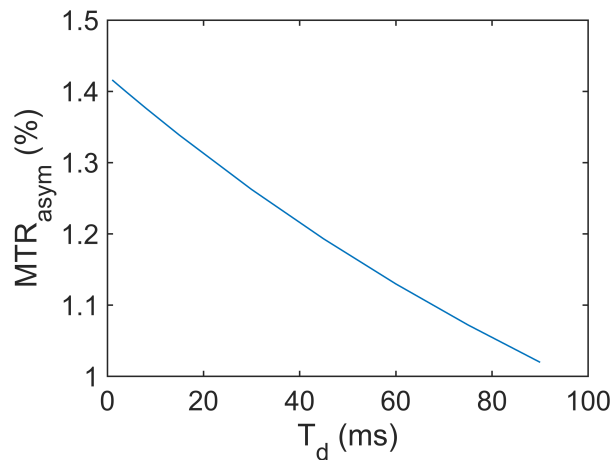


Figure 3.14: Evolution of MTR_{asym} with T_d for the parameters retained for glucoCEST acquisitions.

tral specificity. This kind of pulse/algorithm combination would allow the use of pulses that are more energy-efficient and also shorter than the 50 ms Gaussian pulse. Nevertheless, instead of spending time developing this path, we preferred to focus on the pTx part and the setting up of the clinical study.

To conclude, we have determined saturation parameters for one glucoCEST and one gluCEST protocol. Although these parameters are not globally optimal, they are chosen by making a compromise between CEST contrast, duration, and deposited energy. These protocols are used to provide the results shown in the next chapter are obtained.

3.3 Experimental validation

Through the use of simulations, we have been able to establish a protocol for glucoCEST. However, it is crucial to perform phantom tests to validate the accuracy of these simulations and the model. To optimize the glucoCEST protocol with the CEST-EPI sequence, a series of experiments were performed on Skully. These experiments were then replicated as best as possible using the CEST-EPI fast sequence. In addition, to further optimize and gain a full understanding of gluCEST, acquisitions were performed on the phantom glutamate using the same methodology and are presented in Appendix A.

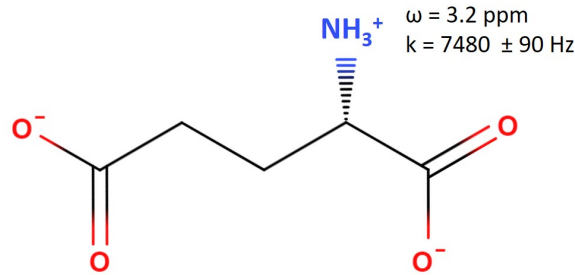


Figure 3.15: *Glutamate chemical structure. Exchanging protons constants from Khlebnikov et al. (2019) are given.*

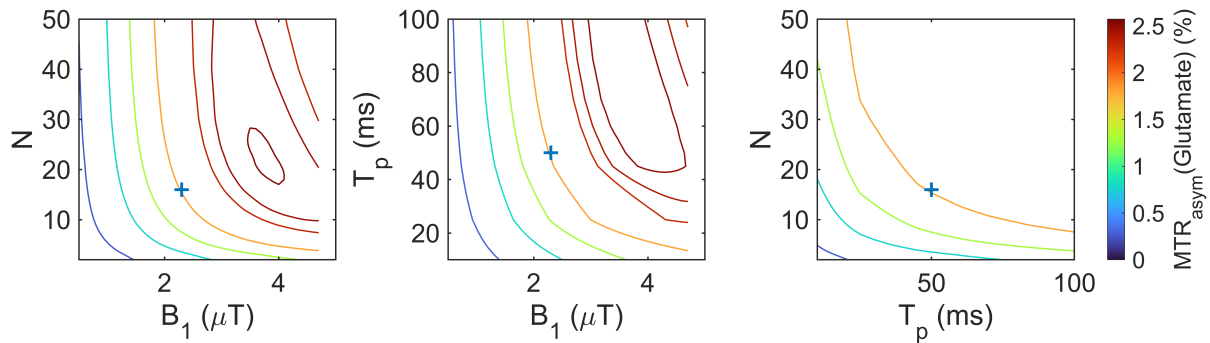


Figure 3.16: *Saturation parameters for optimal glutamate weighted CEST. Isolines of MTR_{asym} are plotted respectively at constant T_p , N and $B_{1,\text{mean}}$. The retained setting is marked by a blue cross.*

3.3.1 CEST-EPI

The experiments were carried out over several hours, and it was kept at room temperature so to avoid any cooling of the phantom during the scans which would make the various experiments not comparable. This temperature induces a drop in exchange rate k and those given Figure 3.7 are reduced by around 3% per $^\circ\text{C}$, i.e. a decrease by a factor of 1.6 when going from 37°C to 20°C (Mareš et al. 2023). Therefore, this variation in temperature induces a difference in MTR_{asym} , as can be seen in Figure 3.17. This change explains the difference between the simulations in the previous section and those measured experimentally here.

At room temperature, the space of parameters is modified and Figure 3.13 has to be re-simulated. This leads to the maps in Figure 3.18. The optimum saturation parameters found experimentally cannot be taken as such for in-vivo measurement, but a good correlation between them and their simulation at 20°C enables the simulations carried out at 37°C to be validated. These experimental results also illustrate the effect of varying critical parameters on Z -spectrum and MTR_{asym} .

In order to experimentally validate the key parameters of the CEST-EPI sequence for glucoCEST, three series of comparisons were carried out, whose experimental parameters are shown in Table 3.2. Saturation intensity, characterized by $B_{1,\text{RMS}}$, is tested for all other parameters being equal. Similarly, the interpulse is tested with all other parameters constant. A final comparison is made by varying the pulse duration and number of pulses, so as to obtain the product $T_p \times N$, which could be called the

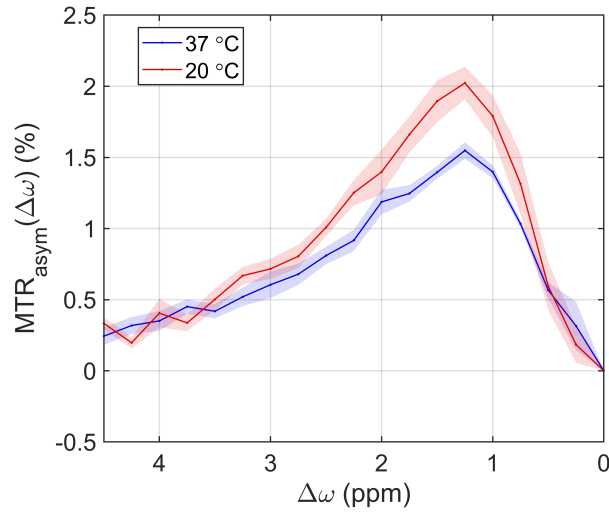


Figure 3.17: Effect of temperature on the MTR_{asym} . Experimental data obtained on Skully with the glucoCEST protocol and the CEST-EPI sequence.

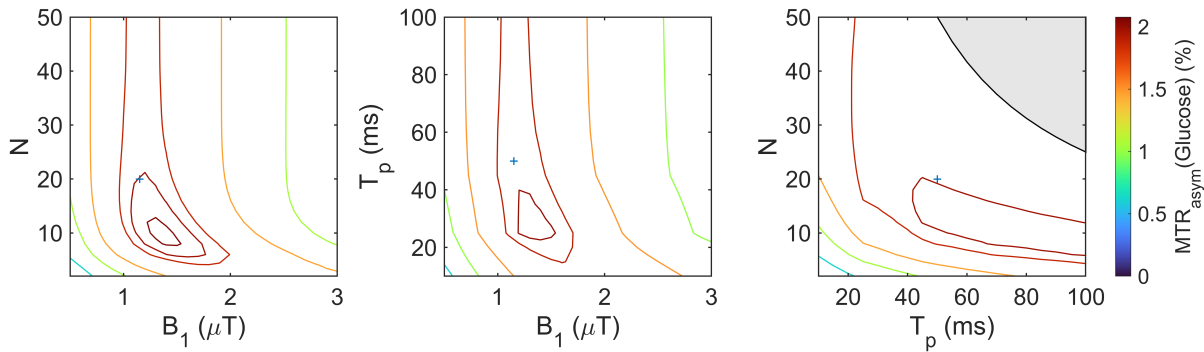


Figure 3.18: Saturation parameters for optimal glucose weighted CEST at 20 °C. Isolines of MTR_{asym} are plotted respectively at constant T_p , N and $B_{1,\text{mean}}$. The retained setting for glucoCEST is marked by a blue cross.

effective saturation time, $T_{\text{sat},\text{eff}}$, which differs from T_{sat} defined in Equation (3.1). This corresponds to the total duration of the CEST presaturation module. These acquisitions were carried out for a TR of 2500 ms, a TE of 17 ms, with a resolution of 3.2 x 3.2 x 4 mm and a matrix size of 64 x 64. The different spectra given in this section correspond to the average signal measured on a 10 x 10 voxels ROI in the center of the phantom.

Protocol	$B_{1,RMS}$ (μT)	T_p (ms)	T_d (ms)	N
Simulations	1.5	50	10	20
Figure 3.19	0.5 1 1.5 2	50	10	20
Figure 3.20	1.5	50	10 20 40 60	20
Figure 3.21	1.5	10 30 50 70 100	10	100 34 20 14 10

Table 3.2: Experimental parameters used for the glucoCEST optimization using the CEST-EPI sequence as well as those obtained from simulations.

From the results obtained by varying $B_{1,RMS}$, it can be identified that the Z-spectrum (Figure 3.19A) becomes increasingly flared with $B_{1,RMS}$. This is due to direct water saturation, which becomes increasingly important with B1 in Equation 1.23 and whose width at mid-height varies linearly with B_1 under the conditions of our experiment (i.e. $\omega_1^2 \cdot T_1 \cdot T_2 \gg 1$). The spectrum also shows a change in the slope at -5 and 5 ppm. This can be explained by the fact that in the implementation of the CEST-EPI sequence, the dummy scans do not perform the CEST saturation module. It is only after a few repetitions of contiguous frequency offset acquisition that the Lorentzian aspect of the Z-spectrum is restored. If we look at the MTR_{asym} (Figure 3.19B), we see that a maximum is reached for a $B_{1,RMS}$ of 1.5 μT . This is not in agreement with the simulations at 37 °C, which showed a maximum value for a B_1 of 1.5 μT or a $B_{1,RMS}$ of 2 μT . However this difference between simulation and experimentation is due to the temperature variation and our simulation at 20 °C (Figure 3.18) and is exactly in accordance with this result. It is interesting to note that for 2 μT , the area under the MTR_{asym} curve is greater than 1.5 μT . However, the peak formed by glucoCEST is less pronounced, so the selectivity of the measurement will be affected. Also, as we plan to study CEST in-vivo and many other metabolites are present, the CEST effect will be measured for a given frequency and avoid as far as possible averaging the MTR_{asym} over several frequencies. In our case, therefore, it is preferable to choose a $B_{1,RMS}$ of 1.5 μT .

The conclusions to be drawn from another comparison, between the different interpulse times, are rather straightforward. There is little difference between the spectra (Figure 3.20A), even for the largest T_d possible to test, at constant TR. This is due to the fact that $T_d \ll T_1$. However, a trend can be observed, and in the same way as in simulations, the MTR_{asym} is maximal for the shortest possible T_d (Figure 3.20B).

A final comparison is made with the CEST-EPI sequence for glucose. There is little difference between the spectra obtained with different pulse duration, except for the 10 ms pulse (Figure 3.21A). The same conclusion can be drawn as in Schmitt et al. (2011). Also, zooming in on the [-1, 1] ppm region shows us the flattened peak aspect of the spectrum for 10 ms, which we had already observed on Figure 3.11B. This appearance is also found for shorter duration pulses, but the spectral sampling, every 0.25 ppm, is not fine enough to observe it. The impact of having a 10 ms pulse is not to be underestimated. However, since the MTR_{asym} , visible in Figure 3.21B, is not only weaker than that obtained with longer pulses, but also shows very significant oscillations around 0 ppm. This effect is probably due to the conjunction between ΔB_0 and the secondary lobes of the saturation pulse.

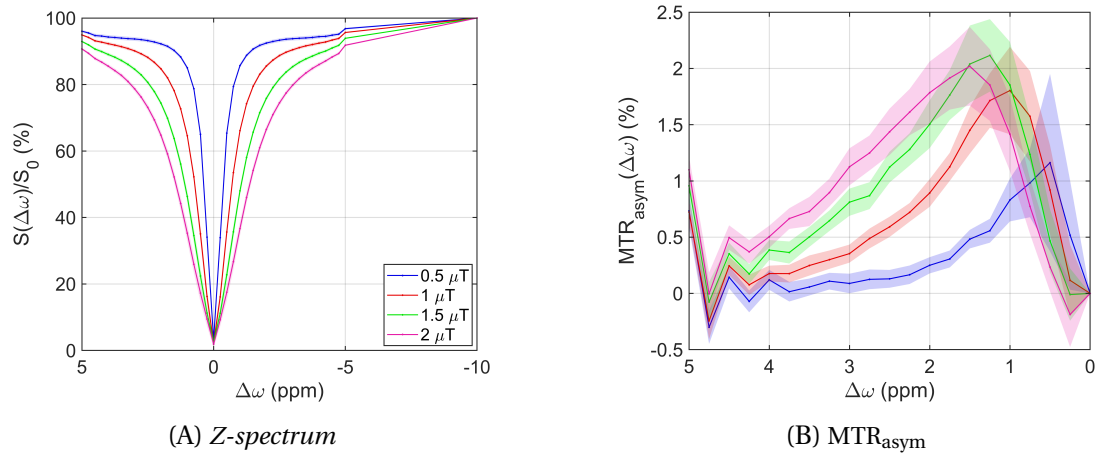


Figure 3.19: Comparison of experimental spectra obtained with different $B_{1,RMS}$.

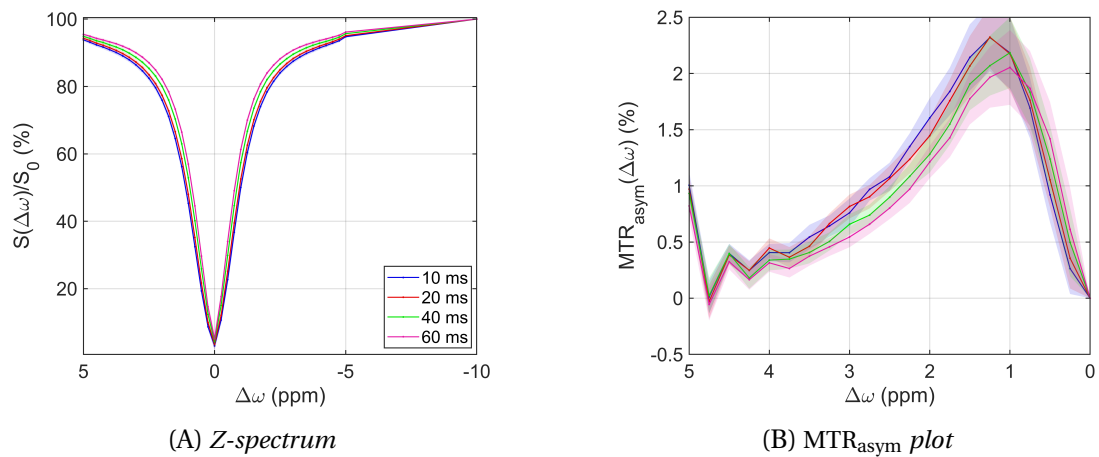


Figure 3.20: Comparison of experimental spectra obtained with different T_a .

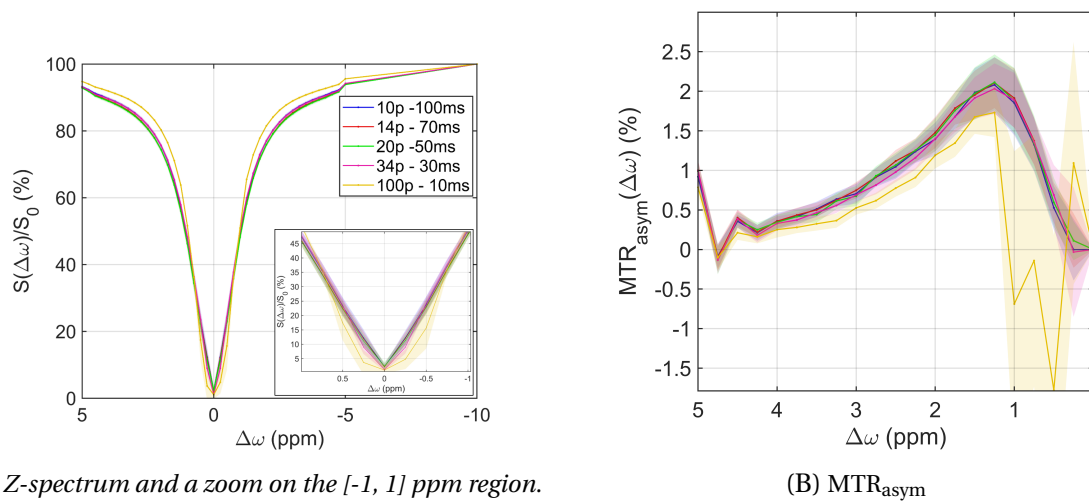


Figure 3.21: Comparison of experimental spectra obtained with variable T_p and N .

These different comparisons show the evolution of glucoCEST as a function of different parameters. Although the comparison with the simulation is not complete due to a difference in k_{ex} , these

figures show that the parameters chosen to produce glucoCEST are consistent with simulations and the literature (Chan et al. 2012; X. Xu et al. 2015; Jihong Wang et al. 2016).

3.3.2 CEST-EPI fast

As presented in Section 3.1.2, the CEST_{fast} sequence uses a steady-state between each measurement, which greatly accelerates the sequence and enables multi-slice. Nevertheless, the resulting CEST is dependent on other parameters, in addition to those we already know. These include the number of slices N_{slice} and the frequency step $\delta\omega$. The same as above should be done, i.e. characterize the evolution of the glucoCEST contrast as a function of the parameters used by the sequence. The Table 3.3 summarizes the parameters tested. Acquisitions were carried out in the same framework as before, with only the TE set to 21 ms and the ROI changed to a $10 \times 10 \times N_{slice}$ cube.

Protocol	$B_{1,RMS}$ (μT)	T_p (ms)	T_d (ms)	N	$\delta\omega$ (ppm)	N_{slice}
CEST-EPI	1.5	50	10	6	0.25	1
Figure 3.22	0.5 1 1.5 2	50	25	20	0.25	5
Figure 3.23	1.5	50	25	6	0.05 0.1 0.2 0.33 0.4 0.5	5
Figure 3.24	1.5	50	25	2 4 6 10 30	0.25	13 7 5 3 1
Figure 3.25	1.5	50	30 20 5 2	6	0.25	5

Table 3.3: Experimental parameters used for the glucoCEST optimization using the CEST-EPI-fast sequence as well as those used for the CEST-EPI sequence.

Figure 3.22 shows that variations in $B_{1,RMS}$ exhibit the same effects as before with the CEST-EPI sequence (Figure 3.19). The linear dependence from width to mid-height of the Z-spectrum with $B_{1,RMS}$ is always present and, here again, the optimum $B_{1,RMS}$ is $1.5 \mu T$.

Figure 3.23 presents a critical aspect for the CEST-EPI-fast sequence, the Z-spectrum $\delta\omega$ sampling step. The general appearance of the Z-spectrum obtained for different steps seems identical, which confirm the reliability of a sparse sampled Z-spectrum. Zooming in around 0 ppm shows the peak flattening pattern that becomes visible when the spectrum is sufficiently sampled, as seen in Figures 3.11B and 3.21A. The evolution of MTR_{asym} in Figure 3.23B is more interesting. It shows that the lower the $\delta\omega$, the higher the MTR_{asym} , reaching a maximum when $\delta\omega \geq 0.1$ ppm. The spectrum sampled at 0.1 ppm shows the highest MTR_{asym} and therefore is higher than that obtained for $\delta\omega = 0.05$ ppm. It can be explained by a ΔB_0 correction that was less well carried out for this acquisition. A element

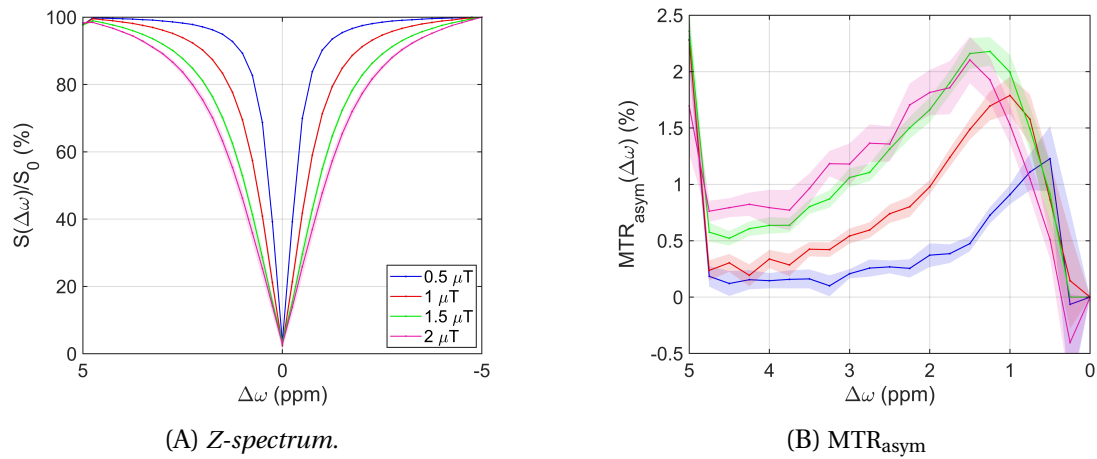


Figure 3.22: Comparison of experimental spectra obtained with different $B_{1,RMS}$, using the CEST-fast sequence.

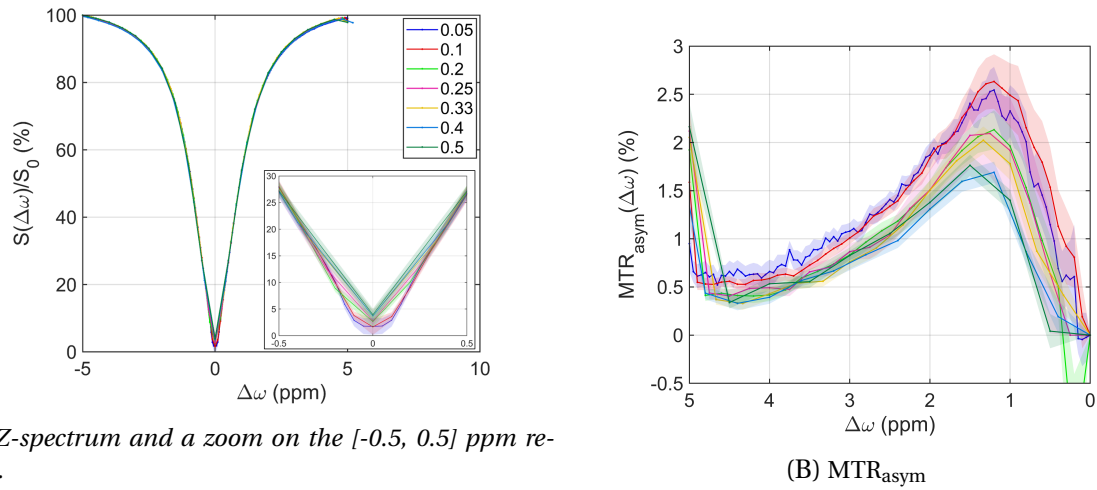


Figure 3.23: Comparison of experimental spectra obtained with different frequency offset steps, $\Delta\omega$, using the CEST-fast sequence.

supporting this conclusion is the slope of the MTR_{asyM} around 0 ppm is the steepest of all the spectra presented and is symptomatic of a bad correction of B_0 inhomogeneities.

As the number of slice plays a key role in the sequence, this parameter was naturally tested. As the pulses are repeated for each slice, the comparison is made at constant effective saturation time. Figure 3.24A shows that the overall appearance of the Z-spectrum does not change with the number of slices, except for the 13-slices, two-pulses situation, where direct water saturation appears slightly less important. This trend is repeated on MTR_{asyM} (Figure 3.24B), where regardless of the number of slices, the CEST contrast obtained is similar, and where only saturation at 13 slices shows a slightly weaker effect.

As with the CEST-EPI sequence, the T_d interpulse here has a slight effect on the CEST obtained, even if it does not induce a noticeable difference on the Z-spectrum (Figure 3.25A). The CEST contrast of glucose is maximal for the shortest interpulse (Figure 3.25B).

In summary, these experiments were performed to optimize glucoCEST with the CEST-EPI fast sequence. It has been found that the $B_{1,RMS}$ must be chosen as for the CEST-EPI sequence, the interpulse time T_d must be chosen to be minimal, the number of slices N_{slice} can be chosen up to 7 slices. This imposes a number of saturation pulses $N = 4$ for the TR of 2500 ms, finally the sampling step $\delta\omega$ is chosen at 0.1 ppm in order to acquire a sufficiently resolved spectrum and a suitable acquisition time. With these parameters, the total acquisition time is 4 min 30s.

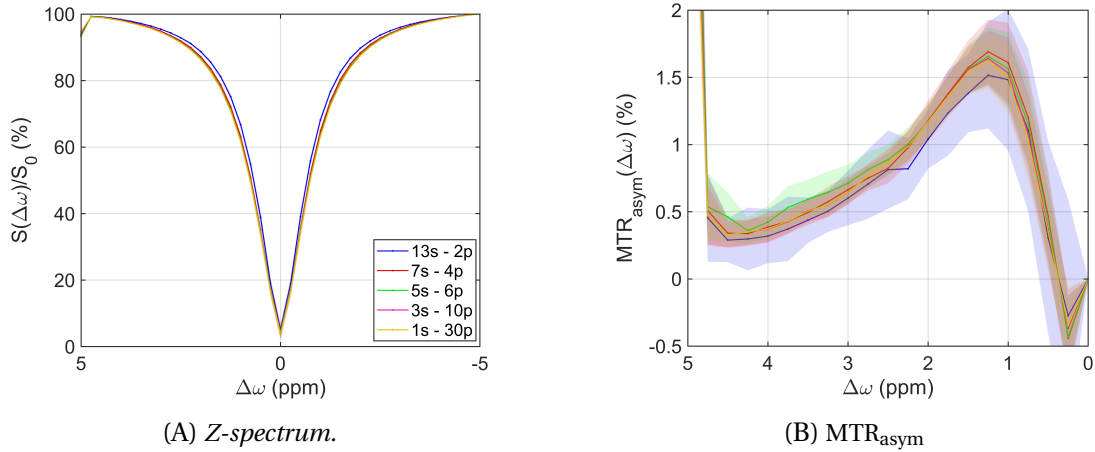


Figure 3.24: Comparison of experimental spectra obtained with a variable number of slices N_{slice} and number of pulses per slice N_p , using the CEST-fast sequence.

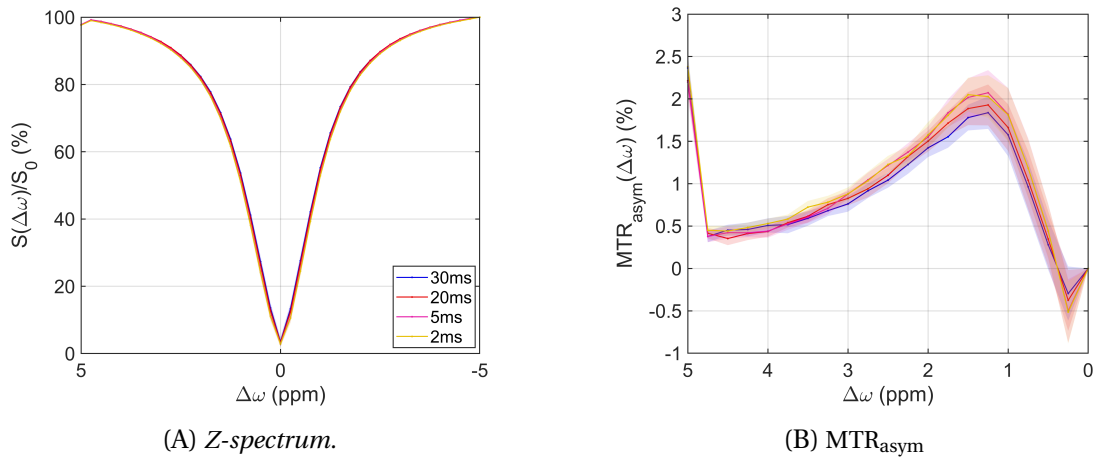


Figure 3.25: Comparison of experimental spectra obtained with different T_d , using the CEST-fast sequence.

3.3.3 MetaPulses

Among the experimental tests, it was necessary to check that the MetaPulses were working properly and that they were well integrated into the sequence. A pulse was designed for the glucoCEST optimization experiments, covering 13 axial Skullly slices. This pulse is designed to achieve a Flip Angle (FA) of 78° and is compared with a Circular Polarization (CP) pulse designed to achieve the same flip angle on average over the imaged volume. Simulations allow the comparison with the FA achieved by this MetaPulse for the 5 central slices, and that achieved by a CP pulse.

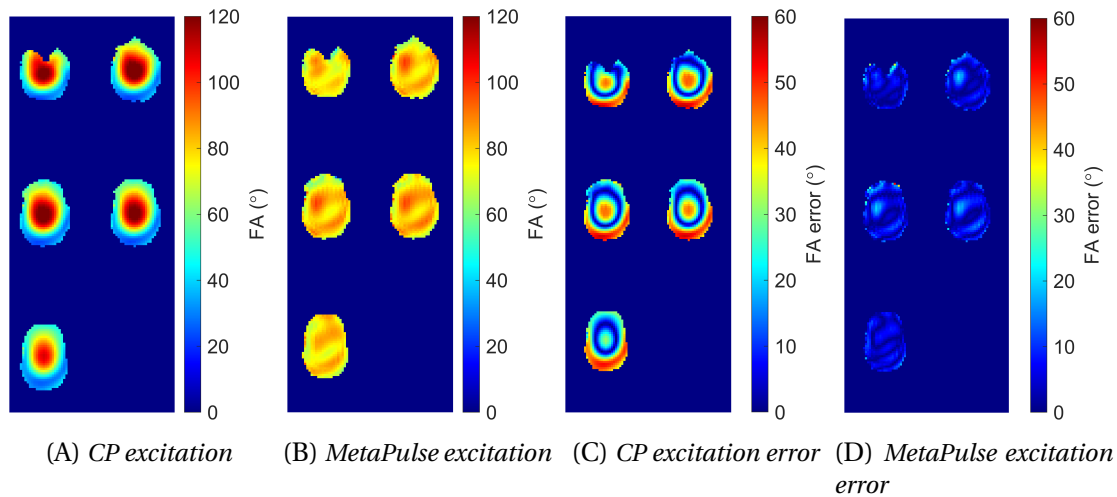


Figure 3.26: Simulations of flip angle and flip angle error maps obtained with CP and MetaPulse excitation.

As can be seen in Figure 3.26A, the flip angle achieved by the CP pulse is spatially inhomogeneous, with a characteristic pattern: the center is excessively excited, while the edges are under-excited. We can do much better with the use of multi-spokes, thanks in particular to their implementation via MetaPulse, as shown in Figure 3.26B. A few inhomogeneity patterns can be observed, but the flip angle map is much closer to the targeted 78° . Error maps of the two pulses are shown in Figures 3.26C and 3.26D, where it is shown that the CP reaches the target angle only for voxels close to the center. In addition, those in the center and on the edges show a strong difference with the target angle. Quantitatively, the Normalized Root-Mean-Square Deviation (NRMSE) of CP excitation across all slices reached 39%. With the MetaPulse, the error on excitation is much more homogeneous across the slices, and achieves an NRMSE of 9%, well below that of the combined mode.

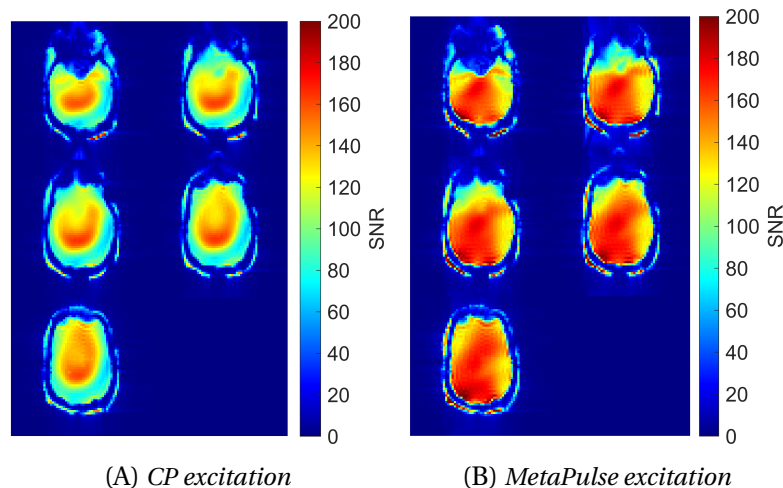


Figure 3.27: Experimental SNR maps of CEST volume acquired using a CP or a MetaPulse excitation.

In this way, the use of MetaPulses provides an effective gain in excitation homogeneity. This translates into better utilization of the available spins and their contribution to image formation. Ultimately, more signal is measured by the antenna and emerges from the noise, resulting in a better SNR. Experimental SNR maps for both excitations have been made (Figure 3.27). SNR is estimated by calculating the ratio between the acquired image at 5 ppm and the standard deviation of the signal in the air next to the brain. It can be seen that the SNR obtained using a CP pulse is at its maximum with

a value of 180 around the center, following the same pattern as that observed in Figure 3.26C. The MetaPulse produces a SNR map with values close to 180, almost homogeneously over the phantom. We can see that the inhomogeneity pattern is different from the one that appears in Figure 3.26D. This can be explained by the fact that the flip angle map does not translate directly into SNR and that other effects must be added to it, such as the inhomogeneities of B_0 or the antenna reception pattern.

Other advantages of MetaPulses have not been highlighted here, such as transparency of use and the possibility of repositioning the slices. A final element to be discussed for the use of such pulses is their energy deposition, potentially greater than for the CP pulse. The total energy used by the MetaPulse used here is 1.0 J for 5 slices, whereas the CP pulse uses 0.14 J, i.e. seven times more. The same applies to the maximum energy per channel, which is 0.24 J versus 0.02 J for the CP pulse, i.e. almost twelve times more. However, these energy differences should be seen in the context of the energy deployed for CEST saturation pulses, for which energy control is critical (for example, 40 J for a TR of 2.5 s for the acquisitions in Chapters 4 and 5).

In this small comparison, MetaPulses demonstrated a significant gain in SNR over all the slices imaged, compared with what could be achieved with a CP pulse. The implementation of these pulses is an additional advantage for obtaining good-quality CEST maps.

3.4 Static field inhomogeneities artifacts correction

Static field inhomogeneities are one of the challenges in performing CEST imaging at high magnetic fields.

B_0 inhomogeneities arise from the difference in permeability and magnetic susceptibility in the subject's tissues which induce changes in the local magnetic field when the subject is inside the magnet. The inhomogeneity of the magnetic field induces negative effects, including signal loss, image distortion, and hypo- and hyper-contrast regions. These inhomogeneities vary linearly with field strength B_0 and their mitigation becomes mandatory for fields above 3 T. Numerous efforts are being made to make the static magnetic field homogeneous, and several solutions are usually combined. Iron piece shim can be introduced for so-called passive shimming. To achieve greater homogeneity and provide patient-specific shim, resistive shimming coils are used to modify the static magnetic field (Gruetter and Boesch 1992; Koch, Rothman, and Graaf 2009). These coils are generally designed to generate spherical harmonics up to a certain order, and 7 T clinical scanners often feature second-order shimming to correct the B_0 to within a few tens of Hertz in the brain (Winkler et al. 2018). Nevertheless, these hardware solutions are not sufficient, as a few Hertz is enough to alter the CEST contrast measurement, as shown in Figure 3.28.

In this section, we will explore the importance of correcting for B_0 inhomogeneities in CEST imaging and what post-processing solution we used.

3.4.1 Consequences of inhomogeneities of static field on CEST

In addition to the effects listed above, B_0 field inhomogeneities have a significant effect on CEST. This is mainly due to the fact that these variations distort and shift the resonance frequencies of the molecules, resulting in inaccurate CEST measurements.

One of the key benefits of correcting B_0 inhomogeneities is the accurate determination of CEST contrast, which is crucial for quantitative analysis. Without correction, variations in B_0 can cause false-positive or false-negative signals, leading to misinterpretation of the molecular information being studied. Correcting B_0 inhomogeneities enhances the sensitivity of CEST imaging by refining the metabolite peak and thus increasing the detection of subtle chemical exchange effects. This is particularly important for detecting low-concentration metabolites or subtle molecular alterations associated with diseases. Moreover, correcting B_0 inhomogeneities ensures the reliability and robustness of CEST quantification methods. Furthermore, B_0 inhomogeneity correction enables more reliable comparisons of CEST images from different subjects or time points. This capability allows for longitudinal studies, assessment of treatment response, and identification of disease progression patterns.

Figure 3.28 illustrates these points. It shows the average Z-spectra over an ROI of Skully with a glucoCEST acquisition. It is clear that without B_0 correction, the MTR_{asym} suffers from many biases. The peak of MTR_{asym} is overestimated by a factor 4, it is shifted by 0.25 ppm, and has half the SNR. After B_0 correction, the MTR_{asym} takes values near those expected from simulations (Figure 3.13) and has less noise. This example demonstrates the necessity of an efficient B_0 correction solution in order to conduct glucose-weighted CEST experiments.

To summarize, for CEST imaging to become clinically viable, accurate and reliable, quantification is crucial. Correcting B_0 inhomogeneities is an essential step towards standardizing CEST protocols and establishing robust CEST imaging.

3.4.2 Post-processing mitigation

There are many methods for correcting the CEST data volume for frequency shifts introduced by B_0 inhomogeneities. The general idea behind ΔB_0 correction algorithms is to first estimate the ΔB_0 map and second, to interpolate and shift the Z-spectrum from the CEST data, voxel by voxel. Some use the

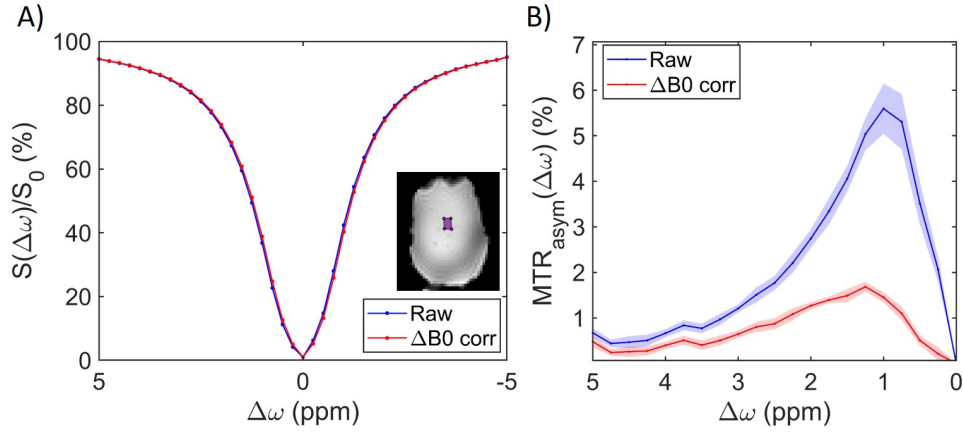


Figure 3.28: Experimental Z-spectra (A) and MTR_{asym} (B) on Skully before and after B_0 correction. Average spectra in the shown ROI. The standard deviation of the MTR_{asym} is represented by the colored area. The average ΔB_0 in the ROI is 0.05 ppm.

CEST data directly to estimate the ΔB_0 , others require the use of a specific sequence. The advantage of using CEST data is that it does not cost extra acquisition time. However, it is at the expense of accuracy. Nevertheless, for metabolites located near water and whose effect is subtle, these methods are not sufficient (M. Kim et al. 2009) and a small estimation error can significantly alter the MTR_{asym} , as shown on Skully in Figure 3.28.

An interesting solution is to use the same sequence as for the CEST data, but change certain parameters to make the ΔB_0 estimate more accurate. This results in a map of ΔB_0 that is spatially consistent with the CEST data, since it is subject to the same distortions and errors. In this context, the Water Saturation Shift Referencing (WASSR) method was developed (M. Kim et al. 2009). In this section we will discuss the estimation of the ΔB_0 map from a WASSR acquisition.

A WASSR acquisition uses the same sequence as a CEST acquisition but works at a much lower $B_{1,\text{mean}}$, around $0.2 \mu T$, to avoid any CEST or NOE effect. The idea is to acquire a spectrum and estimate the ΔB_0 by measuring the position of the water peak minimum. Moreover, we want to avoid any change in the peak due to magnetization transfer effects, as this makes the estimation more difficult. In addition, the saturation must last a few hundred milliseconds in order to accurately define the position of the minimum.

While the vast majority of CEST experiments use the WASSR acquisition, several methods exist for estimating the position of the water peak, voxel by voxel.

- WASSR algorithm

The WASSR algorithm is the one originally proposed with the WASSR acquisition rigorously the one defined by M. Kim et al. (2009). The principle is based on finding the axis of symmetry of the water peak. This is formulated as a minimization problem in the form :

$$\Delta B_0 = \underset{C}{\operatorname{argmin}} \|f(\omega_i) - \tilde{f}(2C - \omega_i)\|_2 \quad (3.3)$$

Where ω_i are the N sample frequencies of the spectrum with $i = \{1, \dots, N\}$. The measured spectrum is f and \tilde{f} is its cubic-spline interpolation.

- Spline interpolation

Often used for reasons of simplicity of implementation and computational cost, this method relies on interpolating the WASSR spectrum and finding its minimum.

$$\Delta B_0 = \underset{C}{\operatorname{argmin}} (\tilde{f}(C)) \quad (3.4)$$

- Lorentzian fit

In order to make the ΔB_0 maps more robust than those obtained by WASSR, [Lim et al. \(2014\)](#) performed a WASSR acquisition and fit a Lorentzian function to the spectrum obtained. The idea is that by using an additional a priori, the direct water saturation response has a Lorentzian shape ([Mulkern and Williams 1993](#)), one makes better use of the information contained in the spectrum. This makes the ΔB_0 more accurate than that obtained with WASSR.

In this case, the minimization problem is as follows :

$$\Delta B_0 = \underset{C,a,b,d}{\operatorname{argmin}} \|f(\omega_i) - L(\omega_i)\|_2 \quad (3.5)$$

$$\text{with } L(\omega_i) = a - \frac{b}{(\omega_i - C)^2 + d} \quad \text{with } a, b, d, \text{ additional free parameters.}$$

These different methods were implemented in Matlab to process our CEST data. In order to study the most efficient method, Monte Carlo simulations were performed. The WASSR acquisition has the following parameters: TR of 2500 ms, $B_{1,mean} = 0.12 \mu T$, $N = 10$ and with the same pulses as those used for the glucoCEST protocol. The spectrum is sampled over 21 frequencies evenly distributed between -1 ppm and 1 ppm. The total protocol time is 40 seconds. The Z-spectrum obtained by this protocol is simulated using the same tools and pools as in Section 3.2. This spectrum was shifted by an arbitrary ΔB_0 and noise was added according to different SNR levels hundreds of times with different realizations to constitute an evaluation dataset. The different methods were then evaluated on their performance in retrieving the ΔB_0 introduced.

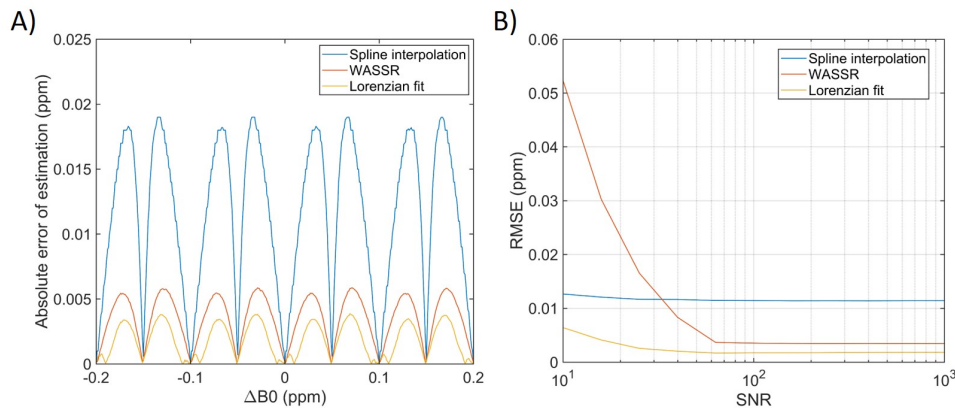


Figure 3.29: Simulations of different ΔB_0 estimation methods. (A) shows the absolute error of estimation $\|\tilde{\Delta B}_0 - \Delta B_0\|$ as function of ΔB_0 in the case of SNR = 500. (B) shows the evolution of RMSE of estimation with SNR for ΔB_0 between -0.2 and 0.2 ppm.

Figure 3.29 shows the results obtained from the simulations. Figure 3.29A shows that spline interpolation estimation is less performing than WASSR and Lorentzian fit. The latter method is the most efficient of the three solutions studied and outperforms WASSR by 30%. There are also some beats, with a local maximum at every 0.05 ppm, due to the sampling of the spectrum. The amplitude of these beats could be reduced by sampling more points, but this would be at the expense of acquisition time. The slight asymmetry observed in the beats can be explained by the fact that the Z-spectrum obtained by the WASSR protocol is not completely symmetrical with respect to the water peak, as a slight transfer of magnetization takes place. Figure 3.29B confirms that the Lorentzian fit performs better than WASSR, whatever the noise level. Here we return to the conclusions of [Lim et al. \(2014\)](#). It is interesting to note that in the context of a very noisy spectrum, for SNR levels below 25, spline interpolation performs also better than WASSR.

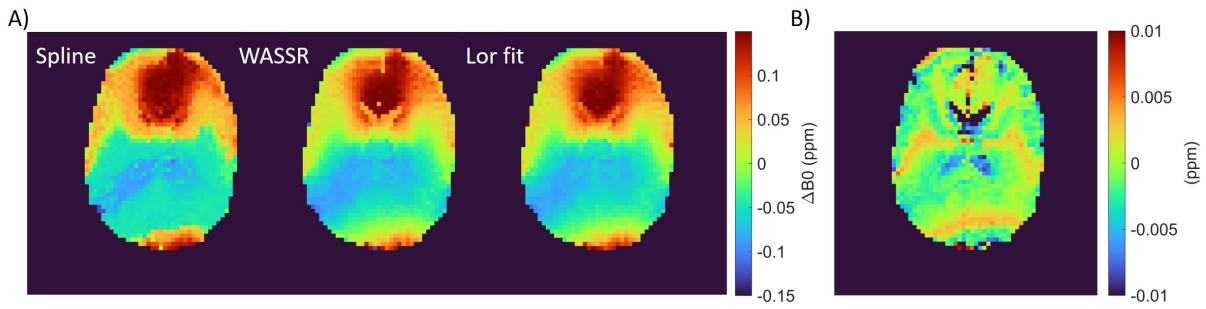


Figure 3.30: Estimation of B_0 inhomogeneities with the spline minimum, the original WASSR algorithm, and the Lorentzian function fit on human data (A). The slice is axial at $z = 15$ mm from the magnet isocenter. The difference between WASSR and Lorentzian fit estimation is given in (B).

The results of these estimation methods on in-vivo data are shown in Figure 3.30. Once again, estimation by spline interpolation does not perform well. Steps are visible and give rise to abrupt changes, sometimes of 0.1 ppm. Although we do not have a ground truth map, the orientation of these steps with respect to the spatial gradient of B_0 , their periodicity and comparison with maps obtained by WASSR and Lorentzian fit tell us about their origin. These steps correspond to the beats visible in the simulations in Figure 3.29A. The amplitude of this estimation error is greater than 0.05 ppm, which is already far too high to observe glucoCEST (Figure 3.28). This method is therefore unfeasible for the subject of this thesis. The maps obtained by WASSR and Lorentzian fit are much better, and it is hard to tell the difference with the naked eye. However, it can be seen that some voxels in the corpus callosum are different between the two maps. The difference between the two maps (Figure 3.30B) shows zebras with an amplitude of 0.003 ppm. Here, the phenomenon is probably the same as for the steps seen on the spline maps. The zebras correspond to the difference in amplitude between the WASSR and Lorentzian fit beats (Figure 3.29A).

3.4.3 Discussion and conclusion

Different methods of estimating the inhomogeneities of B_0 have been studied. Experimentally, WASSR and Lorentzian fit seem to perform very similarly, with only a 0.005 ppm difference between the two maps in regards to the ΔB_0 of 0.1 ppm. But given the impact that a slight ΔB_0 can have, it is preferable to use the Lorentzian fit approach.

Other approaches could have been considered, such as the WASABI (Schuenke, Windschuh, et al. 2017), which simultaneously obtains B_0 and B_1 maps. Prospects for improving the estimation of ΔB_0 are possible. Here, the map is obtained voxel by voxel, and spatial regularization steps could be added to increase the algorithm's accuracy. It might also be possible to study the beats (Figure 3.29A) and combine WASSR and Lorentzian fit to create a synthetic map corrected for residual beats.

In conclusion, correction of B_0 inhomogeneity is essential for accurate and reliable interpretation of CEST MRI data. Several techniques can be used to estimate and correct the impact of B_0 inhomogeneities on CEST. Among these, we have selected an approach using a WASSR protocol and an estimation of the inhomogeneity map by Lorentzian fit. The application of this tool will considerably improve image quality and provide more reliable metabolic information.

Chapter 4

Efficient CEST saturation using pTx and VOPs

In this chapter, an optimized parallel transmission solution for CEST saturation is presented. After describing the background and theory behind the proposed solution, we will discuss the results obtained in simulation, in vitro on a phantom and finally in vivo in humans.

This work was published in Magnetic Resonance in Medicine under the following reference [Delebarre et al. \(2023\)](#).

Contents

4.1 Introduction	60
4.2 Theory	60
4.3 Methods	61
4.3.1 CEST acquisitions	62
4.3.1.1 Tailored and universal pTx pulse design	62
4.3.1.2 Pulse sequence setup	62
4.3.2 Data analysis	63
4.4 Results	63
4.4.1 Pulse scheme efficiency	63
4.4.2 In vitro CEST results	66
4.4.3 An attempt of Dynamic Glucose-Enhanced CEST MRI	67
4.4.4 In vivo pTx CEST results	70
4.4.4.1 Hydroxyl-weighted CEST	70
4.4.4.2 Other CEST contrasts	71
4.5 Discussion and perspectives	73
4.6 Conclusion	76

4.1 Introduction

The increased availability of high and ultra-high magnetic fields promises to broaden the range of CEST applications as the technique benefits significantly from the high sensitivity, the large chemical shift dispersion and the increased water relaxation time T_1 achievable by increasing the B_0 field (Ladd et al. 2018). However, imaging at high magnetic fields increases B_0 and B_1^+ inhomogeneities (Van de Moortele et al. 2005) and implies significant radiofrequency energy deposition in tissues (Wu et al. 2016) which are critical for CEST imaging. Several algorithms have been proposed for the correction of B_0 and B_1^+ inhomogeneities, either independently (M. Kim et al. 2009; Windschuh et al. 2015), or simultaneously (Sun, Farrar, and Sorensen 2007; Schuenke, Windschuh, et al. 2017). Because the CEST contrast is strongly dependent on the saturation RadioFrequency (RF) amplitude (J. Zhou, Wilson, et al. 2004), most of these methods require multiple acquisitions, at several B_1^+ values, and eventually additional B_1^+ mapping, lengthening the total acquisition time.

An elegant solution for mitigating the B_1^+ inhomogeneity is to use parallel transmission (pTx) (Padormo et al. 2016). This method uses multiple RF channels which can be controlled independently. The combined effective B_1^+ is homogenized by carefully designing the spatial and temporal profiles of the RF waveforms for each individual channel. The benefit of pTx for CEST imaging at 7 T has been demonstrated. In the MIMOSA method (Liebert, Zaiss, et al. 2019), the authors use a combination of two modes presenting spatial complementary, without taking into consideration the exact B_1^+ spatial distributions. An additional gain in saturation quality has been obtained by using pre-acquired B_1^+ maps to find the optimal parameters for individual modes by solving an optimization problem (Tse et al. 2017; Leitão et al. 2022), with the drawback of increasing the complexity and the workload during the exam. Importantly, current common practice consists in monitoring SAR by using a very conservative power threshold, provided by the vendor. This approach, as we detail in this thesis, limits the pTx performance as compared to more realistic SAR-based RF monitoring strategies.

In this work, a presaturation CEST module as been designed based on pre-computed Universal Pulses (Gras, Vignaud, et al. 2017) (UP), while ensuring near optimal use of the pTx hardware and the multi-transmit RF coil. This approach can be easily brought to clinics as the pulses are designed offline, avoiding time-consuming and subject-specific optimization. While the use of UPs has been reported previously for anatomical and functional imaging, this is the first time they are used for CEST acquisitions. Moreover, we show that the efficiency of the CEST presaturation pulse train is enhanced by managing the energy deposition using Virtual Observation Points (VOPs) (Eichfelder and Gebhardt 2011; Graesslin et al. 2012). The performance of this design is evaluated using numerical simulations, as well as in vitro and in vivo CEST measurements.

4.2 Theory

Ideal CEST presaturation pulses produce a spatially uniform saturation for a given RF amplitude and at a specific frequency. To this end, the approach is to find the pTx pulse parameters which minimize the distance (L2 norm) between the effective $B_{1,RMS}^+$ and a given target. The effective RF amplitude of a radiofrequency waveform of duration T_s can be expressed as in Liebert, Zaiss, et al. (2019):

$$B_{1,RMS}(\mathbf{r}) = \sqrt{\frac{1}{T_s} \int_0^{T_s} B_1^2(\mathbf{r}, t) dt} \quad (4.1)$$

The magnitude of a single RF pulse, $B_1(\mathbf{r}, t)$, can be decomposed into a space-dependent component and a time-dependent component. For a specific channel i , we denote the spatially dependent component by $b_{1,i}(\mathbf{r})$ (also known as transmit sensitivity) expressed in Tesla/Volt, and the time-dependent component by $V_i(t)$, expressed in Volt. Using a vector formalism, we write $\mathbf{b}_1(\mathbf{r})$ and $\mathbf{V}(t)$ to denote respectively these quantities for all channels, where $\mathbf{b}_1(\mathbf{r})$ is obtained with a B_1^+ mapping

sequence and $\mathbf{V}(t)$ is the result of an optimization, as detailed below. With these notations, the combined effect of N_c transmit channels can be written:

$$B_1^A(\mathbf{r}, t) = \sum_{i=1}^{N_c} V_i^A(t) b_{1,i}(\mathbf{r}) = \mathbf{V}^A(t) \mathbf{b}_1(\mathbf{r}) \quad (4.2)$$

In Equation (4.2), the subscript A identifies a complete set of RF parameters for all channels and will be referred to as "mode A". Given two modes, A and B, of the same shape and duration (T_{pulse}), we can write $\mathbf{V}^A(t) = \mathbf{p}^A \times w(t)$ and $\mathbf{V}^B(t) = \mathbf{p}^B \times w(t)$, where $w(t)$ is the same normalized waveform for each channel and \mathbf{p}^A and \mathbf{p}^B are complex weights (units of Volt) to be optimized for mode A and mode B, respectively. By plugging the expression of $B_1(\mathbf{r}, t)$ from Equation (4.2) in Equation (4.1) we obtain:

$$B_{1,RMS}(\mathbf{r}) = w_{RMS} \sqrt{\frac{(\mathbf{p}^A \mathbf{b}_1(\mathbf{r}))^2 + (\mathbf{p}^B \mathbf{b}_1(\mathbf{r}))^2}{2}} \quad (4.3)$$

Where

$$w_{RMS} = \sqrt{\frac{1}{T_{pulse}} \int_0^{T_{pulse}} w^2(t) dt} \quad (4.4)$$

Using the framework described above, the following minimization problem aims to find an optimal set of modes to reach a given $B_{1,RMS}^{target}$ under the RF energy deposition constraints that are detailed hereafter:

$$\mathbf{p}^A, \mathbf{p}^B = \arg \min_{\mathbf{p}^A, \mathbf{p}^B} \|\mathbf{B}_{1,RMS}^{target} - \mathbf{B}_{1,RMS}\|_2$$

$$\begin{aligned} s.t. \quad & c_{global}(\mathbf{p}^A, \mathbf{p}^B) \leq SAR_{global,max} \\ & c_{local,m}(\mathbf{p}^A, \mathbf{p}^B) \leq SAR_{local,max}, \quad 1 \leq m \leq N_{VOP} \end{aligned} \quad (4.5)$$

This optimization must be subject to energy deposition constraints. The vendor-provided SAR management strategy (so-called "protected mode") sets limits on total and per channel power, namely $P_{total} < 8$ W and $P_{channel} < 1.5$ W, respectively. While these constraints guarantee compliance with the first level SAR mode, they over-restrict the maximum RF power and can be a limitation for some applications, including CEST. To relax these constraints and to improve the optimization in Equation (4.5), a VOP management of the local SAR was used. VOP set is usually obtained by compression (Eichfelder and Gebhardt 2011) of one (or more) full SAR model representing tens of thousands of SAR matrices (one per voxel of the numerical head model). The number of VOPs in our case (Boulant et al. 2018) was 190, allowing manageable RF pulse design algorithms in pTx. The use of this SAR monitoring approach for the optimization leads to the following constraints: $P_{total} < 16$ W, $P_{channel} < 3$ W (set by the coil manufacturer), $SAR_{local} < 10$ W/kg, and $SAR_{global} < 3.2$ W/kg.

4.3 Methods

For the in vivo experiments presented in this Chapter, seven healthy volunteers (between 22 to 52 years old, 2 female and 5 male) were recruited. Except for the first volunteer, which took a glass of grape juice, as we described in Section 4.4.3, no glucose administration was performed before the acquisitions. The study was approved by the local institutional review board.

4.3.1 CEST acquisitions

4.3.1.1 Tailored and universal pTx pulse design

For in vitro experiments, Tailored Pulses (TP) were designed specifically for Skully. Following a B_0 measurement performed using a 3D-GRE protocol, a B_1^+ map was acquired with an in-house made interferometric turbo-FLASH sequence called XFL (Amadon et al. 2011) (5 mm isotropic resolution, matrix size $40 \times 64 \times 40$). This B_1^+ map was used for the optimization in Equation (4.5).

For in vivo acquisitions, TPs were designed for each volunteer following an identical procedure. In addition, UPs were also used for in vivo acquisitions. The use of UPs presents the advantage of an offline design while still offering excellent B_1^+ uniformization capability, comparable to TPs (Gras, Vignaud, et al. 2017). For designing UPs a composite matrix $\mathbf{b}_1(\mathbf{r})$ was built by concatenating B_1^+ maps from a large database of subjects. This consists of 26 subjects (Gras, Boland, et al. 2017), with 13 randomly selected maps serving as optimization group and 13 others as evaluation group.

The pulse optimization was done in MATLAB (Mathworks, version 9.7, R2019b) using an interior-point solving algorithm (Intel Core i7-9850H CPU at 2.60 GHz, 32.0 Go RAM). For TPs, calculated using only one B_1^+ map, the average computational time was 13 seconds, while for UPs, calculated using 13 B_1^+ maps, it was 22 seconds.

4.3.1.2 Pulse sequence setup

The pTx optimized pulses, either TPs or UPs, were integrated in the CEST-EPI sequence as shown in Figure 3.1. The saturation was performed using a train of N pulses consisting of two interleaved modes (mode A, mode B, mode A, ... , mode B). Immediately after saturation, gradient spoilers were applied in all three directions. The excitation pulse of the EPI module was used in the standard Circularly Polarized (CP) mode. For five volunteers, a single axial slice was imaged at position $z = +15$ mm from the isocenter, for the other two volunteers, three axial slices were imaged at $z = +15$, $+40$ and -40 mm from the isocenter. The other experimental parameters were set as follows: echo time = 34 ms, repetition time = 2500 ms, FOV = 3.4×3.4 mm², slice thickness = 4 mm, flip angle = 78°, matrix size = 64×64 . For spectral selectivity considerations, the shape of the saturation pulses was Gaussian with a Hanning window for which $B_{1,\text{mean}}^+ = 0.74 B_{1,\text{RMS}}^+$. The standard deviation of the Gaussian was chosen to be 12.5 ms in order to minimize the second lobe of the pulse spectrum. The length of each saturation pulse was 50 ms.

Hydroxyl-weighted CEST acquisitions were performed with 20 presaturation pulses (10 A-B pairs) of target $B_{1,\text{RMS}}^+ = 1.5 \mu\text{T}$, for an effective saturation time of 1 s (Chan et al. 2012). 42 measurements were performed with saturation offsets equally spaced between -5 and 5 ppm and one, for normalization, at -10 ppm, ending up with a total acquisition time of 2 min 05 s. Although the parameters were optimized for glucose, considering the CEST contrast weighted by hydroxyl groups is more rigorous since other hydroxyl groups such as myo-inositol and glycosaminoglycan and glycogen can contribute to it.

For glutamate-weighted CEST acquisitions, the presaturation RF amplitude was set to $B_{1,\text{RMS}}^+ = 3 \mu\text{T}$ and only 16 pulses were employed for an effective saturation time (Cai, Mohamad Haris, et al. 2012) of 800 ms. Because of the higher RF amplitude target, the repetition time was increased to TR = 5000 ms in order to maintain a similar duty cycle and be able to obtain good saturation homogeneity. 42 acquisitions were performed, 41 with frequency offsets between -5 and 5 ppm and one at -10 ppm, setting the scan time to 3 min 50 s.

For B_0 correction, a WAter Saturation Shift Referencing (M. Kim et al. 2009) (WASSR) strategy was used. The WASSR acquisition was performed using the same presaturation pulses as for the CEST but scaled to reach $B_{1,\text{RMS}}^+ = 0.15 \mu\text{T}$. The presaturation module, with an effective duration of 500 ms, was

applied at 21 frequency offsets equally spaced between -1 and 1 ppm. All other imaging parameters were identical with those for the CEST acquisition except for TR, which was set to 1.5 s.

For the exams performed on volunteers, an anatomical image, necessary for segmentation, was also acquired using an MP2RAGE sequence (Marques et al. 2010) (repetition time = 6000 ms, inversion times = 800 ms / 2700 ms, bandwidth = 240 Hz, flip angle = 4°, isotropic resolution = 0.8 mm, matrix size = 300×320×190).

Following the above-described protocols, hydroxyl-weighted CEST acquisitions were performed using CP, MIMOSA, and optimized pTx pulses (with tailored pulses for phantom and universal pulses in vivo). If the SAR constraints allowed it, the spatially averaged saturation RF amplitude, $B_{1,RMS}^+$, of MIMOSA and CP were kept at the same level as the UPs (made on the evaluation dataset). Otherwise, the magnitude of MIMOSA and CP pulses was scaled down to reach the maximum allowed SAR (see Table 4.2). The two MIMOSA modes had the same amplitude. The TP and UP pulses were optimized on a 10 mm-thick slab, centered on the imaged slice. In vivo, glutamate-weighted CEST acquisitions were also performed but only using pTx with universal pulses.

4.3.2 Data analysis

A retrospective motion correction (image to image) was performed on in vivo CEST acquisitions using SPM12. An extrapolation of movement for frequencies between -0.75 and 0.75 ppm was done to avoid registration of low-intensity images. After the motion correction, a B_0 correction was made using the WASSR acquisition. Specifically, the water peak was fitted with a Lorentzian curve and the acquired Z-spectra to be corrected were linearly interpolated and shifted by the same value as that required to bring the center of the fitted Lorentzian curve to 0 ppm. To produce various CEST weighted maps, the Magnetization Transfer Asymmetry (MTR_{asym}) was computed voxel by voxel according to:

$$MTR_{asym}(\Delta\omega) = \frac{S(-\Delta\omega) - S(\Delta\omega)}{S_{ref}} \quad (4.6)$$

For each volunteer, glutamate and hydroxyl-weighted CEST maps were produced, as well as an rNOE map. The latter is obtained using the hydroxyl-weighted CEST acquisition as saturation parameters are close (Chan et al. 2012; Zaiss, Kunz, et al. 2013) by calculating MTR_{asym} at $\Delta\omega$ of 3 ppm, 1.25 ± 0.25 ppm and -4 ppm, respectively. A composite image was finally produced by overlaying the CEST maps on the anatomical image. For the statistical analysis, the white and gray matter were segmented with SPM12.

4.4 Results

4.4.1 Pulse scheme efficiency

The first pulse optimization result was that, increasing the number of modes beyond two, does not significantly improve $B_{1,RMS}^+$ homogeneity. This is represented in Figure 4.1. The $B_{1,RMS}^+$ Root-Mean-Square Error (RMSE) is plotted as a function of $B_{1,RMS}^+ target \sqrt{DC}$, with $DC = \frac{T_{sat}}{T_R}$ (duty cycle). This representation is justified by the fact that, by increasing the TR, an optimized pulse can be scaled up (higher $B_{1,RMS}^+$), while still respecting the energy constraints. Two regimes can be differentiated, for $B_{1,RMS}^+ target \sqrt{DC} < 1.2 \mu T$, a given pulse type performs consistently and reaches the $B_{1,RMS}^+ target$. Above this threshold, it is no longer always possible to reach the $B_{1,RMS}^+ target$ and the RMSE error increases. In the low-energy regime, going from one mode to two modes improves homogeneity by a factor of 2. In the meantime, going from two to three modes only reduces the error by a factor of 1.02. This is confirmed when we compare three modes with four modes, which gives almost no difference

in the low-energy regime; the distinction is made in the high-energy regime, but the gain is so negligible as to be of no interest. It worth noting that four modes, not only does too great an increase in the number of modes, not improve homogeneity, but it can even lead to less optimal results than with fewer modes. This can be seen between 3-modes and 4-modes UPs, for $B_{1,\text{RMS}target}^+ \sqrt{DC} = 0.8 \mu\text{T}$. The latter, with too many parameters to optimize, has some difficulties to reach the global optimum. These conclusions obviously vary according to the optimizer used, but they call for parsimony. These findings are in agreement with those observed previously in [Leitão et al. \(2022\)](#). We therefore concentrated on optimizing two modes.

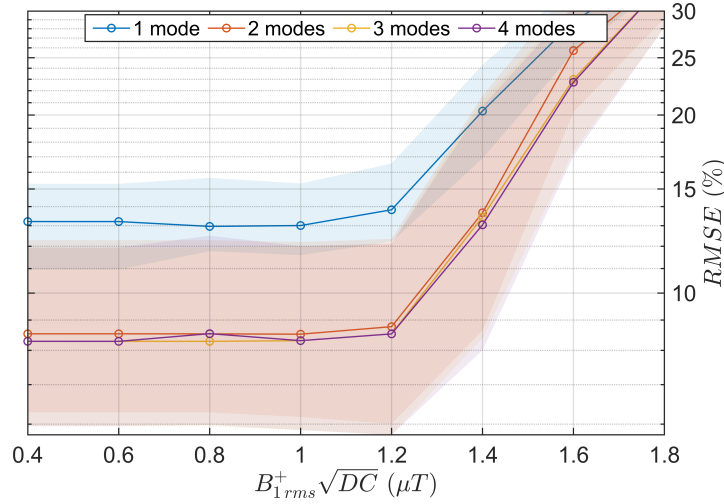


Figure 4.1: $B_{1,\text{RMS}}^+$ RMSE of UPs designed using various number of modes. Lines represent the average performance while colored areas are bounded by the minimum and maximum RMSE over the data-set. Pulses designed for an axial slab ($z = +15 \pm 5 \text{ mm}$) under VOP energy management.

The pulses obtained with two modes are illustrated in Figure 4.2. Typical hydroxyl-weighted CEST maps obtained with TPs optimized for a given volunteer are shown in Figure 4.2A. While the optimization does not result in a trivial solution, we note that, due to the combined optimization of the two modes, the spatial distributions of the $B_{1,\text{RMS}}^+$ show spatial complementarity (Figure 4.2B).

$B_{1,\text{RMS}}^+$ maps obtained on the evaluation data set using Equation (4.3) for both UPs and CP are shown in Figure 4.3. UPs provide a much more homogeneous saturation than CP. The RMSE computed as the ratio of the distance between the target and the effective $B_{1,\text{RMS}}^+$ (Equation (4.3)) to the $B_{1,\text{RMS}target}^+$, decreases from 28% to 7.7% when using UPs compared to the CP mode. The UPs perform also more evenly across subjects, the standard deviation of inter-subject RMSE being 2.2 times smaller than with CP.

Figure 4.4A shows the simulated performance of CP, MIMOSA ([Liebert, Zaiss, et al. 2019](#)), UPs and TPs for a volume saturation when the optimization was performed under protected mode or VOP supervision.

In Figure 4.4, two regimes stand out. For low energy deposition (low duty cycle), the protected and VOP SAR management strategies perform similarly.

For higher duty cycle, starting at $B_{1,\text{RMS}target}^+ \sqrt{DC} = 0.9 \mu\text{T}$, the use of VOPs allows maintaining a constant RMSE while the optimization under protected mode breaks down. In this regime, the UPs and TPs perform similarly. MIMOSA benefits less than the other pTx pulses from VOP supervision, most likely due to the similarity with the CP mode. In practice, it is noted that the local SAR supervision enables shorter TRs without sacrificing saturation homogeneity. The Figure 4.4B shows that optimizing pulses on a slab can dramatically reduce the RMSE, while the trends observed for different pulses in Figure 4.4A are maintained.

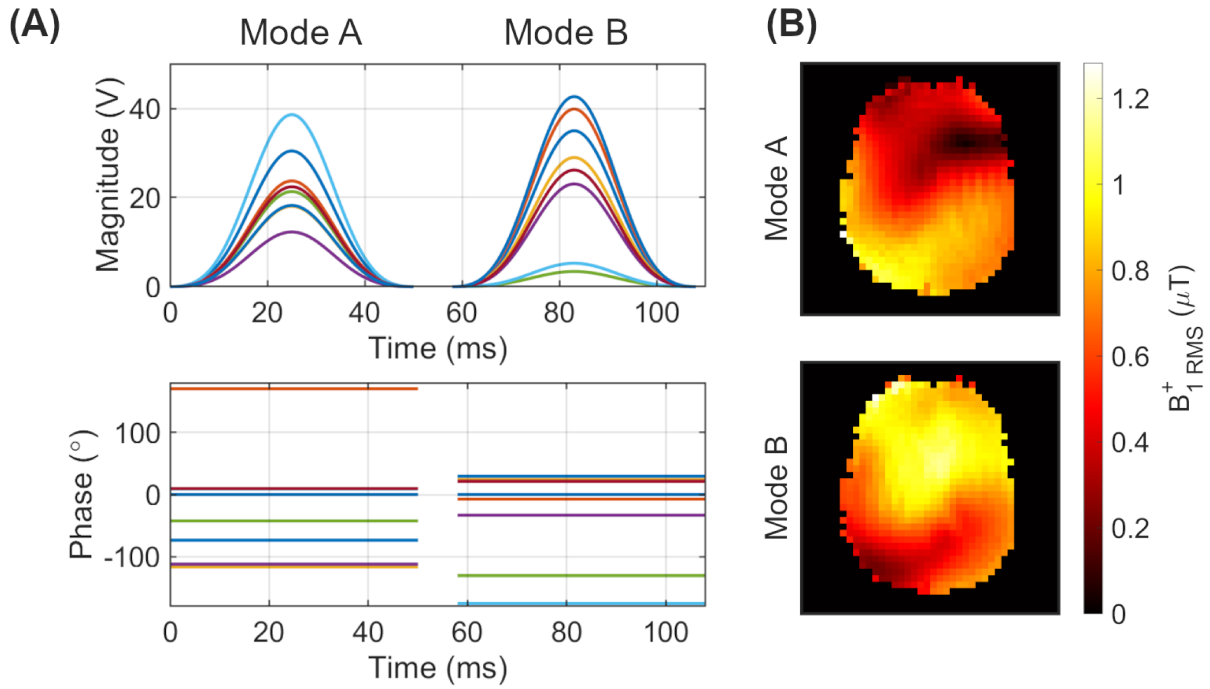


Figure 4.2: Magnitude and phase of optimized tailored pulses for a CEST presaturation targeting hydroxyl protons. Each color represents one channel (A). Spatial distribution of the effective $B_{1,RMS}^+$ for the two modes (B).

For this study, for the hydroxyl-weighted CEST and glutamate-weighted CEST acquisitions performed with the parameters presented in the Section 4.3, the values of $B_{1,RMS}^+ \sqrt{DC}$ are $1.03 \mu T$ and $1.3 \mu T$, respectively (see arrows in Figure 4.4B). Under these conditions, the performances of the different pulses, optimized on a slab, are summarized in Table 4.1. The RMSE is drastically reduced using VOP supervision as it leverages the degrees of freedom of both the amplitude and phase, allowing higher RF amplitudes than the protected mode.

More specifically, it allows UPs to achieve a RMSE three to four times better than CP and up to two times better than MIMOSA in terms of homogeneity. For hydroxyl and glutamate acquisitions, TPs perform better than UPs, with, as noted before, the disadvantage of requiring a subject-specific optimization.

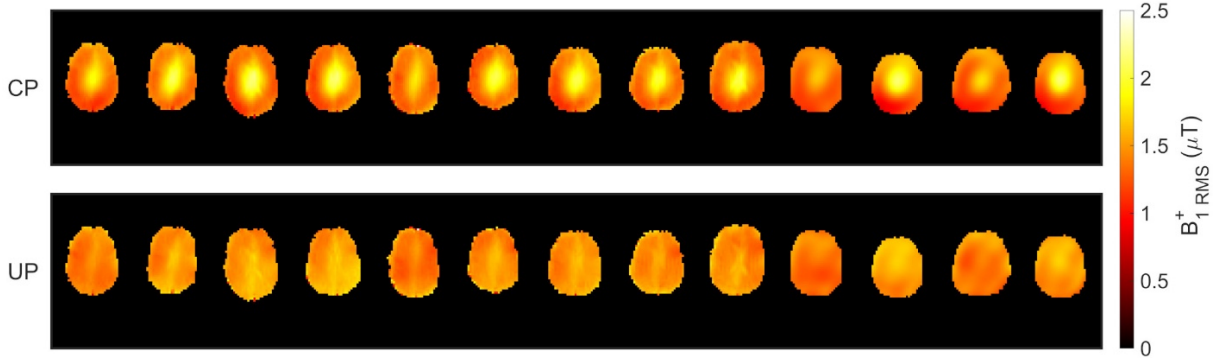


Figure 4.3: $B_{1,RMS}^+$ distribution obtained on the evaluation data set (13 B_1^+ maps independent from those used to design the universal CEST presaturation pulses) using CP versus UPs. For both strategies, the target $B_{1,RMS}^+$ was $1.5 \mu T$ and the other presaturation parameters were those for hydroxyl-weighted CEST.

		Protected mode				VOP supervision			
		CP	MIMOSA	UP	TP	CP	MIMOSA	UP	TP
hydroxyl	P_{total} (W)	8.0	8.0	8.0	8.0	8.0	12	15	13
	$P_{channel}$ (W)	1.0	1.0	1.2	1.3	1.0	1.5	2.7	2.2
	SAR_{local} (W/kg)	10	6.6	6.0	4.7	10	9.6	9.4	8.8
	SAR_{global} (W/kg)	1.2	1.2	1.2	1.2	1.2	1.7	1.8	1.8
	RMSE (%)	25.3	21.4	19.3	18.3	25.3	9.3	8.1	3.9
glutamate	P_{total} (W)	8.0	8.0	8.0	8.0	8.0	12	12	16
	$P_{channel}$ (W)	1.0	1.0	1.0	1.3	1.0	1.5	1.5	2.7
	SAR_{local} (W/kg)	10	6.6	6.0	4.9	10	10	10	10
	SAR_{global} (W/kg)	1.2	1.2	1.2	1.2	1.2	1.8	1.7	2.2
	RMSE (%)	35.7	33.1	31.4	30.3	35.7	17.9	8.70	6.93

Table 4.1: Performance summary of different presaturation strategies for hydroxyl-weighted CEST and glutamate-weighted CEST acquisitions in the study (optimization performed on a slab). The values highlighted in orange are capped by the constraints under both the protected mode and VOPs. The values highlighted in blue are allowed under VOP supervision but forbidden under protected mode.

4.4.2 In vitro CEST results

Simulated $B_{1,RMS}^+$ maps for the two TP modes are shown in Figure 4.5A and their combination in Figure 4.5B (right). In Figure 4.5B the simulated $B_{1,RMS}^+$ map is also presented for CP (left). According to these $B_{1,RMS}^+$ simulations, pTx significantly improves the homogeneity of the saturation in the phantom compared to CP with an eight times smaller RMSE (4% versus 32%). As expected, the MTR_{asym} map experimentally obtained with TP (Figure 4.5C) is also more homogeneous, with an RMSE of 17% versus 30% with CP.

Figure 4.6 shows the Z-spectra obtained in two different ROIs, one located in the center of the phantom, the other in the posterior region exhibiting low B_1^+ with CP. Across the phantom, the CP pulse leads to changes in the width of the Z-spectra with a Full Width at Half Maximum (FWHM) doubled between ROIs 1 and 2 (Figure 4.6A). When the presaturation is performed with TP, the Z-spectrum is constant across the phantom. The MTR_{asym} obtained with TP matches well the simulation results obtained for a saturation RF amplitude of $1.5 \mu T$ (Figure 4.6B). An almost identical MTR_{asym} value is obtained at 1.25 ppm, in both ROIs with TP while CP leads to much higher values in

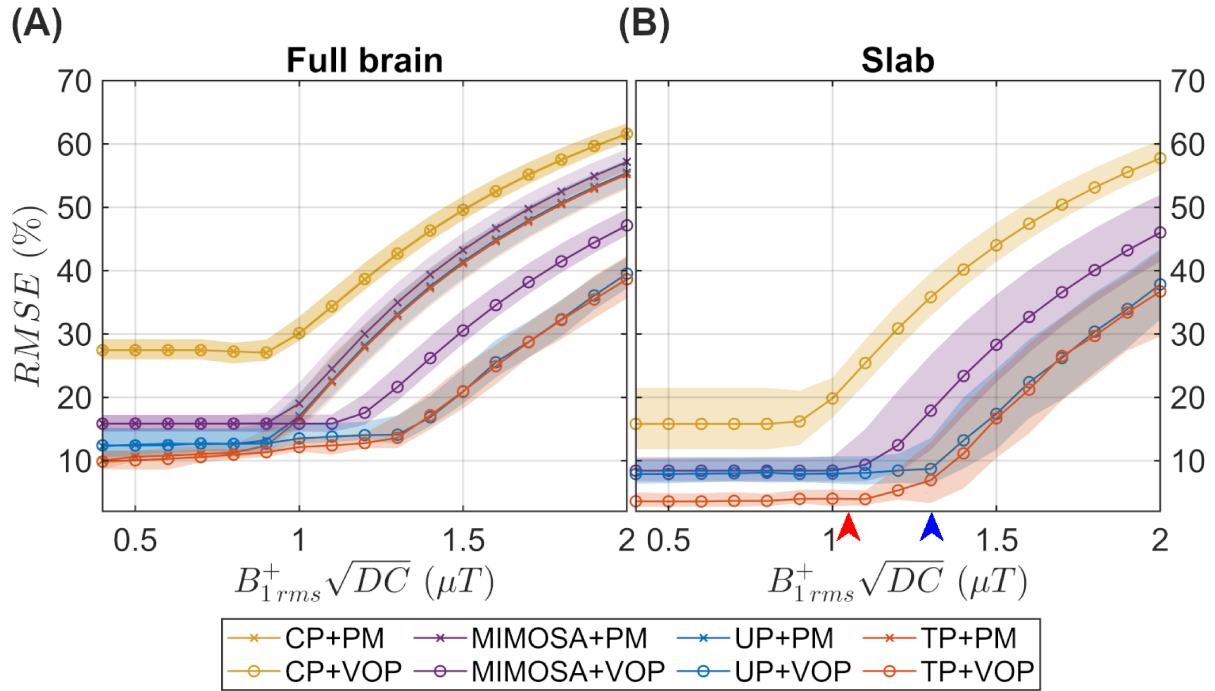


Figure 4.4: $B_{1,rms}^+$ RMSE of CP, MIMOSA, TPs and UPs under different optimization and energy management strategies. TPs were designed subject-by-subject on the evaluation data-set. Lines represent the average performance while colored areas are bounded by the minimum and maximum RMSE. (A) Comparison of CP, MIMOSA, UPs and TPs for a whole brain optimization under protected mode (PM) or virtual observation points (VOP) SAR management. (B) Comparison of CP, MIMOSA, UPs and TPs for an axial slab ($z = +15 \pm 5$ mm) optimization under VOP management. The two arrows point to the values on the abscissa corresponding to experimental protocols described in the Section 4.3 (red for hydroxyl-weighted CEST, blue for glutamate-weighted CEST).

ROI 1 compared to ROI 2.

For TP, the SNR of the MTR_{asym} map reaches 20 on average across the slice. Given the 10 mM glucose concentration in the phantom, we expect, for typical brain glucose concentrations of 1 mM, a SNR of 2 (assuming only glucose CEST contribution).

4.4.3 An attempt of Dynamic Glucose-Enhanced CEST MRI

Switching from phantom to in-vivo is not always easy, as there are additional problems such as motion and physiological noise, which affect the quality of the results. This section presents the results obtained on the first volunteer scanned.

GlucoCEST maps at rest, in-vivo, have never been performed. However, glucoCEST is used in certain cases, with an infusion or bolus of glucose leading to a glycemic rise in the blood, which is visible on CEST MRI. This is called Dynamic Glucose-Enhanced MRI (Chan et al. 2012; Walker-Samuel et al. 2013; X. Xu et al. 2015). Our study protocol does not allow such an experiment. In order to increase the chances of seeing a glucose weighted CEST contrast for this first in-vivo acquisition, we made the patient drink 15 cl of grape juice, in the hope of observing a glycemic rise through CEST MRI. This corresponds to an ingestion of 23 g of sugars, including 12 g of glucose. Given the literature on the subject, it is expected a glycemic peak 30 min after ingestion of around 2.4 - 3.6 mM (Xinlei Wang et al. 2018; Fujii et al. 2019).

This would lead to a variation in MTR_{asym} of the order of 0.5% if we base ourselves on the CEST amplitude obtained on phantom but also if the data are extrapolated from current DGE values (X. Xu

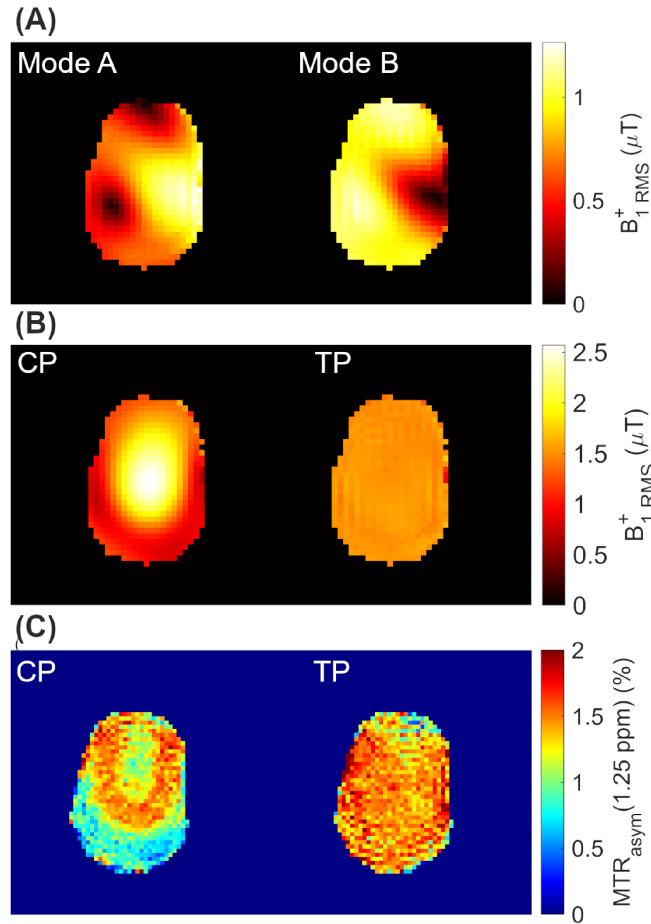


Figure 4.5: (A) $B_{1,RMS}^+$ simulation results for the two modes of a specific tailored pulse. (B) Simulated $B_{1,RMS}^+$ maps for CP and for the combination of the TP modes shown in (A). (C) Experimental $MTR_{asym}(1.25 \text{ ppm})$ maps on phantom for CP and TP.

et al. 2015; Seidemo et al. 2023). This variation is small, but must be within the detectability zone, given the SNR obtained on phantom. In order to implement this protocol, and also to have data for comparison between the different modes, the volunteer's exam was divided into two phases, between which the volunteer exited the MRI, drank 15 cl of juice, and then returned in the MRI.

- Shim, B_0 and B_1^+ mapping, T_1 anatomical map. Duration: 20 min
- hydroxyl-weighted CEST using CP, pTx-UP and pTx-TP. Duration: 15 min
- Subject exits the MRI, takes 15 cl of grape juice, returns to the MRI. Duration: 10 min.
- Shim, T_1 anatomical map. Duration: 15 min
- WASSR, 10x hydroxyl-weighted CEST using pTx-UP, WASSR. Duration: 35 min.

In order to observe glucose dynamics, 10 successive CEST-EPI acquisitions were made using the hydroxyl-weighted CEST protocol. Before and after these measurements, a WASSR acquisition was played to correct for B_0 inhomogeneities. A direct calculation of MTR_{asym} , with correction of ΔB_0 using the WASSR acquired at $t = 0$ gives rise to the map shown below in Figure 4.7.

Each time the hydroxyl-weighted CEST acquisition is repeated, an overall increase in the measured signal is observed. This increase, averaging 1%, is also in line with our predictions. This looks

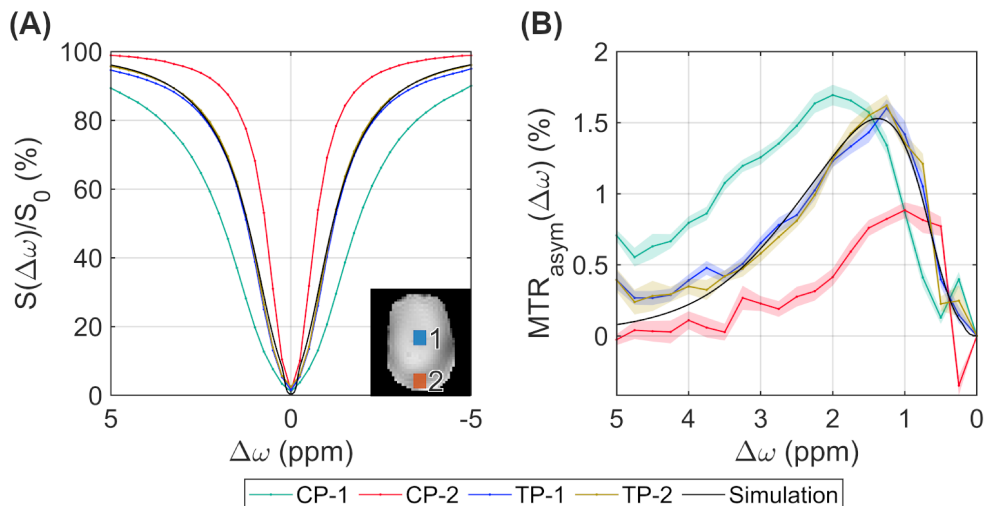


Figure 4.6: (A) Experimental and simulated Z-spectra in the phantom. Using TP, the spectra in the two ROIs are almost superimposed, as expected. However, this is not the case for CP due to the B_1^+ brightening effect in ROI 1 and signal dropout in ROI 2. The simulated Z-spectrum (black line) is almost identical to those obtained with TP. (B) MTR_{asym} calculated in the ROIs shown in (A), demonstrating identical glucose MTR_{asym} values when using TP. The colored areas are delineated by the standard deviation of the signal in the respective ROIs. MTR_{asym} (black line) agrees well with the TP results. The simulations were performed in the same condition as in Chapter 3.2. The CEST saturation was modeled with 20 identical Gaussian-Hanning pulses scaled to reach $1.5 \mu\text{T } B_{1,\text{RMS}}^+$.

promising. Demonstrating that oral glucose allows contrast generation in a similar way to DGE would enable setting up clinical protocols that are simpler to use, than infusion of a large quantity of glucose.

However, a closer analysis of the results leads to temper this statement. A second map of ΔB_0 , measured at the end of the examination is available. By assuming a linear variation of ΔB_0 , these maps are interpolated at all hydroxyl-weighted CEST measurement times to obtain 10 maps, each matched with one acquisition (as shown in Figure 4.8A). If the variation between the maps seems small to the eye, a difference can be seen between each of the 10 maps in Figure 4.8B. A roughly homogeneous shift in water resonance frequency takes place, at around $1\text{e-}3 \text{ ppm/min}$. It also appears to be slower around the temporal lobes. The temperature variation of a few tenths of a degree could be an element of explanation, but as the shift is $0.01 \text{ ppm} / ^\circ\text{C}$ (Rieke and K. B. Pauly 2008; P. Wang 2017), this would imply a variation in brain temperature of the order of $5 ^\circ\text{C}$. This hypothesis can reasonably be set aside, at least as the only explanatory factor.

The reason lies more in the hardware. Indeed, after long acquisitions with sequences that make somewhat intensive use of gradients, the combined effect of vibrations and eddy currents generates heat which, on contact with the shim coils and antenna, modifies their properties and generates a shift in the frequency of water resonance (Foerster, Tomasi, and Caparelli 2005; Benner et al. 2006). The order of magnitude mentioned in Benner et al. (2006) corresponds perfectly with what we observe here and supports this explanation. Moreover, such a drift has inertia and can last for several hours, so the hypothesis of linear interpolation for a 30 mn acquisition is justified.

Sophisticated methods have been studied to provide CEST sequences free of this frequency shift (R. Liu, H. Zhang, Niu, et al. 2019; R. Liu, H. Zhang, Qian, et al. 2021). But in our case, and given that this shift is modeled quite finely by a linear function, a temporal interpolation of the ΔB_0 maps is sufficient to correct our data. Effectively, after this correction, the MTR_{asym} map (Figure 4.9A) presents a much more constant aspect through time. An even cleaner result can be obtained if a motion correction (Breitling et al. 2022) is applied before the field inhomogeneity correction (Figure 4.9B). Standard motion correction algorithms can produce false results with CEST data as it presents a variable illumination especially for saturation offset near 0 ppm. By assuming that the less bright an image is, the

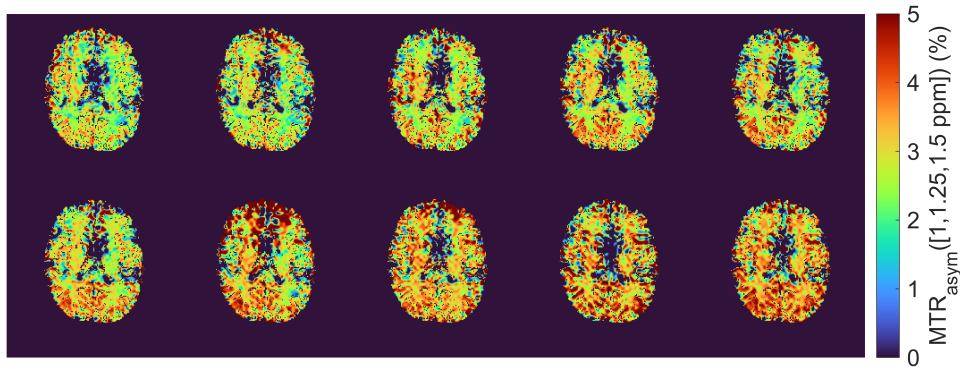


Figure 4.7: The 10 MTR_{asym} maps obtained after grape juice ingestion. It seems that hydroxyl-weighted CEST increases with time, as we would expect for DGE.

less reliable the motion registration, [Breitling et al. 2022](#), introduces a regularization of the estimated motion is performed based on the image brightness. An more in depth description of this method is given in [Appendix B](#). Still, it can be seen that after motion correction, artifactual elements have disappeared, notably in the peripheral regions, around the frontal lobe and finally at the borders of the CerebroSpinal Fluid (CSF).

Coming back to the purpose of this comparison, which is to measure any glucoCEST-related changes following grape juice intake, it can be seen that the [Figure 4.9B](#) maps no longer seem to show any evolution. [Figure 4.10](#) shows this in a different way. On the left, in [Figure 4.10A](#), the evolution of MTR_{asym} for the glucose frequency, uncorrected for machine frequency shift effects, i.e. the same conditions as in [Figure 4.7](#). This shows an average increase of 1% in the brain as found earlier. After correcting for movement and frequency shift, we note that the evolution in [Figure 4.10B](#) is much lower, and a trend would seem to emerge, of the order of 0.1% of MTR_{asym} , but the noise of the measurement makes it impossible to conclude. The trend seems to be equally marked between Grey and White Matter (GM, WM respectively).

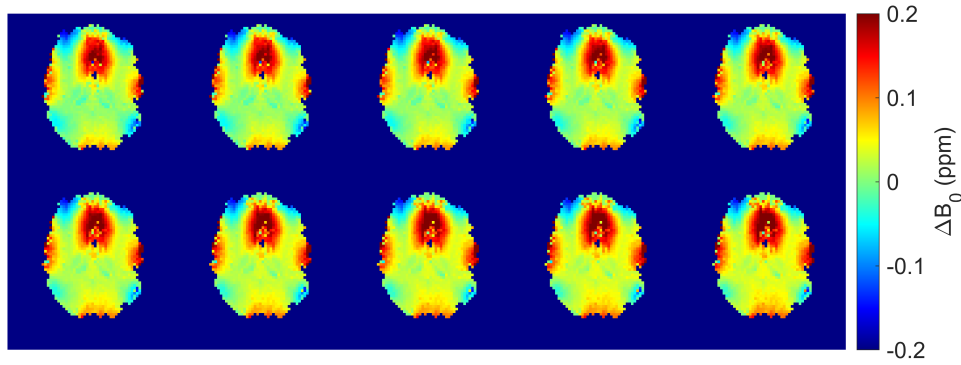
In conclusion, grape juice intake was not observed by a change in the CEST effect during this experiment, but it did highlight the importance of the WASSR correction and its interpolation over time to provide frequency-shift-robust MTR_{asym} maps. It is difficult to draw further conclusions from this experiment and we tried to reproduce it later, using the CEST-EPI-fast sequence, in an attempt to show an increase in MTR_{asym} after grape juice intake. Unfortunately, the scanner malfunctioned during this acquisition, leaving unusable data. The first part of this experiment, i.e. the comparison between CP, UP and TP, yielded very interesting results, and the effectiveness of pTx in resolving B_1^+ field inhomogeneity in vivo is demonstrated in the next section.

4.4.4 In vivo pTx CEST results

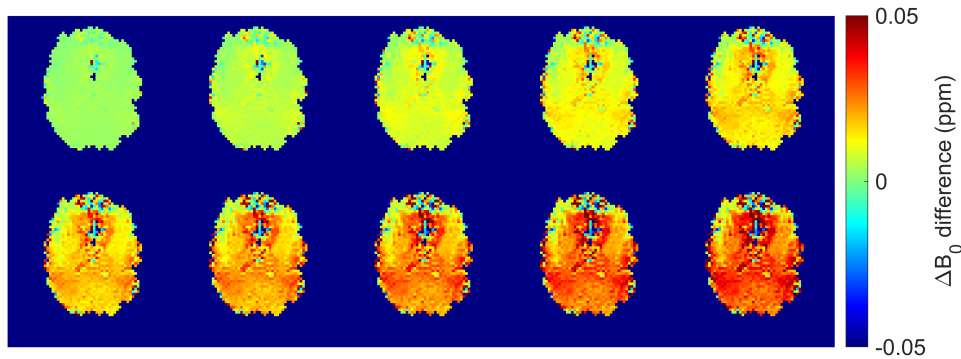
4.4.4.1 Hydroxyl-weighted CEST

We studied the homogeneity of in vivo hydroxyl-weighted CEST maps obtained with UPs and CP CEST presaturation.

The results obtained on four volunteers, shown in [Figure 4.11](#) are consistent with those from simulations and in vitro measurements. Specifically, the hydroxyl-weighted CEST maps obtained with UPs present overall higher MTR_{asym} values than those with CP, especially at the borders of the brain. We can note that with CP, the low saturation at the borders of the brain leads to a strong rNOE effect and, as a result, to a negative MTR_{asym} value. It can be also noted that in the center of the brain, CP and UPs show similar values of MTR_{asym} , thanks to the comparable saturation values. [Figure 4.11B](#) shows $B_{1,\text{RMS}}^+$ obtained with UPs for each subject, the average $B_{1,\text{RMS}}^+$ RMSE is 13%, giving therefore an improvement of a factor 2 compared to the saturation obtained with CP. The corresponding flip



(A) ΔB_0 map used for each acquisition. Original ΔB_0 maps were linearly interpolated to produce 10 ΔB_0 maps for each measurement time.



(B) ΔB_0 map variation, for each CEST acquisition. Computed as: $\Delta B_0(t) - \Delta B_0(t = 0)$.

Figure 4.8: Time drift of water resonance frequency.

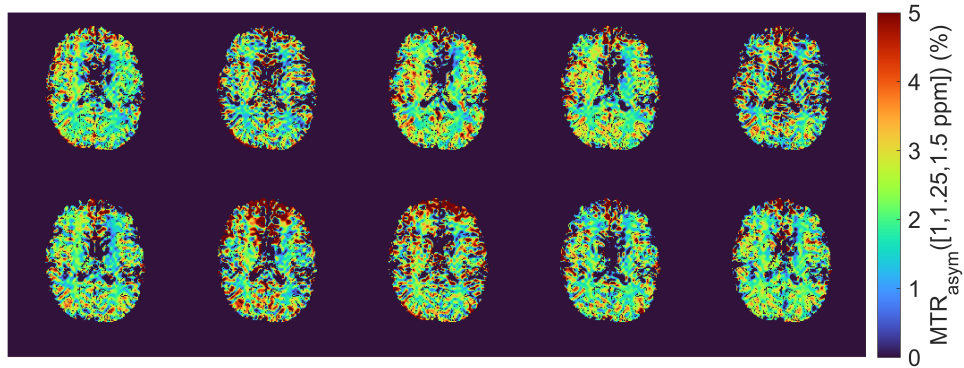
angle maps computed as in [Zu et al. \(2011\)](#) are shown in Figure 4.11C.

The observations above are supported by Figure 4.12. In Figure 4.12A, for all subjects, a higher MTR_{asym} value with a more homogeneous distribution with UPs than with CP can be noted. As it is shown in Figures 4.12B and 4.12C, for UPs the median and the Full Width at Half Maximum (FWHM) of the MTR_{asym} are 4 times higher and 40% narrower, respectively. The MTR_{asym} median for different brain regions, gray matter, white matter and central part, is shown in Figure 4.12D. The UPs provide a high and constant median value in all the different regions. CP gives, like UPs, a 2% MTR_{asym} value in the center of the brain, but overall the values in white matter and gray matter are significantly lower with a near 0% MTR_{asym} median.

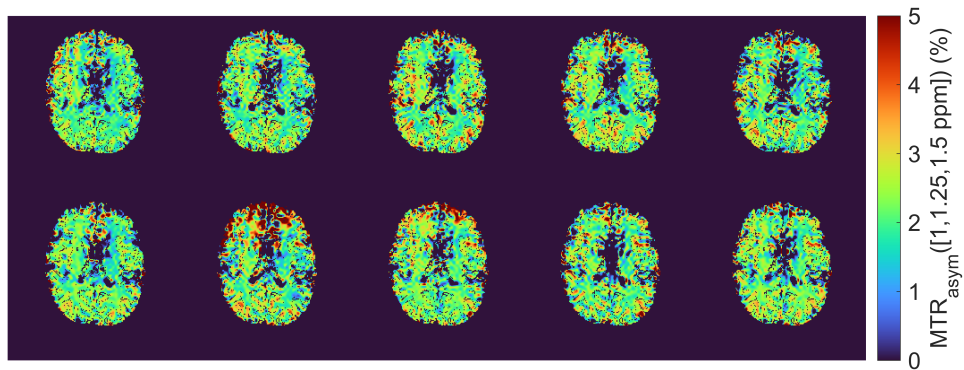
In Figure 4.13 we compare the performances of CP, MIMOSA, and UP on two volunteers at three locations from the isocenter ($z = +15, +40$ and -40 mm). Both the MTR_{asym} (Figure 4.13A) and the $B_{1,\text{RMS}}^+$ (Figure 4.13B) maps demonstrate that UP outperforms the other two approaches in all three slices. For all three methods, the inhomogeneity in MTR_{asym} for the lower slice ($z = -40$ mm) is stronger than that expected based on the $B_{1,\text{RMS}}^+$ maps, due to, nonetheless, strong B_0 inhomogeneities in this brain region. Compared to CP, MIMOSA provides a significant improvement in $B_{1,\text{RMS}}^+$ in the central ($z = +15$ mm) and the lower slices ($z = -40$ mm). However, for the upper slice, MIMOSA leads to a strong $B_{1,\text{RMS}}^+$ on the edge of the brain and suffers from a dropout in the center of the brain. For all three slices, and especially for the upper slice, UP provides the most homogeneous $B_{1,\text{RMS}}^+$ (See Table 4.2).

4.4.4.2 Other CEST contrasts

rNOE and glutamate-weighted CEST weighted maps, acquired using UPs are shown in Figure 4.14. Consistent with our hydroxyl-weighted CEST results, these maps show good contrast across the brain.

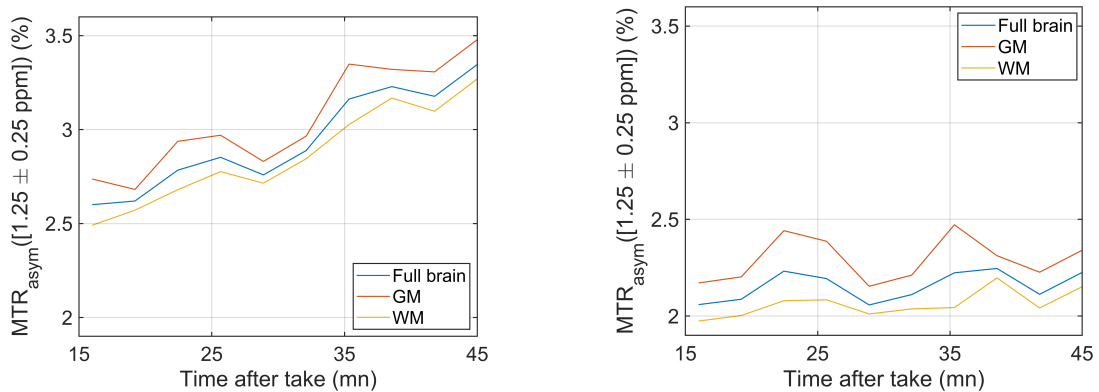


(A) The 10 MTR_{asym} maps obtained after grape juice ingestion, using the improved ΔB_0 correction.



(B) The 10 MTR_{asym} maps obtained after grape juice ingestion, using the improved ΔB_0 correction and motion correction.

Figure 4.9: MTR_{asym} maps after correction shows a constant dynamic of hydroxyl-weighted CEST.



(A) Without frequency shift and motion correction.

(B) After frequency shift and motion correction.

Figure 4.10: Evolution of MTR_{asym} with time, averaged on the slice, on gray matter or on white matter.

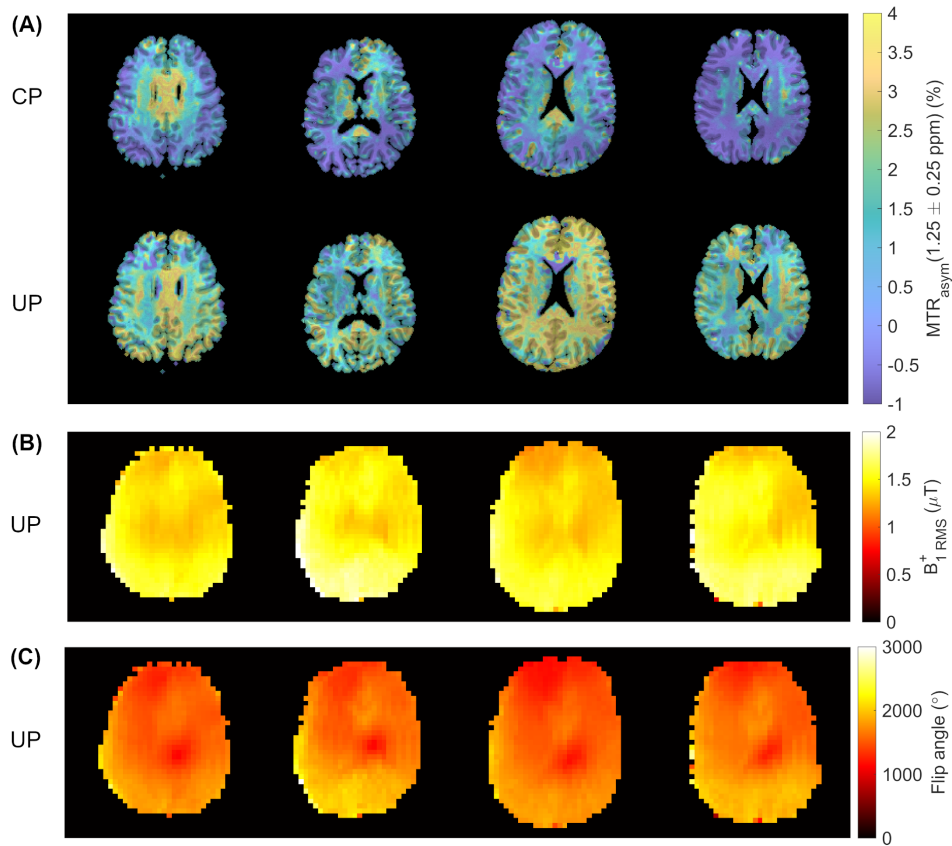


Figure 4.11: (A) Comparison of MTR_{asym} maps obtained with CP and UPs on four volunteers. The MTR_{asym} maps are overlaid on T_1 weighted anatomical images. With UP presaturation, the MTR_{asym} does not suffer of dropout in peripheral areas. (B) $B_{1,\text{RMS}}^+$ and (C) flip angle maps corresponding to the UP images in (A).

The rNOE maps present an average MTR_{asym} of 4% in gray matter and 7.5% in white matter which is similar to average values reported in the literature (Zaiss, Kunz, et al. 2013; Craig K. Jones et al. 2013; Paech, Zaiss, et al. 2014). The glutamate-weighted maps show a gray matter contrast in agreement with that reported by (Debnath et al. 2020). In the white matter, very low MTR_{asym} values are obtained, even negative, most likely because we did not perform a magnetization transfer correction (Debnath et al. 2020).

4.5 Discussion and perspectives

In this work, a pTx based method as been proposed and evaluated to mitigate $B_{1,\text{RMS}}^+$ inhomogeneity effects on the CEST contrast occurring in human brain at 7 T. The developed CEST presaturation scheme is composed of two interleaved modes and optimized using transmit sensitivity maps. We show, in agreement with literature, that this method works not only when tailoring the CEST presaturation pulse to the subject specific $B_{1,\text{RMS}}^+$ map, but also when using a fixed CEST *universal* presaturation pulse optimized offline on a collection of $B_{1,\text{RMS}}^+$ maps. Additionally, the use of VOPs for SAR management allows a significant gain in CEST presaturation uniformity. The VOP boost could also be used for TR reduction, as one can design pulses minimizing SAR deposition while keeping the inhomogeneity of $B_{1,\text{RMS}}^+$ under a given threshold. Our simulations show that such an approach enables TRs two times shorter than when using the protected mode SAR management strategy.

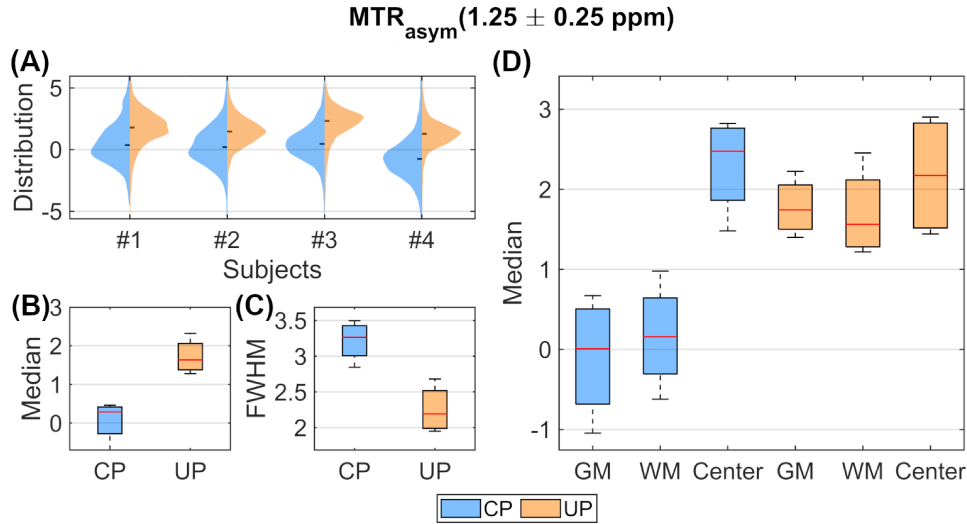


Figure 4.12: Distribution statistics of the $MTR_{asym}(1.25 \pm 0.25 \text{ ppm})$ obtained in vivo ($N = 4$ volunteers) for CP or UP CEST presaturation. (A) MTR_{asym} distribution across subjects. (B) MTR_{asym} median across subjects. (C) MTR_{asym} full width at half maximum. (D) Median MTR_{asym} for segmented regions, Gray Matter (GM), White Matter (WM), and a central part of the white matter (Center).

We note that the use of subject-tailored pulses optimized under VOP energy management constraints has been reported recently for magnetization transfer imaging (Leitão et al. 2022) with similar performance as that presented in this manuscript. From a practical point of view, the approach introduced here with the use of UPs and VOPs, brings a substantial improvement as it considerably simplifies the workflow in a clinical setting. The simulations show that, while the UPs are outperformed by TPs, they perform better than CP and other pTx approaches. This high level of performance, the absence of in-line optimization and the improved B_1^+ robustness to subject motion provides an opportunity to bring CEST MRI closer to clinical applications. To further improve B_1^+ homogeneity, this method can be combined with a B_1^+ correction strategy (Windschuh et al. 2015) requiring however additional scans, and therefore increasing the acquisition time. As an example, using a one-point B_1^+ correction leads to the obtention of an average of 7% increase in intra-tissue homogeneity for the hydroxyl-weighted MTR_{asym} maps presented in Figure 4.11. The present work proposes optimizing the $B_{1,RMS}^+$, a convenient metric as it is consistent with previous studies (Liebert, Zaiss, et al. 2019; Leitão et al. 2022), and because it is proportional with the deposited energy, for a given spatial distribution. However, the processes governing CEST are sensitive to B_1^+ , as the contrast generated arises more from spin rotation than from spin saturation, especially for fast exchanging protons. It would therefore be more accurate to seek to optimize the $B_{1,mean}^+$. However, given the small angles involved, the difference between optimizing one or the other of these two metrics produces extremely similar results.

This solution has been implemented in a single slice, 2D sequence, making the optimization on a slab possible, in order to design a more efficient saturation. However, this this approach can also be used for 3D CEST acquisitions. As the efficiency of the solution depends on the variability of B_1^+ profile in the optimization region, the performance can change drastically from one region of interest to another. As mentioned by Leitão et al. (2022), optimized pTx methods (and it is also the case of the one presented here) can greatly benefit from the development of coils with a larger number of transmission channels or increased complementarity between channels. The presented implementation takes advantage of pTx only for the CEST presaturation module but the excitation can also be performed in pTx mode in order to enhance the flip-angle homogeneity and the SNR as in Liebert, Tkotz, et al. (2021). In vivo imaging is inevitably susceptible to subject motion, which can have deleterious effects on CEST contrast maps (Zaiss, Herz, et al. 2019). Given the 2D single slice acquisitions

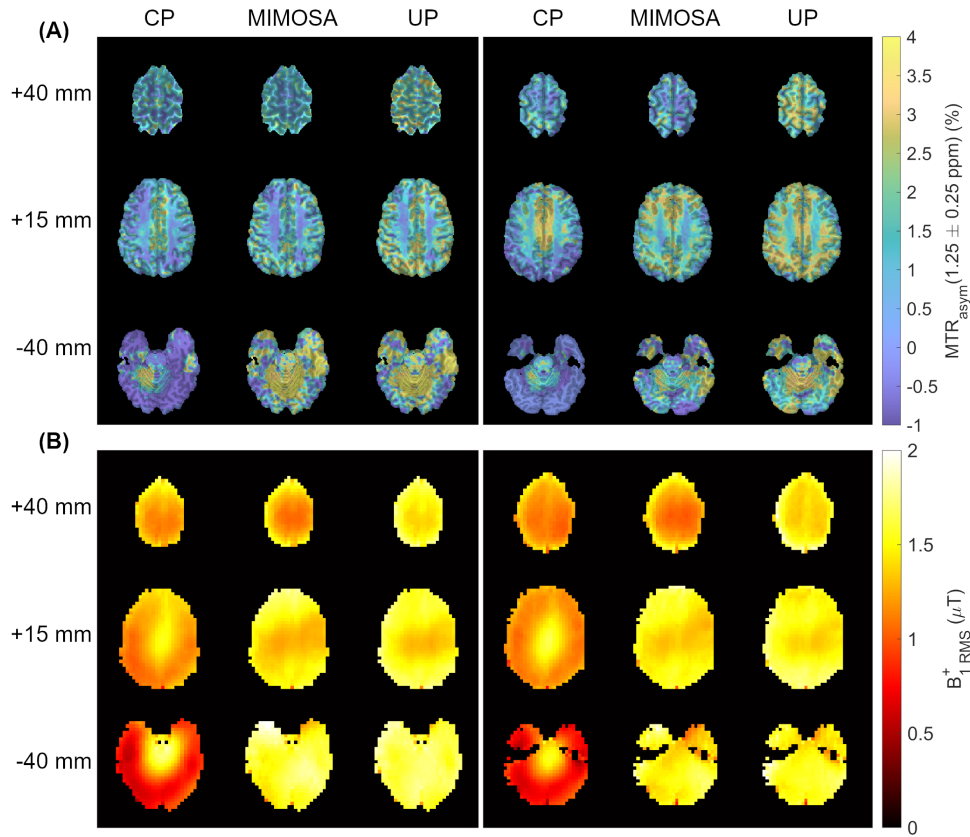


Figure 4.13: (A) MTR_{asym} and (B) $B_{1,RMS}^+$ maps obtained on two subjects using CP, MIMOSA and UPs using for hydroxyl-weighted CEST saturation parameters. Three slices were imaged at positions +40 mm, +15 mm and -40 mm from isocenter.

carried out in this study, only an in-plane correction could be applied, while significant out-of-plane movements, if any, were not corrected. The implementation of a multi-slice sequence, which overcomes this drawback, is used in the Chapter 5.

This study aims to enable endogenous glucose weighted CEST imaging. While our in vivo data is supported both by in vitro and simulation results, the MTR_{asym} maps presented reflect several CEST signals. Robust separation of different metabolic contributions remains a major challenge for CEST imaging and it is beyond the scope of this paper. The presented approach can also be used to perform dynamic glucose studies (Jihong Wang et al. 2016; Paech, Schuenke, et al. 2017). Moreover, by acquiring data only at strategically chosen frequency offsets in order to minimize the acquisition time, metabolic functional imaging studies, similar to those performed in rodents (Roussel et al. 2019), are conceivable.

(A) $B_{1,RMS}^+$ (μT)						
Slice	Subject 1			Subject 2		
	CP	MIMOSA	UP	CP	MIMOSA	UP
+40 mm	1.28	1.27	1.54	1.21	1.23	1.48
+15 mm	1.27	1.45	1.53	1.25	1.45	1.52
-40 mm	1.01	1.62	1.67	0.96	1.55	1.58

(B) $B_{1,RMS}^+$ RMSE (%)						
Slice	Subject 1			Subject 2		
	CP	MIMOSA	UP	CP	MIMOSA	UP
+40 mm	16.9	18.7	8.8	21.2	21.4	9.8
+15 mm	17.7	9.7	9.2	18.9	8.3	8.2
-40 mm	39.0	12.5	13.1	39.7	10.6	10.4

Table 4.2: (A) Average $B_{1,RMS}^+$ and (B) $B_{1,RMS}^+$ RMSE corresponding to the maps shown in Figure 4.13.

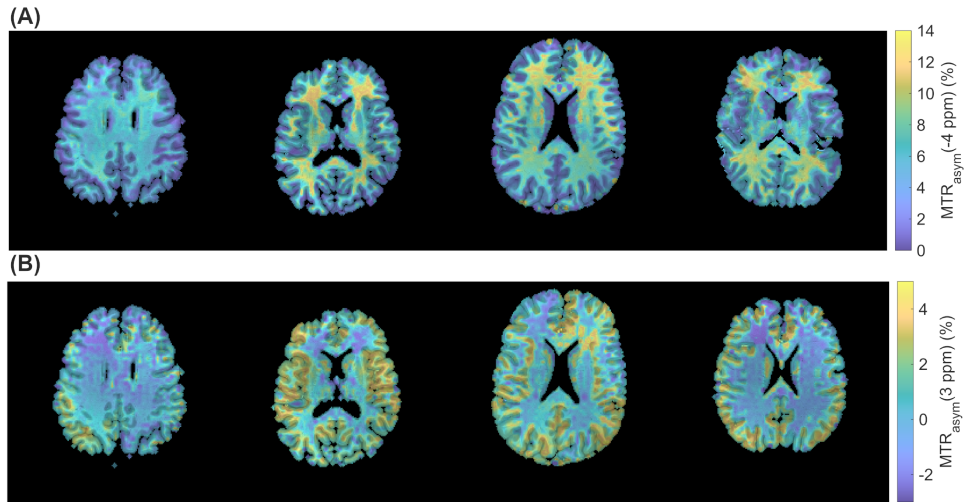


Figure 4.14: (A) *In vivo* rNOE and (B) glutamate-weighted CEST MTR_{asym} maps obtained with UP CEST presaturation overlaid on T_1 weighted anatomical images. (The images in the fourth column come from different subjects due to a technical problem during the first rNOE data acquisition.)

4.6 Conclusion

In this study, an optimized CEST presaturation scheme is presented that effectively addresses $B_{1,RMS}^+$ inhomogeneities even when dealing with high saturation-time/repetition-time ratios. To achieve this, we take advantage of virtual observation points, which allows us to fully exploit the potential of parallel transmission. The results show that the use of universal pulses UP outperforms the conventional CP mode and even compares to subject-specific tailored pulses TP. The key advantage of UPs lies in their offline optimization capability. By using UPs, significantly higher hydroxyl-weighted CEST MTR_{asym} values are observed compared to conventional CP CEST presaturation. On average, MTR_{asym} values were four times higher and the distribution was 40% narrower. Omitting the inhomogeneities of $B_{1,RMS}^+$, playing the glutamate-weighted CEST protocol with pTx and VOPs is two times faster than in the standard way for the state of the art of the literature. These results highlight the potential of our optimized CEST presaturation scheme to improve the accuracy and speed of CEST imaging.

Chapter 5

Application in young, elderly and Alzheimer’s disease patients

After the methodological development of CEST at 7T presented in the previous chapter of this manuscript, we wanted to assess the capabilities of CEST as a biomarker for normal aging and eventually for Alzheimer’s disease (AD). Therefore, this chapter presents the realization of a case/witness study of this objective. After presenting the core question and the methods used, we will look at the results obtained and discuss the conclusions and future perspectives, in particular with regard to the development of an unbiased CEST metric.

Contents

5.1 Introduction	78
5.2 Methods	78
5.2.1 MRI protocol	79
5.2.2 PET protocol	80
5.2.3 CEST processing pipeline	81
5.3 Results	82
5.3.1 Posterior brain volume	82
5.3.2 Hippocampi volume	85
5.4 Discussion and perspectives	85
5.4.1 An unbiased CEST metric	86
5.4.1.1 Interdependency effect	87
5.4.1.2 Results	88
5.4.1.3 Conclusion	92
5.5 Conclusion	93

5.1 Introduction

The imaging techniques currently used to diagnose and monitor AD are anatomical MRI and PET (Oostveen and Lange 2021). Anatomical MRI detects mostly disease-related atrophy of the brain. Unfortunately, atrophy occurs much later compared to metabolic changes and also occurs with other neurodegenerative diseases, which limits the accuracy of the diagnosis and makes it impossible to differentiate between the different sub-types of AD. PET provides a different contrast, obtained from the disintegration of radio-tracer. Several tracers can be used for AD such as glucose-analog, β -amyloid plaques or tau proteins (Marcus, Mena, and Subramaniam 2014; Maschio and Ni 2022). It is also possible to detect amyloid plaques using T_2^* weighted imaging, but this is still limited to preclinical applications as is difficult to use in clinical settings mainly because of the resolution required (Dhenain et al. 2009; Adlard et al. 2014)

Besides PET, few other methods exist for measuring glucose. Among these, MRI spectroscopy enables the direct detection of glucose. The main drawback of MRS is the low SNR leading to long acquisition times and low spatial coverage and resolution. Producing maps with ^1H MRSI, with comparable resolution to the CEST maps, would take more than an hour (Feyter et al. 2018; Niess et al. 2023). The gain in duration obtained with CEST is tempered by the greater selectivity of spectroscopy.

The reference method for studying glucose metabolism in clinical practice is PET, which requires the injection of a radioactive glucose analog. This has several limitations, starting with the logistical constraint of obtaining 18-FDG, since it requires a cyclotron. Moreover, as 18-FDG is not completely metabolized, it is stored in cells that consume a lot of endogenous glucose. This gives a different contrast to that observed with endogenous D-glucose, which is completely consumed and whose local concentration does not necessarily indicate the active regions. Rapid and robust measurements of relative endogenous glucose concentration with CEST would provide a different contrast compared to PET but it has many advantages as eliminating the need for radioactive material and allowing finer resolution.

One aim of this work is to assess the usefulness of glucoCEST as a biomarker for Alzheimer's disease. A second objective of this study is to compare glucoCEST maps obtained with MRI with those obtained with PET. Because the measurement of other metabolites in CEST can come almost for free once a Z-spectrum is acquired, additional CEST measurements, gluCEST and rNOE, are also planned. Although not comparable with PET, these contrasts may give rise to interesting biomarkers.

In order to evaluate these points, a case-control study has been set up. We plan to scan 50 subjects: 10 young and 20 elderly healthy volunteers and 20 Alzheimer's patients. Two MRI scans and one PET scan are planned for healthy volunteers, and only two MRI scans are planned for Alzheimer's Disease patients (AD). We hope to obtain authorization for PET scanning of AD patients, which should enable CEST measurements to be compared with PET measurements between healthy volunteers and patients.

This chapter presents preliminary results. These include scans of young healthy volunteers and scans of early aged healthy volunteers. The main conclusions of this chapter will therefore focus on these data with the aim of studying healthy aging. No conclusions are drawn regarding Alzheimer's disease or the correspondence between CEST and PET. Nevertheless, the results presented here are encouraging for further study.

5.2 Methods

If carried out in its entirety, the study should enable the following results to be exploited. By comparing resting CEST MRIs from young and elderly healthy volunteers, we can study age induced metabolic changes. By adding PET, correlation with MRI results can potentially be done. Then, at the same way, but comparing results from healthy elderly volunteers and AD patients, a bio marker of Alzheimer's disease may be identified. A second MRI in which we perform functional CEST MRI was

initially planned, thus, PET scans are performed dynamically during visual stimulation, so that the regions of functional activation observed with the two methods can again be compared. But this application was too ambitious at this stage of the project, and we did not set up a protocol for functional glucoCEST. In cases where the first MRI scan was disrupted by a machine bug or volunteer motion, the volunteers were called for a second MRI, following the same protocol as the first MRI.

The methodological developments presented in the previous chapters are used to enable efficient CEST measurement. In particular, the fast EPI sequence described in Section 3.1.2 is used. The optimized pTx saturation presented in Chapter 4 is also used.

In total, we have so far 10 MRIs from young subjects, 9 from old subjects and 1 from an AD patient. We also have data from 1 PET scan of one elderly subject.

5.2.1 MRI protocol

The aim of the first MRI scan was relatively straightforward: producing an anatomical T_1 map and then accumulating as much CEST data as possible, with different settings to maximize the amount of data while exploring the parameter space, in order to increase our ability to generate a selective and robust metabolic map. The CEST-EPI-fast sequence allows the measurement of a limited number of slices, so a choice had to be made regarding the region to be imaged. The choice of the number of slices imaged is the result of a compromise between saturation quality, $B_{1,RMS}$ and TR. Indeed, having many slices means repeating a large number of pulses and therefore having a low $B_{1,RMS}$ at a constant $B_{1,RMS,TR}$. On the other hand, it is not advantageous to have a very few slices, since the advantage of working in steady-state is lost and, above all, the image volume will be small, which is not in our interest. An arbitrary compromise has therefore been made by choosing 5 slices. This allows for 2-pulses saturation with a $B_{1,RMS}$ of 4 μT and a TR of 5 s. The slices were 4 mm thick and placed 2 mm apart covering a total volume of 30 mm. This volume was selected in an almost coronal plane, passing through the precuneus and the visual cortex (see Figure 5.1). This makes it possible to visualise the areas affected by Alzheimer's disease and to be located in the same plane as the one for which functional glucoCEST and PET is intended, with the regions showing strong activation during visual stimulation.

A anatomical image, necessary for atlas normalization and data parcelization, was also acquired using a MP2RAGE sequence (Marques et al. 2010) (repetition time = 6000 ms, inversion times = 800 ms / 2700 ms, bandwidth = 240 Hz, flip angle = 4°, resolution = 0.8 mm isotropic, matrix size = 300×320×190). Then two blocks of acquisitions are made to target glucose and glutamate. For simplicity, the same pTx pulses are used for these blocks but with different scaling to adjust the $B_{1,RMS}$. Specifically, the pulse intensity set at 100% gives $B_{1,RMS} = 4 \mu T$ which is the optimal for glutamate-weighted CEST and 40% gives $B_{1,RMS} = 1.6 \mu T$ which is the optimal for glucose-weighted CEST. Note that although the parameters were optimized for glucose, considering the CEST contrast weighted by hydroxyl groups is more rigorous since other hydroxyl groups such as myo-inositol and glycosaminoglycan and glycogen can contribute to it.

The two blocks acquisitions are named 'HydroxylXX' and 'GlutamateXX' with XX being the saturation intensity. Therefore, Hydroxyl40 and Glutamate100 refers to the sequence targeting hydroxyl or glutamate with 40% or 100% of the pulse nominal $B_{1,RMS}$. For each CEST contrast, glutamate and hydroxyl, several acquisitions were performed with different B_1 values as presented in Table 5.1. Other experimental parameters are echo time = 22 ms, bandwidth 2170 Hz/Px, FOV = 3.4 × 3.4 mm², slice thickness = 4 mm, slice number = 5, flip angle = 78°, matrix size = 64×64, excitation BTP = 2.2, excitation duration of 2560 μs .

Interleaved with these acquisitions, a WASSR scan necessary to correct for B_0 inhomogeneities is acquired every 15 min. A 30 s scan in the reverse phase direction to correct for B_0 distortions in post-processing was also run. It is important to note that, to limit the energy deposition over 6 min, acquisitions at high $B_{1,RMS}$ are interleaved with acquisitions at low $B_{1,RMS}$. The order of hydroxyl se-

quences is Hydroxyl40, Hydroxyl12, Hydroxyl32 and Hydroxyl22. The total acquisition scan duration for one volunteer was 1.5 hours.

After scanning the first five volunteers, as we wanted to make the most of the time available, we modified the protocol to add three additional Glutamate weighted CEST acquisitions, keeping the same orientation but focusing on the hippocampi. These three acquisitions are identical to the Glutamate100 acquisition, made for $B_{1,RMS}$ of 4 μT , 2.6 μT and 1.3 μT .

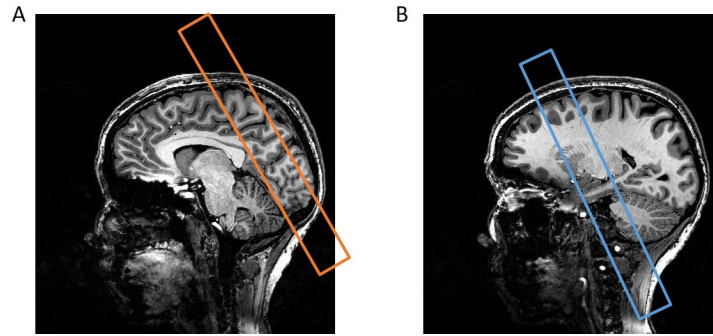


Figure 5.1: Sagittal view of volume position over a T_1 anatomical image. (A) FOV of interest on the posterior brain, including precuneus and visual cortex. (B) FOV on the central brain, for hippocampi

Name	$B_{1,RMS}$ (μT)	$\delta\omega$ (ppm)	N_{slice}	TR	duration
Hydroxyl40	1.6	0.1	6	2500	4'35"
Hydroxyl32	1.3				
Hydroxyl22	0.9				
Hydroxyl12	0.5				
Glutamate100	4	0.25	2	5000	3'50"
Glutamate75	3				
Glutamate50	2				
Glutamate25	1				
WASSR	0.16	0.05		1500	1'09"

Table 5.1: The different CEST acquisition settings used.

5.2.2 PET protocol

Once included in the study, typically after the MRI, healthy volunteers undergo a PET scan. This takes place at the SHFJ lab in Orsay. The equipment used is a SIGNA PET/MR scanner from GE Healthcare. MRI and 18-FDG PET scans are performed in parallel. The anatomical MRI allows precise co-registration with the MRI performed at Neurospin. The anatomical MRI is a T_1 weighted GRE sequence acquired at 1 mm isotropic resolution, with the following parameters: 256 x 256 x 176 matrix, TE = 2.7 ms, TR = 7 ms, FA = 10°.

PET is performed with the following parameters resolution 1.17 x 1.17 x 2.77 mm, with a frame acquired every 30 seconds for 60 minutes.

During PET, visual stimulation is performed in the same way as (Villien et al. 2014; Jamadar et al. 2020). An illustration of the results obtained for PET acquisitions is shown in Figure 5.2.

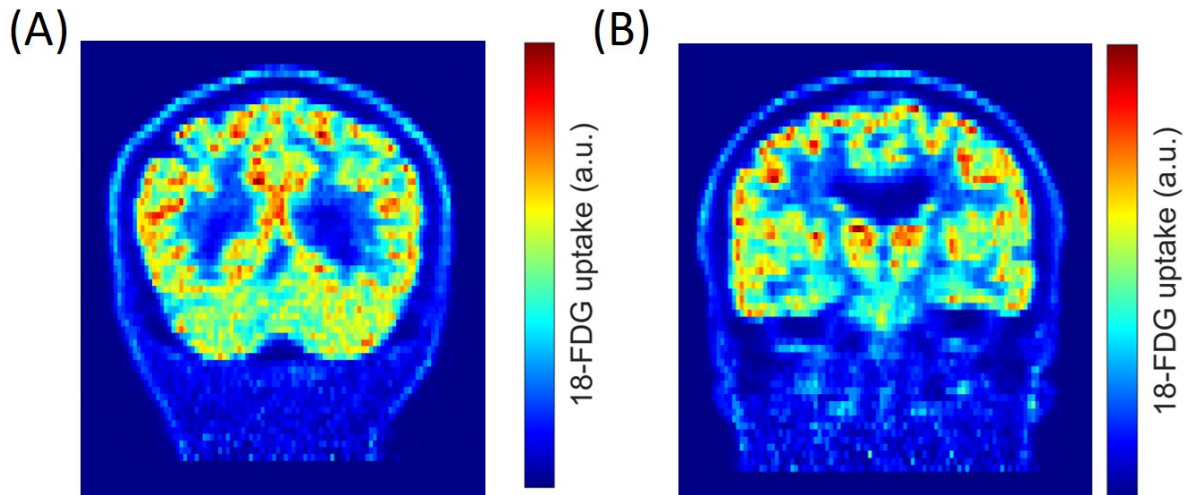


Figure 5.2: Example of 18-FDG uptake map integrated over 60 min. One slice is shown for the Posterior volume (A) and the Hippocampi centred volume (B) (see Figure 5.1).

5.2.3 CEST processing pipeline

The data collected is analyzed through the pipeline shown in Figure 5.3. In this pipeline, corrections are performed in this order: the distortions due to ΔB_0 , then the shift induced by ΔB_0 in the Z-spectra is corrected. Once the artifactual effects have been removed from the CEST data, the parcelization is used to extract values by region of interest. This can be done with automatic methods such as freesurfer, but in this case, for simplicity reasons of implementation, the data is parcelized using an atlas (MNI-ICBM2009c-symmetric atlas with Mindboggle 101 parcelization) (Manera et al. 2020). After co-registering the atlas with the subject's T_1 image, the transformation is applied to the atlas to obtain the segmented volume in the same space as the CEST data. An example of this parcelization is shown for subject No 19, for the posterior volume, precuneus/visual cortex as well as for the volume containing the hippocampi in Figure 5.4. Additionally, a white matter segmentation is performed with SPM12, subject by subject, using the T_1 image.

Figure 5.3 pipeline includes the ΔB_0 correction discussed above in Section 3.4. The ΔB_0 distortion correction is based on Matlab `imregdemons` (Thirion 1998; Vercauteren et al. 2009). This algorithm, developed for non-parametric diffeomorphic image registration, accurately computes the displacement field between an image and its phase-reversed counterpart. Subsequently, the displacement map magnitude is halved before regriding the entire CEST volume to produce a ΔB_0 -distortion corrected map. While TopUp from FSL was initially utilized, it exhibited issues with 5-slices data, particularly boundary effects on the first and last slices. The present solution has proven to work precisely with our CEST data.

CEST data are first analyzed using the MTR_{asym} in Equation (1.24) for simplicity. There are many drawbacks to using this metric, starting with its lack of selectivity. Therefore the use of another metric (Section 5.4.1) based on peak water estimation has been explored, but this was not sufficiently mature to be used in the analysis of the CEST data presented here. We have therefore retained the MTR_{asym} . We estimate the glutamate-weighted CEST, the hydroxyl-weighted CEST, and the rNOE-weighted CEST by taking the MTR_{asym} ([2.25 : 3.25] ppm) of the Glutamate100 acquisition, the MTR_{asym} ([1 : 1.5] ppm) of the Hydroxyl40 acquisition and the MTR_{asym} ([-2 : -4] ppm) of the Hydroxyl22 acquisition, respectively.

The acquired data are processed in Matlab. The only data analyzed at the time of writing are the MRI-CEST data from the young and elderly volunteer groups ($N = 10$ and $N = 9$ respectively). The median of MTR_{asym} , is extracted region by region for each subject, with left and right regions merged together. Regions with too few voxels are discarded (≤ 20). Statistical tests are performed to

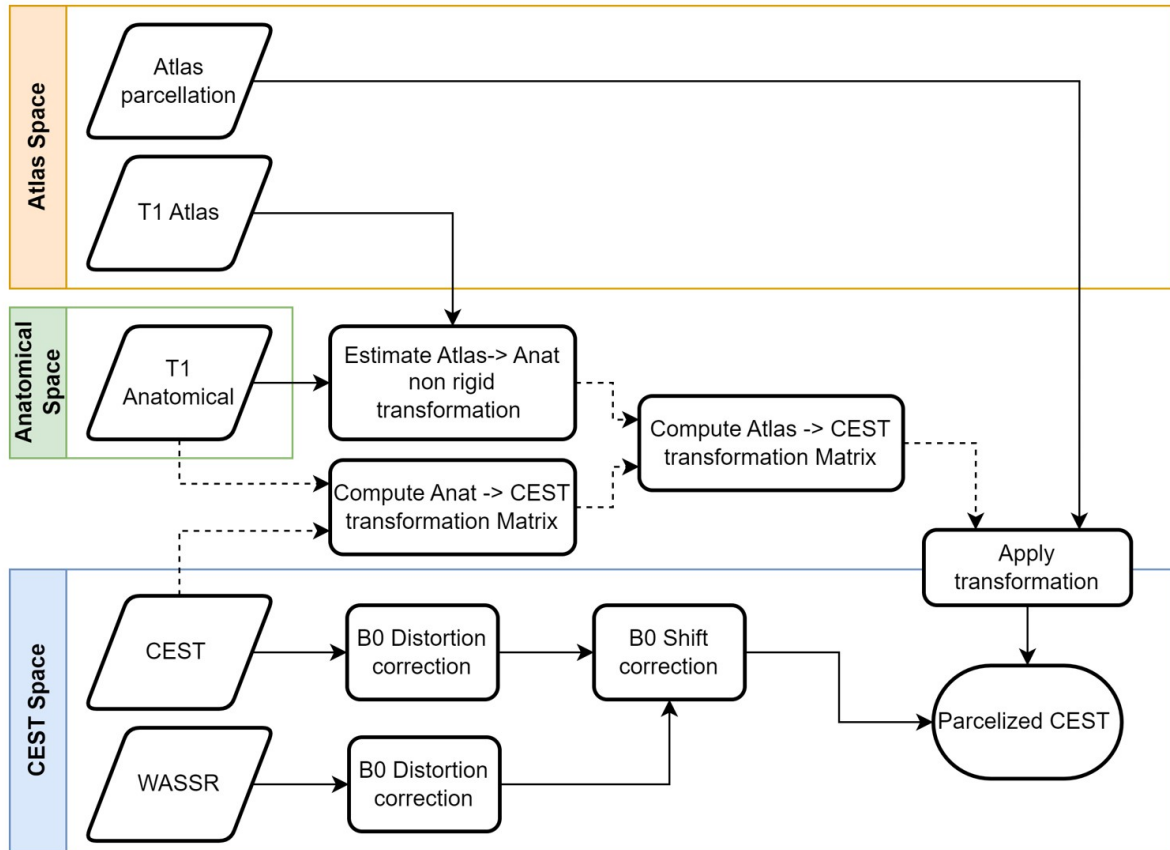


Figure 5.3: Scheme of the pipeline used for CEST data processing in this work. The purpose is to obtain the most bias-corrected CEST data, parcellized in the subject world.

estimate the significance of the results using R. When conditions were met, two-way ANOVA test were done to evaluate the group/region hypothesis. Otherwise, Kruskal-Wallis test was done for the group hypothesis. Since rNOE was measured only in the white matter, a t-test was sufficient to assess the significance of MTR_{asym} with differences between the young and elderly groups.

5.3 Results

5.3.1 Posterior brain volume

To illustrate the data acquired, Z-spectra of on one subject (No 15) are shown in Figure 5.5. These spectra show the influence of saturation intensity. It is interesting to note that the rNOE effect, seen at its maximum between -2 and -4 ppm at $0.9 \mu T$, is more important for long saturation (6 pulses - Figure 5.5A) than short saturation (2 pulses - Figure 5.5B). Other effects, such as hydroxyl and glutamate weighted CEST, are too weak to be visible directly on the spectra.

The MTR_{asym} maps obtained for hydroxyl-weighted CEST, glutamate-weighted CEST and rNOE are shown in Figure 5.6, for subject number No 15. It is worth noting that the contrasts obtained are different for each of these modalities. Hydroxyl-weighted CEST tends to show a stronger signal for the gray matter periphery and for the cuneus and precuneus regions. Glutamate-weighted CEST appears at first glance to show a similar contrast, but this is different in several respects. It appears to be more correlated with the presence of gray matter, entering the sulci more deeply. It also seems less present in the cuneus region. Finally, rNOE presents an inverse contrast, more intense in the white matter, in line with the literature (Craig K. Jones et al. 2013; Paech, Zaiss, et al. 2014). It seems that the rNOE is

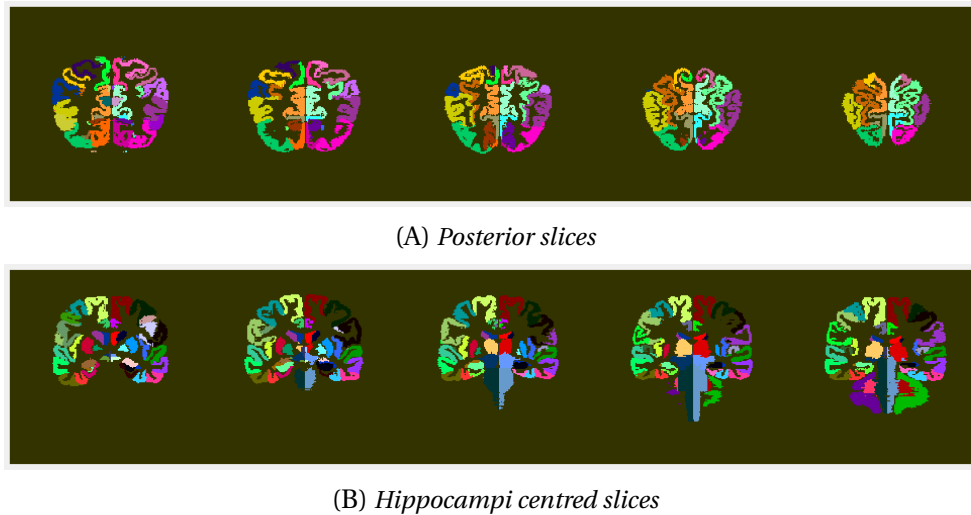


Figure 5.4: Atlas normalized in subject reference frame, for the two acquired volumes.

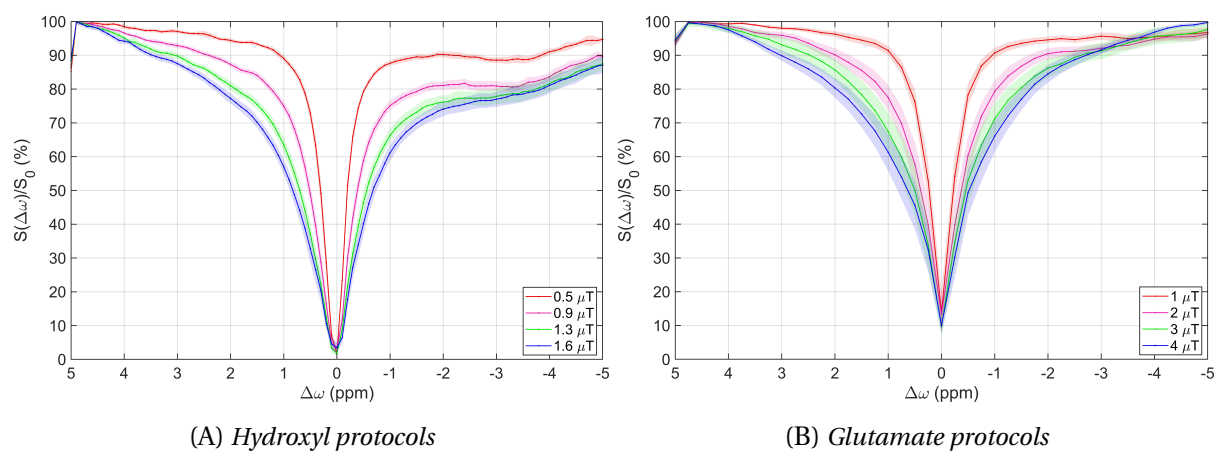


Figure 5.5: Z-spectra obtained in a 50 voxels ROI in the white matter of subject N° 15.

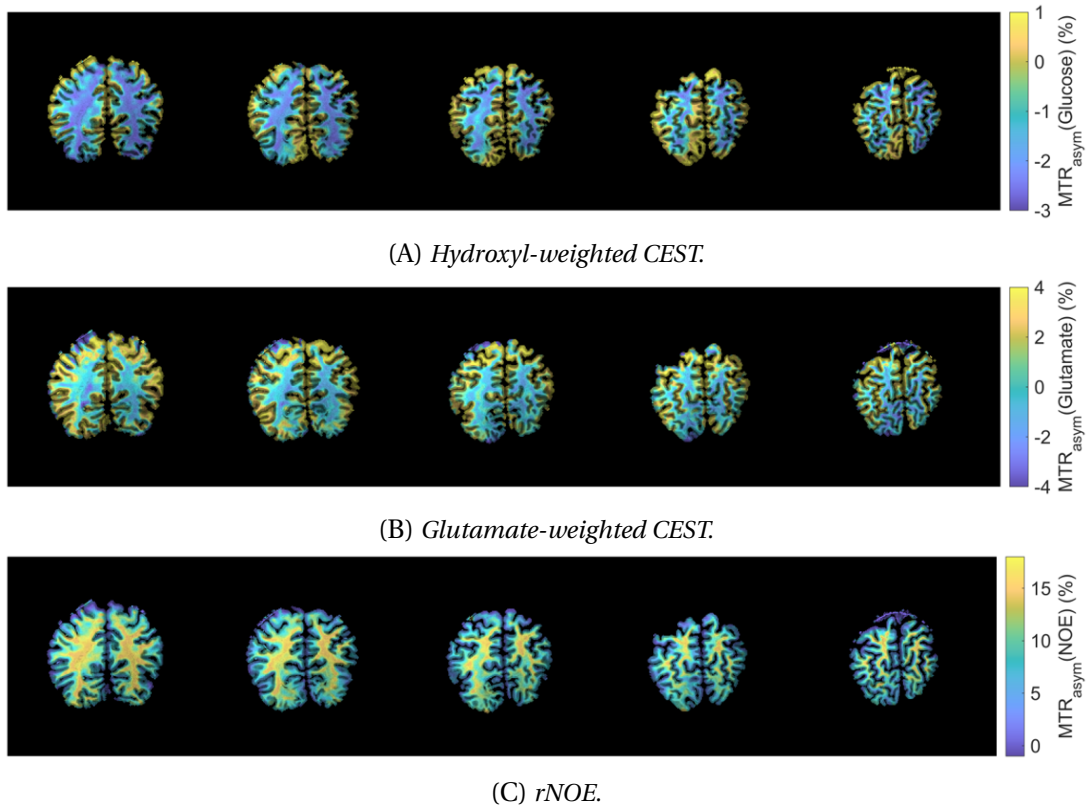


Figure 5.6: MTR_{asym} maps obtained on visual cortex/precuneus slice, data from subject N° 2. The MTR_{asym} maps are overlaid on T_1 weighted anatomical images.

all the more important for deep white matter regions. This may correlate with the presence of larger axon bundles in these regions.

Parcelizing the data obtained by region, and comparing the two groups, young and elderly healthy volunteers, produces interesting results. These are shown in Figure 5.7 for hydroxyl and glutamate weighed CEST. The MTR_{asym} of hydroxyl weighted CEST is significantly lower on average in elderly people by 0.5% ($p = 0.01$). This difference is doubled for glutamate-weighted CEST ($p = 1.43\text{e-}6$). Although there were significant variations between the two groups, and significant variations from one region to another, no significant variations of the CEST in a specific region were found with aging. This means that it is not possible to conclude that one region is more affected by age than another. However, there are an interesting trend that could become significant by increasing the number of volunteers. For hydroxyl-weighted CEST, the largest difference ($\Delta MTR_{\text{asym}} = 1.10\%$) was found in postcentral gyrus (Figure 5.7A), for which the metabolic rate of glucose is known to be negatively correlated with age (Q. Cao et al. 2003). For glutamate-weighted CEST the largest difference ($\Delta MTR_{\text{asym}} = 1.45\%$) was found in the precuneus (Figure 5.7B), a major cortical region for which glutamate concentration decreases with age were previously reported (Cleeland et al. 2019).

For rNOE weighted-CEST, a significant decrease of MTR_{asym} in white matter was detected ($11.5 \pm 0.42\%$ versus $10.54 \pm 0.67\%$, $p = 1.08\text{e-}3$) which is in agreement with Mennecke et al. (2023). The data obtained on the only AD patient are also plotted in Figure 5.7. The data from this first patient seem close to the data from the older volunteers, perhaps slightly lower for hydroxyl-weighted CEST, especially in the precuneus and isthmus cingulate. It is difficult to draw any further conclusions, as the variation in measurement is very large, but perhaps that more volunteers will confirm or infirm these first findings. Also one can note that the standard deviation of the elderly volunteers data is greater than in young subjects, perhaps because the inter-subject variability is greater, but also maybe because older subjects find it more difficult to remain motionless throughout the acquisition.

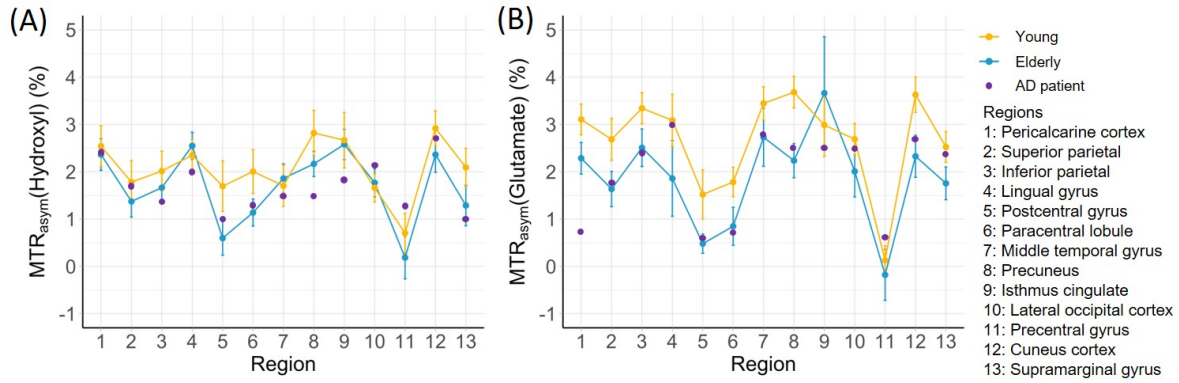


Figure 5.7: Median MTR_{asym} distribution for hydroxyl and glutamate weighted CEST in each ROIs of the posterior volume for young, elderly volunteers and the only AD patient currently scanned.

5.3.2 Hippocampi volume

Similar work was carried out in a more central region, allowing capture of the hippocampi head and its peripheral regions. Figure 5.8 concatenates the different results obtained. As before, glutamate-weighted CEST is highest in the gray matter. In addition, hippocampi stands out quite well, something that can be found again in results obtained in mice (Figure 5.15B) (Luo et al. 2021; Pépin et al. 2016; Cember, Nanga, and R. Reddy 2023). Here again, a significant variation of MTR_{asym} for glutamate-weighted CEST is found between young and elderly volunteers ($p = 1e-9$). This variation of roughly 1.5% is larger than on the posterior volume. As before, there is no significance of a region variation with aging. Nevertheless, it worth noting that the variation between the groups seems larger for the temporal gyrus, superior frontal gyrus and hippocampi, regions known for their strong change with aging (Beason-Held, Kraut, and Resnick 2008; Kokudai et al. 2021). Additional subject scans could make this impression significant.

5.4 Discussion and perspectives

This initial analysis of the acquired data reveals significant variations in CEST contrast between healthy and elderly volunteers. This may be a marker of different metabolic activity between these two groups. Comparison of PET data between these groups of subjects could reinforce these observations. These results are also extremely encouraging for the continuation of the study, which will compare healthy subjects and Alzheimer's patients. Now that we have obtained significant and clear results in healthy subjects, it is reasonable to expect to obtain biomarkers of Alzheimer's disease in CEST once more subjects have been scanned. The scan of healthy volunteers is continuing in order to refine these initial results.

The analysis presented here can be improved. Among the steps that would be crucial to implement for this study are motion correction and correction of B_1 inhomogeneities. Motion correction as implemented for Chapter 4 works very well, with sub-tenths of a voxel accuracy, for slices centered in the brain. For this image region, at the posterior part of the brain with 5 slices, SPM12 did not work robustly. Even after regularization, motion was incorrectly corrected for 30% of subjects, which would have meant throwing away the data. This was not feasible, as it would reduce the number of volunteers in each group, and cherry-picking poses problems of scientific rigor. We therefore dispensed with this correction step, which is detrimental to the quality of the data. Similarly, the correction of B_1 inhomogeneities is an important issue. The use of pTx results in a homogeneity far superior to CP, but some regions are better corrected than others, due to the coil design and the position of its

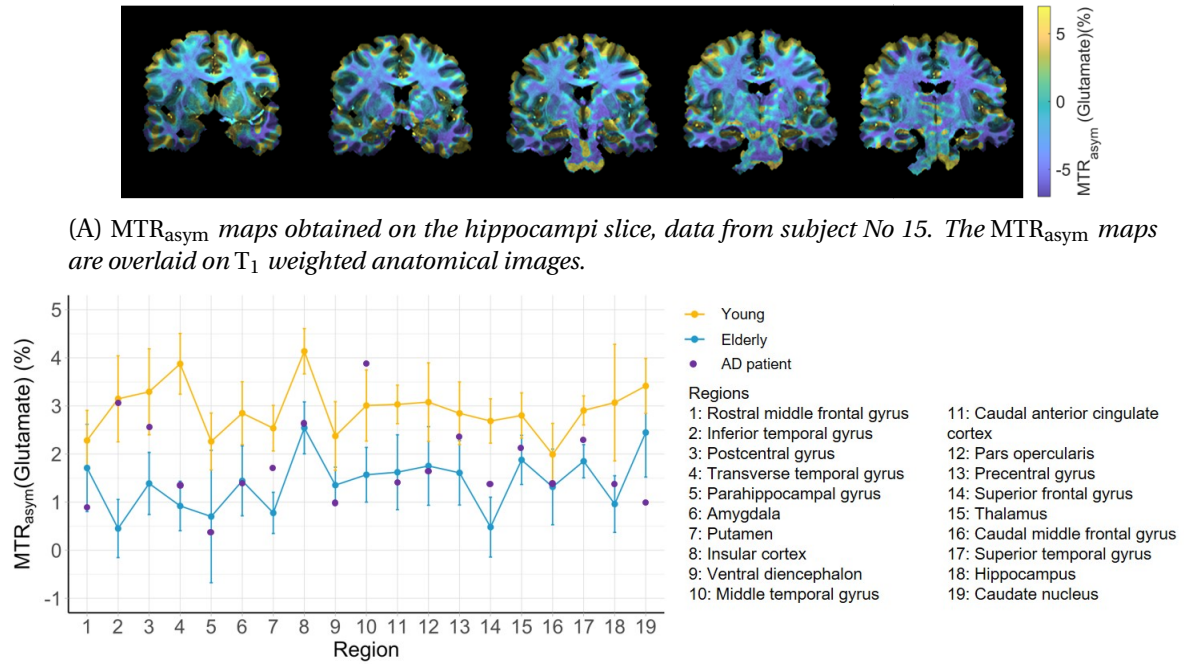


Figure 5.8: Results obtained on the hippocampi centred slices.

loops. The equatorial regions of the brain show a slightly higher saturation in our data, of the order of 10%. We can correct for these effects with a multi-point correction (Windschuh et al. 2015), but this requires a map of B_1 . It is possible to estimate the order of magnitude of the B_1 map by measuring the width at half-height of the acquired Z-spectra, but this method is not very precise, as T_1 and T_2^* also influence this parameter. A solution for estimating the B_1 map would be to use the optimization dataset of our universal pulse to simulate the mean B_1 map, correlate it with the atlas, and then pass it on to the subject reference frame. B_1 would then be corrected directly.

Other ways of improving the quality of our data could be to parcelize the subject data on freesurfer, in order to obtain a precise, tailor-made estimate of cortical regions. This solution, which can be implemented in the short term, requires a great deal of computing power, which we have at our disposal on Neurospin's servers, but setting up this pipeline requires additional work, which is why an atlas has been used here.

A final point to consider is the metric used to estimate the CEST contrast produced by a specific metabolite. As discussed previously in Section 1.1.3, other methods can be considered, such as Lorentzian multi-fit, or fit with analytical solutions.

Compared with MTR_{asym}, these methods have their advantages: they avoid contaminating the estimate by the opposite side of the spectrum, they allow greater use of the available information by combining spectra obtained for different parameterizations, but have the major drawback of requiring numerous initial parameters and constraints in order to be efficient, and only take into account a limited number of pools. In the following section, we aim to develop a CEST metric that enables both simple and robust estimation of CEST.

5.4.1 Simple CEST metric robust to potential frequency sampling trajectory biases

As discussed, quantification is a major problem for CEST. Our project is to develop a metric that will enable simple measurement of the CEST without being disrupted by DS, MT and rNOE. This metric

must be simple to use and not require any additional measurement, as the cost in acquisition time quickly becomes a barrier.

In addition to the quantification challenge in CEST, another problem arises when using the CEST fast steady-state sequence. As explained in Chapter 3, images acquired at different frequencies show an interdependency effect.

In the CEST-EPI-fast sequence implementation, the creation of most of the bias can be avoided by using a symmetrical saturation scheme (see Figure 3.5) and by using a relatively small frequency offset step. This comes with an additional time cost, and getting rid of it would make CEST acquisition even faster and more reliable.

We sought to do two things at once and improve the data processing and CEST estimation while correcting for this interdependency effect.

The work in this section was presented at ESMRMB 2023.

5.4.1.1 Interdependency effect

The interdependency effect is due to the fact that the magnetization is not completely at equilibrium when a new frequency is measured. This effect is also present, but to a smaller extent, in the classic CEST sequence. This means that when switching from one frequency to another, the magnetization retains a trace of the previous state. This subject was touched on briefly in the description of the CEST-fast sequence, but this is an opportunity to come back to it in order to study it in greater detail and propose a solution.

This effect can reach quite significant amplitudes. A simulation of CEST data for a phantom of 10 mM glutamate in water at 17.2 T was carried out, and the results are shown in Figure 5.9. We observe the introduction of a bias with a magnitude comparable to the expected MTR_{asym} . This bias depends on the trajectory, frequency offset step ($\delta\omega$), T_1 , T_2 and B_1 .

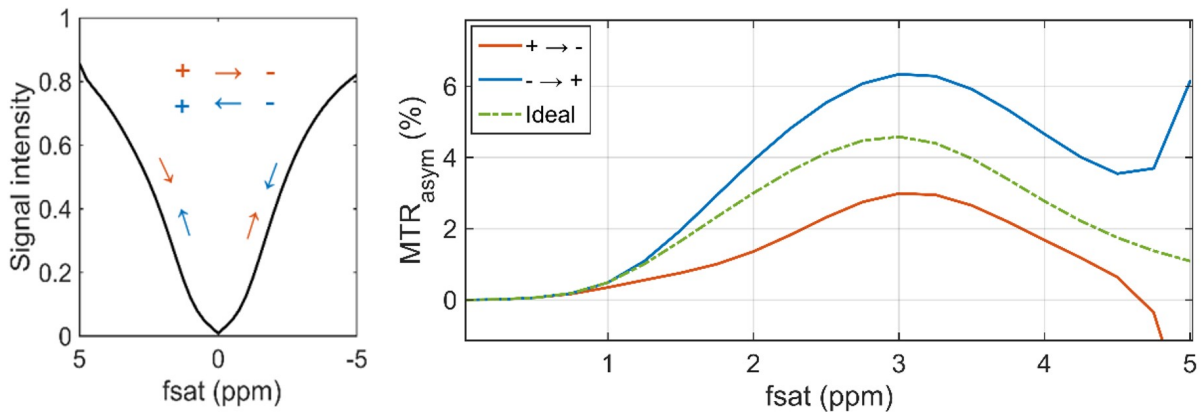


Figure 5.9: Z-spectrum and MTR_{asym} obtained for different sampling trajectories. Simulation of CEST-fast sequence for 10 mM glutamate at 17.2 T. Parameters are $TR = 2500$ ms, $N = 20$, $B_1 = 6$ μ T. Glutamate CEST pool parameters are from (Khlebnikov et al. 2019), Water relaxation time are $T_{1,w} = 3000$ ms, $T_{2,w} = 25$ ms

This effect was repeated experimentally. Figure 5.10 shows spectra obtained experimentally under the same conditions as the simulation in Figure 5.9. The effect on the Z-spectrum is considerable, with over 30% variation in the signal measured between the $\{+, -\}$ and $\{-, +\}$ trajectories at the 40 and -40 ppm points. This can be explained by the jump of 35 ppm between -5 and -40 and between 5 and 40 ppm. On the other hand, if only the spectrum measured between -5 and 5 ppm is considered, the difference is smaller, of the order of 1%. This is confirmed on the MTR_{asym} shown in Figure 5.10B, with the estimated CEST contrast varying by 50% of its value between the two trajectories. Here the bias observed in simulations is found again. This trend is very marked for the first slice imaged, and

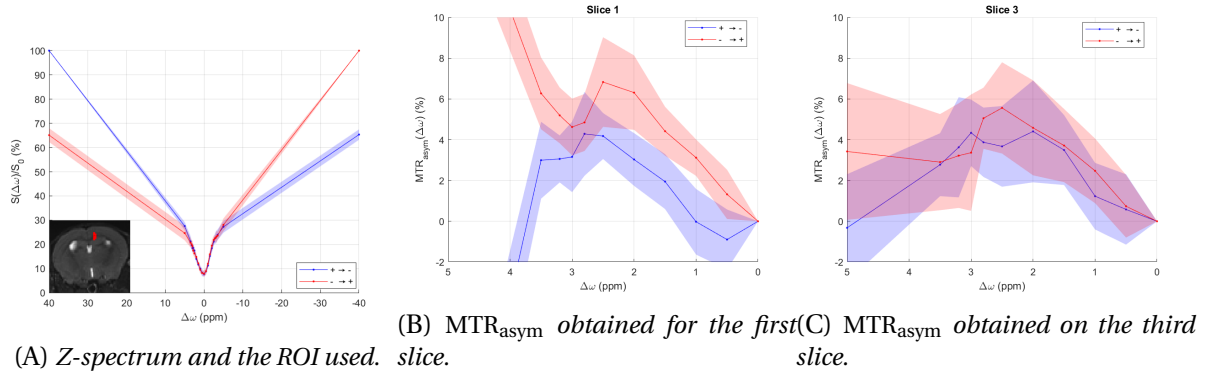


Figure 5.10: Experimental data obtained with CEST-EPI-fast sequence at 17.2 T, for $\{+, -\}$ and $\{-, +\}$ sampling trajectories. 7 slices were acquired.

becomes smaller with each successive slice. Figure 5.10C, which presents the MTR_{asymp} on the third slice, i.e. acquired 3 seconds after the first slice, shows a much smaller bias between the two trajectories, divided by 10.

To correct Z-spectra asymmetries due to frequency sampling order, a simple model is introduced, using one parameter $\beta \in [0, 1]$, accounting for the interdependence between consecutive measurements ($\beta = 1$ corresponds to independent measurements). The relationship between the measurement at ω_n frequency, $S(\omega_n)$, and the previous one at ω_{n-1} , $S(\omega_{n-1})$, is expressed as follows:

$$S_{exp}(\omega_n) = S_{ideal}(\omega_n) (\beta + (1 - \beta) S_{exp}(\omega_{n-1})) \quad (5.1)$$

This model can be used directly to correct the acquired Z-spectra, but this raises the question of how to estimate the parameter β . One can estimate the CEST effect by fitting the direct water saturation and magnetization transfer with a Voigt function and subtracting the fit from the experimental Z-spectrum (Tietze et al. 2014; X.-Y. Zhang et al. 2017; L. Zhang et al. 2019). We propose to modify the Voigt profile used for the fit by introducing this interdependency model to estimate simultaneously the CEST contrast and correct for this bias. Explicitly, the Z-spectrum data is fitted and the residuals are calculated as $S_{fit}(\omega_n) - S_{exp}(\omega_n)$, which gives the CEST contrast corresponding to saturation offsets ω_n .

Here, an estimated Voigt profile $S_{fit}(\omega_n)$ is fitted to the corrected Z-spectrum $S_{corr}(\omega_n)$. With $S_{fit}(\omega) = 1 - L_{DS}(\omega) - G_{MT}(\omega)$, a linear combination of a Lorentzian function to model water direct saturation and a Gaussian function accounting for the MT.

Rewriting Equation (5.1) and combining it with the residual computation, we have:

$$R_{exp}(\omega_n) = S_{fit}(\omega_n) - \frac{S_{exp}(\omega_n)}{\beta + (1 - \beta) S_{exp}(\omega_{n-1})} \quad (\text{modVP}) \quad (5.2)$$

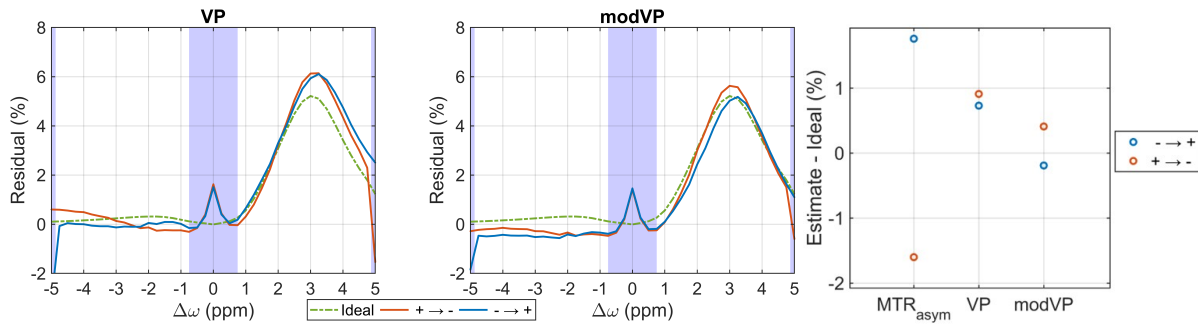
This improved metric is compared with a standard residual approach:

$$R_{exp}(\omega_n) = S_{fit}(\omega_n) - S_{exp}(\omega_n) \quad (\text{VP, Voigt profile})$$

5.4.1.2 Results

In the same way as above, the glucoCEST contrast has been simulated for the two sampling trajectories studied, as well as for the ideal case, i.e. with no interdependence effect. The two metrics, VP or modVP, are estimated over regions of the spectrum with small CEST effects, to make the estimate more reliable. Here the interval $[-0.75, 0.75]$ ppm has been chosen, as well as the points -5 ppm and 5 ppm to fit the model. Figure 5.11A shows that the residuals obtained with the classical estimation,

VP, present a discrepancy with the ideal case, for both trajectories. Similarly, using the modified Voigt profile, the deviation is smaller than the one from the ideal residual for both trajectories. Specifically, the error can be calculated for the gluCEST estimate at 3 ppm. These results are shown in Figure 5.11B. Here it can be identified that the MTR_{asym} introduces an error of a few percent, which, given the size of the peaks observed in CEST, represents an extremely large error. With the use of VP, this error is reduced to around 0.8% for both trajectories. Finally, we obtain the best estimation results with modVP, for which the error is less than 0.5%.



(A) Residuals obtained with VP and modVP for $\{+, -\}$ and $\{-, +\}$ sampling trajectories. (B) Bias introduced in the gluCEST contrast estimation.

Figure 5.11: Simulated performances for glutamate CEST estimation using MTR_{asym} , VP and modVP.

Due to the significant noise present in CEST data, achieving a reliable residual fit can be challenging. However, we have overcome this challenge by employing an iterative fit approach, as described in (I. Y. Zhou et al. 2017), shown in Figures 5.12. In this method, the CEST data sets are first spatially blurred and heavily undersampled. This artificially increases the SNR and allows the first fitting routine to run efficiently. Then, the CEST data volume is iteratively sampled at higher and higher resolution until the original resolution is reached. The result of each step is used as a starting point and regularization for the next step to ensure a stable diffusion of the fitted parameters. Through this iterative fit method, a robust estimation of the modVP parameter is obtained, even in the presence of heavy noise.

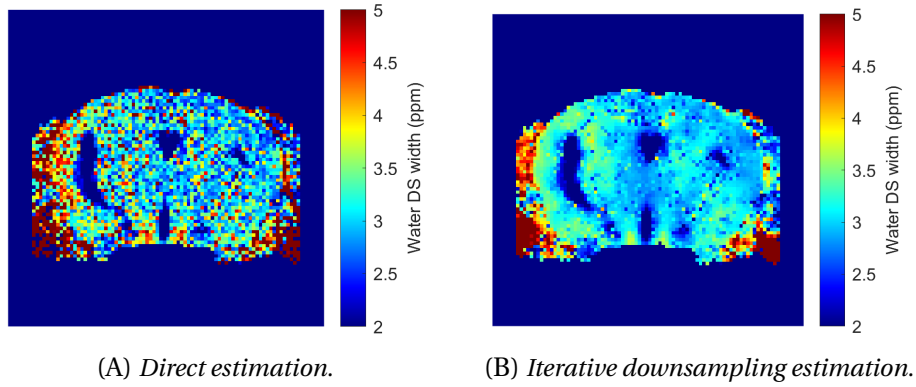


Figure 5.13: Map of parameter obtained for a direct and iterative estimation. The parameter shown here accounts for water peak width.

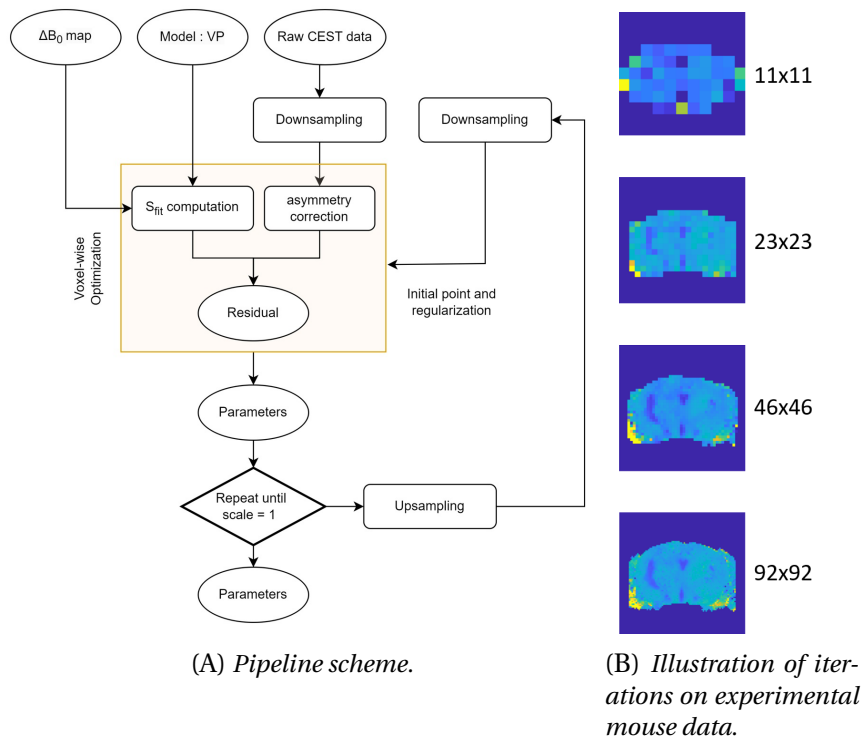


Figure 5.12: Pipeline used for residual estimation, with iterative downsampling.

This approach has proven to be effective in improving the accuracy and reliability of the estimations. This is demonstrated in Figure 5.13, where a great gain in homogeneity of the estimate can be seen, which is now much more robust to noise. Here, the images are taken from data acquired with a CEST-RARE sequence on a mouse at 17.2 T. The acquisition parameters used are: RARE factor = 4, matrix size 92 x 92 x 7, resolution = 150 x 150 x 500 μm , $T_{sat} = 500$ ms, TR = 4000 ms, $B_{1,RMS} = 6 \mu\text{T}$, saturation frequency range = [-40, -5 : 0.25 : 5 40]. It may be noted that the map obtained with the iterative downsampling method, Figure 5.13B, still presents some noise, of the salt-and-pepper type. However, this can easily be remedied by applying a median filter.

The modVP solution is then applied to 7 T experimental data with the robustified pipeline. Scans for both the {+, -} and {-, +} trajectories are acquired. When utilizing the VP fit method, significant differences can be observed in the residuals between these trajectories. However, when switching to the modVP approach, the residuals became comparable, as displayed in Figure 5.14A. It is worth noting here the value of using the residual as a metric. This spectrum clearly distinguishes between

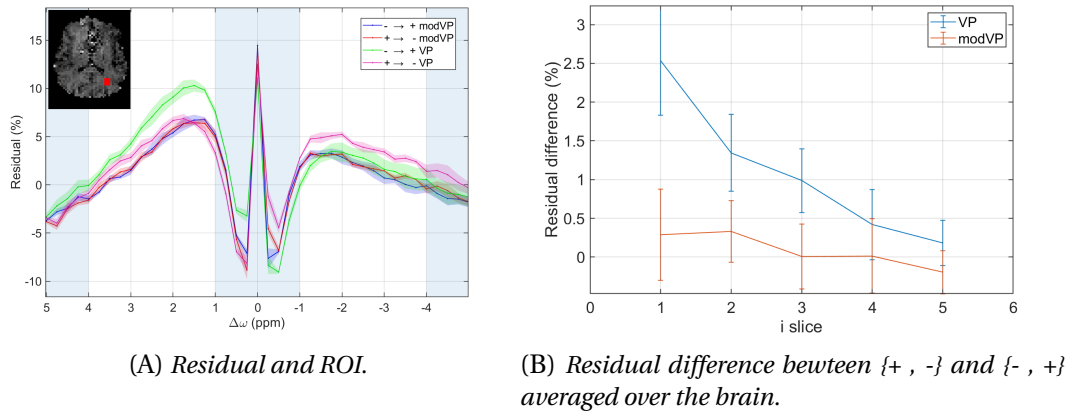


Figure 5.14: Human experimental residuals, obtained for VP and modVP.

CEST contributions on the positive side and rNOE contributions on the negative side. This is not possible with the MTR_{asym} , which mixes the two sides.

The difference between the $\{+, -\}$ and $\{-, +\}$ trajectories was more pronounced when using the VP fit method than modVP, according to the results obtained earlier with simulations. However, by employing the modVP approach instead of VP, this bias was largely eliminated, as demonstrated in Figures 5.14B and 5.15A.

Figure 5.15A exhibits the CEST contrast maps obtained on our human data. Although the maps are extremely noisy and far from being ideal glutamate maps, the best correspondence of the two trajectories can be observed when the effect of measurement interdependence is corrected by modVP. We also observe that the effect of over-contrast and under-contrast that we have for the first slice with the VP metric, disappears when using modVP. These two observations demonstrate that our solution works well.

One drawback of this solution is that the adjustment of this fit is very sensitive. The choice of fit interval, over which the residual of Equation (5.2) is minimized, can have important consequences on the quality of parameter estimation and also on measurement reliability. Choosing an interval that is too wide will include areas of the spectrum with rNOE and CEST variations. The model used, having no parameters to fit the DS and MT, will make a compromise to fit the best and this leads to a drop in the quality of the parameter map (like the one shown in Figure 5.13B). This causes a problem, as the residual is considered to carry the CEST contrast, and if this is matched, it will be attenuated or even erased from the residual. This will result in an artefactual decrease in CEST contrast. On the other hand, if the zone chosen is not wide enough, the parameters will not fit properly, as the rank of our equation system will be too small in comparison with the number of variables to be fitted.

This solution has been applied to data acquired from mice using a CEST-RARE sequence at 17.2 T. This sequence has been set to steady-state condition, enabling a substantial time gain in acquired data. In the same period of time, where 1 slice is traditionally acquired, the steady-state sequence allows the acquisition of 7 slices. The parameters are as follows: Rare factor = 4, matrix size $92 \times 92 \times 7$, resolution = $150 \times 150 \times 500 \mu\text{m}$, $T_{sat} = 500 \text{ ms}$, $TR = 4000 \text{ ms}$, $B_{1rms} = 6 \mu\text{T}$, saturation frequency range = $[-40, -5 : 0.25 : 5 \ 40]$. Figure 5.15B shows the results obtained on three averages of these acquisitions, with trajectories $\{+, -\}$ and $\{-, +\}$. It can be seen that there is a very small difference between the two trajectories for this sequence, which can be explained by the fact that, with a RARE sequence, the time spent on each frequency is long enough for the interdependence effect of the previous frequency to fade. This also explains why there is no difference between slices, unlike in humans with the CEST-EPI-fast sequence.

Figure 5.15B shows on the top line, the MTR_{asym} map at 3 ppm, which is the value corresponding to the maximum weighting for glutamate. With this metric, white matter and ventricles show very similar contrast values, on the order of percent. This is due to the ventricles showing no effect other

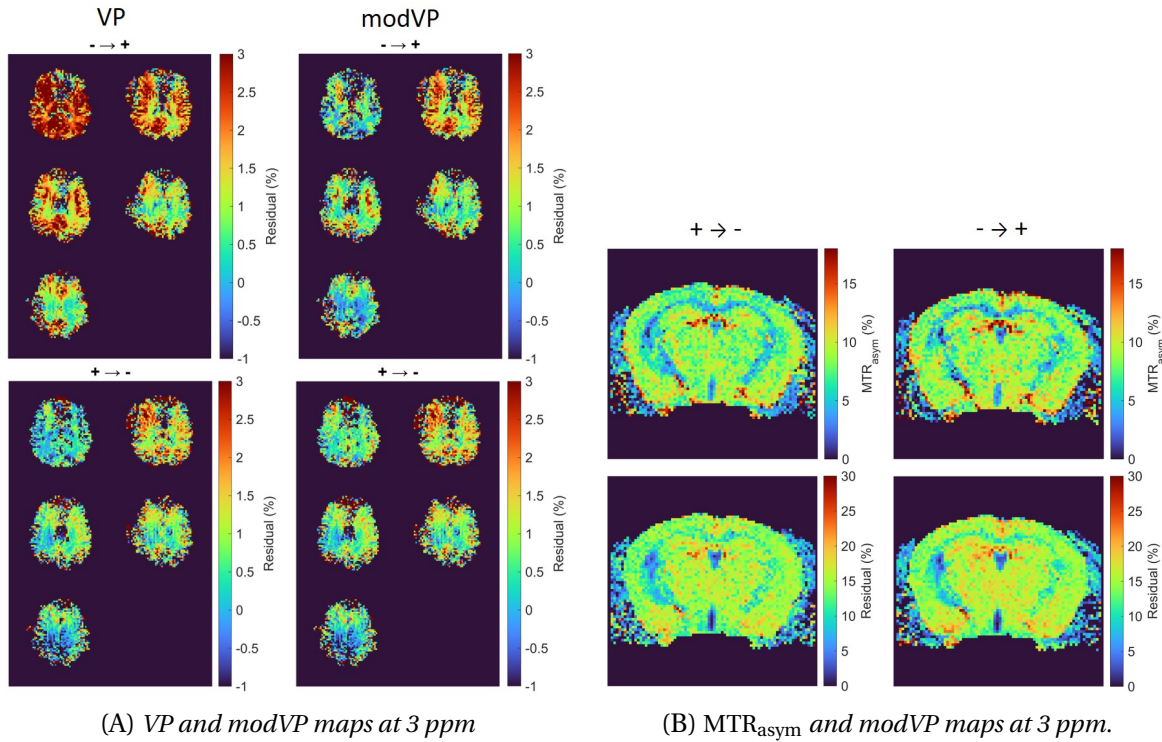


Figure 5.15: Human and mouse experimental CEST contrasts, obtained with the two studied trajectories.

than water direct saturation. For the white matter, this can be explained by the intensity of CEST produced by glutamate and other metabolites resonating at this frequency, which corresponds to the intensity of rNOE in this region, but on the other side of the Z-spectrum. This makes sense, as white matter is known to exhibit significant rNOE due to axon (Craig K. Jones et al. 2013; Zaiss, Kunz, et al. 2013; Paech, Zaiss, et al. 2014). These two contributions cancel each other out when calculating MTR_{asym} . Thus, by simply observing the MTR_{asym} , one would wrongly conclude that the glutamate-weighted CEST contrast is weaker there than in the gray matter, for which the MTR_{asym} is of the order of tens of percent. It should also be noted that the hippocampi stands out particularly well on this contrast, the high density of cell nuclei being at the origin of the more intense contrast in this region (Luo et al. 2021; Pépin et al. 2016; Cember, Nanga, and R. Reddy 2023).

The use of residual to characterize the CEST effect shows its value here: a strong difference is visible between white matter and ventricles, which appear with intensities of around 10% and 1% respectively. With this metric, a good contrast is retained, similar to the one in other regions with the MTR_{asym} . To sum up, the use of residual provides a better estimate of glutamate-weighted CEST than MTR_{asym} .

5.4.1.3 Conclusion

The modVP approach offers several benefits in CEST analysis compared to MTR_{asym} or standard Voigt Profile estimation. First, it effectively reduces bias in CESTfast sequences, leading to more accurate results. Compared to MTR_{asym} , it does not mix informations of up-field and down-field contributions and therefore gives more precise estimations of the CEST contrast. Another advantage is the adaptability of the model presented here, in Equation (5.1), which can be adapted to different fitting strategies, such as multi-Lorentzian fitting or analytic solution fitting.

However, it is important to acknowledge the challenges associated with the modVP approach. One challenge is its sensitivity to noise, which can affect the reliability of the results. Additional work is needed to develop robust metrics that can provide accurate measurements even in the presence of noise. Additionally, fine-tuning the model fitting process can be complex and requires careful attention to achieve optimal outcomes.

5.5 Conclusion

In conclusion, a group of 10 young and 9 elderly subjects and one AD patient were scanned on MRI. The study of the CEST data acquired revealed variation in MTR_{asym} in many brain regions, for glutamate and hydroxyl-weighted CEST as well as for rNOE. This preliminary analysis could be improved on many points, but shows encouraging results, and future comparison with PET data and more Alzheimer's patients could lead to interesting findings. In the longer term, the development of CEST methods and estimation following this work could allow to monitor neuronal activity in human brain using glucoCEST as [Roussel et al. \(2019\)](#) did in rats.

Chapter 6

Conclusion and perspectives

This final chapter summarizes the results obtained in this thesis and discusses the remaining challenges. Then, a vision of the perspectives of this work is given.

Contents

6.1 General conclusion	96
6.2 Perspectives	97
6.2.1 CEST acquisition	97
6.2.2 CEST quantification	97
6.2.3 Futures applications	97
6.3 Conclusion	98

6.1 General conclusion

The objective of this work was to develop CEST MRI in humans at high field ($\geq 7 T$) for evaluating its performance as a biomarker for aging and neurodegenerative diseases.

CEST has proven to be a highly efficient and promising imaging technique, surpassing MRS in measuring metabolites with improved temporal and spatial resolution. CEST can offer valuable insights for diagnosing and understanding various pathologies, ranging from oncology to musculoskeletal diseases and neurodegeneration.

In this context, this thesis aimed to develop rapid and robust CEST routines at high field, facilitating the discovery of new metabolic biomarkers for Alzheimer's disease. The initial project phase involved developing sequences and routines using a realistic phantom to mimic brain inhomogeneities. Parameters specific to pulsed saturation were studied to define protocols for maximizing glucose and glutamate CEST contrast, initially through simulations and subsequently through validation on the phantom. The CEST sequence underwent iterative improvements, resulting in two noteworthy versions: one is single-slice and use pTx for saturation only and the other one allowing multi-slice full pTx (saturation and acquisition). The latter provided a valuable signal-to-noise ratio gain and more efficient data acquisition, crucial for faster and information-rich CEST acquisitions. B_0 inhomogeneities, which are critical for CEST measurements, were estimated using a Lorentzian fit on a WASSR-type acquisition, demonstrating optimal performance.

Following the development of these components, the performance of our sequence in correcting B_1^+ inhomogeneities was investigated. The CEST saturation module used, composed of two pTx pulse modes using VOPs for energy management showed significant gains in saturation homogeneity and time compared to conventional saturations using CP or MIMOSA pulses. Simulations demonstrated that an optimized single-mode pulse already outperforms the conventional CP pulse while using more than two modes does not significantly improve homogeneity. This pTx saturation could be implemented using tailored but also universal pulses, enhancing ease of use in clinical settings. By using VOPs for SAR management instead of Siemens' "protected mode," saturation capabilities were significantly increased, allowing options such as reducing TR, increasing saturation B_1^+ , and also possibly achieving better homogeneity by increasing the optimization's degrees of freedom. As an example, for a level of homogeneity equivalent as the one obtained with MIMOSA, our solution enables a two times shorter TR for the glutamate-weighted CEST protocol. Simulation results were validated in vitro through phantom experiments, demonstrating that improved B_1^+ homogeneity translates into enhanced MTR_{asym} homogeneity and, consequently, improved CEST contrast metric estimation. These promised homogeneity gains were also observed in vivo in six volunteers across different transverse slices for both glutamate and hydroxyl-weighted CEST protocol.

Leveraging these developments CEST data from two groups of healthy subjects were acquired: young (32 ± 4 years old) and elderly (70 ± 4 years old). Statistical analyses showed a significant variation in hydroxyl and in glutamate weighted CEST with age. However, no significant conclusions could be drawn about age related variations in specific regions. The use of MTR_{asym} with the multislice sequence revealed the introduction of a bias due to measurement dependence. An empirical model was developed to account for and correct this effect post-acquisition. Implementing this model into the CEST estimation, achieved through a Voigt function fit, demonstrated in simulations that such correction removes the introduced bias. This implies that multislice CEST acquisitions could be more robust and shorter by eliminating the need for dummy scans. This solution was implemented on both human and mouse data, showing promising results despite challenges related to in-vivo noise sensitivity. The model successfully separated up-field and down-field contributions, which is not possible when using MTR_{asym} .

Overall, this project led to the development of faster and more robust CEST acquisition schemes, bringing it closer to clinical utility. While CEST specificity remains challenging at this stage, improvements in advanced MRI sequences and quantification techniques are promising. The study of cerebral metabolism opens new avenues for understanding various pathologies, and the progress made in this project contributes to the potential of CEST as a valuable tool in the study of neurodegenerative diseases.

6.2 Perspectives

The work undertaken here spans from the programming and optimization of MR pulse sequences to the evaluation of CEST as a biomarker for aging and neurodegeneration. Numerous perspectives arise from these endeavors, and while not all are extensively discussed, three major axes for improvement can be highlighted.

6.2.1 CEST acquisition

Several enhancements in the acquisition method could render CEST even faster and more reliable.

The most refined sequence in this work could be improved in numerous ways. For instance, considering fat saturation might prevent artifacts observed on frontal regions in some data. However, fat saturation is challenging due to energy deposition being a limiting factor. It could restrict the sequence's utility or necessitate a longer TR, which is undesirable. Implementing GRAPPA for a more efficient readout could lead to acquisitions with finer resolution or shorter TE, enhancing SNR. Non-Cartesian k-space sampling, as the sparkling approach developed in the laboratory [Lazarus et al. 2019](#); [Chaithya et al. 2022](#), might also improve SNR. Shifting to a segmented 3D-EPI sequence, using a steady-state approach and full pTx, could provide both SNR gains and better brain coverage.

From a more speculative standpoint, one could exploit the spatial and spectral correlations in CEST data by the combination of high-spectral-resolution CEST linescan ([Bardin et al. 2022](#)) and measures with sparse Z-spectrum acquisitions at specific frequency offsets. Using both type of acquisitions, it would be possible to reconstruct a volume of data with high spatial and temporal resolution, significantly saving acquisition time.

6.2.2 CEST quantification

While it is possible to optimize acquisition parameters for a specific metabolite, extracting quantitative data poses a major challenge for CEST, due to the overlap of different contributions on the Z-spectrum. As presented in Section 1.1.3, various metrics and solutions exist to address this challenge, but none emerge as the ideal solution. Some require substantial a priori knowledge and measurements, others introduce errors and biases, and generally they are limited by the size of the model used (rarely exceeding 6 Lorentzians functions or 6 pools for analytical equations). Promising approaches like fingerprinting could offer better analysis, but they are constrained by the dictionary's size. Solutions using deep learning could help avoid complex, computationally expensive modeling. The critical lever here is the training aspect. Camelia Ressam's work, a PhD student in our team, could solve these issues by employing deep learning solutions on data obtained at different field strengths (clinical 7 T, clinical 11.7 T, and preclinical 17.2 T). This approach could leverage the advantages of ultra-high magnetic fields to quantify data obtained at lower fields.

6.2.3 Futures applications

Although it is interesting to apply the methods developed to the study of aging, the real value lies in the study of neurodegenerative disorders. Scans of Alzheimer's patients are underway with the hope

of obtaining new disease biomarkers. In addition to this, comparison with PET in healthy volunteers will provide an additional line of study, which will certainly raise interesting points about the glucoCEST/PET-FDG complementarity.

Some of the routines and expertise used in this thesis, such as CEST data processing and the use of steady-state, are currently used in preclinical projects by Romain Gaudin, a PhD student in the team. The acquisition of data from mice of different ages could lead to interesting translational conclusions regarding variations in glutamate-weighted CEST and other metabolites. An application of glucoCEST to measure neuronal activity was performed in the team (Roussel et al. 2019) and was one of the motivations for this work. At present, such measurements are not feasible in humans. However, ongoing advances in the field and new quantification methods may one day allow the measurement of metabolic changes associate with neuronal activation by using CEST.

More generally, the gains in time, homogeneity and robustness made possible by the work presented in this thesis can be exploited to bring CEST even closer to clinical use. This may one day make CEST a reference method for the characterization of tumors or neurodegenerative diseases, and thus enable better management of these pathologies.

6.3 Conclusion

In conclusion, this work has significantly advanced CEST for practical clinical use, overcoming the challenges associated with high magnetic fields. The methodology developed, which incorporates innovative pulse strategies and recent sequence design, has brought significant improvements to CEST acquisitions, enhancing homogeneity, speed, and robustness. Thanks to a comprehensive exploration, the study revealed global age-related variations in glutamate and hydroxyl weighted CEST. From sequence refinement to in vivo applications, this project contributes to the dynamic landscape of CEST MRI, offering promising prospects for biomarkers of neurodegenerative disease and underlining its potential in clinical neuroimaging.

Chapter 7

List of publications

The projects of this PhD thesis led to a publication and several scientific communications.

Peer-reviewed article

- **T Delebarre**, V Gras, F Mauconduit, A Vignaud, N Boulant and L Ciobanu, *Efficient optimization of chemical exchange saturation transfer at 7 T using universal pulses and virtual observation points*, Magnetic Resonance in Medicine 2023

Conference communications

- T Delebarre, **C Ressam**, V Gras, F Mauconduit, A Vignaud, M Bottlaender, N Boulant and L Ciobanu, *Characterization of metabolic changes in healthy aging using high-field CEST MRI*, EMIM 2024, Porto - poster
- **R Gaudin**, T Delebarre, E Selingue, M Glatigny, L Ciobanu and D Boido, *Mapping glutamate in the mouse brain with Chemical Exchange Saturation Transfer at 17.2T*, EMIM 2024, Porto - poster
- **T Delebarre**, D Boido and L Ciobanu, *A simple CEST metric robust to potential frequency sampling trajectory biases*, ESMRMB 2023, Basel - oral
- **T Delebarre**, V Gras, F Mauconduit, A Vignaud, N Boulant and L Ciobanu, *Schéma de saturation RF optimisé en transmission parallèle pour l'IRM CEST à 7T*, SFRMBM 2023, Paris - poster and power pitch
- **T Delebarre**, V Gras, F Mauconduit, A Vignaud, N Boulant and L Ciobanu, *CEST MRI at 7T using an optimized parallel transmission saturation scheme*, ISMRM 2022, London - poster

Appendix A

Glutamate CEST experiments

Some work, similar to those performed for gluCEST (Section 3.2) were also done on the glutamate phantom ball to correlate simulations and experiments. These experiments were also performed to assess the dependence of gluCEST on experimental parameters. The comparison was also done using the CEST-EPI and CEST-EPI fast sequences to maximize the contrast obtained with glutamate for both sequences. The different experiments performed with the two sequences are summarized in Table A.1.

Protocol from	$B_{1,RMS}$ (μT)	T_p (ms)	T_d (ms)	N	$\delta\omega$ (ppm)	N_{slice}
Simulations	3	50	10	16	-	1
CEST-EPI Figure A.1	3.75	50	10	6	0.25	1
	3			10		
	2.25			16		
	1.5			40		
CEST-EPI-fast Figure A.2	3	50	10	2	0.25	5
	2.1			4		
	1.5			8		
CEST-EPI-fast Figure A.3	3	50	6	2	0.25	5
			30			
			100			
			300			
			600			

Table A.1: Experimental parameters used for the gluCEST optimization using CEST-EPI and CEST-EPI-fast sequence as well as those obtained in simulation.

Because energy deposition is crucial in CEST and especially if we are aiming for maximum glutamate contrast, a compromise is needed, as it has already been done for the choice of parameters based on simulations (Section 3.2.4). Thus, it is not interesting to vary $B_{1,RMS}$ as the only parameter in the experiments, but rather to carry out the experiments at constant energy deposits, i.e. at constant $B_{1,RMS,TR}$. This explains why the relationship between $B_{1,RMS}$ and the number of pulses, Table A.1, is quadratic.

Using the CEST-EPI sequence first, we obtain the results shown in Figure A.1. The Z-spectrum shows less dependence on $B_{1,RMS}$ than that observed for Figures 3.19 and 3.22, but this is explained by the variable duration of saturation, which counterbalances the difference in $B_{1,RMS}$. The MTR_{asym} is highest for 2.25 μT and 16 pulses. More intense but shorter saturation, or less intense but longer saturation, all generate less gluCEST contrast.

Similarly, for results obtained with the CEST-EPI fast threshold (Figure A.2), maximum contrast

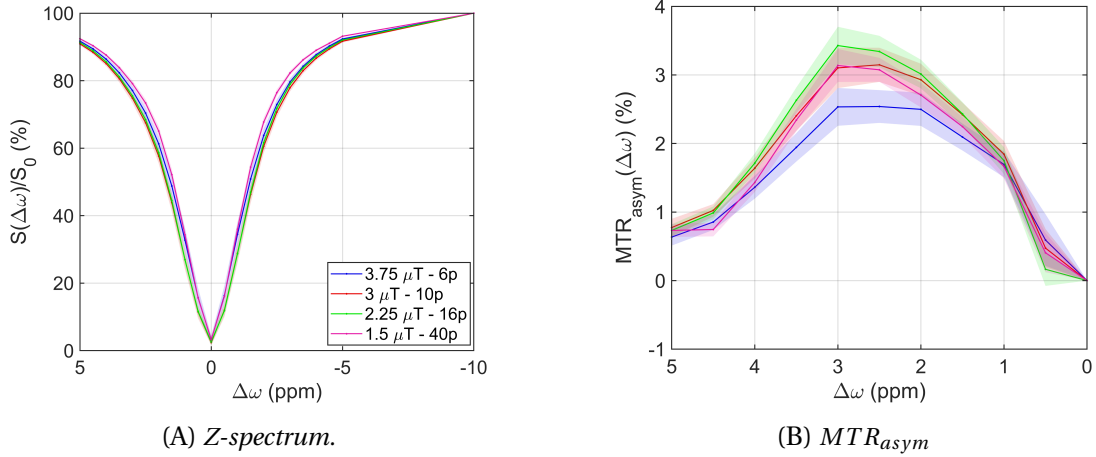


Figure A.1: Comparison of experimental spectra obtained with different B_1 and pulse number N , with the CEST-EPI sequence.

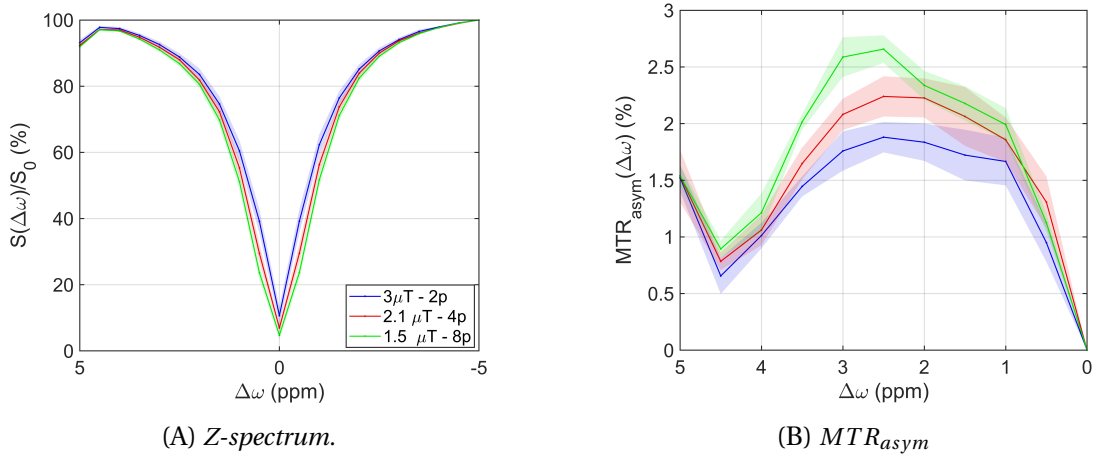


Figure A.2: Comparison of experimental spectra obtained with different B_1 and pulse number N , with the CEST-EPI-fast sequence.

is obtained at a saturation of $1.5 \mu\text{T}$ and 8 pulses. These two experimental optimums are obtained at 17°C . This temperature difference may explain why a $B_{1,RMS}$ of $1.5 \mu\text{T}$ gives better contrast than a $B_{1,RMS}$, which is, a priori, in contradiction with the simulations shown in Figure 3.16.

Figure A.3B shows results in line with expectations. As the interpulse interval increases, the contrast obtained decreases. This is an interesting point to study. As protons with an exchange rate low enough to be in slow-exchange conditions could exhibit a variation in contrast, that is not monotonic with interpulse.

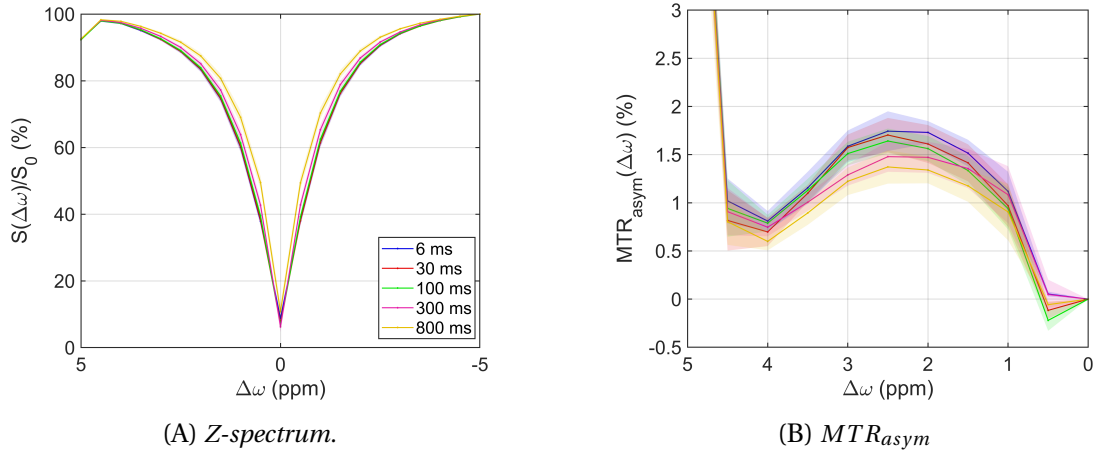


Figure A.3: Comparison of experimental spectra obtained with different B_1 and pulse number N , with the CEST-EPI-fast sequence.

Conclusion

The experimental results obtained here on the glutamate phantom are sometimes far from what had been optimized on the simulator. This can be explained by the phantom temperature, which was much lower than that used in the simulations. Further experiments could be carried out to refine these results. The results obtained on the simulators correlate well with experience for gluco-CEST, and may help to ensure that the screens used are reliable. For glutamate, the parameters used throughout this manuscript were therefore be those obtained by numerical resolution of the Bloch-McConnell equations. These parameters are also extremely consistent with the high values used in the literature for glutamate (Cai, Mohammad Haris, et al. 2012; Jia et al. 2020).

Appendix B

Motion correction

Motion is a source of disturbance for all MRI acquisitions and can lead to alterations in the image if it occurs during the k space acquisition. As is often the case in CEST, disturbances that affect MRI have extremely significant consequences on the CEST contrast. It is therefore critical to correct for motion in the acquired data. Motion may occur during image acquisition, but it can also occur slowly, throughout the examination. In this case, the acquired data are all of good quality, but the position in the brain of a voxel acquired at different frequencies may be altered. One solution to this problem is to measure movement, frame by frame, in order to register the data set on an average image or on the first image acquired. This ensures that each acquired Z-spectra corresponds to a single voxel. To register such an image set, it is convenient to use the algorithms developed for fMRI. A major difference between CEST and fMRI data is the variation in image intensity during saturation in CEST, whereas fMRI images present a relatively constant contrast throughout the data set.

Several approaches have been explored to regularize the motion correction performed by fMRI algorithms such as those available on SPM or FSL. These include the simple approach of linearly interpolating images over an interval $[-0.6, 0.6]$ ppm (Liebert, Tkotz, et al. 2021). Other more sophisticated approaches were explored, using for example the low-rank information present in the saturated image series (Wech and Köstler 2018; Bie et al. 2019). After exploring and benchmarking several of the methods presented above, I settled on the solution proposed by Breitling et al. (2022) as the latter worked best on my data set.

This method is based on a sliding average of the affine transformation matrix. This sliding average has a Gaussian shape, and its standard deviation is weighted by image intensity. In this way, images that are strongly darkened will have a larger window size than those with maximum light intensity.

This is formalized in the following equation:

$$\tilde{T}_i = \exp \left(\frac{1}{a_i} \sum_{k=0}^{N-1} w_k \exp \left(-\frac{(i-k)^2}{2 \left(\frac{\sigma}{w_k+c} \right)^2} \ln(T_k) \right) \right) \quad (\text{B.1})$$

With:

$$a_i = \frac{1}{a_i} \sum_{k=0}^{N-1} w_k \exp \left(-\frac{(i-k)^2}{2 \left(\frac{\sigma}{w_k+c} \right)^2} \right) \quad (\text{B.2})$$

where σ and c are parameters, N is the number of images in the time series, T_k is the transformation matrix and w_k is an image brightness index so that $w_k = \|\mathbf{M}_k\|^2 / \max_j \|\mathbf{M}_j\|^2$.

Using this moving average, it is possible to detect outliers - data that deviates too far from the median - and replace them with data from the moving average.

This method was used for the results presented in Section 4.4.3, and Figure B.1 shows the motion estimation using SPM, without any additional regularization, and with the method of Breitling et al. (2022).

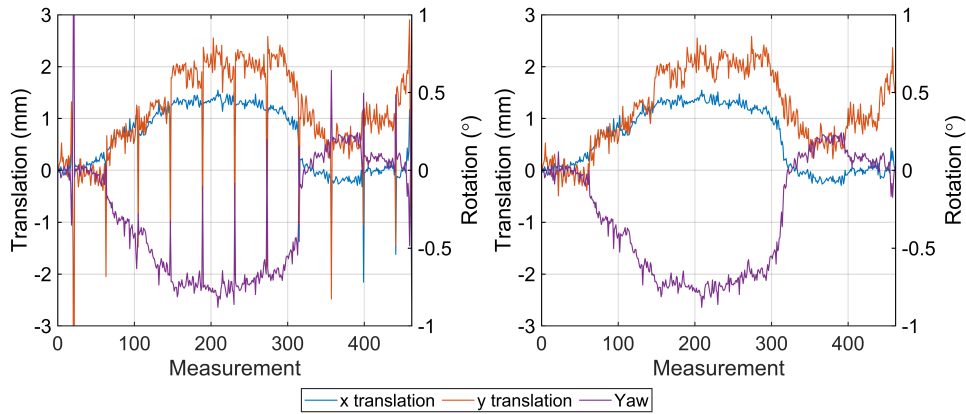


Figure B.1: *Example of motion correction before and after regularization. Result obtained on the data used for Section 4.4.3.*

It can be seen that on the motion values estimated by SPM, without regularization, peaks appear periodically. These peaks correspond to the acquisition of an image at 0 ppm. Using this raw motion correction on our CEST data would corrupt them. After regularization, the peaks disappear and the estimated motion over the 40-minute test period is much more realistic.

Conclusion

The motion correction presented by [Breitling et al. \(2022\)](#) enables us to obtain much more reliable results than those obtained with simple co-registration using an algorithm designed for fMRI. This solution has been successfully implemented on the data presented in Section 4.4.3.

Bibliography

- Adlard, Paul A. et al. (Oct. 31, 2014). “A review of β -amyloid neuroimaging in Alzheimer’s disease”. In: *Front Neurosci* 8. ISSN: 1662-4548.
- Adriany, Gregor et al. (2005). “Transmit and receive transmission line arrays for 7 Tesla parallel imaging”. In: *Magnetic Resonance in Medicine* 53.2, pp. 434–445. ISSN: 1522-2594.
- Aime, Silvio et al. (2002). “Paramagnetic lanthanide (III) complexes as pH-sensitive chemical exchange saturation transfer (CEST) contrast agents for MRI applications”. In: *Magnetic Resonance in Medicine: An Official Journal of the International Society for Magnetic Resonance in Medicine* 47.4, pp. 639–648.
- Alsop, David C., Thomas J. Connick, and Gabor Mizsei (July 1998). “A spiral volume coil for improved RF field homogeneity at high static magnetic field strength”. In: *Magnetic Resonance in Medicine* 40.1, pp. 49–54. ISSN: 0740-3194, 1522-2594.
- Amadon, Alexis et al. (2011). “Validation of a very fast B 1-mapping sequence for parallel transmission on a human brain at 7 T”. In: ISMRM.
- Arnold, JT and ME Packard (1951). “Variations in absolute chemical shift of nuclear induction signals of hydroxyl groups of methyl and ethyl alcohol”. In: *The Journal of Chemical Physics* 19.12, pp. 1608–1609.
- Bardin, Solene et al. (Sept. 1, 2022). “In vivo detection of carnosine and its derivatives using chemical exchange saturation transfer”. In: *Magnetic Resonance in Medicine* 88.3, pp. 1314–1323. ISSN: 0740-3194.
- Beason-Held, L. L., M. A. Kraut, and S. M. Resnick (Apr. 2008). “II. Temporal Patterns of Longitudinal Change in Aging Brain Function”. In: *Neurobiol Aging* 29.4, pp. 497–513. ISSN: 0197-4580.
- Benner, Thomas et al. (2006). “Real-time RF pulse adjustment for B0 drift correction”. In: *Magnetic Resonance in Medicine* 56.1, pp. 204–209. ISSN: 0740-3194.
- Bie, Chongxue et al. (Oct. 2019). “Motion correction of chemical exchange saturation transfer MRI series using robust principal component analysis (RPCA) and PCA”. In: *Quantitative Imaging in Medicine and Surgery* 9.10, pp. 1697–1713. ISSN: 22234292, 22234306.
- Biria, Marjan, Lucia-Manuela Cantonas, and Paula Banca (2021). “Magnetic Resonance Spectroscopy (MRS) and Positron Emission Tomography (PET) Imaging in Obsessive-Compulsive Disorder”. In: *The Neurobiology and Treatment of OCD: Accelerating Progress*. Ed. by Naomi A. Fineberg and Trevor W. Robbins. Vol. 49. Cham: Springer International Publishing, pp. 231–268.

- Bloch, Felix (1946). "Nuclear induction". In: *Physical review* 70.7-8, p. 460.
- Boulant, Nicolas et al. (2018). "Workflow proposal for defining SAR safety margins in parallel transmission". In: ISMRM.
- Breitling, Johannes et al. (2022). "Motion correction for three-dimensional chemical exchange saturation transfer imaging without direct water saturation artifacts". In: *NMR in Biomedicine* 35.7, e4720. ISSN: 1099-1492.
- Cai, Kejia, Mohammad Haris, et al. (Feb. 2012). "Magnetic resonance imaging of glutamate". In: *Nat Med* 18.2, pp. 302–306. ISSN: 1546-170X.
- Cai, Kejia, Anup Singh, et al. (2015). "CEST signal at 2 ppm (CEST@ 2ppm) from Z-spectral fitting correlates with creatine distribution in brain tumor". In: *NMR in biomedicine* 28.1, pp. 1–8.
- Cao, Qiuyun et al. (2003). "Brain glucose metabolism and neuropsychological test in patients with mild cognitive impairment". In: *Chinese medical journal* 116.08, pp. 1235–1238.
- Cao, Zhipeng et al. (May 2015). "Numerical evaluation of image homogeneity, signal-to-noise ratio, and specific absorption rate for human brain imaging at 1.5, 3, 7, 10.5, and 14T in an 8-channel transmit/receive array: Simulating High-Field Human Brain MRI". In: *Journal of Magnetic Resonance Imaging* 41.5, pp. 1432–1439. ISSN: 10531807.
- Cember, Abigail T. J., Ravi Prakash Reddy Nanga, and Ravinder Reddy (2023). "Glutamate-weighted CEST (gluCEST) imaging for mapping neurometabolism: An update on the state of the art and emerging findings from in vivo applications". In: *NMR in Biomedicine* 36.6, e4780. ISSN: 0952-3480.
- Chaithya, GR et al. (2022). "Optimizing full 3d sparkling trajectories for high-resolution magnetic resonance imaging". In: *IEEE Transactions on Medical Imaging* 41.8, pp. 2105–2117.
- Chan, Kannie W. Y. et al. (2012). "Natural D-glucose as a biodegradable MRI contrast agent for detecting cancer". In: *Magnetic Resonance in Medicine* 68.6, pp. 1764–1773. ISSN: 0740-3194.
- Cleeland, Carlee et al. (2019). "Neurochemical changes in the aging brain: A systematic review". In: *Neuroscience & Biobehavioral Reviews* 98, pp. 306–319.
- Cloos, M. A. et al. (2012). "kT-points: Short three-dimensional tailored RF pulses for flip-angle homogenization over an extended volume". In: *Magnetic Resonance in Medicine* 67.1, pp. 72–80. ISSN: 1522-2594.
- Crescenzi, Rachelle et al. (2014). "In vivo measurement of glutamate loss is associated with synapse loss in a mouse model of tauopathy". In: *Neuroimage* 101, pp. 185–192.
- Dagher, Azar P et al. (2000). "Imaging of urea using chemical exchange-dependent saturation transfer at 1.5 T". In: *Journal of Magnetic Resonance Imaging* 12.5, pp. 745–748.
- Davis, Kathryn Adamiak et al. (Oct. 14, 2015). "Glutamate imaging (GluCEST) lateralizes epileptic foci in nonlesional temporal lobe epilepsy". In: *Science Translational Medicine*.

- Debnath, Ayan et al. (Aug. 1, 2020). “Glutamate-Weighted CEST Contrast After Removal of Magnetization Transfer Effect in Human Brain and Rat Brain with Tumor”. In: *Mol Imaging Biol* 22.4, pp. 1087–1101. ISSN: 1860-2002.
- Delebarre, Thaddée et al. (July 2023). “Efficient optimization of chemical exchange saturation transfer MRI at 7 T using universal pulses and virtual observation points”. In: *Magnetic Resonance in Medicine* 90.1, pp. 51–63. ISSN: 0740-3194.
- Dhenain, Marc et al. (Jan. 2009). “Characterization of in vivo MRI detectable thalamic amyloid plaques from APP/PS1 mice”. In: *Neurobiology of Aging* 30.1, pp. 41–53. ISSN: 01974580.
- Diakova, Galina, Jean-Pierre Korb, and Robert G. Bryant (July 2012). “The Magnetic Field Dependence of Water T1 in Tissues”. In: *Magn Reson Med* 68.1, pp. 272–277. ISSN: 0740-3194.
- Dixon, W. Thomas et al. (2010). “A multislice gradient echo pulse sequence for CEST imaging”. In: *Magnetic Resonance in Medicine* 63.1, pp. 253–256. ISSN: 1522-2594.
- Dula, Adrienne N., Elizabeth M. Asche, et al. (Sept. 1, 2011). “Development of chemical exchange saturation transfer at 7T”. In: *Magnetic Resonance in Medicine* 66.3, pp. 831–838. ISSN: 0740-3194.
- Dula, Adrienne N., Siddharama Pawate, et al. (Sept. 1, 2016). “Chemical exchange saturation transfer of the cervical spinal cord at 7 T”. In: *NMR in Biomedicine* 29.9, pp. 1249–1257. ISSN: 0952-3480.
- Eichfelder, Gabriele and Matthias Gebhardt (Nov. 1, 2011). “Local specific absorption rate control for parallel transmission by virtual observation points”. In: *Magnetic Resonance in Medicine* 66.5, pp. 1468–1476. ISSN: 0740-3194.
- Feyter, Henk M. De et al. (2018). “Deuterium metabolic imaging (DMI) for MRI-based 3D mapping of metabolism in vivo”. In: *Science Advances* 4.8, eaat7314.
- Filippi, Massimo and Maria A. Rocca (July 2007). “Magnetization transfer magnetic resonance imaging of the brain, spinal cord, and optic nerve”. In: *Neurotherapeutics* 4.3, pp. 401–413. ISSN: 1933-7213.
- Foerster, Bernd U., Dardo Tomasi, and Elisabeth C. Caparelli (Nov. 1, 2005). “Magnetic field shift due to mechanical vibration in functional magnetic resonance imaging”. In: *Magnetic Resonance in Medicine* 54.5, pp. 1261–1267. ISSN: 0740-3194.
- Forsén, Sture and Ragnar A Hoffman (1963). “Study of moderately rapid chemical exchange reactions by means of nuclear magnetic double resonance”. In: *The Journal of Chemical Physics* 39.11, pp. 2892–2901.
- Fujii, Masashi et al. (Sept. 2, 2019). “Logical design of oral glucose ingestion pattern minimizing blood glucose in humans”. In: *npj Systems Biology and Applications* 5.1. ISSN: 2056-7189.
- Gao, Tianxin et al. (Oct. 26, 2021). “A Brief History and Future Prospects of CEST MRI in Clinical Non-Brain Tumor Imaging”. In: *Int J Mol Sci* 22.21, p. 11559. ISSN: 1422-0067.

- Goffeney, Nicholas et al. (2001). "Sensitive NMR detection of cationic-polymer-based gene delivery systems using saturation transfer via proton exchange". In: *Journal of the American Chemical Society* 123.35, pp. 8628–8629.
- Graesslin, Ingmar et al. (Nov. 1, 2012). "A specific absorption rate prediction concept for parallel transmission MR". In: *Magnetic Resonance in Medicine* 68.5, pp. 1664–1674. ISSN: 0740-3194.
- Gras, Vincent, Markus Boland, et al. (2017). "Homogeneous non-selective and slice-selective parallel-transmit excitations at 7 Tesla with universal pulses: A validation study on two commercial RF coils". In: *PLOS ONE* 12.8, e0183562. ISSN: 1932-6203.
- Gras, Vincent, Alexandre Vignaud, et al. (Feb. 1, 2017). "Universal pulses: A new concept for calibration-free parallel transmission". In: *Magnetic Resonance in Medicine* 77.2, pp. 635–643. ISSN: 0740-3194.
- Gruetter, Rolf and Chris Boesch (Feb. 1992). "Fast, noniterative shimming of spatially localized signals. In vivo analysis of the magnetic field along axes". In: *Journal of Magnetic Resonance (1969)* 96.2, pp. 323–334. ISSN: 00222364.
- Guivel-Scharen, V et al. (1998). "Detection of proton chemical exchange between metabolites and water in biological tissues". In: *Journal of Magnetic Resonance* 133.1, pp. 36–45.
- Hadar, Peter N. et al. (2021). "Volumetric glutamate imaging (GluCEST) using 7T MRI can lateralize nonlesional temporal lobe epilepsy: A preliminary study". In: *Brain and Behavior* 11.8, e02134. ISSN: 2162-3279.
- Haris, Mohammad, Kavindra Nath, et al. (2013). "Imaging of glutamate neurotransmitter alterations in Alzheimer's disease". In: *NMR in Biomedicine* 26.4, pp. 386–391. ISSN: 0952-3480.
- Haris, Mohammad, Anup Singh, et al. (2013). "MICEST: a potential tool for non-invasive detection of molecular changes in Alzheimer's disease". In: *Journal of neuroscience methods* 212.1, pp. 87–93.
- Harris, Robert J. et al. (Nov. 2015). "pH-weighted molecular imaging of gliomas using amine chemical exchange saturation transfer MRI". In: *Neuro-Oncology* 17.11, pp. 1514–1524. ISSN: 1522-8517, 1523-5866.
- Harston, George WJ et al. (2015). "Identifying the ischaemic penumbra using pH-weighted magnetic resonance imaging". In: *Brain* 138.1, pp. 36–42.
- Henkelman, R. M., G. J. Stanisz, and S. J. Graham (Apr. 2001). "Magnetization transfer in MRI: a review". In: *NMR in Biomedicine* 14.2, pp. 57–64. ISSN: 0952-3480, 1099-1492.
- Heo, Hye-Young et al. (2017). "Accelerating chemical exchange saturation transfer (CEST) MRI by combining compressed sensing and sensitivity encoding techniques". In: *Magnetic Resonance in Medicine* 77.2, pp. 779–786. ISSN: 0740-3194.
- Hoult, D.I and R.E Richards (Oct. 1976). "The signal-to-noise ratio of the nuclear magnetic resonance experiment". In: *Journal of Magnetic Resonance (1969)* 24.1, pp. 71–85. ISSN: 00222364.

- Hoult, David I. and D. Phil (2000). "Sensitivity and power deposition in a high-field imaging experiment". In: *Journal of Magnetic Resonance Imaging* 12.1. Cited by: 398; All Open Access, Bronze Open Access, pp. 46–67.
- Hua, Jun et al. (Oct. 2007). "Quantitative Description of the Asymmetry in Magnetization Transfer Effects around the Water Resonance in the Human Brain". In: *Magn Reson Med* 58.4, pp. 786–793. ISSN: 0740-3194.
- Huang, Jianpan et al. (Oct. 28, 2021). "Relayed nuclear Overhauser effect weighted (rNOEw) imaging identifies multiple sclerosis". In: *Neuroimage Clin* 32. ISSN: 2213-1582.
- Huang, Shuning et al. (2017). "Quantitative chemical exchange saturation transfer (CEST) imaging with magnetic resonance fingerprinting (MRF)". In: *Proceedings of the 25th Annual Meeting of ISMRM, Honolulu, HI*, p. 196.
- Hwang, Janice J. et al. (Oct. 19, 2017). "Blunted rise in brain glucose levels during hyperglycemia in adults with obesity and T2DM". In: *JCI Insight* 2.20. ISSN: 2379-3708.
- Jamadar, Sharna D. et al. (Oct. 21, 2020). "Simultaneous BOLD-fMRI and constant infusion FDG-PET data of the resting human brain". In: *Sci Data* 7.1, pp. 1–12. ISSN: 2052-4463.
- Jia, Yanlong et al. (July 28, 2020). "Glutamate Chemical Exchange Saturation Transfer (GluCEST) Magnetic Resonance Imaging in Pre-clinical and Clinical Applications for Encephalitis". In: *Front Neurosci* 14. ISSN: 1662-4548.
- Jiang, Shanshan et al. (2016). "Molecular MRI differentiation between primary central nervous system lymphomas and high-grade gliomas using endogenous protein-based amide proton transfer MR imaging at 3 Tesla". In: *European radiology* 26.1, pp. 64–71.
- Jin, Tao et al. (Aug. 2014). "Mapping brain glucose uptake with chemical exchange-sensitive spin-lock magnetic resonance imaging". In: *J Cereb Blood Flow Metab* 34.8, pp. 1402–1410. ISSN: 0271-678X.
- Jona, Ghil, Edna Furman-Haran, and Rita Schmidt (Jan. 1, 2021). "Realistic head-shaped phantom with brain-mimicking metabolites for 7 T spectroscopy and spectroscopic imaging". In: *NMR in Biomedicine* 34.1, e4421. ISSN: 0952-3480.
- Jones, Craig K et al. (2006). "Amide proton transfer imaging of human brain tumors at 3T". In: *Magnetic Resonance in Medicine: An Official Journal of the International Society for Magnetic Resonance in Medicine* 56.3, pp. 585–592.
- Jones, Craig K. et al. (Aug. 2013). "Nuclear Overhauser enhancement (NOE) imaging in the human brain at 7T". In: *NeuroImage* 77, pp. 114–124. ISSN: 10538119.
- Katscher, Ulrich et al. (Jan. 1, 2003). "Transmit SENSE". In: *Magnetic Resonance in Medicine* 49.1, pp. 144–150. ISSN: 0740-3194.
- Khlebnikov, Vitaliy et al. (Jan. 31, 2019). "Analysis of chemical exchange saturation transfer contributions from brain metabolites to the Z-spectra at various field strengths and pH". In: *Sci Rep* 9, p. 1089. ISSN: 2045-2322.

- Kim, Byungjai et al. (2020). "A deep learning approach for magnetization transfer contrast MR fingerprinting and chemical exchange saturation transfer imaging". In: *Neuroimage* 221, p. 117165.
- Kim, Jinsuh et al. (2015). "A review of optimization and quantification techniques for chemical exchange saturation transfer MRI toward sensitive in vivo imaging". In: *Contrast Media & Molecular Imaging* 10.3, pp. 163–178. ISSN: 1555-4309.
- Kim, Mina et al. (June 2009). "WATER Saturation Shift Referencing (WASSR) for chemical exchange saturation transfer experiments". In: *Magn Reson Med* 61.6, pp. 1441–1450. ISSN: 0740-3194.
- Koch, Kevin M., Douglas L. Rothman, and Robin A. de Graaf (Feb. 2009). "Optimization of static magnetic field homogeneity in the human and animal brain in vivo". In: *Progress in Nuclear Magnetic Resonance Spectroscopy* 54.2, pp. 69–96. ISSN: 00796565.
- Kogan, Feliks, Mohammad Haris, et al. (Jan. 1, 2014). "Method for high-resolution imaging of creatine in vivo using chemical exchange saturation transfer". In: *Magnetic Resonance in Medicine* 71.1, pp. 164–172. ISSN: 0740-3194.
- Kogan, Feliks, Anup Singh, et al. (July 2012). "Investigation of chemical exchange at intermediate exchange rates using a combination of chemical exchange saturation transfer (CEST) and spin-locking methods (CESTRho)". In: *Magnetic Resonance in Medicine* 68.1, pp. 107–119. ISSN: 0740-3194, 1522-2594.
- Kokudai, Yumika et al. (2021). "Cascade process mediated by left hippocampus and left superior frontal gyrus affects relationship between aging and cognitive dysfunction". In: *BMC Neuroscience* 22.1, p. 75. ISSN: 1471-2202.
- Ladd, Mark E. (Apr. 2007). "High-Field-Strength Magnetic Resonance: Potential and Limits". In: *Topics in Magnetic Resonance Imaging* 18.2, pp. 139–152. ISSN: 0899-3459.
- Ladd, Mark E. et al. (Dec. 2018). "Pros and cons of ultra-high-field MRI/MRS for human application". In: *Progress in Nuclear Magnetic Resonance Spectroscopy* 109, pp. 1–50. ISSN: 00796565.
- Lazarus, Carole et al. (2019). "SPARKLING: variable-density k-space filling curves for accelerated T2*-weighted MRI". In: *Magnetic resonance in medicine* 81.6, pp. 3643–3661.
- Le Ster, Caroline et al. (Nov. 1, 2022). "Magnetic field strength dependent SNR gain at the center of a spherical phantom and up to 11.7T". In: *Magnetic Resonance in Medicine* 88.5, pp. 2131–2138. ISSN: 0740-3194.
- Lee, Dong-Hoon et al. (2019). "In vivo mapping and quantification of creatine using chemical exchange saturation transfer imaging in rat models of epileptic seizure". In: *Molecular Imaging and Biology* 21.2, pp. 232–239.
- Lee, Hoonjae et al. (2020). "Model-Based Chemical Exchange Saturation Transfer MRI for Robust z-Spectrum Analysis". In: *IEEE Transactions on Medical Imaging* 39.2, pp. 283–293. ISSN: 1558-254X.

- Leitão, David et al. (2022). “Parallel transmit pulse design for saturation homogeneity (PUSH) for magnetization transfer imaging at 7T”. In: *Magnetic Resonance in Medicine* 88.1, pp. 180–194. ISSN: 1522-2594.
- Li, Chunmei et al. (2015). “Chemical exchange saturation transfer MR imaging is superior to diffusion-tensor imaging in the diagnosis and severity evaluation of Parkinson’s disease: a study on substantia nigra and striatum”. In: *Frontiers in aging neuroscience* 7, p. 198.
- Liddel, Urner and Norman F Ramsey (1951). “Temperature dependent magnetic shielding in ethyl alcohol”. In: *The Journal of Chemical Physics* 19.12, pp. 1608–1608.
- Liebert, Andrzej, Katharina Tkotz, et al. (2021). “Whole-brain quantitative CEST MRI at 7T using parallel transmission methods and correction”. In: *Magnetic Resonance in Medicine* 86.1, pp. 346–362. ISSN: 1522-2594.
- Liebert, Andrzej, Moritz Zaiss, et al. (Aug. 1, 2019). “Multiple interleaved mode saturation (MIMOSA) for B1+ inhomogeneity mitigation in chemical exchange saturation transfer”. In: *Magnetic Resonance in Medicine* 82.2, pp. 693–705. ISSN: 0740-3194.
- Lim, Issel Anne L. et al. (Feb. 2014). “Quantitative magnetic susceptibility mapping without phase unwrapping using WASSR”. In: *NeuroImage* 86, pp. 265–279. ISSN: 10538119.
- Liu, Dapeng et al. (Oct. 1, 2013). “Quantitative characterization of nuclear overhauser enhancement and amide proton transfer effects in the human brain at 7 tesla”. In: *Magnetic Resonance in Medicine* 70.4, pp. 1070–1081. ISSN: 0740-3194.
- Liu, Guanshu et al. (2009). “PARACEST MRI with improved temporal resolution”. In: *Magnetic Resonance in Medicine* 61.2, pp. 399–408. ISSN: 0740-3194.
- Liu, Ruibin, Hongxi Zhang, Weiming Niu, et al. (2019). “Improved chemical exchange saturation transfer imaging with real-time frequency drift correction”. In: *Magnetic Resonance in Medicine* 81.5, pp. 2915–2923. ISSN: 0740-3194.
- Liu, Ruibin, Hongxi Zhang, Yue Qian, et al. (Mar. 1, 2021). “Frequency-stabilized chemical exchange saturation transfer imaging with real-time free-induction-decay readout”. In: *Magnetic Resonance in Medicine* 85.3, pp. 1322–1334. ISSN: 0740-3194.
- Luo, Xunrong et al. (2021). “Glutamate Chemical Exchange Saturation Transfer Imaging and Functional Alterations of Hippocampus in Rat Depression Model: A Pilot Study”. In: *Journal of Magnetic Resonance Imaging* 54.6, pp. 1967–1976. ISSN: 1053-1807.
- Lustig, Michael, David Donoho, and John M. Pauly (2007). “Sparse MRI: The application of compressed sensing for rapid MR imaging”. In: *Magnetic Resonance in Medicine* 58.6, pp. 1182–1195. ISSN: 0740-3194.
- Malik, Shaihan J. et al. (2012). “Tailored excitation in 3D with spiral nonselective (SPINS) RF pulses”. In: *Magnetic Resonance in Medicine* 67.5, pp. 1303–1315. ISSN: 0740-3194.
- Manera, Ana L. et al. (July 15, 2020). “CerebrA, registration and manual label correction of Mindboggle-101 atlas for MNI-ICBM152 template”. In: *Scientific Data* 7.1. ISSN: 2052-4463.

- Mao, Weihua, Michael B. Smith, and Christopher M. Collins (Oct. 2006). “Exploring the Limits of RF Shimming for High-Field MRI of the Human Head”. In: *Magn Reson Med* 56.4, pp. 918–922. ISSN: 0740-3194.
- Marcus, Charles, Esther Mena, and Rathan M. Subramaniam (Oct. 2014). “Brain PET in the Diagnosis of Alzheimer’s Disease”. In: *Clin Nucl Med* 39.10, e413–e426. ISSN: 0363-9762.
- Mareš, J. et al. (Aug. 30, 2023). “Glucose exchange parameters in a subset of physiological conditions”. In: 25.34, pp. 22965–22978. ISSN: 1463-9084.
- Marques, José P. et al. (Jan. 15, 2010). “MP2RAGE, a self bias-field corrected sequence for improved segmentation and T1-mapping at high field”. In: *Neuroimage* 49.2, pp. 1271–1281. ISSN: 1095-9572.
- Maschio, Cinzia and Ruiqing Ni (Apr. 22, 2022). “Amyloid and Tau Positron Emission Tomography Imaging in Alzheimer’s Disease and Other Tauopathies”. In: *Front Aging Neurosci* 14. ISSN: 1663-4365.
- Mauconduit, Franck et al. (2022). “MetaPulse2D: methodology to enable universal slice specific spokes pulses in parallel transmission”. In: ISMRM.
- McConnell, Harden M (1958). “Reaction rates by nuclear magnetic resonance”. In: *The Journal of chemical physics* 28.3, pp. 430–431.
- McMahon, Michael T et al. (2006). “Quantifying exchange rates in chemical exchange saturation transfer agents using the saturation time and saturation power dependencies of the magnetization transfer effect on the magnetic resonance imaging signal (QUEST and QUESP): pH calibration for poly-L-lysine and a starburst dendrimer”. In: *Magnetic Resonance in Medicine: An Official Journal of the International Society for Magnetic Resonance in Medicine* 55.4, pp. 836–847.
- Mennecke, Angelika et al. (2023). “7 tricks for 7 T CEST: Improving the reproducibility of multipool evaluation provides insights into the effects of age and the early stages of Parkinson’s disease”. In: *NMR in Biomedicine* 36.6, e4717.
- Michaeli, Shalom et al. (2002). “Proton T2 relaxation study of water, N-acetylaspartate, and creatine in human brain using Hahn and Carr-Purcell spin echoes at 4T and 7T”. In: *Magnetic Resonance in Medicine* 47.4, pp. 629–633. ISSN: 0740-3194.
- Min, Lisa A. et al. (Oct. 1, 2021). “A decade of multi-modality PET and MR imaging in abdominal oncology”. In: *Br J Radiol* 94.1126. ISSN: 0007-1285.
- Moser, Ewald et al. (2012). “7-T MR—from research to clinical applications?” In: *NMR in Biomedicine* 25.5, pp. 695–716. ISSN: 0952-3480.
- Moses, William W. (Aug. 21, 2011). “Fundamental Limits of Spatial Resolution in PET”. In: *Nucl Instrum Methods Phys Res A* 648 Supplement 1, S236–S240. ISSN: 0168-9002.
- Msayib, Y. et al. (2019). “Quantitative CEST imaging of amide proton transfer in acute ischaemic stroke”. In: *NeuroImage: Clinical* 23, p. 101833. ISSN: 22131582.

- Msayib, Yunus et al. (2022). “Quantitative chemical exchange saturation transfer imaging of nuclear overhauser effects in acute ischemic stroke”. In: *Magnetic Resonance in Medicine* 88.1, pp. 341–356. ISSN: 0740-3194.
- Mulkern, Robert V. and Michael L. Williams (Jan. 1, 1993). “The general solution to the Bloch equation with constant rf and relaxation terms: Application to saturation and slice selection”. In: *Medical Physics* 20.1, pp. 5–13. ISSN: 0094-2405.
- Nasrallah, Fatima A et al. (2013). “Imaging brain deoxyglucose uptake and metabolism by glucoCEST MRI”. In: *Journal of Cerebral Blood Flow & Metabolism* 33.8, pp. 1270–1278.
- Neal, Andrew et al. (2019). “Glutamate weighted imaging contrast in gliomas with 7 Tesla magnetic resonance imaging”. In: *NeuroImage: Clinical* 22, p. 101694. ISSN: 22131582.
- Ng, Man-Cheuk et al. (Mar. 2009). “Magnetization Transfer (MT) Asymmetry Around the Water Resonance in Human Cervical Spinal Cord”. In: *J Magn Reson Imaging* 29.3, pp. 523–528. ISSN: 1053-1807.
- Niess, Fabian et al. (2023). “Reproducibility of 3D MRSI for imaging human brain glucose metabolism using direct (2H) and indirect (1H) detection of deuterium labeled compounds at 7T and clinical 3T”. In: *NeuroImage* 277, p. 120250. ISSN: 1053-8119.
- O’Grady, Kristin P et al. (Oct. 1, 2019). “Glutamate-sensitive imaging and evaluation of cognitive impairment in multiple sclerosis”. In: *Mult Scler* 25.12, pp. 1580–1592. ISSN: 1352-4585.
- Oostveen, Wieke M. van and Elizabeth C. M. de Lange (Feb. 20, 2021). “Imaging Techniques in Alzheimer’s Disease: A Review of Applications in Early Diagnosis and Longitudinal Monitoring”. In: *Int J Mol Sci* 22.4. ISSN: 1422-0067.
- Orzada, Stephan et al. (2010). “RF excitation using time interleaved acquisition of modes (TIAMO) to address B1 inhomogeneity in high-field MRI”. In: *Magnetic Resonance in Medicine* 64.2, pp. 327–333. ISSN: 0740-3194.
- Padormo, Francesco et al. (Sept. 1, 2016). “Parallel transmission for ultrahigh-field imaging”. In: *NMR in Biomedicine* 29.9, pp. 1145–1161. ISSN: 0952-3480.
- Paech, Daniel, Patrick Schuenke, et al. (June 16, 2017). “T1 ρ -weighted Dynamic Glucose-enhanced MR Imaging in the Human Brain”. In: *Radiology* 285.3, pp. 914–922. ISSN: 0033-8419.
- Paech, Daniel, Moritz Zaiss, et al. (2014). “Nuclear Overhauser Enhancement Mediated Chemical Exchange Saturation Transfer Imaging at 7 Tesla in Glioblastoma Patients”. In: *PLOS ONE* 9.8, e104181. ISSN: 1932-6203.
- Pépin, Jérémy et al. (2016). “GluCEST imaging of spinal cord in a mouse model of Friedreich ataxia”. In: ISMRM.
- Perlman, Or et al. (2020). “CEST MR-Fingerprinting: Practical considerations and insights for acquisition schedule design and improved reconstruction”. In: *Magnetic resonance in medicine* 83.2, pp. 462–478.

- Petcharunpaisan, Sasitorn, Joana Ramalho, and Mauricio Castillo (Oct. 28, 2010). "Arterial spin labeling in neuroimaging". In: *World J Radiol* 2.10, pp. 384–398. ISSN: 1949-8470.
- Posner, Michael I et al. (1988). "Localization of cognitive operations in the human brain". In: *Science* 240.4859, pp. 1627–1631.
- Rieke, Viola and Kim Butts Pauly (Feb. 2008). "MR Thermometry". In: *J Magn Reson Imaging* 27.2, pp. 376–390. ISSN: 1053-1807.
- Robitaille, P.-M. L. et al. (Oct. 1, 1998). "Human magnetic resonance imaging at 8 T". In: *NMR in Biomedicine* 11.6, pp. 263–265. ISSN: 0952-3480.
- Roemer, P. B. et al. (Nov. 1, 1990). "The NMR phased array". In: *Magnetic Resonance in Medicine* 16.2, pp. 192–225. ISSN: 0740-3194.
- Ross, B.D. et al. (Jan. 2010). "Hyperpolarized MR Imaging: Neurologic Applications of Hyperpolarized Metabolism". In: *American Journal of Neuroradiology* 31.1, pp. 24–33. ISSN: 0195-6108, 1936-959X.
- Roussel, Tangi et al. (Mar. 14, 2019). "Brain sugar consumption during neuronal activation detected by CEST functional MRI at ultra-high magnetic fields". In: *Sci Rep* 9.1, p. 4423. ISSN: 2045-2322.
- Schmitt, Benjamin et al. (2011). "Optimization of pulse train presaturation for CEST imaging in clinical scanners". In: *Magnetic Resonance in Medicine* 65.6, pp. 1620–1629. ISSN: 1522-2594.
- Schuenke, Patrick, Daniel Paech, et al. (Feb. 7, 2017). "Fast and Quantitative T1 ρ -weighted Dynamic Glucose Enhanced MRI". In: *Scientific Reports* 7.1. ISSN: 2045-2322.
- Schuenke, Patrick, Johannes Windschuh, et al. (Feb. 1, 2017). "Simultaneous mapping of water shift and B1(WASABI)—Application to field-Inhomogeneity correction of CEST MRI data". In: *Magnetic Resonance in Medicine* 77.2, pp. 571–580. ISSN: 0740-3194.
- Schüre, Jan-Rüdiger et al. (2021). "A fast and novel method for amide proton transfer-chemical exchange saturation transfer multislice imaging". In: *NMR in Biomedicine* 34.7, e4524. ISSN: 0952-3480.
- Sehgal, Akansha Ashvani et al. (2019). "CEST MRI of 3-O-methyl-D-glucose uptake and accumulation in brain tumors". In: *Magnetic resonance in medicine* 81.3, pp. 1993–2000.
- Seidemo, Anina et al. (June 1, 2023). "Tissue response curve-shape analysis of dynamic glucose-enhanced and dynamic contrast-enhanced magnetic resonance imaging in patients with brain tumor". In: *NMR in Biomedicine* n/a (n/a), e4863. ISSN: 1099-1492.
- Setsompop, Kawin et al. (2008). "Slice-selective RF pulses for in vivo B inhomogeneity mitigation at 7 tesla using parallel RF excitation with a 16-element coil". In: *Magnetic Resonance in Medicine* 60.6, pp. 1422–1432. ISSN: 0740-3194.
- Singh, Anup et al. (2012). "Chemical exchange saturation transfer magnetic resonance imaging of human knee cartilage at 3 T and 7 T". In: *Magnetic Resonance in Medicine* 68.2, pp. 588–594. ISSN: 0740-3194.

- Snoussi, Karim et al. (2003). "Sensitive CEST agents based on nucleic acid imino proton exchange: detection of poly (rU) and of a dendrimer-poly (rU) model for nucleic acid delivery and pharmacology". In: *Magnetic Resonance in Medicine: An Official Journal of the International Society for Magnetic Resonance in Medicine* 49.6, pp. 998–1005.
- Song, Xiaolei et al. (Oct. 2012). "CEST phase mapping using a Length and Offset VARied Saturation (LOVARS) scheme". In: *Magn Reson Med* 68.4, pp. 1074–1086. ISSN: 0740-3194.
- Statsenko, Yauhen et al. (July 14, 2023). "Multimodal diagnostics in multiple sclerosis: predicting disability and conversion from relapsing-remitting to secondary progressive disease course - protocol for systematic review and meta-analysis". In: *BMJ Open* 13.7. ISSN: 2044-6055.
- Stilianu, Clemens et al. (2022). "Optimization of Pulsed Chemical Exchange Saturation Transfer MRI by Optimal Control". In: ISMRM.
- Sun, Phillip Zhe, Christian T. Farrar, and A. Gregory Sorensen (Dec. 1, 2007). "Correction for artifacts induced by B0 and B1 field inhomogeneities in pH-sensitive chemical exchange saturation transfer (CEST) imaging". In: *Magnetic Resonance in Medicine* 58.6, pp. 1207–1215. ISSN: 0740-3194.
- Sun, Phillip Zhe, Peter CM Van Zijl, and Jinyuan Zhou (2005). "Optimization of the irradiation power in chemical exchange dependent saturation transfer experiments". In: *Journal of magnetic resonance* 175.2, pp. 193–200.
- Sun, Phillip Zhe, Enfeng Wang, et al. (Oct. 2011). "Simulation and optimization of pulsed radio frequency (RF) irradiation scheme for chemical exchange saturation transfer (CEST) MRI - demonstration of pH-weighted pulsed-amide proton CEST MRI in an animal model of acute cerebral ischemia". In: *Magn Reson Med* 66.4, pp. 1042–1048. ISSN: 0740-3194.
- Sun, Phillip Zhe, Jinyuan Zhou, et al. (2007). "Detection of the ischemic penumbra using pH-weighted MRI". In: *Journal of Cerebral Blood Flow & Metabolism* 27.6, pp. 1129–1136.
- Tannús, Alberto and Michael Garwood (Dec. 1997). "Adiabatic pulses". In: *NMR in Biomedicine* 10.8, pp. 423–434. ISSN: 0952-3480, 1099-1492.
- Tee, Y. K. et al. (Sept. 1, 2014). "Comparing different analysis methods for quantifying the MRI amide proton transfer (APT) effect in hyperacute stroke patients". In: *NMR in Biomedicine* 27.9, pp. 1019–1029. ISSN: 0952-3480.
- Thirion, J.-P. (Sept. 1998). "Image matching as a diffusion process: an analogy with Maxwell's demons". In: *Medical Image Analysis* 2.3, pp. 243–260. ISSN: 13618415.
- Tietze, Anna et al. (2014). "Assessment of ischemic penumbra in patients with hyperacute stroke using amide proton transfer (APT) chemical exchange saturation transfer (CEST) MRI". In: *NMR in biomedicine* 27.2, pp. 163–174.
- Togao, Osamu et al. (Mar. 1, 2014). "Amide proton transfer imaging of adult diffuse gliomas: correlation with histopathological grades". In: *Neuro-Oncology* 16.3, pp. 441–448. ISSN: 1522-8517.

- Tolomeo, Daniele et al. (June 22, 2018). “Chemical exchange saturation transfer MRI shows low cerebral 2-deoxy-D-glucose uptake in a model of Alzheimer’s Disease”. In: *Scientific Reports* 8.1. ISSN: 2045-2322.
- Tse, Desmond H.Y. et al. (2017). “inhomogeneity mitigation in CEST using parallel transmission”. In: *Magnetic Resonance in Medicine* 78.6, pp. 2216–2225. ISSN: 1522-2594.
- Van Damme, L. et al. (2021). “Universal nonselective excitation and refocusing pulses with improved robustness to off-resonance for Magnetic Resonance Imaging at 7 Tesla with parallel transmission”. In: *Magnetic Resonance in Medicine* 85.2, pp. 678–693. ISSN: 0740-3194.
- Van de Moortele, Pierre-François et al. (Dec. 2005). “B(1) destructive interferences and spatial phase patterns at 7 T with a head transceiver array coil”. In: *Magn Reson Med* 54.6, pp. 1503–1518. ISSN: 0740-3194.
- Van Zijl, Peter CM et al. (2007). “MRI detection of glycogen in vivo by using chemical exchange saturation transfer imaging (glycoCEST)”. In: *Proceedings of the National Academy of Sciences* 104.11, pp. 4359–4364.
- Varma, Gopal et al. (2015). “Magnetization transfer from inhomogeneously broadened lines: A potential marker for myelin”. In: *Magnetic Resonance in Medicine* 73.2, pp. 614–622. ISSN: 0740-3194.
- Vercauteren, Tom et al. (Mar. 2009). “Diffeomorphic demons: Efficient non-parametric image registration”. In: *NeuroImage* 45.1, S61–S72. ISSN: 10538119.
- Viale, Alessandra et al. (2009). “Hyperpolarized agents for advanced MRI investigations”. In: *The Quarterly Journal of Nuclear Medicine and Molecular Imaging* 53.6, p. 604.
- Villano, Daisy et al. (Mar. 2021). “A fast multislice sequence for 3D MRI-CEST pH imaging”. In: *Magn Reson Med* 85.3, pp. 1335–1349. ISSN: 0740-3194.
- Villien, Marjorie et al. (2014). “Dynamic functional imaging of brain glucose utilization using fPET-FDG”. In: *NeuroImage* 100, pp. 192–199. ISSN: 1053-8119.
- Walker-Samuel, Simon et al. (Aug. 2013). “In vivo imaging of glucose uptake and metabolism in tumors”. In: *Nat Med* 19.8, pp. 1067–1072. ISSN: 1546-170X.
- Wang, Jihong et al. (Nov. 2016). “Magnetic Resonance Imaging of Glucose Uptake and Metabolism in Patients with Head and Neck Cancer”. In: *Scientific Reports* 6.1. ISSN: 2045-2322.
- Wang, Ping (Apr. 2017). “Evaluation of MR thermometry with proton resonance frequency method at 7T”. In: *Quant Imaging Med Surg* 7.2, pp. 259–266. ISSN: 2223-4292.
- Wang, Rui et al. (2015). “Amide proton transfer magnetic resonance imaging of Alzheimer’s disease at 3.0 Tesla: a preliminary study”. In: *Chinese medical journal* 128.05, pp. 615–619.
- Wang, Xinlei et al. (Nov. 2018). “Delay in glucose peak time during the oral glucose tolerance test as an indicator of insulin resistance and insulin secretion in type 2 diabetes patients”. In: *J Diabetes Investig* 9.6, pp. 1288–1295. ISSN: 2040-1116.

- Ward, KM, AH Aletras, and Robert S Balaban (2000). “A new class of contrast agents for MRI based on proton chemical exchange dependent saturation transfer (CEST)”. In: *Journal of magnetic resonance* 143.1, pp. 79–87.
- Webb, Andrew G. and Christopher M. Collins (Mar. 1, 2010). “Parallel transmit and receive technology in high-field magnetic resonance neuroimaging”. In: *International Journal of Imaging Systems and Technology* 20.1, pp. 2–13. ISSN: 0899-9457.
- Wech, Tobias and Herbert Köstler (Nov. 1, 2018). “Robust motion correction in CEST imaging exploiting low-rank approximation of the z-spectrum”. In: *Magnetic Resonance in Medicine* 80.5, pp. 1979–1988. ISSN: 0740-3194.
- Wen, Zhibo et al. (2010). “MR imaging of high-grade brain tumors using endogenous protein and peptide-based contrast”. In: *Neuroimage* 51.2, pp. 616–622.
- Windschuh, Johannes et al. (2015). “Correction of B1-inhomogeneities for relaxation-compensated CEST imaging at 7 T”. In: *NMR in Biomedicine* 28.5, pp. 529–537. ISSN: 0952-3480.
- Winkler, Simone A. et al. (Mar. 2018). “Gradient and shim technologies for ultra high field MRI”. In: *Neuroimage* 168, pp. 59–70. ISSN: 1053-8119.
- Woessner, DE (1961). “Nuclear transfer effects in nuclear magnetic resonance pulse experiments”. In: *The Journal of Chemical Physics* 35.1, pp. 41–48.
- Woessner, Donald E et al. (2005). “Numerical solution of the Bloch equations provides insights into the optimum design of PARACEST agents for MRI”. In: *Magnetic Resonance in Medicine: An Official Journal of the International Society for Magnetic Resonance in Medicine* 53.4, pp. 790–799.
- Wolff, Steven D and Robert S Balaban (1989). “Magnetization transfer contrast (MTC) and tissue water proton relaxation in vivo”. In: *Magnetic resonance in medicine* 10.1, pp. 135–144.
- (Jan. 1, 1990). “NMR imaging of labile proton exchange”. In: *Journal of Magnetic Resonance* 86.1, pp. 164–169.
- Wright, P.J. et al. (Mar. 2008). “Water proton T1 measurements in brain tissue at 7, 3, and 1.5T using IR-EPI, IR-TSE, and MPRAGE: results and optimization”. In: *Magn Reson Mater Phy* 21.1, pp. 121–130. ISSN: 1352-8661.
- Wu, B. et al. (Dec. 2016). “An overview of CEST MRI for non-MR physicists”. In: *EJNMMI Physics* 3.1. ISSN: 2197-7364.
- Xu, Xiang et al. (Dec. 2015). “Dynamic Glucose-Enhanced (DGE) MRI: Translation to Human Scanning and First Results in Glioma Patients”. In: *Tomography* 1.2, pp. 105–114. ISSN: 2379-139X.
- Yadav, Nirbhay N. et al. (Oct. 2012). “Detection of rapidly exchanging compounds using on-resonance frequency labeled exchange (FLEX) transfer”. In: *Magn Reson Med* 68.4, pp. 1048–1055. ISSN: 0740-3194.

- Yan, Kun et al. (2015). "Assessing amide proton transfer (APT) MRI contrast origins in 9 L gliosarcoma in the rat brain using proteomic analysis". In: *Molecular imaging and biology* 17.4, pp. 479–487.
- Yang, Qing X., Weihua Mao, et al. (2006). "Manipulation of image intensity distribution at 7.0 T: Passive RF shimming and focusing with dielectric materials". In: *Journal of Magnetic Resonance Imaging* 24.1, pp. 197–202. ISSN: 1053-1807.
- Yang, Qing X., Jinghua Wang, et al. (2002). "Analysis of wave behavior in lossy dielectric samples at high field". In: *Magnetic Resonance in Medicine* 47.5, pp. 982–989. ISSN: 0740-3194.
- Yang, Yonggui et al. (2020). "Preliminary application of 3.0 T magnetic resonance chemical exchange saturation transfer imaging in brain metastasis of lung cancer". In: *BMC Medical Imaging* 20.1, pp. 1–8.
- Zaiss, Moritz, Goran Angelovski, et al. (Mar. 1, 2018). "QUESTP and QUEST revisited - fast and accurate quantitative CEST experiments". In: *Magnetic Resonance in Medicine* 79.3, pp. 1708–1721. ISSN: 0740-3194.
- Zaiss, Moritz and Peter Bachert (2013). "Exchange-dependent relaxation in the rotating frame for slow and intermediate exchange - modeling off-resonant spin-lock and chemical exchange saturation transfer". In: *NMR in Biomedicine* 26.5, pp. 507–518. ISSN: 0952-3480.
- Zaiss, Moritz, Kai Herz, et al. (2019). "Possible artifacts in dynamic CEST MRI due to motion and field alterations". In: *J Magn Reson* 298, pp. 16–22. ISSN: 1096-0856.
- Zaiss, Moritz, Patrick Kunz, et al. (2013). "MR imaging of protein folding in vitro employing Nuclear-Overhauser-mediated saturation transfer". In: *NMR in Biomedicine* 26.12, pp. 1815–1822. ISSN: 0952-3480.
- Zaiss, Moritz, Johannes Windschuh, Steffen Goerke, et al. (Jan. 1, 2017). "Downfield-NOE-suppressed amide-CEST-MRI at 7 Tesla provides a unique contrast in human glioblastoma". In: *Magnetic Resonance in Medicine* 77.1, pp. 196–208. ISSN: 0740-3194.
- Zaiss, Moritz, Johannes Windschuh, Daniel Paech, et al. (2015). "Relaxation-compensated CEST-MRI of the human brain at 7T: Unbiased insight into NOE and amide signal changes in human glioblastoma". In: *NeuroImage* 112, pp. 180–188. ISSN: 1053-8119.
- Zaiss, Moritz, Junzhong Xu, et al. (Mar. 1, 2014). "Inverse Z-spectrum analysis for spillover-, MT-, and T1-corrected steady-state pulsed CEST-MRI - application to pH-weighted MRI of acute stroke". In: *NMR in Biomedicine* 27.3, pp. 240–252. ISSN: 0952-3480.
- Zhang, Lihong et al. (Oct. 2019). "Voxel-wise Optimization of Pseudo Voigt Profile (VOPVP) for Z-spectra fitting in chemical exchange saturation transfer (CEST) MRI". In: *Quantitative Imaging in Medicine and Surgery* 9.10, pp. 1714730–1711730. ISSN: 2223-4306, 2223-4292.
- Zhang, Shanrong and A Dean Sherry (2003). "Physical characteristics of lanthanide complexes that act as magnetization transfer (MT) contrast agents". In: *Journal of solid state chemistry* 171.1-2, pp. 38–43.

- Zhang, Shanrong, Patrick Winter, et al. (2001). "A novel europium (III)-based MRI contrast agent". In: *Journal of the American Chemical Society* 123.7, pp. 1517–1518.
- Zhang, Xiao-Yong et al. (2017). "Accuracy in the quantification of chemical exchange saturation transfer (CEST) and relayed nuclear Overhauser enhancement (rNOE) saturation transfer effects". In: *NMR in Biomedicine* 30.7, e3716. ISSN: 0952-3480.
- Zhang, Yi et al. (2022). "Acquisition sequences and reconstruction methods for fast chemical exchange saturation transfer imaging". In: *NMR in Biomedicine* n/a (n/a), e4699. ISSN: 1099-1492.
- Zhao, Xuna, Zhibo Wen, Fanheng Huang, et al. (2011). "Saturation power dependence of amide proton transfer image contrasts in human brain tumors and strokes at 3 T". In: *Magnetic resonance in medicine* 66.4, pp. 1033–1041.
- Zhao, Xuna, Zhibo Wen, Ge Zhang, et al. (2013). "Three-dimensional turbo-spin-echo amide proton transfer MR imaging at 3-Tesla and its application to high-grade human brain tumors". In: *Molecular imaging and biology* 15.1, pp. 114–122.
- Zhou, Iris Yuwen et al. (Mar. 7, 2017). "Quantitative chemical exchange saturation transfer (CEST) MRI of glioma using Image Downsampling Expedited Adaptive Least-squares (IDEAL) fitting". In: *Scientific Reports* 7.1. ISSN: 2045-2322.
- Zhou, Jinyuan, Jaishri O Blakeley, et al. (2008). "Practical data acquisition method for human brain tumor amide proton transfer (APT) imaging". In: *Magnetic Resonance in Medicine: An Official Journal of the International Society for Magnetic Resonance in Medicine* 60.4, pp. 842–849.
- Zhou, Jinyuan, Bachchu Lal, et al. (Dec. 2003). "Amide proton transfer (APT) contrast for imaging of brain tumors". In: *Magnetic Resonance in Medicine* 50.6, pp. 1120–1126. ISSN: 0740-3194, 1522-2594.
- Zhou, Jinyuan, Jean-Francois Payen, et al. (2003). "Using the amide proton signals of intracellular proteins and peptides to detect pH effects in MRI". In: *Nature medicine* 9.8, pp. 1085–1090.
- Zhou, Jinyuan, David A Wilson, et al. (2004). "Quantitative description of proton exchange processes between water and endogenous and exogenous agents for WEX, CEST, and APT experiments". In: *Magnetic Resonance in Medicine: An Official Journal of the International Society for Magnetic Resonance in Medicine* 51.5, pp. 945–952.
- Zhou, Yang et al. (2023). "The relayed nuclear Overhauser effect in magnetization transfer and chemical exchange saturation transfer MRI". In: *NMR in Biomedicine* 36.6, e4778. ISSN: 0952-3480.
- Zijl, Peter C. M. van and Nirbhay N. Yadav (2011). "Chemical exchange saturation transfer (CEST): What is in a name and what isn't?" In: *Magnetic Resonance in Medicine* 65.4, pp. 927–948. ISSN: 0740-3194.
- Zijl, Peter C.M. van et al. (Mar. 2018). "Magnetization Transfer Contrast and Chemical Exchange Saturation Transfer MRI. Features and analysis of the field-dependent saturation spectrum". In: *NeuroImage* 168, pp. 222–241. ISSN: 10538119.

Zu, Zhongliang et al. (Oct. 2011). "Optimizing Pulsed-Chemical Exchange Saturation Transfer (CEST) Imaging Sequences". In: *Magn Reson Med* 66.4, pp. 1100–1108. ISSN: 0740-3194.

Titre: Développement d'imagerie métabolique rapide et robuste chez l'Homme à très haut champ magnétique
Mots clés: CEST, IRM, haut champ magnétique, transmission parallèle, métabolisme cérébral

Résumé: L'imagerie par résonance magnétique de l'échange chimique et du transfert de saturation (CEST MRI) représente un outil puissant pour l'étude du métabolisme, offrant une résolution temporelle et spatiale supérieure ainsi qu'une sensibilité accrue par rapport à la spectroscopie par résonance magnétique (SRM). L'IRM CEST permet la détection indirecte de certains métabolites grâce à l'interaction entre leurs protons labiles et ceux de l'eau en vrac. La CEST peut cartographier le glucose, le glutamate et la créatine, qui sont des métabolites importants impliqués dans les cancers et les maladies neurodégénératives et musculosquelettiques, ce qui en fait un outil de bio-imagerie prometteur. Le développement rapide de l'IRM à haut champ magnétique (≥ 7 T) au cours des dernières décennies a grandement bénéficié au CEST, ouvrant la voie à de nouvelles applications et suscitant ainsi un intérêt croissant. L'objectif de cette thèse est de développer l'IRM CEST dans un contexte clinique, en tirant pleinement parti des champs magnétiques élevés pour augmenter la robustesse et la vitesse des acquisitions CEST. Pour ce faire, nous nous concentrons sur deux objectifs principaux. Le premier est de développer la méthode d'imagerie CEST dans un environnement clinique, en surmontant les limitations pratiques associées aux scanners IRM cliniques à haut champ, notamment les contraintes strictes du débit d'absorption spécifique (DAS) et des hétérogénéités de champ

(B1) des RadioFréquences (RF). Pour atteindre ce premier objectif, une séquence CEST à transmission parallèle a été mise au point. La transmission parallèle utilise une antenne d'émission RF multicanal, qui peut être contrôlée indépendamment pour réduire l'hétérogénéité B1. En utilisant la transmission parallèle, nous avons mis en œuvre une stratégie d'acquisition CEST multi-coups en régime permanent, qui nous a permis de produire des images CEST avec trois fois moins d'hétérogénéité B1, et deux fois plus rapidement que l'état de l'art de la littérature. Le deuxième objectif est d'évaluer la performance du CEST, pondérée en glucose et glutamate, dans la détection et la caractérisation du vieillissement normal et pathologique. Une étude clinique a été réalisée, impliquant des volontaires sains jeunes et âgés ainsi que des patients atteints de la maladie d'Alzheimer. Les résultats ont montré que le CEST peut détecter les variations globales de glutamate et de glucose dans le cerveau associées au vieillissement. L'acquisition et l'exploitation de données provenant de patients atteints de la maladie d'Alzheimer sont, eux, toujours en cours. En conclusion, cette thèse a permis de développer des méthodes CEST à haut champ et d'évaluer leurs performances dans l'étude du vieillissement. Ces résultats ouvrent des perspectives encourageantes pour l'utilisation de la CEST comme biomarqueur de la maladie d'Alzheimer et d'autres maladies neurodégénératives.

Title: Development of fast and robust metabolic imaging in human at very high magnetic field
Keywords: CEST, MRI, high magnetic field, parallel transmission, cerebral metabolism

Abstract: Chemical Exchange Saturation Transfer Magnetic Resonance Imaging (CEST MRI) represents a powerful tool for the study of metabolism, offering superior temporal and spatial resolution as well as increased sensitivity compared to Magnetic Resonance Spectroscopy (MRS). CEST MRI enables the indirect detection of certain metabolites through the interaction between their labile protons and those of bulk water. CEST can map glucose, glutamate, creatine, which are important metabolites involved in cancers, and neurodegenerative and musculoskeletal diseases, representing therefore a promising bioimaging tool. The rapid development of high magnetic field MRI (≥ 7 T) in recent decades greatly benefits CEST, opening up new applications and generating growing interest. The aim of this thesis is to develop CEST MRI in a clinical context, taking full advantage of high magnetic fields to increase the robustness and speed of CEST acquisitions. To this end, we focus on two main objectives. The first is to develop the CEST imaging method in a clinical environment, overcoming the practical limitations associated with high-field clinical MRI scanners, notably the strict constraints of Specific Absorption Rate (SAR) and RadioFrequency (RF) field heterogeneities (B1). To achieve this first objective, a parallel transmission CEST sequence was de-

veloped. Parallel transmission uses a multi-channel RF transmit antenna, which can be controlled independently to reduce B1 heterogeneity. Moreover, parallel transmission also allows optimized energy management using virtual observation points (a strategy developed in the laboratory) By making use of parallel transmission we have implemented a multi-slice, steady-state CEST acquisition strategy, which allowed us to produce CEST images with three times less B1 heterogeneity, and two times faster than compared to the state of the art literature reports. The second objective is to evaluate the performance of CEST, glucose, and glutamate weighted, in detecting and characterizing normal and pathological aging. A clinical study was carried out, involving young and elderly healthy volunteers as well as Alzheimer's disease (AD) patients. The results showed that CEST can detect global variations in glutamate and glucose in the brain associated with aging. The acquisition and exploitation of data from AD patients is still in progress. In conclusion, this thesis has enabled the development of high-field CEST methods and the evaluation of their performance in the study of aging. These results open up encouraging prospects for the use of CEST as a biomarker of AD and other neurodegenerative diseases.